Thermochronological approach to the late Neogene exhumation of the European Alps

Antoine J. Vernon

Thesis submitted for the degree of Doctor of Philosophy (PhD)

The University of Edinburgh

Thèse présentée pour obtenir le grade de Docteur en Sciences de l'Université Joseph Fourier, Grenoble I

Spécialité Sciences de la Terre, de l' Univers et de l'Environnement

Submitted, 14th May 2008

Defended in Edinburgh, 18th September 2008

Abstract

Sediment flux from the Alps shows a sharp increase around the Mio-Pliocene boundary (~5 Ma). This observation, linked to the exhumation of the Swiss Molasse basin since ca. 5-4 Ma has led to the suggestion that the Alps experienced accelerated exhumation and isostatic uplift at the orogen scale since this time. The core objectives of this thesis are to assess whether we can document post 5 Ma exhumation of the Alps and its spatial and temporal development, and to review the different potential (tectonic or climatic) factors controlling this denudation. I have developed a novel technique that uses isoage contours associated with age-elevation relationships to exploit the unique density of fission-track ages in the western European Alps, reconstruct cooling isoage surfaces and estimate exhumation rates on the orogen scale between 13.5 and 2.5 Ma. The exhumation histories reconstructed for eight areas of the Western Alps display strong similarities in timing and rate with orogen-wide average denudation rates inferred from sediment volumes. Exhumation rates increased more than twofold since Late Miocene times, and may have been locally modulated by the distinct response of different tectonic units. I then searched for correlation between the spatial pattern of long-term exhumation rates, from the apatite fission-track record, and potential controlling parameters. In the Western Alps, long-term exhumation rates correlate strongly with present-day rates of rock uplift, implying that the rock uplift pattern observed today is ancient. I also observed that the spatial pattern of released seismic energy does not correlate with rock uplift or exhumation, which suggests that exhumation is controlled by isostatic rebound rather than by active tectonic uplift. The lack of correlation between exhumation rates and the present-day distribution of precipitation suggests that the present-day pattern is either non representative of the long-term trend or that factors other than precipitation rate dominate the intensity of exhumation. In order to study the exhumation history in more detail, I sampled two elevation profiles in the central Aar massif (Switzerland) and the western Lepontine Alps (Italy) for AFT and AHe dating which are characterised by steep age-elevation relationships around 8 and 4 Ma. I used the *Pecube* model to predict AFT and AHe ages according to several tens of exhumation scenarios and compared modeled and measured ages. The results of numerical modeling do not reject the hypothesis of two exhumation pulses at 9-7 and 5-3 Ma in the Aar massif. However, this signal is not detected in the Lepontine Alps, and contingent upon further flexural modeling, the exhumation recorded in the Aar massif since 5 Ma does not match the amount required to explain the denudation in the Swiss Molasse basin by flexural isostatic rebound. Rather, the data hint at an additional mechanism of rock uplift, such as the delamination of lithospheric mantle.

Résumé

Le flux de sédiments en provenance des Alpes montre une importante augmentation à la limite Mio-Pliocène (~5 Ma). Cette observation, liée à l'exhumation du bassin molassique suisse depuis 5-4 Ma, a conduit à suggérer que les Alpes ont connu une exhumation et un uplift isostatique accélérés à l'échelle de l'orogène depuis cette période. Les objectifs principaux de cette thèse sont de déterminer s'il existe une hausse de l'exhumation alpine après 5 Ma, de préciser son extension spatiale et temporelle, et de passer en revue les différents facteurs potentiels (tectoniques ou climatiques) contrôlant cette dénudation. J'ai développé durant la thèse une nouvelle technique utilisant les contours isoâge associés aux relations âge-élévation pour, à partir de la mise à jour d'une base de données d'âges par traces de fission dans les Alpes Européennes occidentales, reconstruire des surfaces de refroidissement isoâge et estimer les taux d'exhumation de l'orogène entre 13,5 et 2,5 Ma. Les taux et les périodes d'exhumation obtenus pour huit zones des Alpes Occidentales présentent de fortes similarités avec la dénudation moyenne de l'orogène estimée à partir du volume de sédiments péri-alpins. Les taux d'exhumation ont plus que doublé depuis la fin du Miocène, et peuvent avoir été modulés localement par les caractéristiques des différentes unités tectoniques. J'ai ensuite recherché des corrélations entre les valeurs de taux d'exhumation à long terme, dérivées des données d'âge par traces de fission, et les paramètres de contrôle potentiels. Dans les Alpes Occidentales, les taux d'exhumation à long terme sont fortement corrélés avec les taux d'uplift rocheux présents, suggérant que les valeurs d'uplift actuelles ont peu changé récemment. J'ai aussi observé que la distribution de l'énergie sismique libérée n'est pas corrélée avec l'uplift rocheux ou l'exhumation, ce qui suggère que l'exhumation est contrôlée par rebond isostatique plutôt que par un uplift tectonique actif. L'absence de corrélation entre les taux d'exhumation et la distribution des précipitations actuelles suggère qu'elles ne sont pas représentatives d'une tendance à long terme, ou bien que des facteurs autres que le taux de précipitations contrôlent l'intensité de l'exhumation. Dans le but d'étudier davantage en détail l'histoire de l'exhumation, j'ai réalisé un échantillonnage le long de deux profils altitudinaux dans le centre du massif de l'Aar (Suisse) et à l'ouest des Alpes Lepontines (Italie). Les âges AFT et AHe obtenus se caractérisent par des pentes très élevées de la relation âge-élévation aux alentours de 8 et 4 Ma. J'ai utilisé le modèle *Pecube* pour prédire des âges AFT et AHe selon plusieurs dizaines de scénarios d'exhumation, et j'ai comparé les âges mesurés et prédits. Les résultats des modèles numériques ne permettent pas de rejetter l'hypothèse de deux phases de forte exhumation à 9-7 et 5-3 Ma dans le massif de l'Aar. Cependant, ce signal n'est pas détecté dans les Alpes Lepontines, et sous-réserve de l'apport d'une modélisation flexurale additionnelle, la quantité d'exhumation dans le massif de l'Aar depuis 5 Ma ne permet pas d'expliquer l'exhumation du bassin molassique suisse par rebond flexural isostatique. Au contraire, ces résultats sont de nature à conforter l'existence d'un mécanisme d'uplift rocheux additionnel tel que le détachement de manteau lithosphérique épaissi.

Declaration

This thesis has been composed by myself and represents my own work. Although I wrote the text of this thesis, Chapters 2-4 were written in paper format in collaboration with co-authors. I confirm that as first author, I developed the intellectual arguments and prepared all of the diagrams presented therein. This work has not been submitted for any other degree or professional qualification.

Antoine J. Vernon

Acknowledgements

I would like to thank Michel Ballevre, Pete Cobbold and Denis Gapais who advised me on this position while still a DEA student in Rennes University. My two main supervisors, Hugh Sinclair and Peter van der Beek, designed the original project and kept a vivid interest for it during these several years, always expressing enthusiasm for new ideas while making sure I avoided time-consuming traps. Their availability and great efficiency enabled me to work in a very stimulating and pleasant environment.

I regret I could not spend more time working with Patience Cowie and Finlay Stuart, and would like to thank them for their involvement and very stimulating discussions at different steps of this project. Meinert Rahn, although not an official supervisor, played a major role in my research by providing an early version of the Alpine AFT and ZFT database that I perused, and by always being available to share expert advice on fission-tracks. I also want to thank Didier Marquer, Charlotte Cederbom and Jean-Daniel Champagnac for very stimulating conversations about the Western Alps.

Bardhyl Muceku, Erika Labrin, Cristina Persano and Peter van der Beek taught me AFT counting, while Roderick Brown offered me to use FT microscopes in Glasgow. Fin Stuart and Jurgen Foeken taught me Helium laser extraction in East Kilbride, while Cristina Persano and Valerie Olive helped me with the Uranium-Thorium dissolution prior to ICP-MS quantification. To all, thanks for your clear and patient, and sometimes repeated, explanations. François Senebier in Grenoble provided mineral separations skillfully and in short delays. I am indebted to seatbelt manufacturers and a comforting Swiss police, who enabled me to start this project despite the inopportune attempt of a motorbiker to sabotage my field-work plans.

I would like to thank my colleagues in Grenoble and Edinburgh labs, in particular Benoît, François, Jeremie, Marion, Pierre, Romain, and Xavier; Ciaran, Karin, Laetitia and Mikael for sharing hiking, cycling, climbing, cinema, botany, programming, cheese or karst exploration enthusiasm, as well as their wits on science developments. I shall not forget to thank John, Adam and Tim for leading a memorable mineralogy expedition to southern Greenland. I also want to acknowledge the richness of discussions with students in the geomorphology lab in Grenoble, on exciting projects about the Alps, Venezuela or the Himalayas, and finally my successive office- and flat-mates, who made long working days enjoyable.

I wish to close the list by expressing my deepest thanks to my sisters and parents for their constant support and cheer, and to my grand-parents for an early initiation to the appreciation of fossils and minerals.

I have learned a lot from you all.

Contents

Chapter I
General Introduction
Thermochronological approach to the late Neogene exhumation of the European Alps

I.1. Overview 11
I.2. Research questions 11
I.3. Geodynamic context 12
I.4. Methods and thesis outline 15

Chapter II
Increase in late Neogene denudation of the European Alps confirmed by analysis of a fission-track thermochronology database

II.1. Chapter overview 19
II.1.1. Publication 19
II.1.2. Presentation at international meetings 19
II.1.3. Contributors to Chapter II 20
II.2. Increase in late Neogene denudation of the European Alps confirmed by analysis of a fission-track thermochronology database 21
II.2.1. Introduction 21
II.2.2. Geological setting of the Alps 25
II.2.3. Data 26
II.2.3.1. Apatite and zircon fission-track databases 26
II.2.3.2. Quality and homogeneity of the data 26
II.2.4. Methods 31
II.2.4.1. Maps of interpolated ages / track lengths 31
II.2.4.2. Exhumation rates calculated from paired ZFT and AFT ages 31
II.2.4.3. Reconstruction of isoage surfaces 32
II.2.4.3.1. Production of arrays of isoage points 34
II.2.4.3.2. Interpolation of isoage point arrays 38
II.2.4.4. Estimation of exhumation rates 38
II.2.5. Results 39
II.2.5.1. Main features of the fission-track age patterns 39
II.2.5.2. Variation in exhumation rate from paired AFT and ZFT ages 42
II.2.5.3. Description of isoage surfaces 43
II.2.5.4. Spatial and temporal evolution of exhumation rates 43
II.2.6. Discussion 44
II.2.6.1. Conditions of use of isoage surfaces 44
II.2.6.2. Errors affecting exhumation rate calculations 44
II.2.6.3. Comparison between exhumation rates and the volume of sediment deposited through time 45
II.2.6.4. Possible causes for increased recent exhumation 45
II.2.7. Conclusions 46
II.3. Appendix to Chapter II 48
II.3.1. Map of paired ZFT and AFT ages: ratio between final / initial exhumation rates 48
II.3.2. Maps of AFT isoage surfaces elevation 54
II.3.2.1. Neighbourhood age-elevation relationship 55
II.3.2.2. Calculation of AFT isoage surfaces 55
II.3.2.3. Calculation of exhumation rates using isoage surfaces 71

II.3.2.4. Assessing the use of average distance between isoage surfaces as a proxy for exhumation rate 79
II.3.2.5. Cumulated exhumation rates 80

Chapter III
Spatial correlation between long-term exhumation rates and present-day forcing parameters in the western European Alps

III.1. Chapter overview 85
III.1.1. Publication:..... 85
III.1.2. Presentation at international meetings: 85
III.1.3. Contributors to Chapter III..... 85
III.2. Spatial correlation between long-term exhumation rates and present-day forcing parameters in the western European Alps 86
III.2.1. Introduction 86
III.2.2. Data and methods 88
III.2.3. Correlation results 90
III.2.4. Discussion and conclusions..... 93
III.2.5. Data repository 96
III.2.5.1. Additional tables of Kendall τ-b values in the Western Alps 96
III.2.5.2. Maps used in the study of correlations between long-term exhumation trends and present-day forcing parameters 97
III.3. Appendix to Chapter III 104
III.3.1. Correlation study..... 104
III.3.2. Study areas: Western Alps versus five sub-areas..... 104
III.3.2.1. Western Alps..... 105
III.3.2.2. Queyras area..... 105
III.3.2.3. Ecrins area 105
III.3.2.4. Mont Blanc area 106
III.3.2.5. Lepontine area..... 106
III.3.2.6. Aar area 106
III.3.3. Cross-sections through the raster maps and age database..... 120
III.3.3.1. Aar-Lepontine section 120
III.3.3.2. Simplon section 126

Chapter IV
Late Neogene exhumation of the central European Alps: low-temperature thermochronology from the Aar Massif (Switzerland) and the Lepontine Dome (Italy)

IV.1. Chapter overview..... 131
IV.1.1 Publication 131
IV.1.2. Presentation in international meetings 131
IV.1.3. Contributors to Chapter IV 131
IV.2. Late Neogene exhumation of the central European Alps: low-temperature thermochronology from the Aar Massif (Switzerland) and the Lepontine Dome (Italy) . 132
IV.2.1. Introduction..... 133
IV.2.2. Geological setting 135
IV.2.3. Thermochronology dating..... 136
IV.2.3.1 Sample collection and preparation..... 136
IV.2.3.2 Apatite fission track (AFT) dating..... 137
IV.2.3.3. Apatite Uranium-Thorium / Helium (AHe) dating..... 137
IV.2.4. Results..... 139

IV.2.4.1. AFT ages 139
IV.2.4.2. AHe ages 144
IV.2.4.2.1. Criteria of selection among replicates 144
IV.2.4.2.2. Alpha-ejection correction 144
IV.2.4.3. Modeling the role of apatite zoning on AHe age 148
IV.2.4.4. Age-elevation relationships in the Guttannen and the Formazza elevation profiles 149
IV.2.5. Interpreting exhumation histories using *Pecube* 153
IV.2.6. Discussion and conclusions 159
IV.3. Appendix to Chapter IV 162
IV.3.1. Sampling 162
IV.3.2. Apatite fission-track dating 163
IV.3.2.1. Determination of Zeta value 163
IV.3.2.2. AFT radial plots 165
IV.3.2.3. Quality of AFT dating 166
IV.3.3. Apatite (U-Th) / He dating 174
IV.3.3.1. He yield in laser reheating of single grains 175
IV.3.3.2. Quality of AHe dating 175
IV.3.3.3. Comparison between single grain replicate AHe ages 176
IV.3.4. Comparison between AFT and AHe ages 177
IV.3.5. Dating deformation in the Aar massif 185
IV.3.5.1. Foliation in the Aar massif 185
IV.3.5.2. AFT dating across the Aar frontal thrust 186

Chapter V
Discussion

V.1. Overview and synthesis 191
V.2. Description, interpretation and implications of results 191
V.2.1. Present-day controls on exhumation rates 191
V.2.2. Late Neogene increase in exhumation rate 192
V.3 Future work 196
V.3.1. Following on Chapter II 196
V.3.2. Following on Chapter III 196
V.3.3. Following on Chapter IV 197
V.3.4. Understanding the causes and effects of recent exhumation 197

Chapter VI
General Conclusions 199

References 201

Chapter I
General Introduction

Thermochronological approach to the late Neogene exhumation of the European Alps

I.1. Overview

This thesis investigates the hypothesis of a recent increase in denudation rates in the western European Alps, with the objectives of using thermochronometry and Geographical Information Systems to describe temporal and spatial variations in exhumation. The results of this thesis are detailed in three chapters consisting in a journal article that is either accepted, submitted or in prepatation, followed by an appendix in which some aspects of the study are treated in more details than space in the manuscripts allows. In this introduction, I present the rationale of the research subject, I introduce the context that made this work possible, briefly describe the methods, and outline the structure of the thesis.

I.2. Research questions

Within the long-standing debate on interwoven relationships of orogenic uplift and climate change started by Molnar and England (1990) and Raymo and Ruddiman (1992), the observation of a late Cenozoic worldwide increase in sediment deposition rate (Davies et al., 1977; Zhang et al., 2001; Molnar, 2004) suggested a control of increased frequency and intensity of climate change, including the effect of glacial erosion in elevated areas, on the erosion of mountain belts. Kuhlemann (2000) described a similar ~twofold increase in sediment volume deposited after ca. 5 Ma in the basins collecting detrital material from the western European Alps, (Figure I.2.2). The simultaneous un-loading of the down-flexed European plate was proposed by Cederbom et al. (2004) as the leading factor to explain the ~1 km of exhumation occurring in the Swiss Molasse foreland basin during the same period. Their model requires at least 6.5 km of concomitant exhumation of the chain axis (Figure I.2.3). The high Pliocene denudation rates in the Western Alps are likely to play an important role in present-day rock uplift rate (relative to a reference point located in the north of the Swiss foreland basin), as proposed by Champagnac et al. (2007). Willett et al. (2006) proposed a refinement of the notion of increased Late Miocene denudation, highlighting the role of the Messinian crisis: the lowering of the base level on the southern flank of the Alps, occurring at a time of waning convergence rates, may have contributed to increase erosion

rates. The hypothesis of a widespread exhumation pulse affecting the European Alps is contradicted by the interpretation of sustained exhumation of the Lepontine Alps in SW Switzerland based on detrital thermochronology (Bernet et al., 2001). However, the history of this area is atypical due to the northward indentation of Apulian lower crust underneath the Lepontine nappes, leading to the exhumation of high grade metamorphic material (Pfiffner et al., 2002; Garzanti and Malusa, 2008).

This thesis grew out of the need to validate the hypothesis of extensive exhumation of the Alpine mountain belt since 5 Ma and to determine whether the signal was widespread or localised. The synthesis component of this study was made possible by the availability of a fission-track database covering the Western Alps with unprecedented density (provided by Meinert Rahn in its original version), joined to maps of seismic energy released between 1959 and 2000 (Delacou et al., 2004), average yearly rock uplift from the Swiss Federal Office of Topography (SwissTopo) geodetic database (Schlatter, 2007), and average yearly precipitation from the Swiss Federal Office of Meteorology and Climatology (MeteoSwiss) 1971-1990 database (Frei and Schär, 1998; Schwarb et al., 2001). In addition to the previously available data, this study chose to test further the details of the predictions from Cederbom et al. (2004) by generating new thermochronological data from a traverse across the central Alps.

I.3. Geodynamic context

The European Alps are the result of the collision of several continental and oceanic units formerly part of the margins of the Neotethys Ocean (Schmid et al., 2004). Early high-pressure metamorphism associated with subduction processes was dated between 65 and 35 Ma depending on the area (Rosenbaum and Lister, 2005). The orogen is arc-shaped (Figure I.2.1) in response to the geometry of the Apulian plate indenter (Keller et al., 2006; Garzanti and Malusa, 2008), whose anti-clockwise rotation is responsible for strike-slip deformation (Tricart, 2004) on the southern flank of the chain.

The structures and tectonic units of the Alps have been precisely described for several decades (see for instance Debelmas and Lemoine, 1970). In the Western and Central Alps, the focus has been put on the one hand on metamorphic and deformation histories of internal areas (e.g. Milnes, 1974; Frey et al., 1980; Abrecht, 1994; von Raumer et al., 1999), and on the other hand on the relationships between the mountain chain and its foreland basin, involving processes of lithospheric flexure, sedimentation and deformation of sediments (e.g.

Allen et al., 1986; Homewood et al., 1986; Sinclair, 1996; Schlunegger et al., 1997). The Central Alps constitute also an important milestone in the history of geo- and thermochronology, with the proposition by Platt (1966) that mid-tertiary Rb-Sr and K-Ar ages from the Pennine nappes were not ages of intrusion but ages of unroofing, and the early application of the apatite fission-track dating technique to the understanding of uplift movements in the Swiss and Italian Alps (Wagner and Reimer, 1972).

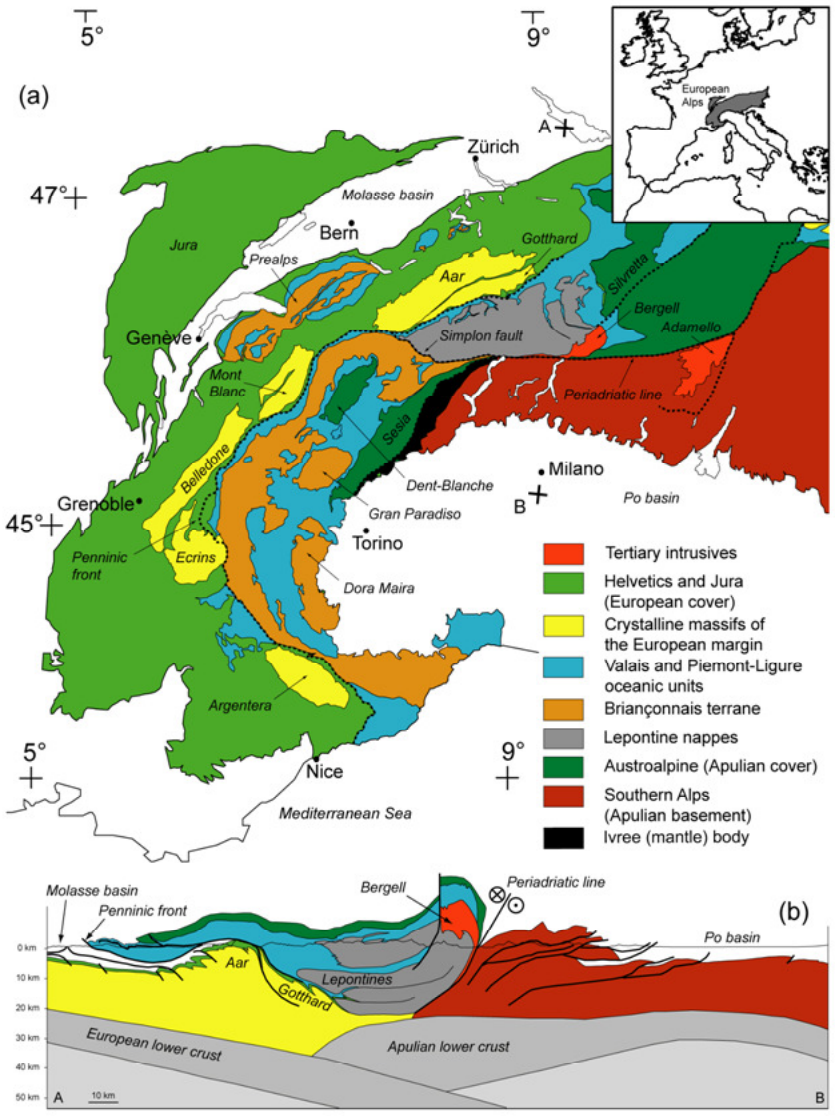

Figure I.2.1. (a) Simplified geologic map of the western European Alps (modified from Schmid et al., 2004). (b) Crustal-scale cross-section along the north-south transect A-B across the central Swiss Alps (modified from Schmid et al., 1996).

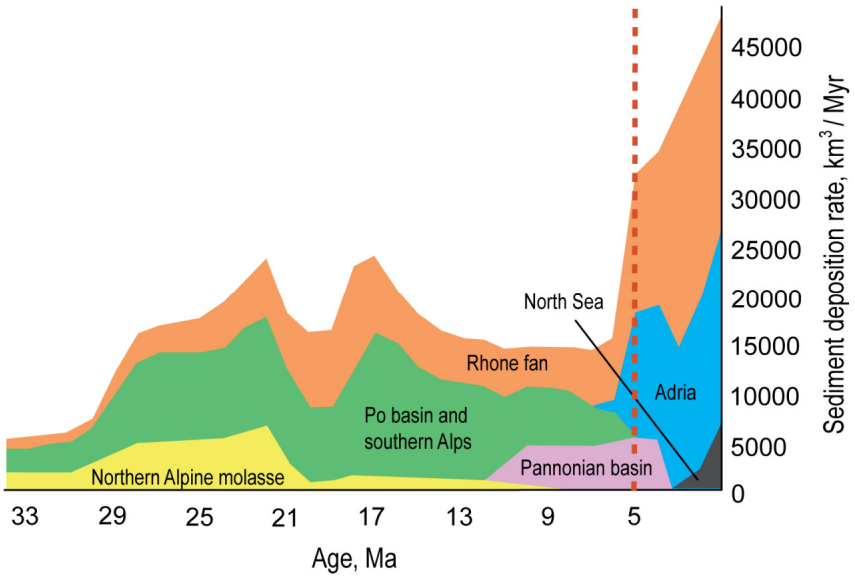

Figure I.2.2. Deposition rates of sediments from the Western Alps, since the Oligocene (after Kuhlemann, 2000). Rates of deposition increased more than twofold since the Mio-Pliocene boundary (red dashed line).

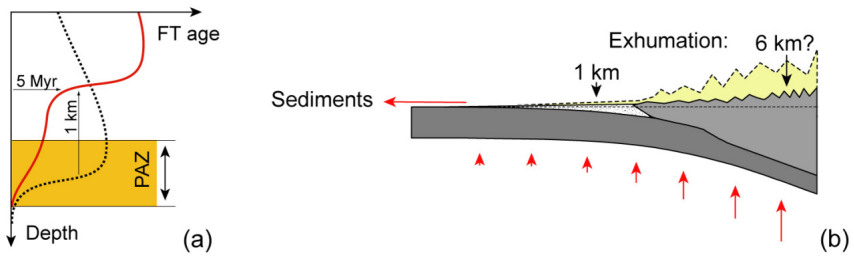

Figure I.2.3. Illustration of the use of detrital apatite fission-track (AFT) ages from a borehole to infer the burial and exhumation history (after Cederbom et al., 2004). (a) Schematic representation of AFT ages measured in a borehole from an area in sedimentation (black line): the detrital ages increase with depth, until reaching the temperature range of the partial annealing zone (PAZ), below which AFT ages are zero. In the Swiss Molasse foreland basin boreholes studied by Cederbom et al. (2004), a "fossil" PAZ has been exhumed ca. 1 km in 5 Myr (red curve). (b) Assuming that1 km of exhumation happening in the Swiss Molasse foreland basin is controlled by flexural isostasy of the European plate, at least 6 km of exhumation are needed over the inner chain.

The low present-day convergence rate between the Apulian and European plates, as demonstrated by GPS data (Calais et al., 2002), joined to the halt of active thrusting at the orogen front (Becker, 2000; Pieri and Groppi, 1981), the exhumation of the northern foreland basin since 5 Ma (e.g. Cederbom et al., 2004) and the extensional focal mechanism of seismicity in the border of the Western Alps (Delacou et al., 2004), all indicate that the Western Alps are not actively deforming by convergence any more, but instead undergoing limited extensional collapse (Selverstone, 2005; Sue et al., 2007b and references therein).

I.4. Methods and thesis outline

Exhumation and **Denudation**. In this study, I will use the terms exhumation and denudation as defined by England and Molnar (1990) and Ring et al. (1999): denudation is the difference between rock uplift and surface uplift, it describes the removal of material from rock column by surficial and / or tectonic processes. Exhumation, or unroofing describes the fact that rock material is brought closer to the Earth surface due to denudation. Thus, the amount of exhumation equals denudation, but they are defined with a different perspective.

The thermochronometers used in this study are the apatite and zircon fission-track techniques (AFT and ZFT), based on the density of crystal defaults (tracks) caused by the spontaneous fission of ^{238}U, and the apatite (U-Th) / He technique (AHe) based on radiogenic He concentration resulting from U and Th alpha-decay through time. Details on the methods can be found e.g. in Laslett et al. (1987); Gallagher et al. (1998); Donelick et al. (2005) for AFT, and in Farley et al. (1996) and Farley (2002) for AHe. A summary of methods is also given in section IV.2.3.

The use of apatite fission-track ages to study the exhumation history of the Alps goes back to the early period of development of this technique (e.g. Wagner and Reimer, 1972; Schär et al., 1975). Later, compilations of high- and low-temperature thermochronology data by Hunziker et al. (1992) and Schlunegger and Willett (1999) contributed to outlining the long-term evolution of the orogen. However, due to the nature of the compiled ages, these studies were not specifically focused on late-Neogene exhumation. Three routes were explored to tackle the question of temporal evolution, spatial variability and the controls of exhumation rates in the Western Alps since the late Neogene:

Firstly, (in **Chapter II**) I updated a uniquely dense database of apatite fission-track (AFT) and zircon fission-track (ZFT) ages covering the Western Alps and used it to describe thermochronological age patterns over the Alps, calculate exhumation rates from samples with double dating (ZFT and AFT), and calculate the elevation of AFT cooling isoage surfaces according to a new technique. "Isoage surfaces" are equivalent to a 3-D generalization of age-elevation relationships (see Figure I.2.4), and constitute the exhumational counterpart of "isopachs" in a sedimentary basin; i.e. they enable the estimation of a volume of material removed during a specified period of time. The age of the isoage surfaces that can be calculated over an area depends on the thermochronological ages encountered at the topographic surface: in this study, 13 isoage surfaces, between 14 and 2

Ma, were constructed. The elevation of successive AFT isoage surfaces was used to estimate Mio-Pliocene exhumation rates over a selection of sub-areas and I compared the results with denudation-rate estimates obtained independently from the sedimentary record.

Secondly (in **Chapter III**), I compared a series of maps describing the pattern of long-term exhumation (AFT ages, elevation of the 2- and 4-Ma isoage surfaces, amount of exhumation between 4 and 2 Ma) with maps of parameters potentially affecting the denudation rate (average elevation, topographic relief, rock uplift, precipitation, runoff, stream power, seismic energy released) compiled with a Geographical Information System. High values of these parameters are expected to be spatially linked to high values of exhumation rates, high elevation of isoage surfaces and young AFT ages. I sampled the parameters value at several thousands of locations within these maps, and performed rank correlation tests between the parameters taken two by two.

Thirdly (in **Chapter IV**), I obtained new AFT and apatite AHe ages along a N-S transect in the central Alps, focusing on two elevation profiles in the Aar massif and the Lepontine Dome (spanning respectively 1800 and 1400 m of relief). I used a modified version of the numerical model *Pecube* (Braun, 2003) to test the effect of several tens of scenarios of exhumation and relief variation on the cooling history of rocks currently at the surface, and compared measured ages with predictions made according to the cooling history (Figure I.2.5).

Following the three chapters where I report the results of this thesis, **Chapter V** provides a synthesis of the results obtained in the light of the general context, and proposes leads for future work destined to further our understanding of the relationships between internal and external forcing factors, and the exhumation history of an orogen. **Chapter VI** contains a final reformulation of the main outcomes of this thesis.

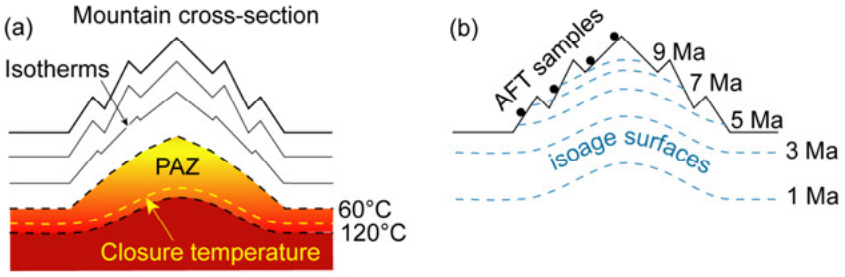

Figure I.2.4. Illustration of the apatite fission-track isoage surface concept. (a) sketch showing isotherms under a mountain cross-section. The closure temperature of the apatite fission-track system is comprised within the partial annealing zone (PAZ) temperature range. (b) Isoage surfaces are inherited from the 3-D shape of the closure temperature surface. As denudation moves the topography downward relative to the thermal reference frame, the closure temperature surface follows this trend and leaves behind a series of isoage surfaces that can be studied by combining surface samples.

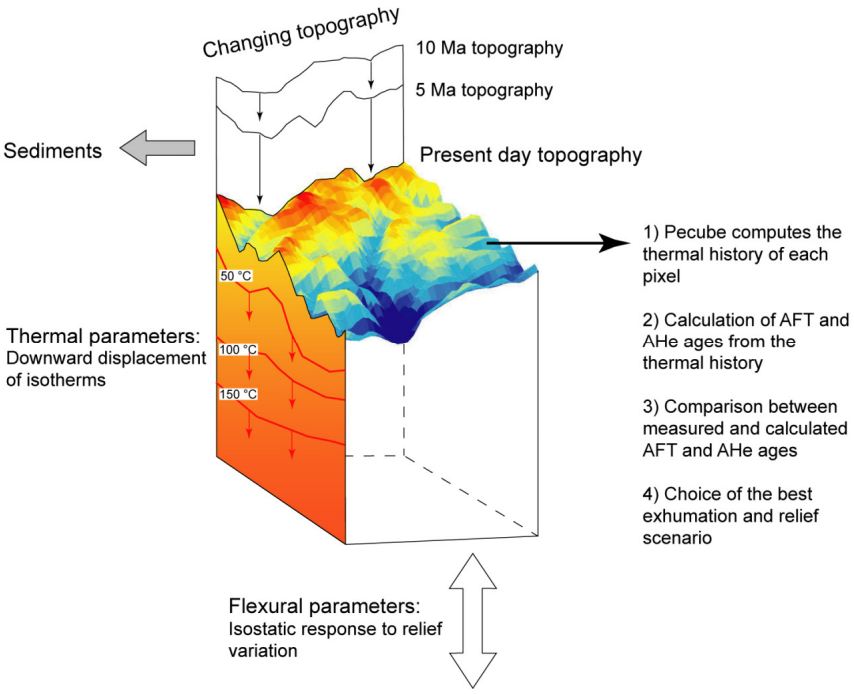

Figure I.2.5. The Pecube 3D heat equation solver (Braun, 2003) was used to predict AFT and AHe ages for different exhumation scenarios. Thermal and flexural parameters constrain the thermal response of the modeled area to exhumation and relief changes. The thermal history of points at the surface is used to predict AFT and AHe ages taking in account the temperature control on track annealing and He diffusivity.

Chapter II

Increase in late Neogene denudation of the European Alps confirmed by analysis of a fission-track thermochronology database

II.1. Chapter overview

II.1.1. Publication

This chapter presents a paper published in *Earth and Planetary Science Letters* (2008) 270: 316-329 (submitted July 11th 2007, accepted March 26th 2008).

II.1.2. Presentation at international meetings

- April 2006, European Geological Union Vienna (Austria):

Vernon, A.J., van der Beek, P.A., Rahn, M.K., Sinclair, H.D. Apatite fission-track ages and Neogene denudation in the Western Alps: the qualities of quantity. *Geophysical Research Abstracts, 8*, SRef-ID: 1607-7962/gra/EGU2006-A-04858.

- September 2006, Geologische Vereinigung Potsdam (Germany):

Vernon, A.J., van der Beek, P.A., Rahn, M.K., Sinclair, H.D. Quantifying late Cenozoic denudation of the European Alps: insights from a compilation of fission-track ages. GV International Conference, Shaping the Earth's Surface: Dynamics and Changing Environments, 25-29 September 2006, Potsdam, Germany. *Terra Nostra, 2006/3*, 101.

- October 2007, Workshop on Alpine Geological Studies, Davos (Switzerland):

Vernon, A.J., van der Beek, P.A., Sinclair, H.D., **Rahn**, M.K. Late Cenozoic increase of denudation: analysis of fission track data from the western European Alps. 8th Workshop on Alpine Geological Studies 10-12 October 2007, Davos, Switzerland. Abstract volume, 84.

- December 2007, American Geophysical Union, Fall meeting San Francisco (USA):

Vernon, A.J., **van der Beek**, P.A., Sinclair, H.D., Rahn, M.K. Tectonic vs. climatic controls on accelerated Mio-Pliocene denudation of the western European Alps. *Eos Transactions AGU, 88(52)*, Fall Meeting Supplement, Abstract T14C-07.

- **April 2008**, European Geological Union Vienna (Austria):

Vernon, A.J., van der Beek, P.A., Sinclair, H.D., Persano, C., Stuart, F.M. Mechanisms of late Neogene exhumation of the Alps: Insights from AFT and AHe vertical profiles in the Aar massif (Switzerland) and the Lepontine Alps (Italy). *Geophysical Research Abstracts, 10*, SRef-ID: 1607-7962/gra/EGU2008-A-10428.

II.1.3. Contributors to Chapter II

Meinert Rahn compiled the original version of AFT and ZFT database covering the European Alps. My contribution was to update with the most recent journal papers, MSc and PhD theses, additional information received from authors, and add sorting criteria in order to select the data relevant for specific uses. Peter van der Beek wrote Fortran codes used in sections II.2.4.2. and II.2.4.3.1.

II.2. Increase in late Neogene denudation of the European Alps confirmed by analysis of a fission-track thermochronology database

Antoine J. Vernon[1,2,*], Peter A. van der Beek[2], Hugh D. Sinclair[1], Meinert K. Rahn[3]

[1]School of Geosciences, Grant Institute, University of Edinburgh, Edinburgh EH9-3JW, United-Kingdom

[2]Laboratoire de Géodynamique des Chaînes Alpines, Université Joseph Fourier, 38400 Grenoble, France

[3]Swiss Federal Nuclear Safety Inspectorate, 5232 Villigen-HSK, Switzerland

* Corresponding author: vernon.antoine@gmail.com

Abstract

A sharp increase in deposited sediment volume since Pliocene times has been observed worldwide and in particular around the European Alps. This phenomenon has been linked to a rise in denudation rates controlled by an increase of either climatic or tectonic forcing. Observation of in situ cooling histories for orogens is critical to assess the reality of the inferred increase in denudation rates, and to determine whether this phenomenon is widespread or localized at active tectonic structures. We exploit the unique density of fission track ages in the Western European Alps to reconstruct cooling isoage surfaces and to estimate exhumation rates on the orogen scale between 13.5 and 2.5 Ma. Our novel technique is based on the association of isoage contours with age-elevation relationships. It uses map-view interpolation, enabling a spatio-temporal analysis of exhumation rates over the entire Western Alps. The resulting exhumation histories reconstructed for eight areas of the Western Alps display strong similarities in timing and rates with orogen-wide average denudation rates inferred from sediment volumes. This consistency validates the use of both techniques for the study of an orogen characterized by strong relief and high recent exhumation rates. We conclude that exhumation rates in the Western Alps have increased more than twofold since Late Miocene times. This increase may have been locally modulated by the distinct response of different tectonic units.

Keywords: Neogene exhumation, Fission track, Isoage surface, Western Alps

II.2.1. Introduction

Widespread indications for an increase of global sedimentation rates in the Early Pliocene have been reported from localities around the world (e.g., Molnar, 2004; Zhang et al., 2001). However, the cause of this event, its exact timing and synchronicity remain controversial.

Possible causes that have been proposed include global cooling and incipient glaciations (Ehlers et al., 2006; Hinderer, 2001), an increase in the magnitude and frequency of climate oscillations (Molnar, 2004; Zhang et al., 2001), and a recent increase in the uplift rates of major orogens (Raymo and Ruddiman, 1992).

The quantification of sediment volumes in the basins surrounding the European Alps by Kuhlemann et al. (2002) shows a more than twofold increase in sediment supply from both the Western and Eastern Alps around 5 Ma (Figure II.2.1). An independent study of the exhumation of the Molasse basin (Figure II.2.2), based on borehole apatite fission-track data, demonstrated approximately 1400 m of basin exhumation since 5 Ma, interpreted as a record of isostatic rebound of the basin driven by accelerated erosional unloading of the Alps (Cederbom et al., 2004).

The estimation of source-area denudation rates from the sediment record suffers, however, from poorly quantified uncertainties in both the volumetric calculations and the dating accuracy (Kuhlemann et al., 2002). Moreover, the impossibility of quantifying the roles of chemical erosion and sediment recycling may lead to an underestimation or overestimation, respectively, of source-area denudation rates through time.

An increase in exhumation at ca. 5 Ma, if real, should be recorded more directly by low-temperature thermochronometers in the bedrock of the mountain belt. Classically, the derivation of exhumation rates from thermochronometry is based on temperature-time paths reconstructed from multiple thermochronometric analyses, age-elevation profiles from altitudinal transects or boreholes, or kinetic modeling of apatite fission-track annealing using track-length distributions (e.g., Gallagher et al., 1998; Hurford, 1991). In different regions of the Western Alps, Neogene-age exhumation rates quantified using these approaches range between 0.1 and 1.5 mm yr^{-1} (e.g., Leloup et al., 2005; Malusa et al., 2005; Michalski and Soom, 1990; Tricart et al., 2007). However, most of these studies are local or at best regional in scope and a consistent denudation history at the orogen scale has yet to emerge. Apatite fission-track (AFT) thermochronology appears the most suitable technique to study Mio-Pliocene exhumation rates over a large area such as the Western Alps because of the abundance of ages ready for database compilation, and because the AFT age range (Figure II.2.3-a) comprises the target period of the late Neogene time interval.

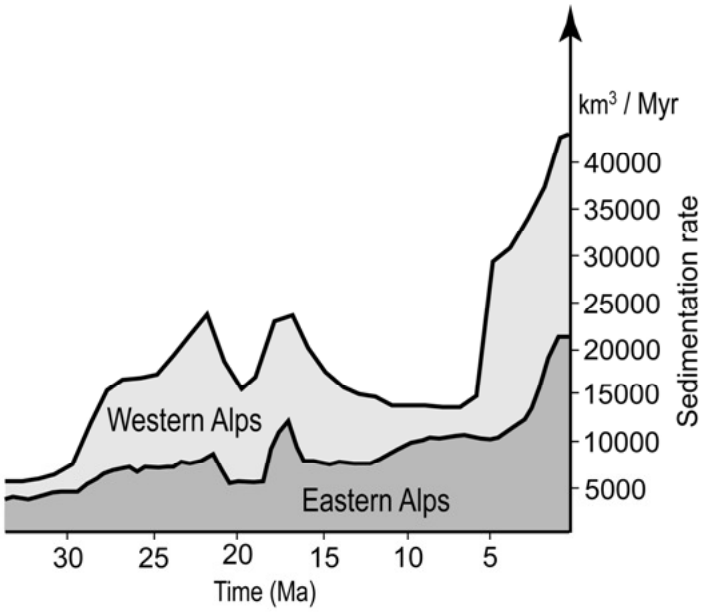

Figure II.2.1. Evolution of sedimentation rates through time, reconstructed from the preserved volume of sediments originating from the Western and the Eastern Alps, respectively (modified from Kuhlemann et al., 2002).

The spatial integration of discrete thermochronological data covering large study areas is most easily achieved by interpolating between ages in map view (e.g., Hunziker et al., 1992; Figures II.2.3-a and 3-b). However, this simple technique only presents the integrated result of a possibly complex denudation history and does not allow variations in denudation rate through time to be inferred. Published methods aimed at describing the history of exhumation rates in map view have used either analysis of multiple thermochronometers, or kinetic modeling of fission-track length distributions (e.g., Bistacchi and Massironi, 2000; Gallagher and Brown, 1999; Morris et al., 1998; Schlunegger and Willet, 1999; Stephenson et al., 2006). Despite many years of intensive thermochronological studies in the Alps, samples permitting such analyses are still relatively rare, disallowing such a study at the orogen scale. Techniques based on modeling of fission-track length distributions offer the greatest wealth of interpretation in settings characterized by slow long-term denudation, such as rifted continental margins (e.g. Gallagher and Brown, 1999). In rapidly exhuming orogens, in contrast, track-length distributions are not easily measured (because of generally young AFT ages) and are much less discriminative.

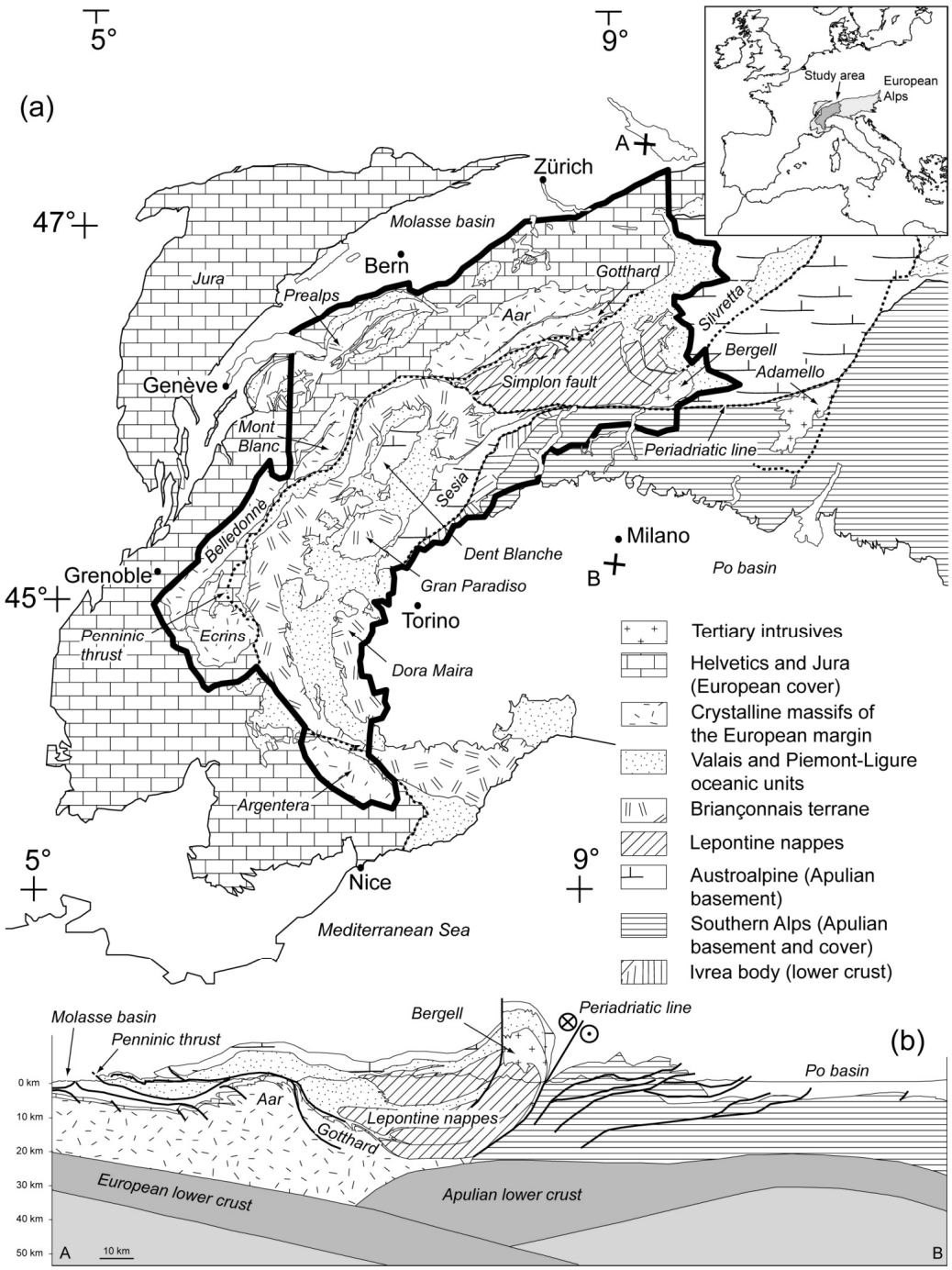

Figure II.2.2. (a) Simplified geologic map of the Western Alps (modified from Schmid et al., 2004). The study area (shown by bold outline) covers the geological units with the highest density of fission track ages (cf. Figure II.2.3), limited to the east by the Austroalpine Silvretta nappe boundary at about 9°55' E. (b) Cross-section following north-south transect A-B across the central Swiss Alps (modified from Schmid et al., 1996).

We propose a new method in which we exploit the extensive AFT dataset available for the Western Alps (Figures II.2.2 and 3) together with the significant relief of the mountain belt to reconstruct three-dimensional surfaces of equal AFT age (referred to here as isoage surfaces). We subsequently use the difference in elevation between these surfaces to estimate the spatial pattern in rates of exhumation back to Middle Miocene times (13.5 Ma), as recorded in the spatial relationship between AFT ages at outcrop today. The aims of this study are to test for the presence of changing exhumation rates during late Neogene times across the Western Alps, and if present, to describe the temporal and spatial variability of this signal. In addition, we present updated maps of interpolated apatite fission-track ages and mean track lengths, as well as zircon fission-track ages. We complete this study by the assessment of evolving trends of exhumation rates using samples with paired zircon and apatite fission-track ages. In the following, we first briefly outline the geological setting and evolution of the Alps and present the thermochronological database we constructed. We then explain the different methods we used to analyze the database. Finally, we present our main results and their implications for the late Neogene denudation history of the Alps as well as its possible tectonic or climatic controls.

II.2.2. Geological setting of the Alps

The European Alps (Figure II.2.2) are located at the boundary between the European and Apulian plates. They are the product of the Early Cretaceous closure of the Piemont-Ligurian ocean, followed by continental subduction resulting in nappe stacking (cf. reviews in Rosenbaum and Lister, 2005; Schmid et al., 2004).

The main tectonic units in the Alps and their structural relationships have been described extensively within the last century (e.g., Debelmas and Lemoine, 1970; Schmid et al., 2004; Trümpy, 1960). They originate from the European continental margin basement (External Crystalline Massifs) and overlying deposits (Helvetic sediments), the Briançonnais micro-continent and its two bordering oceanic units (Piemont-Ligure and Valais oceanic crust and flysh), and finally basement and sedimentary units of the Apulian margin, grouped as the Austroalpine and the South Alpine units (Figure II.2.2). The North (Molasse) and South (Po) Alpine foreland basins formed by flexure of the lithosphere in response to the weight of the orogenic prism on the European and Apulian plates and are filled with Eocene to Recent flysch, molasse and glacial deposits (e.g., Homewood et al., 1986; Scardia et al., 2006).

One of the most important arc-parallel tectonic boundaries, the Penninic thrust, may have been extensionally reactivated (Seward and Mancktelow, 1994) as part of a series of Neogene extensional features observed throughout the axial region of the Western Alps (e.g., Sue et al., 2007b; Tricart et al., 2007 and references therein). Most of these extensional features may be caused by a Neogene dextral transtensive event (Sue et al., 2007b) triggered by the anti-clockwise rotation of the Apulian plate. Such rotation can also explain the current strain pattern in the Western Alps (Calais et al., 2002). At present, geodetic and GPS data show limited ($\leq$ 2 mm yr^{-1}) east-west extension in the Western Alps (Calais et al., 2002; Sue et al., 2007a). The lack of present-day convergence in the Western Alps, together with the observation of sediment-sealed thrusts in the western part of the Po basin (Pieri and Groppi, 1981), and the cessation of thin-skinned deformation in the Jura at ca. 4 Ma (Becker, 2000) all suggest very limited current orogenic activity within the chain.

We limit our study area to the Western half of the Alps, as far east as the Silvretta nappe / Engadine window, or approximately the Swiss-Austrian border, which marks the western limit of widespread outcrop of Austroalpine units. The reason for this eastern limit to the study area is that few AFT studies have been published for the Austroalpine units because of the low abundance of apatite in their constitutive lithologies.

II.2.3. Data

II.2.3.1. Apatite and zircon fission-track databases

During the last thirty-five years, the Western Alps have been extensively sampled for thermochronological analyses, in particular using the apatite and zircon fission-track thermochronometers, characterized by closure temperatures of ca. 120 and 240 °C respectively (e.g., Brandon et al., 1998; Gallagher et al., 1998). We have compiled 740 AFT ages, from data in 37 publications completed by 160 unpublished ages (references are given in the caption of Figure II.2.3-a) from samples located in the European Alps west of 10° 20' east (an area of ca. 48000 km^2). We similarly compiled 380 zircon fission-track (ZFT) ages from 24 publications completed by 22 unpublished ages (see Figure II.2.3-b for references).

II.2.3.2. Quality and homogeneity of the data

Early studies (in the 1970's and early 1980's, see for instance Wagner and Reimer, 1972) used the population method for AFT dating, whereas the more reliable external detector method (Hurford and Green, 1982) has become the norm since the mid 1980's. The database contains ages obtained both with the population and the external-detector dating techniques

because we feel that, at the regional scale of the study, the benefits of increasing data density outweigh the drawbacks of the error introduced by less reliable data points. We rejected three samples with an obvious mistake in dating, in cases where a ZFT age was younger than or equal to (within error) the AFT age of the same sample.

Additional information collected for each sample included (where reported): (1) geographic coordinates, (2) elevation, (3) mean track length for AFT samples, (4) whether the sample is from a tunnel / borehole or the surface, and (5) whether fission-track ages of samples from Mesozoic and Cenozoic sediments are younger than their stratigraphic age (that is, whether they have been reset during Alpine orogeny). To apply the latter criterion, we assumed that ages from sedimentary samples were non-reset unless we could estimate the depositional age and verify that it was older than the fission-track age. A few publications contained more than one age at a given geographic location (referred to later as points with non-unique ages). We discarded such points from part of the study, in order to prevent problems with map interpolation. Many of the original publications did not report sample elevations and / or coordinates. We obtained this missing information by interviewing the authors whenever possible, or alternatively by reading it off topographic maps or figures from the original publications. As a last resort, we estimated the elevation of samples from the Digital Elevation Model (DEM), which consists of a mosaic of the 38-03, 38-04, 39-03 and 39-04 DEM tiles available from the CGIAR-CSI SRTM 90 m database (http://srtm.csi.cgiar.org). All numerical data fields in the database (coordinates, altitude, age, etc.) carry a degree of uncertainty that varies between publications. For instance, the relative standard errors affecting the AFT and ZFT ages used in this paper vary between 2.2 and 51.6 % (average: 11.6 %) for the former, and between 0.7 and 23.3 % (average 8.0 %) for the latter.

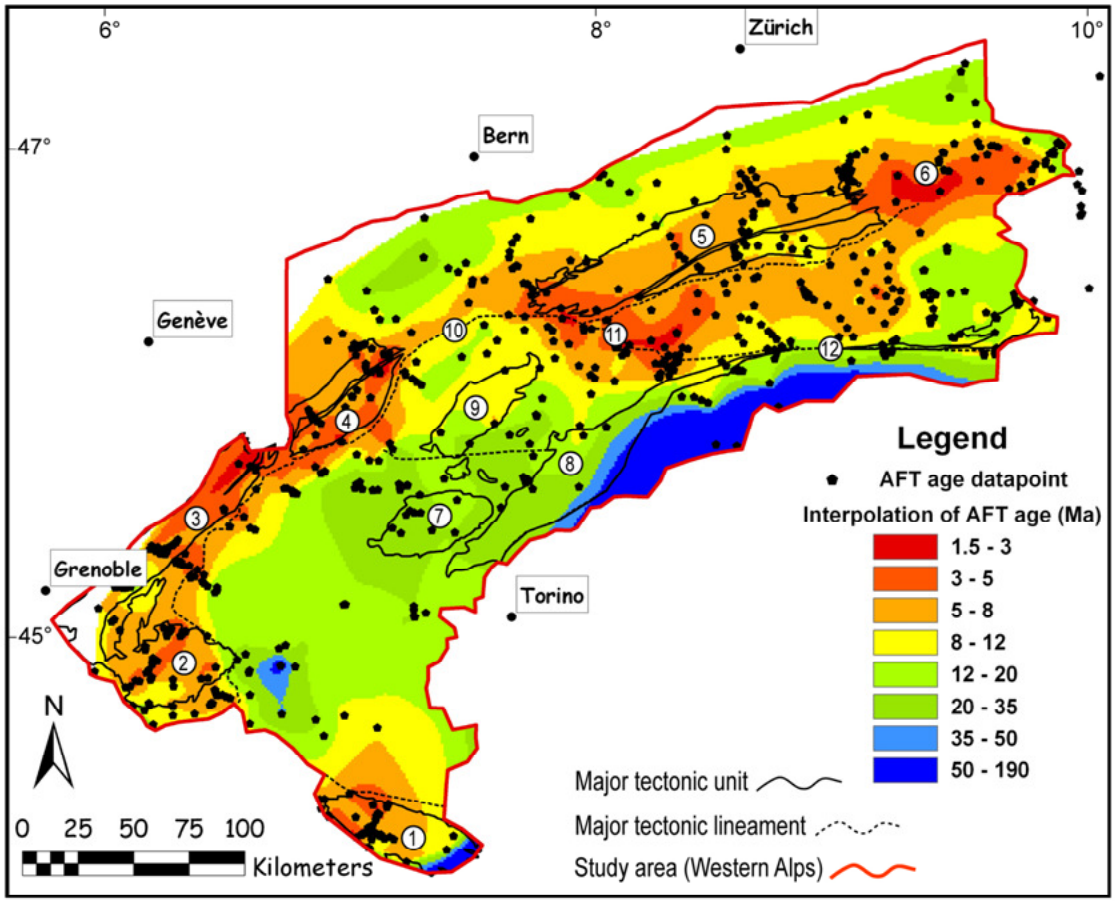

Figure II.2.3-a. Map of 635 AFT ages from the Western Alps, interpolated using a natural-neighbor algorithm. Morphotectonic regions and units referred to in the text: (1) Argentera, (2) Ecrins, (3) Belledonne, (4) Mont-Blanc, (5) Aar, (6) Chur area, (7) Gran Paradiso, (8) Sesia, (9) Dent-Blanche, (10) Penninic thrust, (11) Simplon fault, (12) Peri-Adriatic line. AFT data are compiled from Bigot-Cormier 2002; Bogdanoff et al. 2000; Bürgi and Klötzli 1990; Carpéna and Caby 1984; Carpéna 1992; Ciancaleoni 2005; Flisch 1986; Fügenschuh and Schmid 2003; Fügenschuh et al. 1999; Giger 1991; Hunziker et al. 1992; Hurford and Hunziker 1989; Hurford 1986; Hurford et al. 1991; Keller et al. 2005; Knaus 1990; Lelarge 1993; Leloup et al. 2005; Malusà et al. 2005; Michalski and Soom 1990; Pawlig 2001; Rahn et al. 1997; Sabil 1995; Schär et al. 1975; Schwartz 2000; Seward and Mancktelow 1994; Seward et al. 1999; Soom 1990; Steiner 1984; Timar-Geng et al. 2004; Trautwein 2000; Tricart et al. 2007; Viola 2000; Wagner and Reimer 1972; Wagner et al. 1977; Wagner et al. 1979; Weh 1998; as well as unpublished ages provided by M. Ford, D. Seward and our own data.

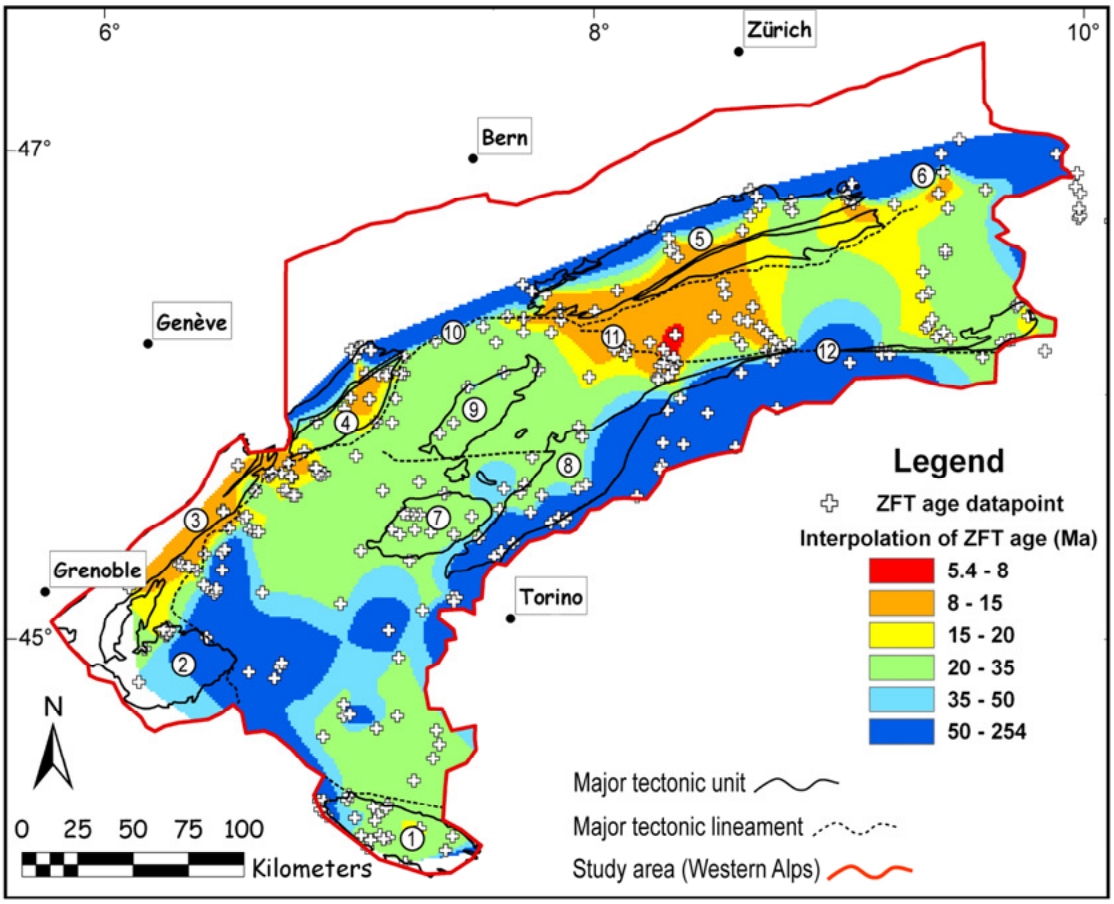

Figure II.2.3-b. Map of 296 interpolated ZFT ages from the Western Alps. Numbers are as in Figure II.2.3-a. ZFT data are compiled from Bernet et al. 2001; Bigot-Cormier 2002; Bürgi and Klötzli 1990; Carpéna 1992; Carpéna et al. 1986; Ciancaleoni 2005; Flisch 1986; Fügenschuh and Schmid 2003; Fügenschuh et al. 1999; Giger 1991; Hunziker et al. 1992; Hurford and Hunziker 1985; Hurford and Hunziker 1989; Hurford 1986; Hurford et al. 1991; Keller et al. 2005; Michalski and Soom 1990; Rahn 1994; Schwartz 2000; Seward and Mancktelow 1994; Seward et al. 1999; Soom 1990; Vance 1999; Weh 1998; as well as unpublished ages provided by M. Ford, D. Seward and our own data.

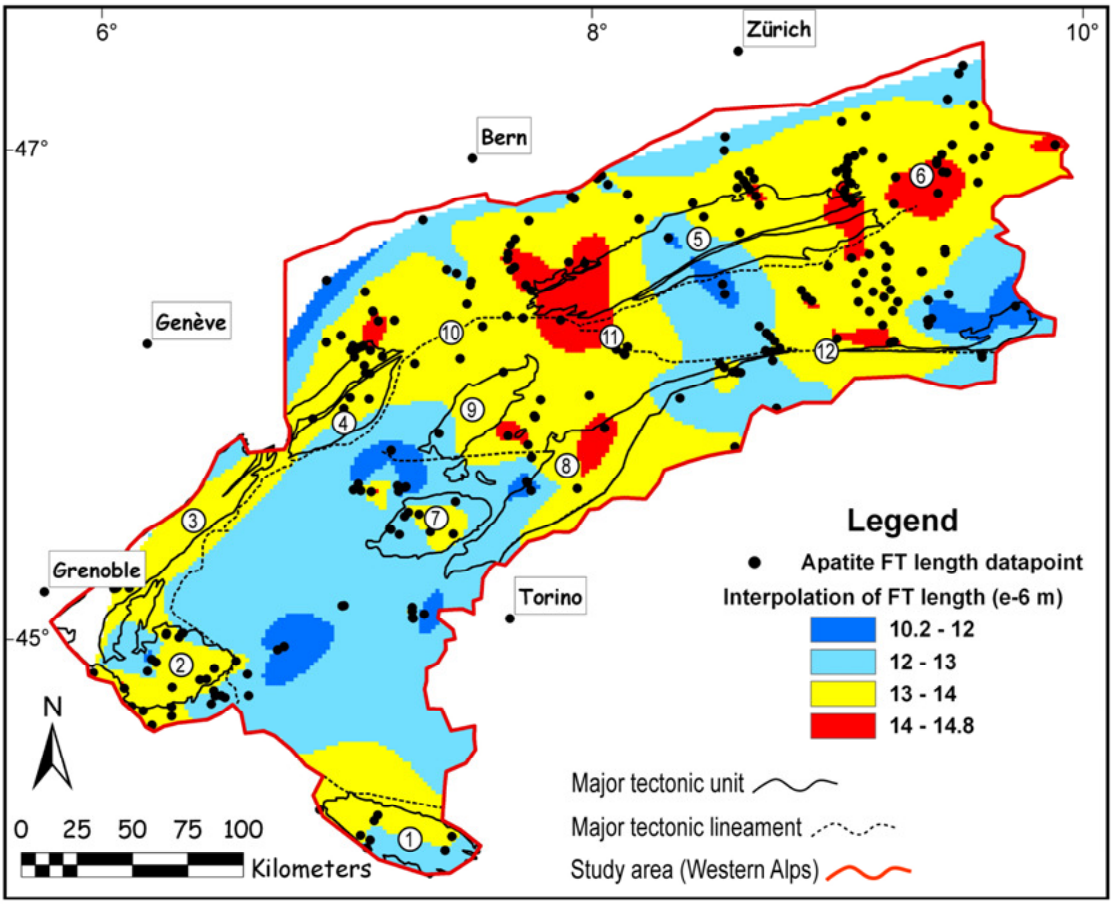

Figure II.2.3-c. Interpolated map of 258 mean apatite fission-track lengths (µm) from the Western Alps. Short mean lengths (< 13 µm) indicate slow passage of the sample through the AFT partial annealing zone, indicative of a slow exhumation rate. Long mean track lengths, in contrast, indicate rapid exhumation. Note the strong spatial overlap between mean track lengths > 13 µm and AFT ages < ~10 Ma (Figure II.2.3-a), particularly in the Simplon and Chur areas, as well as more generally in the Mont-Blanc-Ecrins and the Argentera Massifs. Numbers are as in Figure II.2.3-a. Apatite fission-track lengths compiled from Bigot-Cormier 2002; Bürgi and Klötzli 1990; Ciancaleoni 2005; Giger 1991; Hunziker et al. 1992; Hurford and Hunziker 1989; Hurford 1986; Hurford et al. 1991; Knaus 1990; Malusà et al. 2005; Michalski and Soom 1990; Pawlig 2001; Rahn et al. 1997; Sabil 1995; Seward and Mancktelow 1994; Seward et al. 1999; Soom 1990; Timar-Geng et al. 2004; Trautwein 2000; Tricart et al. 2007; Wagner and Reimer 1972; as well as our own unpublished data.

II.2.4. Methods

We have developed three joint approaches to take advantage of the high spatial density of fission-track ages in the Western Alps. First, we interpolated AFT and ZFT ages (Figures II.2.3-a and 3-b); second, we calculated cooling and exhumation rates using samples dated with both methods; and third, we constructed isoage surfaces. The latter were used to infer histories of exhumation rates for different areas of the Western Alps between 13.5 and 2.5 Ma.

II.2.4.1. Maps of interpolated ages / track lengths

Using the natural-neighbor interpolation tool provided by the ESRI-ArcMap9^{tm} GIS, we created two maps of 635 AFT ages and 296 ZFT ages covering the Western Alps (Figures II.2.3-a and 3-b). For this interpolation, we selected points from the database following three criteria: (1) ages in sedimentary rocks should be reset; (2) samples should be from the surface; and (3) points with non-unique ages are discarded. No potentially arbitrary constraints such as tectonic boundaries or elevation corrections were used in this initial interpolation. The choice of a natural-neighbor interpolator is justified by its conservative properties, resulting in finding at each pixel of the map a weighted average of the neighborhood data points without introducing artefacts (Watson, 1999). However, as we could not introduce a maximum distance of interpolation, localities within the inner Alpine arc are often interpolated between data points located very far apart, at two extremities of the arc. Figure II.2.3-c shows a map of 258 mean AFT lengths, interpolated in the same manner as the ages.

II.2.4.2. Exhumation rates calculated from paired ZFT and AFT ages

We extracted from the database a subset of 143 samples with paired AFT and ZFT ages, following the requirements that (1) they are surface samples; (2) both AFT and ZFT ages are younger than 35 Ma (i.e., Alpine cooling ages); (3) AFT and ZFT ages differ by at least 1.6 Myr (an empirical limit set by convergence problems for smaller age differences in the numerical code used); finally (4) points with non-unique ages are discarded. The 143 age pairs offer the opportunity to estimate two successive average exhumation rates: an initial rate during the time between closure of the ZFT and AFT thermochronometers, and a final rate for the time since closure of the AFT system. We used a modified version of the one-dimensional model of Brandon et al. (1998) to calculate iteratively the depth of closure of the ZFT and AFT systems, and then calculate exhumation rate from the value of closure depth and age. This model takes into account the advective perturbation of a steady-state geotherm by exhumation, as well as the dependence of closure temperature on cooling rate (e.g., Dodson,

1973). It does not, however, include 2-D or 3-D effects such as non-vertical rock-particle paths, spatial variation in geothermal gradient or topographic effects. We have adapted the Brandon et al. (1998) model to simultaneously estimate closure temperatures and depths for both the ZFT and AFT systems (cf. Braun et al., 2006 and van der Beek et al., 2006 for details), using values for the kinetic parameters as estimated by Brandon et al. (1998): AFT: E_a = 186.4 kJ mol^{-1}, $D_0/a^2 = 3.64 \times 10^{10}$ s^{-1}; ZFT: E_a = 208.2 kJ mol^{-1}, $D_0/a^2 = 3.70 \times 10^6$ s^{-1}. Other parameter values used in the model are: surface temperature T_s = 15 - (6 × elevation (km)) °C, initial (non-perturbed) geothermal gradient G = 25 °C km^{-1}, model thickness L = 30 km, thermal diffusivity κ = 25 km^2 Myr^{-1}. The model predicts initial and final exhumation rates that are consistent with both ages; the ratio between the final and initial rates indicates whether the average exhumation rate accelerated or decelerated after closure of the AFT system. An interpolated map of this ratio is plotted in Figure II.2.4. Absolute values of predicted exhumation rates are affected by the assumed initial geothermal gradient, which is largely unknown and may vary spatially. However, the *ratio* between final and initial rates is not sensitive to this parameter, providing the geothermal gradient does not change through time, other than through advective perturbation[1].

II.2.4.3. Reconstruction of isoage surfaces

Apatite fission-track isoage surfaces join all rocks predicted to have cooled through the AFT closure temperature at the same time (Figure II.2.5). They are obtained by interpolation in map view between the elevations of points having the same AFT age. Providing the assumption that the depth of the AFT closure isotherms is only moderately affected by changes in exhumation rate, the latter can be estimated using the vertical distance between two successive isoage surfaces. In this respect, isoage surfaces may be viewed as a 3-D generalization of the 1-D age-elevation profile concept, allowing the same information on denudation history to be extracted on a regional scale and potentially recording spatial variations in denudation rates through time.

[1] See complementary details on the method in section II.3.1.

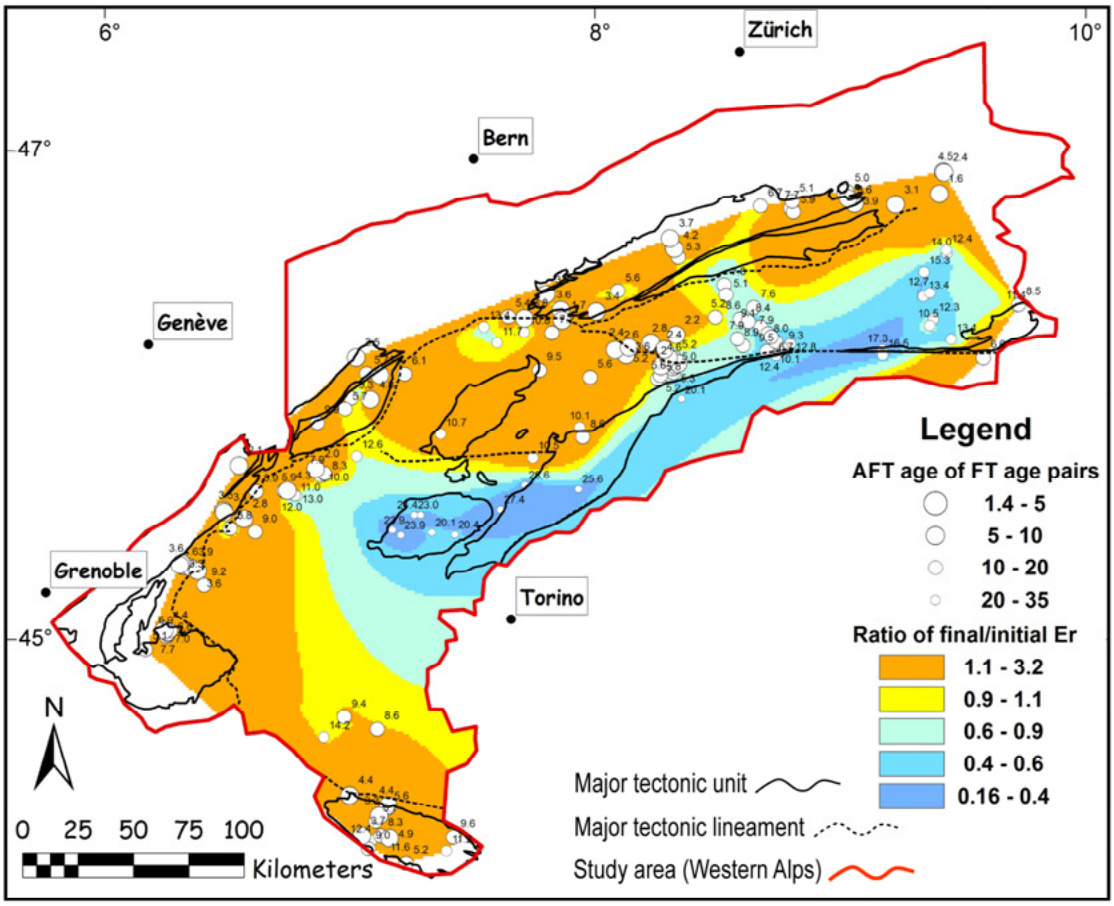

Figure II.2.4. Variation of exhumation rate (Er) through time, calculated from samples with paired AFT and ZFT ages. Samples with both ages younger than 35 Ma (i.e., Alpine cooling ages) are used to calculate an initial rate during the time between closure of the ZFT and AFT thermochronometers and a final rate for the time since closure of the AFT system (see text for details). The color scale presents the ratio between final and initial exhumation rates and enables to distinguish between localities where average exhumation rates have accelerated (ratio > 1), remained steady (ratio ≈ 1) or decelerated (ratio < 1) after AFT closure. Data points are labeled by their AFT age. Data origin is given in the legends of Figures II.2.3-a and 3-b.

Regional variability in geothermal gradient, cooling history and / or apatite annealing kinetics may cause the closure temperature and depth to vary spatially between samples from different tectonic units, thus potentially imposing secondary effects on the spatial variation in elevation of isoage surfaces. However, as for age-elevation profiles, the denudation rate inferred from the elevation difference between successive isoage surfaces is independent of the absolute closure temperature and depth, as long as these remain constant through time. Temporal variations in exhumation rates may affect the AFT closure temperature (Dodson, 1973) as well as the geometry of near-surface isotherms (e.g., Braun, 2002; Stüwe et al., 1994). These two factors tend respectively toward over- or under-estimation of the exhumation rate in the case of an increase in exhumation rate. Nevertheless, the characteristic diffusive timescales are rather large (e.g., Braun et al., 2006) so that these variations will be relatively small over the 1 Myr time span separating two isoage surfaces. In any case, the latter effect significantly outweighs the former (e.g., Braun et al., 2006), so that estimated exhumation rates during a period of increase before reaching a thermal steady-state are likely to be minimum estimates.

II.2.4.3.1. Production of arrays of isoage points

The most obvious way to obtain x, y, z coordinates of isoage points is to use the elevation of isoage contours, which, by definition, are the lines of intersection between isoage surfaces and the Earth's surface. We extracted the elevation of each isoage contour traced on the maps of interpolated AFT ages (Figure II.2.3-a) by projection on the Digital Elevation Model (DEM). The spatial resolution of the DEM (90 m) is much higher than the resolution of the isoage contours (controlled by interpolated points often separated by several kilometers). Therefore, the elevation of any segment of an isoage contour has a high pixel-to-pixel variability (or noise) due to the short-wavelength topography sampled. Nevertheless, the average local value should accurately reflect the elevation of the intersection between an isoage surface and the topography.

We added a second series of isoage points to the array, based on local estimates of AFT age-elevation relationships (AER) in the neighborhood of data points where the correlation between these two parameters was statistically significant (Figure II.2.6). The aim is to document areas where the AER are well correlated and use them to interpolate the elevation of isoage surfaces. We used a subset of 660 AFT samples with an age younger than 35 Ma for this approach. Sample elevation values that had to be derived from the DEM were found to introduce too much noise in the calculation of regression coefficients for age-elevation relationships and were therefore rejected. We did include, however, data points with non-

unique ages, as they comply with the requirements to estimate age-elevation relationships. The condition of sample ages younger than 35 Ma aims to avoid introducing samples that are manifestly partially reset, such as those with Mesosoic ages from the Southern Alps (cf. Figure II.2.3-a), into the calculation of AER regression lines.

For our semi-automated AER analysis, we first selected the neighbors of every point in the database, included in a circle of increasing radius (from 3 to 15 km). For every selection containing more than 4 points, we calculated a regression line between age (dependent variable) and elevation (independent variable), together with its correlation coefficient. The AER was judged significant and was retained if the correlation coefficient for the regression was higher than the critical Pearson's product-moment coefficient at 95 % confidence level for the appropriate number of degrees of freedom (cf. Figures II.2.6-b and 6-c). When the initial selection around a data point (3 km radius) failed this statistical test, we incrementally increased the search radius by 2 km steps to a maximum of 15 km. This maximum presents a characteristic distance between adjacent valleys: for larger search radii, the samples selected may belong to adjacent valleys with distinct exhumation histories. We used the regression equations calculated from the set of points selected within the smallest successful search radius possible, because they constitute the closest equivalent to an elevation profile and therefore carry the smallest risk for the AER to be affected by either large-scale tilting (Rahn et al., 1997) or the deflection of isotherms in large Alpine valleys (e.g., Braun, 2002; Stüwe et al., 1994).

The local AER is described by the simple linear equation $z = A_0 + (A_1 \times t)$, where A_0 is the elevation of the zero-age intercept, and A_1 is the slope of the AER (with z: elevation [m]; t: age [Ma])[2]. Statistically significant AERs extracted from the data are used to interpolate the elevations of isoage surfaces at the location of the center of the search radius, limiting the extrapolation to between 1 Myr before the oldest and 1 Myr after the youngest age in the neighborhood selection. This limitation is imposed in order to avoid extrapolating age-elevation trends into periods during which they are not locally documented. In case of a slightly kinked AER (i.e. change in exhumation rate with time), the slope A_1 would be averaged; if the kink is more pronounced the linear correlation coefficient will be insignificant and the neighborhood selection rejected. Given that this study is aimed at testing for changing exhumation rates through time, the rejection of kinked AERs in the generation of isoage data points is conservative, and will downplay any signal.

[2] A map of interpolated A_1 and A_0 values is reported in Figure II.3.6.

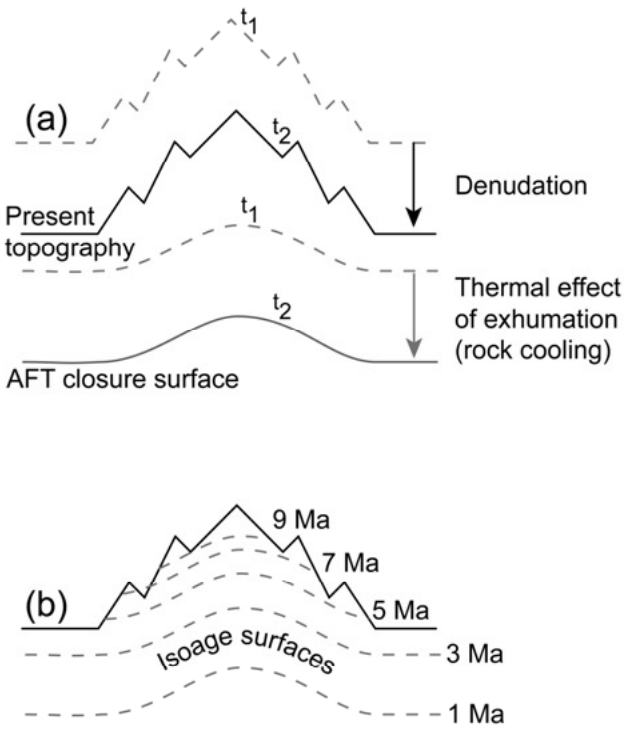

Figure II.2.5. Generic sketch of AFT isoage surface concept. (a) Denudation (i.e., removal of material) occurring between times t_1 and t_2 over the present-day topography is reflected by the migration of shallow isotherms, downwards with respect to the exhuming rock mass such that a rock particle is cooled during exhumation (see definitions in Ring et al., 1999). The 120 – 60 °C AFT partial annealing zone is shifted downwards, and so are the AFT closure temperature (the temperature at which the first track is recorded) and the AFT closure surface (the surface linking all samples crossing the closure temperature at a given moment). (b) Former closure surfaces become isoage surfaces, younging downwards and intersecting the topography.

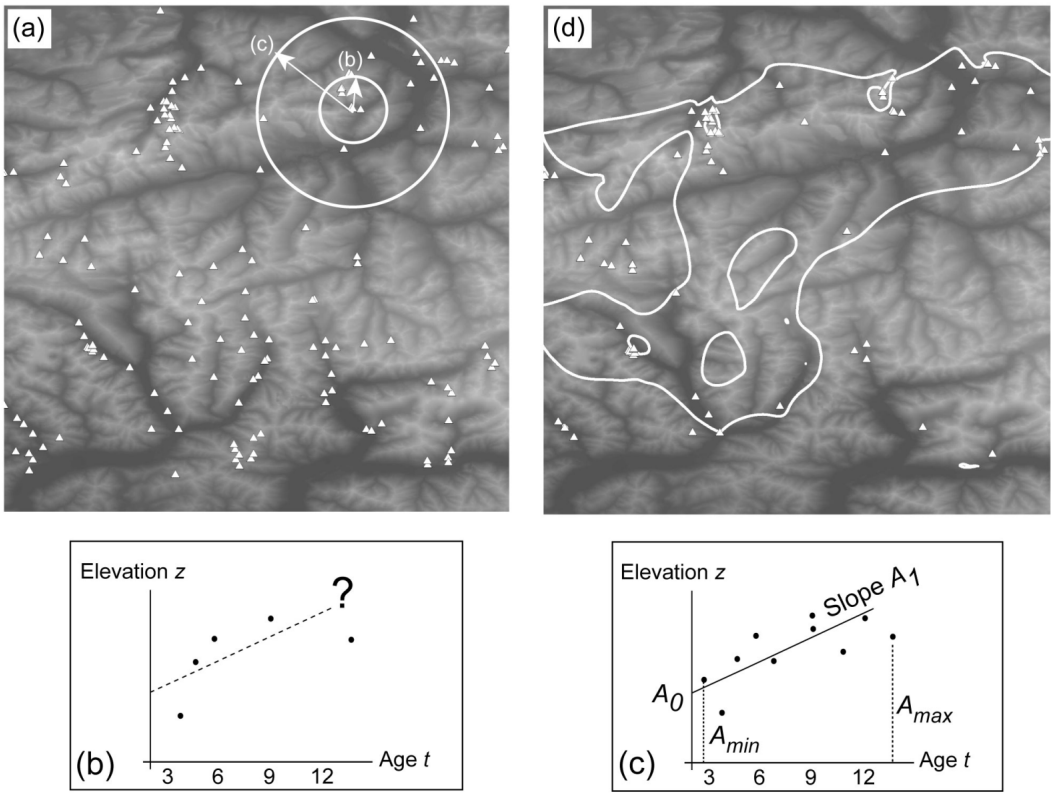

Figure II.2.6. Steps toward the interpolation of isoage surfaces. A neighborhood search of significant age-elevation relationships (AER) is performed within 3 km around each data point (a, b). If the correlation coefficient between age and elevation is not statistically significant at the 95 % confidence level (b), the radius for selection of points is increased stepwise up to a maximum of 15 km (c). The A_0 and A_1 parameters defining the regression lines are used to interpolate the elevation of isoage surfaces between 1 Myr before the oldest age selected (A_{max}) and 1 Myr after the youngest age selected (A_{min}). Finally, isoage surfaces are obtained by interpolation of isoage point arrays combining the results of neighborhood AER search and the elevation of isoage contours (d). The figure shows a zoom of the Lepontine area and the sources of data points are as in Figure II.2.3a.

II.2.4.3.2. Interpolation of isoage point arrays

We constructed isoage surfaces by natural-neighbor interpolation applied to the elevations of the points constituting each isoage array (Figure II.2.6-d). In order to remove unconstrained parts of the surfaces, which have been interpolated far from any point of the isoage arrays, a mask is applied at 15 km around the point arrays. The oldest isoage surfaces have been eroded from large parts of the study area, while the youngest surfaces remain buried in other areas, resulting in a heterogeneous scatter of each array of isoage points. The result is a series of thirteen maps showing isoage surfaces between 14 and 2 Ma where they can be reconstructed with reasonable accuracy; a representative selection of six isoage surfaces is reported in Figure II.2.7.[3]

II.2.4.4. Estimation of exhumation rates

The vertical distance between two isoage surfaces corresponds, in principle, to the amount of exhumation during the time period separating them, with the same caveats that apply to the interpretation of 1-D age-elevation profiles, notably the effect of topography on the AER slope (Braun, 2002). In the crystalline massifs of the Western Alps, geomorphic data suggest a significant recent increase in relief (e.g., Champagnac et al., 2007; van der Beek and Bourbon, 2008) so that we expect topographic effects to be limited and the distance between successive isoage surfaces to provide a reliable estimate of exhumation.

After being clipped by the 15 km mask, each isoage surface covers only a limited portion of the Western Alps, and two successive surfaces are never completely superposed. Therefore, it is not possible to calculate the total volume exhumed over the entire surface of the Western Alps during any time period. Instead, we focused on eight specific areas characterized by several million years of continuous isoage surface coverage (Figure II.2.8).

The difference in elevation between successive isoage surfaces is calculated for all 1.2 km^2 pixels of each study area[4] and the average distance constitutes our estimate of exhumation during the corresponding time period. Some pixels show negative differences, i.e. the younger isoage surface lies above the older one. These correspond either to artefacts introduced by our treatment of the data, or to local areas of strong recent relief decrease. We decided to exclude these pixels from our calculation of the average distance between isoage surfaces, as two

[3] The thirteen maps of isoage surface elevation are reported in Figures II.3.8 to II.3.14.
[4] The maps of elevation difference between pairs of successive isoage surfaces are reported in Figures II.3.15 to II.3.20.

isoage surfaces cannot cross each other in an exhuming massif[5]. To illustrate pixel value distributions, Figure II.2.9 presents the values measured between the surfaces aged 5 and 4 Ma for the Mont Blanc area[6]. Plotted against time, the average distances between isoage surfaces enable quantifying the temporal evolution of exhumation rates over each area (Figure II.2.10).

Samples that underwent slow cooling through the partial annealing zone may lead to apparent AERs that do not correspond to the exhumation rate (e.g., Gallagher et al., 1998). The mean track lengths can be used to monitor whether this is the case, as samples that cooled slowly through the partial annealing zone are characterized by mean track length ≤ ~12.5 µm. Most areas covered by our constructed isoage surfaces are characterized, in contrast, by sample mean track length ≥ 13 µm (compare Figures II.2.3-c and 8), with the exception of the Bergell and the Aar-Leventina (areas 1 and 6 in Figure II.2.8).

II.2.5. Results

II.2.5.1. Main features of the fission-track age patterns

Young AFT ages (< 10 Ma) appear in the axial region of the Western Alps (Figure II.2.3-a) and particularly over the Argentera, Ecrins - Mont-Blanc, and Aar External Crystalline Massifs. Very young ages (< 5 Ma) are also found in the Chur region, between the eastern Aar and the Silvretta nappe, and in the western Lepontine Dome, east of the Simplon fault. In contrast, the internal crystalline massifs (Gran Paradiso, Dora Maira) as well as the Austroalpine units are characterized by Early Miocene or older AFT ages (> 10 Ma). An inverse relationship between AFT age and mean track length appears, with ages < 10 Ma generally characterized by mean track length > 13 µm (compare Figures II.2.3-a and 3-c). The only exception to this pattern is a band of short mean track lengths extending from the central Aar Massif to the SSE (Figure II.2.3-c). Young ZFT ages (< 15 Ma) characterize the Aar, Mont-Blanc, Belledonne and Lepontine Massifs (Figure II.2.3-b). Extensive regions of both the external and internal parts of the orogen show early Alpine ZFT ages (20-35 Ma), whereas two orogen-parallel bands (an external band covering the frontal parts of the Mont-Blanc and Aar Massifs and an internal band running from the eastern Ecrins across the Southern Alps) show ZFT ages that were not reset by the Alpine orogeny (i.e., ZFT age ≥ 35 Ma).

[5] More arguments can be found in section II.3.2.3, II.3.2.4 and figures therein.
[6] All the histograms used to calculate exhumation rates are reported in Figures II.3.21 to II.3.28.

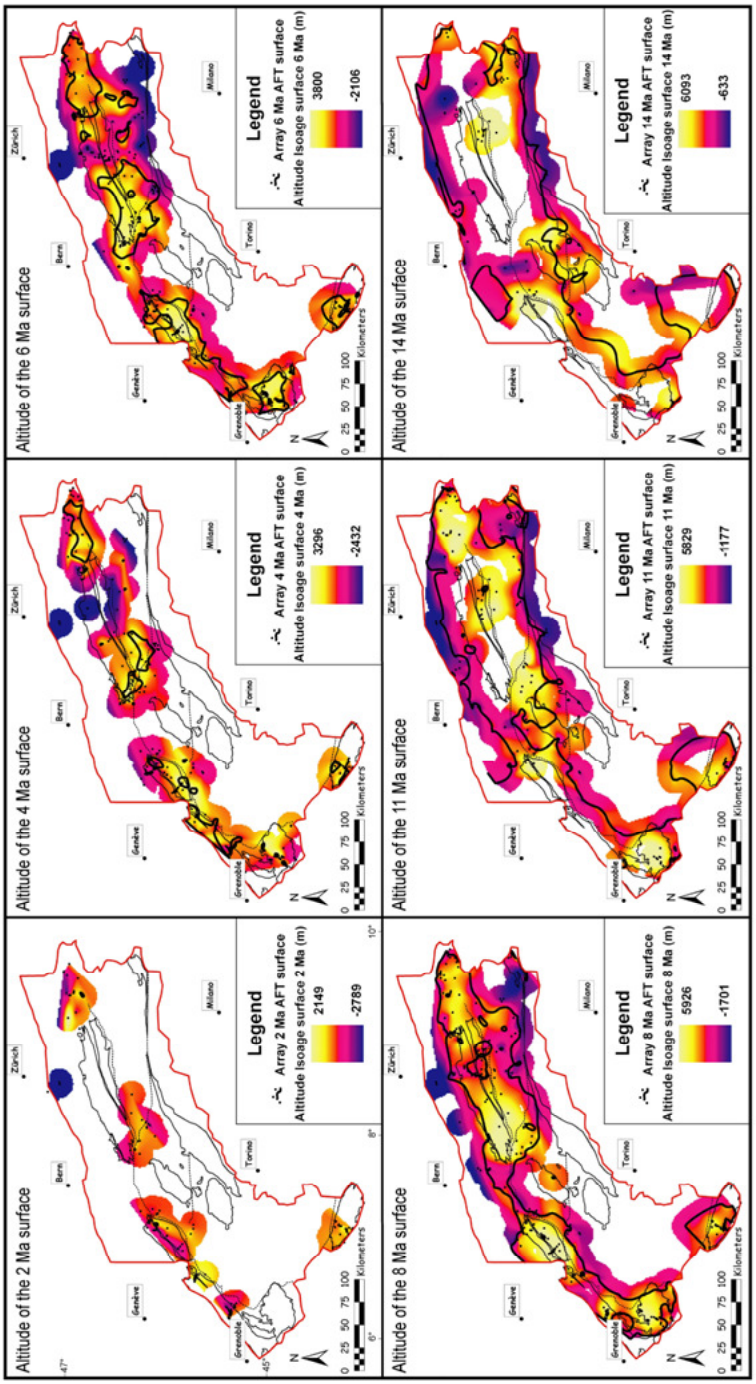

Figure II.2.7. Six examples of isoage surfaces among the 13 obtained between 14 and 2 Ma. Following a natural-neighbor interpolation between isoage points, the grid is clipped with a mask at 15 km to reduce the number of pixels located far from any source of information. The color scale represents the elevation in meters above sea level (note that the scale is different for each panel). The overall elevation of old isoage surfaces (e.g., 11 Ma; 14 Ma) is higher than the elevation of younger isoage surfaces (2 Ma; 4 Ma) which is in agreement with the generic sketch in Figure II.2.5.

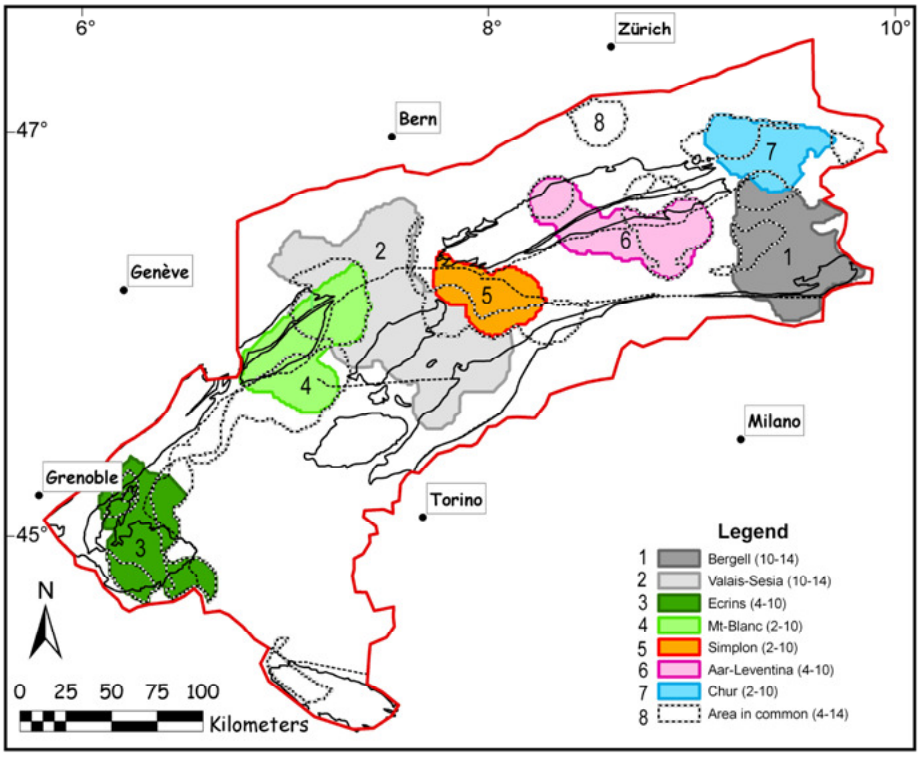

Figure II.2.8. Areas with continuous isoage surface coverage. Eight areas with isoage surfaces covering 4 to 10 Myr were obtained by comparing the area covered by the 13 isoage surfaces obtained between 14 and 2 Ma (Figure II.2.6). Different periods of time are documented in different areas, as indicated in the legend, depending on the ages accessible at outcrop.

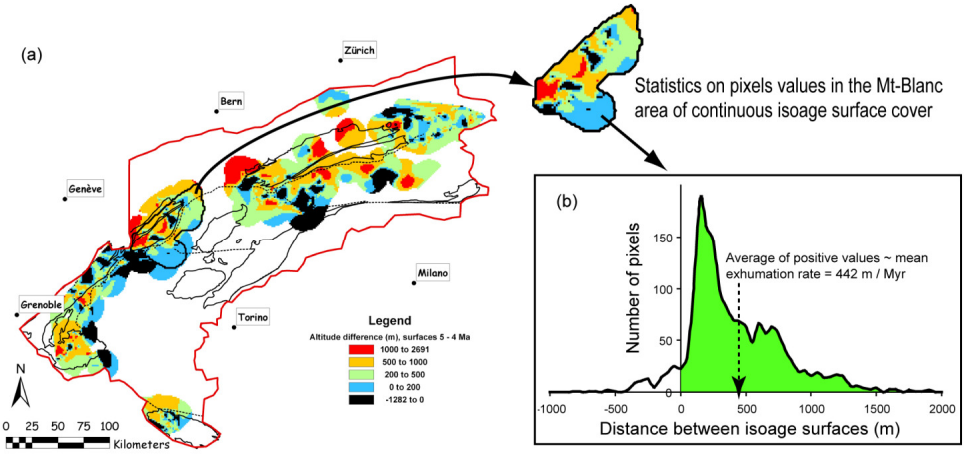

Figure II.2.9. Calculation of denudation rate from the elevation difference of isoage surfaces. (a) Map of the elevation difference between the 5 and 4 Ma isoage surfaces. (b) In this example, values of elevation difference are extracted from the area of continuous isoage surface coverage located on the Mont-Blanc Massif (area 4 in Figure II.2.8), and plotted in a frequency histogram. The pixels with a negative value (in black on the map) cannot be used to infer denudation rates and are discarded. The average distance between isoage surfaces is calculated over the remaining histogram and considered to be equivalent to the amount of exhumation affecting the Mont-Blanc area during the corresponding period.

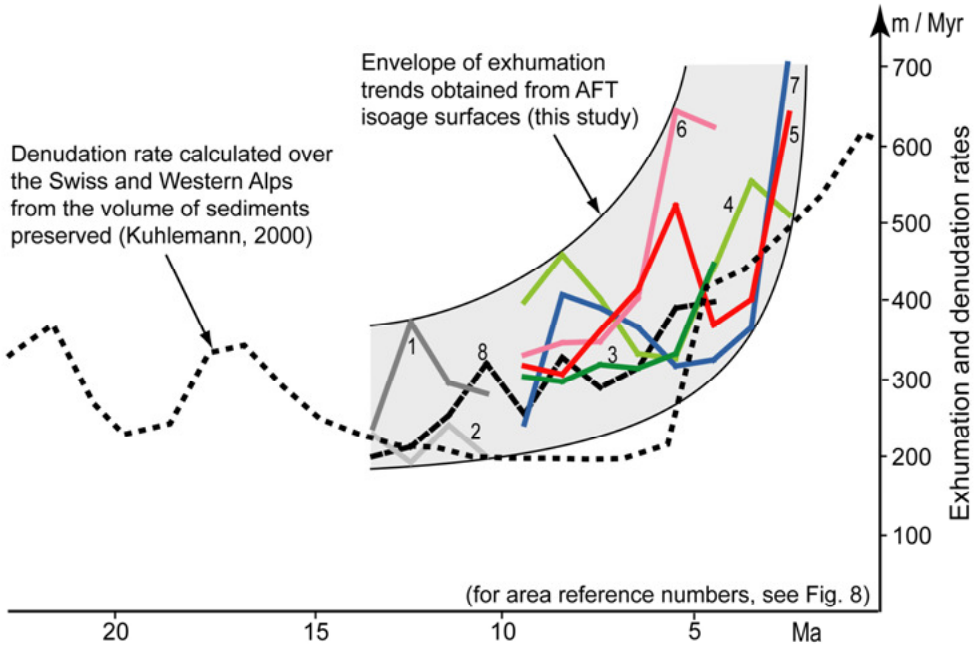

Figure II.2.10. Comparison between the estimates of average denudation rate (recorded in sediment volume) and exhumation rate (using AFT isoage surfaces, this study) over the Western Alps. The average Western Alps denudation rate calculated by Kuhlemann (2000) is the ratio between the peri-Alpine sedimentation rates (Figure II.2.1) and the provenance area. The exhumation rate was estimated over 8 regions of the Western Alps by the isoage surface technique (Figures II.2.5 to 9). Both the envelope of exhumation trend and the denudation curve show an increase centered around 5 Ma (with likely regional variability). See sections 6.3. and 6.4. for a discussion of the features observed in exhumation rate trends.

The AFT and ZFT age patterns run parallel to two major Alpine tectonic lineaments: the Penninic thrust, bordering the External Crystalline Massifs, and the Simplon fault. Both areas show younger ages in their footwalls (Figures II.2.3-a and 3-b), which suggests that a component of tectonic exhumation may affect the age patterns, as previously suggested in more local studies (Fügenschuh and Schmid, 2003; Seward and Mancktelow, 1994; Tricart et al., 2007).

II.2.5.2. Variation in exhumation rate from paired AFT and ZFT ages

A pattern of recent accelerated exhumation, dominantly affecting the external side of the belt (and the External Crystalline Massifs in particular), is evidenced in Figure II.2.4. This map demonstrates an overall acceleration in exhumation rate along the northern and western borders of the orogen, since these areas crossed the AFT closure temperature of ~120 °C. AFT ages in the region showing accelerated denudation are mostly ≤ 8 Ma (compare Figures II.2.3-a and 4). However, exhumation rates used in this ratio calculation are average values for initial cooling between the ZFT and AFT closure temperatures and final cooling between

the AFT closure temperature and the surface, and do not enable us to resolve when the acceleration occurred.

II.2.5.3. Description of isoage surfaces

The elevation of isoage surfaces generally increases with age (see legend on each map of Figure II.2.7), which is consistent with the assumption that isoage surfaces are mainly controlled by the effect of denudation on isotherms (Figure II.2.5). The overall shape of the isoage surfaces is that of arcuate domes, the axes of which are roughly superposed with the External Crystalline Massifs (Aar, Mont-Blanc and Ecrins, see Figure II.2.2) for the younger surfaces, and with more internal massifs (Lepontine Alps, Dent-Blanche) for older surfaces. Young isoage surfaces are defined mostly by points from high-relief areas with young fission-track ages in the valleys, whereas old isoage surfaces are controlled by locally old fission-track ages encountered on topographic peaks and the elevation of isoage contours in the periphery of the orogen.

II.2.5.4. Spatial and temporal evolution of exhumation rates

The difference in elevation of AFT isoage surfaces was used to estimate exhumation rates between 13.5 and 2.5 Ma over the Western Alps (Figures II.2.7-10). Comparing curves of exhumation rate against time for different sub-areas (Figure II.2.10) highlights a series of eight overlapping segments from 9.5 to 2.5, 9.5 to 4.5, 13.5 to 10.5 and 13.5 to 4.5 Ma, which all share a similar trend. The estimates of exhumation rate vary between 200 and 700 m Myr^{-1}, with an acceleration centered around 5 Ma, which is in surprisingly good agreement with peri-alpine sedimentation rates and inferred alpine denudation rates reported by Kuhlemann and co-workers (Kuhlemann, 2000; Kuhlemann et al., 2002). While we are mostly interested in the pattern of denudation rates at the orogen scale, regional variations in the exhumation history demonstrate the localization of denudation (Figure II.2.10). The exhumation rates estimated in the Bergell and Valais-Sesia areas (curves 1 and 2) are similar and indicate a denudation rate of ~300 m Myr^{-1} between 13.5 and 10.5 Ma. The Ecrins and Mont-Blanc Massifs (curves 3 and 4) share a similar pattern of increase in exhumation rate between 5.5 and 4.5 Ma, with recent rates reaching 500 m Myr^{-1}. Further east, the Aar-Leventina area (curve 6) shows a slightly earlier increase in exhumation rate (~6 Ma). However, the occurrence of short mean track lengths in the Aar-Leventina and the Bergell areas (cf. section 4.4) may lead us to overestimate recent exhumation. In contrast, the onset of the acceleration in the Simplon and Chur areas (curves 5 and 7) appears to be younger than 3.5 Ma, with recent denudation rates reaching over 600 m Myr^{-1}. The sub-area with the longest continuous

coverage in isoage surfaces (area 8 on Figure II.2.8) combines a suite of small areas in the Western Alps. The values of exhumation rate it provides between 13.5 and 4.5 Ma (curve 8 on Figure II.2.10) are included within the range of the seven other sub-areas.

II.2.6. Discussion

II.2.6.1. Conditions of use of isoage surfaces

The use of isoage surfaces to calculate exhumation rates through time requires that the surfaces have not been significantly deformed. Therefore, actively deforming thrust belts would need to be treated with caution. Locations undergoing relief reduction are also to be avoided because age-elevation relationships would provide overestimates of exhumation rates (Braun, 2002). The optimal conditions are met in orogens where relief is either steady or increasing, and tectonic activity is insufficient to significantly deform the isoage surfaces. The Western Alps are a successful candidate because relief appears to have increased recently due to glaciations (Champagnac et al., 2007; van der Beek and Bourbon, 2008), whereas present-day tectonic activity is limited (e.g., Calais et al., 2002). Moverover, the European Alps are covered by an exceptional density of existing AFT ages, allowing us to use the approach developed here.

II.2.6.2. Errors affecting exhumation rate calculations

Several types of error potentially affect the calculation of exhumation rates from isoage surfaces: (1) uncertainties affecting the ages, elevations and coordinates of samples in the database used to compute isoage surfaces, (2) heterogeneous scatter of the interpolated data points, and (3) geological factors such as the composition of apatites (defining their precise closure temperature) and spatial or temporal variations in relief and geothermal gradient. While errors of type 1 can be estimated on a sample per sample basis, propagating these into an uncertainty in isoage surface elevation cannot be done rigorously, although a Monte Carlo approach in which the surfaces are created thousands of times while varying the input data within error could be envisaged. Whereas uncertainties of type 2 (role of sampling density and scatter) are generally assessed using kriging techniques, these are limited for geological applications because of strong assumptions on spatial continuity and statistics of the data. Alternatively such errors may be evaluated using calculation-intensive boot-strap techniques. Uncertainties of type 3, however, are practically impossible to quantify. Moreover, the weight of these three types of errors within the final uncertainty in exhumation rates is unknown. Therefore, we chose to present the estimates of exhumation rates as such, without the addition of an inherently partial and, therefore, misleading error.

II.2.6.3. Comparison between exhumation rates and the volume of sediment deposited through time

The exhumation rates calculated from the AFT isoage surfaces over the Western Alps (Figure II.2.10) are of the same order (200-600 m Myr^{-1}) as those calculated from the sedimentary record (Kuhlemann, 2000; Willett et al., 2006). They are also, more expectedly, comparable with denudation rates obtained from local thermochronological studies (e.g., Michalski and Soom, 1990; Schär et al., 1975; Schlunegger and Willett, 1999; Tricart et al., 2007). Thus, both the sedimentary record and the in-situ thermochronological record show a similar increase in exhumation rates around 5 Ma. However, the thermochronometric estimates of denudation rates are overall slightly higher than those obtained from the sedimentary record (Figure II.2.10). This small offset may be explained by the fact that areas with the most complete isoage surface coverage, which are used in the calculations, are biased toward the more rapidly eroding massifs with young AFT ages in the valleys, and therefore do not constitute a representative sampling of the entire Western Alps. Other explanations could be an overestimation of exhumation rates obtained from age-elevation relationships (Braun, 2002) or a general bias in the calculation of sediment volume, which, for instance, does not take chemical weathering or sediment recycling into account.

II.2.6.4. Possible causes for increased recent exhumation

Over the last 14 Myr, the shift of the apex of isoage surface domes through time from the inner Alps to the External Crystalline Massifs (Figure II.2.7) suggests a shift of the most actively exhuming regions during Late Miocene and Pliocene times. This idea is in agreement with the map of the ratio of final / initial exhumation rates (Figure II.2.4), where acceleration of exhumation is observed after AFT closure in the External Crystalline Massifs.

Within this general frame, we observe a broad increase in exhumation rate in the Western Alps centered around 5 Ma, with local variations in the timing of this increase (Figure II.2.10). Assuming that these variations are significant compared to the unquantified uncertainty, they suggest that the rise in Alpine denudation described as happening around 5 Ma (e.g. Cederbom et al., 2004; Kuhlemann, 2000), actually varied considerably, taking place between 6.5 and 2.5 Ma depending on local tectonic and structural conditions. A clear expression of regional diversity within a general trend of exhumation increase is found in the Simplon and Chur areas (Figure II.2.8 and Figure II.2.10). The resent surge in exhumation rates in these areas can be linked spatially to present-day high rock uplift rates in the western and eastern Aar Massif (e.g., Persaud and Pfiffner, 2004). Although a significant part of

present-day rock uplift rates could be due to the isostatic response to erosional unloading (Champagnac et al., 2007; Schlunegger and Hinderer, 2001), this spatial link may suggest that these two locations are characterized by high rock uplift rates since at least the time of AFT closure. Furthermore, this pattern suggests that current exhumation of the Aar Massif is concentrated on its western and eastern borders, and has been so for several million years.

Based on the approximate temporal coincidence between Mio-Pliocene acceleration of exhumation in the Western Alps, and the closure of the Panama isthmus and subsequent reorganization of Atlantic Ocean currents, Cederbom et al. (2004) proposed that the increase in exhumation around 5 Ma was externally controlled by increased precipitation over Europe. An alternative, and more global mechanism, is that the increased variability of climate witnessed by the ocean oxygen isotope record forced accelerated erosion rates, although the data suggest that this happened between 4 and 3 Ma (e.g., Molnar, 2004; Zhang et al., 2001). Although this explanation remains difficult to confirm, it is seducing as a cause of a global scale, or at least a continental scale could explain the simultaneous increase in exhumation in other orogens (e.g., Molnar, 2004; Zhang et al., 2001). Uplift of the Western Alps followed by widespread exhumation may also be controlled by a deep-seated event such as slab detachment; however, no evidence exists to tie such an event down at this particular time.

II.2.7. Conclusions

Our analysis of the complete fission-track thermochronology database in the Western Alps leads to the following general conclusions:

1) Although different regions of the Western Alps show a variable absolute amount of exhumation since 13.5 Ma, they share a common trend of doubling in exhumation rates at approximately 5 Ma. If one accepts the assumptions on error values, it is possible to distinguish between areas where the rise in Alpine denudation took place at different periods within a 6.5 to 2.5 Ma time frame.

2) The overall consistency between estimated denudation rates using sediment volumes (Kuhlemann, 2000), and bedrock thermochronology (this study) demonstrates that, although both records are fragmentary and error-prone, they are appropriate to describe the general exhumation history at the orogen scale since at least 13.5 Ma.

3) The maps of zircon and apatite fission-track ages share a pattern of young ages over an arc linking the External Crystalline Massifs, as well as in the area of the Lepontine Alps, suggesting that these areas underwent the strongest recent denudation in the Western Alps.

The observed longer mean AFT lengths in the areas with young fission track ages further supports this conclusion.

4) This pattern fits with the trend of accelerated exhumation rates calculated from samples with paired zircon and apatite fission-track ages. This trend indicates that most of the Western Alps, in particular the external side of the arc, was on average exhumed faster after AFT closure than between the times of ZFT and AFT closure.

Acknowledgements

L. Keller, P. Leloup, S. Schwartz and P. Tricart kindly provided complementary details on their published material. We are grateful to M. Ford and D. Seward for permission to use unpublished AFT and ZFT ages. The manuscript benefited from thorough and constructive reviews by Kerry Gallagher and an anonymous reviewer. This study was supported by an INSU-CNRS "Reliefs de la Terre" program grant to PvdB, and a "University of Edinburgh PhD teaching studentship" and an international student mobility (MIRA) grant of the Rhône-Alpes region to AV.

II.3. Appendix to Chapter II

In section II.2, I exploited a AFT and ZFT ages database covering the western European Alps, to describe the temporal and spatial evolution of exhumation rates over the Western Alps. Here, I provide details on how exhumation rates were calculated from samples with paired ZFT and AFT ages, and give further details on the construction of isoage surfaces and their use to estimate local exhumation rate using pixel-value distribution histograms calculated from maps of the elevation difference between successive isoage surfaces.

II.3.1. Map of paired ZFT and AFT ages: ratio between final / initial exhumation rates

Where available, samples from the database (see references in Figures II.2.3-a and 3-b) with paired zircon fission track age (ZFT) and apatite fission track ages (AFT) were used to compare the average exhumation rates between the closure of the two thermochronometers, and the closure of the AFT system and outcrop at the surface, in section II.2.4.2.

The values of exhumation rates were calculated in a five-step iterative approach, using the following equations (Dodson, 1973; Brandon et al., 1998; Braun et al., 2006):

$$\dot{E}_Z = \frac{z_{cZ} - z_{cA}}{a_Z - a_A} \quad ; \quad \dot{E}_A = \frac{z_{cA}}{a_A} \tag{II.3.1}$$

$$\begin{aligned} z_{cZ} &= -\frac{\kappa}{\dot{E}_Z}\left(1 - \frac{T_{cZ} - T_S}{G_0 L}\left(1 - e^{-\dot{E}_Z L/\kappa}\right)\right) \quad ; \\ z_{cA} &= -\frac{\kappa}{\dot{E}_A}\left(1 - \frac{T_{cA} - T_S}{G_0 L}\left(1 - e^{-\dot{E}_A L/\kappa}\right)\right) \end{aligned} \tag{II.3.2}$$

$$T_{cZ} = \frac{E_{aZ}}{R \ln\left(B_Z \dfrac{R(T_{cZ})^2}{E_{aZ}\dot{T}_Z}\right)} \quad ; \quad T_{cA} = \frac{E_{aA}}{R \ln\left(B_A \dfrac{R(T_{cA})^2}{E_{aA}\dot{T}_A}\right)} \tag{II.3.3}$$

$$\begin{aligned} \dot{T}_Z &= \frac{(\dot{E}_Z)^2}{\kappa}\left(\frac{G_0 L}{1 - e^{-\dot{E}_Z L/\kappa}} - (T_{cZ} - T_s)\right) \quad ; \\ \dot{T}_A &= \frac{(\dot{E}_A)^2}{\kappa}\left(\frac{G_0 L}{1 - e^{-\dot{E}_A L/\kappa}} - (T_{cA} - T_s)\right) \end{aligned} \tag{II.3.4}$$

where $\dot{E}$ is exhumation rate, z_c is closure depth, a is thermochronological age, T_c is closure temperature, T_s is surface temperature, $\dot{T}$ is the cooling rate at the closure depth, κ is thermal diffusivity, G_0 is "initial" unperturbed geothermal gradient, L is the characteristic depth of the exhuming column, E_a is activation energy, R is the universal gas constant, B is a constant that combines a geometry factor and the diffusivity of the thermochronological system, and the subscripts A and Z refer to apatite and zircon, respectively. Equations II.3.1-II.3.4 are solved iteratively, using the parameters value in Table II.3.1 and initial values of 120 °C, 240 °C and 25 °C / km for T_{cA}, T_{cZ} and G_0, respectively.

κ	25 km^2 / Myr
L	30 km
R	*8.315 J / mol / K*
T_s	*T_s = 273.15 + (15 – 6h) K; with h the elevation in km*
E_{aA}	186.43 kJ / mol
E_{bZ}	208.16 kJ / mol
B_A	9.8 10^{11} s^{-1}
B_Z	10^8 s^{-1}

Table II.3.1. Parameters used in the iterative calculation of exhumation rates (Brandon et al., 1998; Braun et al., 2006).

The ratio between final / initial exhumation rates were interpolated over the Western Alps, and presented in Figure II.2.4. The maps of interpolated intermediate parameters used to calculate the final / initial exhumation ratio are reported in Figures II.3.1 to 5: closure temperature of the ZFT and the AFT systems; closure depth of the ZFT and the AFT systems; average cooling rate between ZFT and AFT closure, and between AFT closure and the surface; average geothermal gradient between ZFT and AFT closure, and between AFT closure and the surface; average exhumation rate between ZFT and AFT closure, and between AFT closure and the surface. Note that all of these measures are more or less dependent on the initial value of geothermal gradient chosen, which is not strongly constrained. The ratio between the two denudation rates is much less sensitive to this initial condition, which is the reason why I chose to report only this ratio in the paper section II.2.4.2.

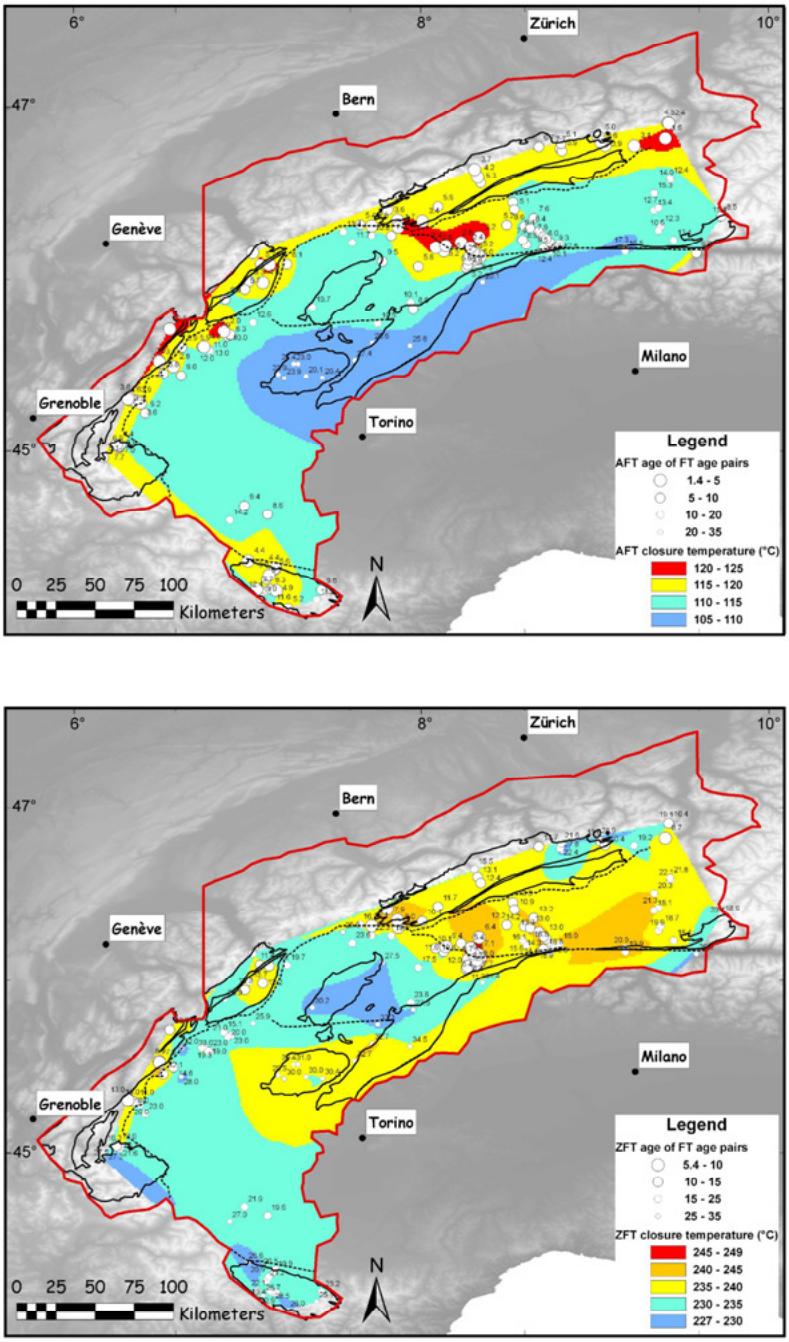

Figure II.3.1. Computed closure temperature of the ZFT and the AFT thermochronometers. See Figures II.2.3-a and 3-b for references to original data.

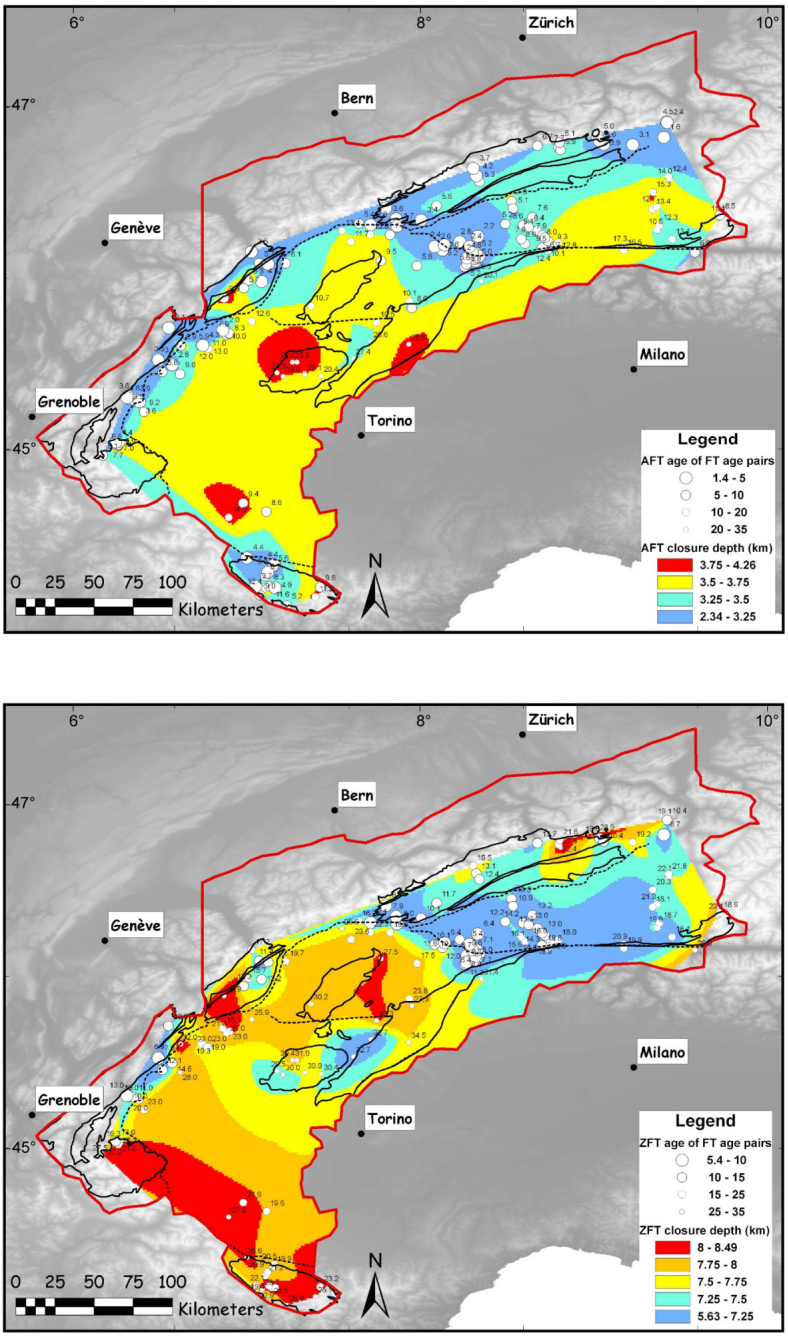

Figure II.3.2. Computed closure depth below the surface of the ZFT and the AFT thermochronometers.

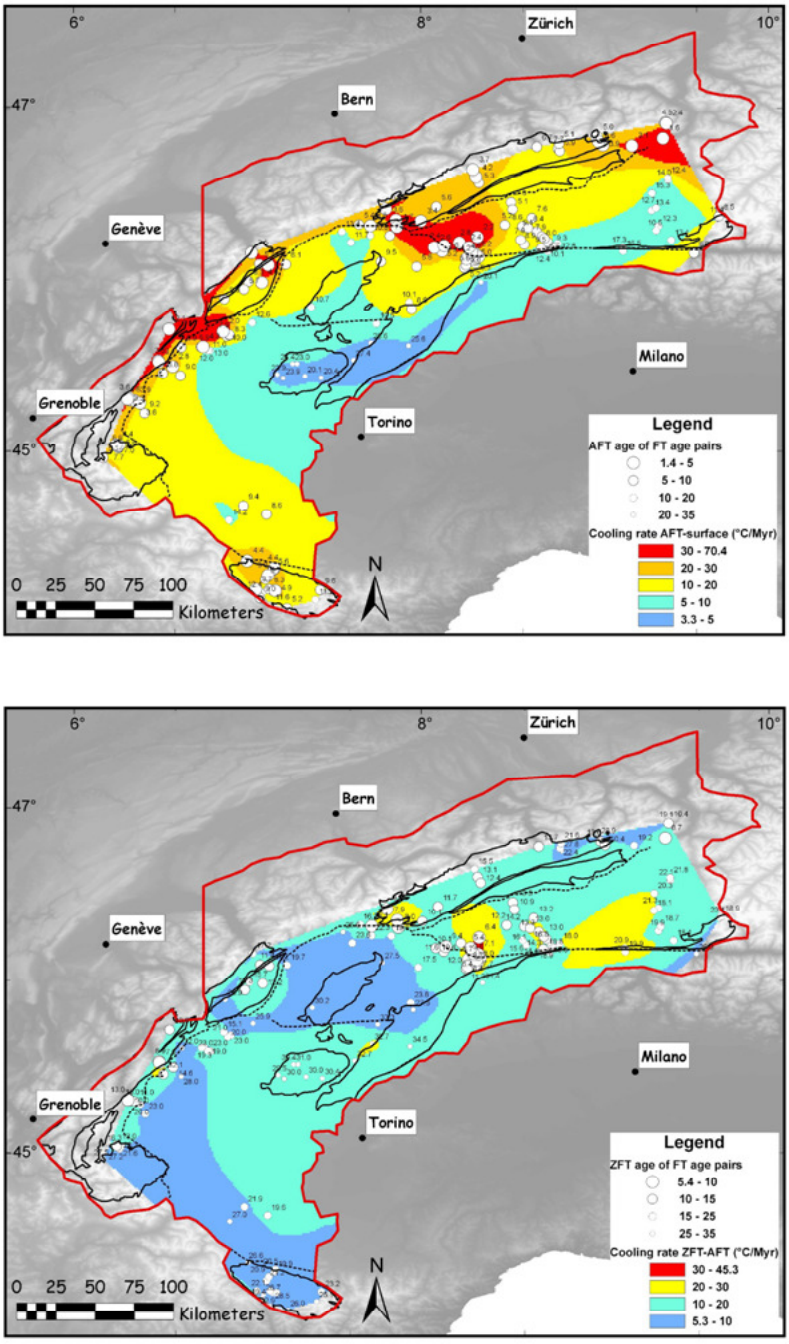

Figure II.3.3. Computed cooling rate between ZFT and AFT closure, and between AFT closure and the present.

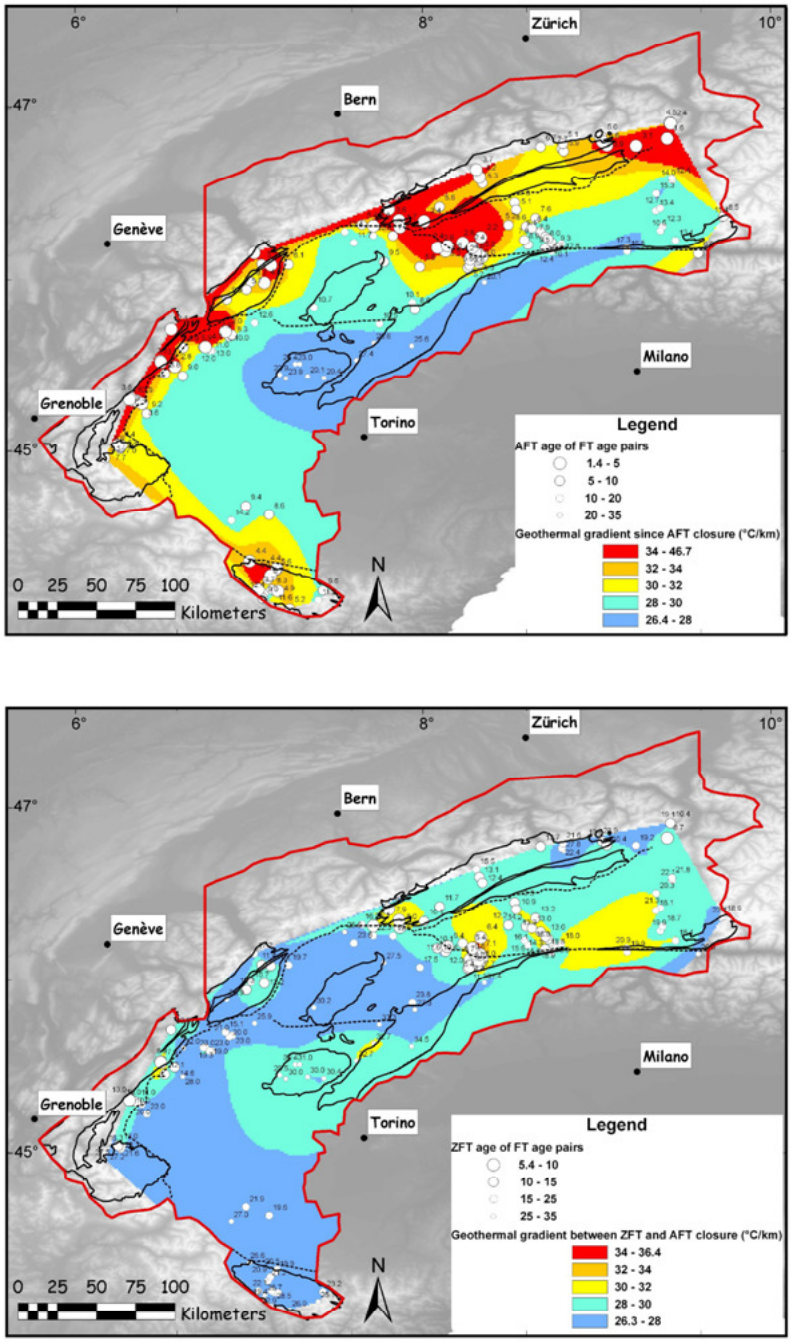

Figure II.3.4. Computed geothermal gradient between ZFT and AFT closure, and between AFT closure and the present, calculated as the ratio between cooling rate and exhumation rate.

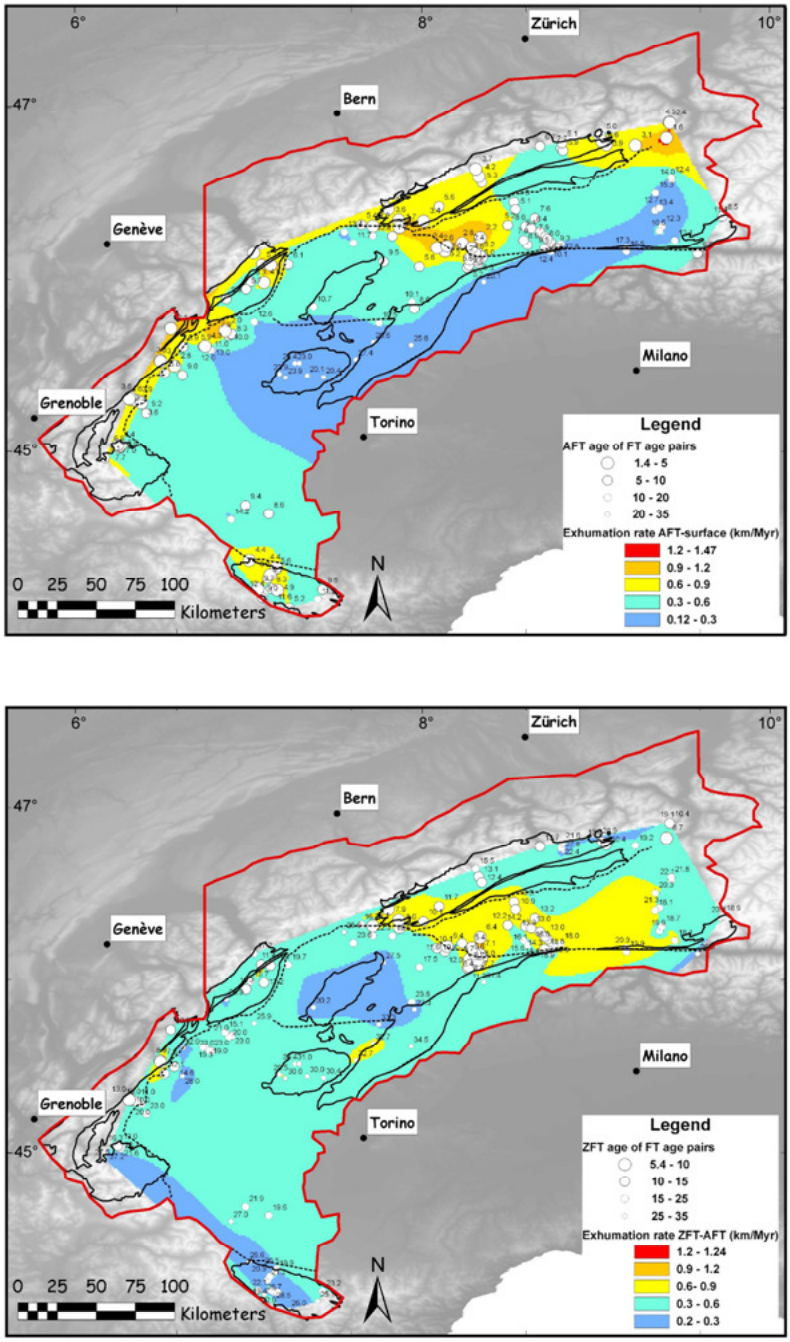

Figure II.3.5. Computed exhumation rate between ZFT and AFT closure, and between AFT closure and the present.

II.3.2. Maps of AFT isoage surfaces elevation

In this section, I will provide additional details on the manner in which I constructed AFT isoage surfaces according to a novel method detailed in section II.2. I will also detail how these surfaces were used to estimate exhumation rates, and assess the quality of our dataset of isoage surface elevations.

II.3.2.1. Neighbourhood age-elevation relationship

The search for strongly correlated age-elevation relationships in the neighbourhood of each data point described in section II.2.4.3.1 leads to the calculation of regression lines defined by A1 (the slope of age-elevation relationship) and A0 (the elevation of the zero-age intersect). Although these were not shown in section II.2.4.3, the A1 and A0 values may carry in themselves information on the denudation history: A1 relates to the denudation rate in the time interval spanned by the age points in the neighbourhood, and A0 may indicate whether denudation rates have increased or decreased since. Not all points in the database were used to interpolate A1 and A0 maps (Figure II.3.6) but only the ones in the neighbourhood of which a strong age-elevation relationship has been validated during the radial search. These two maps are characterized by a wide range of A0 and A1 values, with a "Y" shaped area of negative A1 (inverse slope in the age-elevation relationship) located over the Valais area and the Sesia Massif. As expected for inverse slope age-elevation relationships, the values of A0 calculated in the same areas are very high above sea level, standing out from negative values observed otherwise on the map.

The effect exerted by topography on the shape of closure temperature isotherm may lead to the overestimation of age-elevation relationships determined from surface sampling (Braun, 2002). Exhumation rates calculated from the elevation of isoage surfaces are therefore likely to be overestimated close to locations where isoage surfaces have been defined using the estimated values of A1 and A0. The estimation of age-elevation relationships is also affected by post-closure relief change; in particular a significant relief reduction can cause apparently inverse age-elevation relationships when the slope of the topography becomes smaller than the slope of the isoage surfaces; this could be an explanation to inverse age-elevation relationships (negative A1 value) observed in the Valais and Sesia areas (Figure II.3.6). Large-scale shifts of the water-divide such as described by Rahn (2005) in the Adula nappe (Lepontine Alps), or block-tilting (Rahn and Grasemann, 1999) are other possible error factors in the estimation of exhumation rates from surface samples age-elevation relationship.

II.3.2.2. Calculation of AFT isoage surfaces

The maps of AFT isoage surface elevation are obtained by interpolation between data points, comprising dots along isoage contours derived from the map of interpolated AFT ages (Figure II.2.3-a), and locations where a statistically signficant age-elevation relationship has been identified (see details of the method in section II.2.4.3). The raw interpolated maps of isoage

surface elevation are clipped at 15 km around every data point, in order to remove less well constrained areas of the maps (Figure II.3.7).

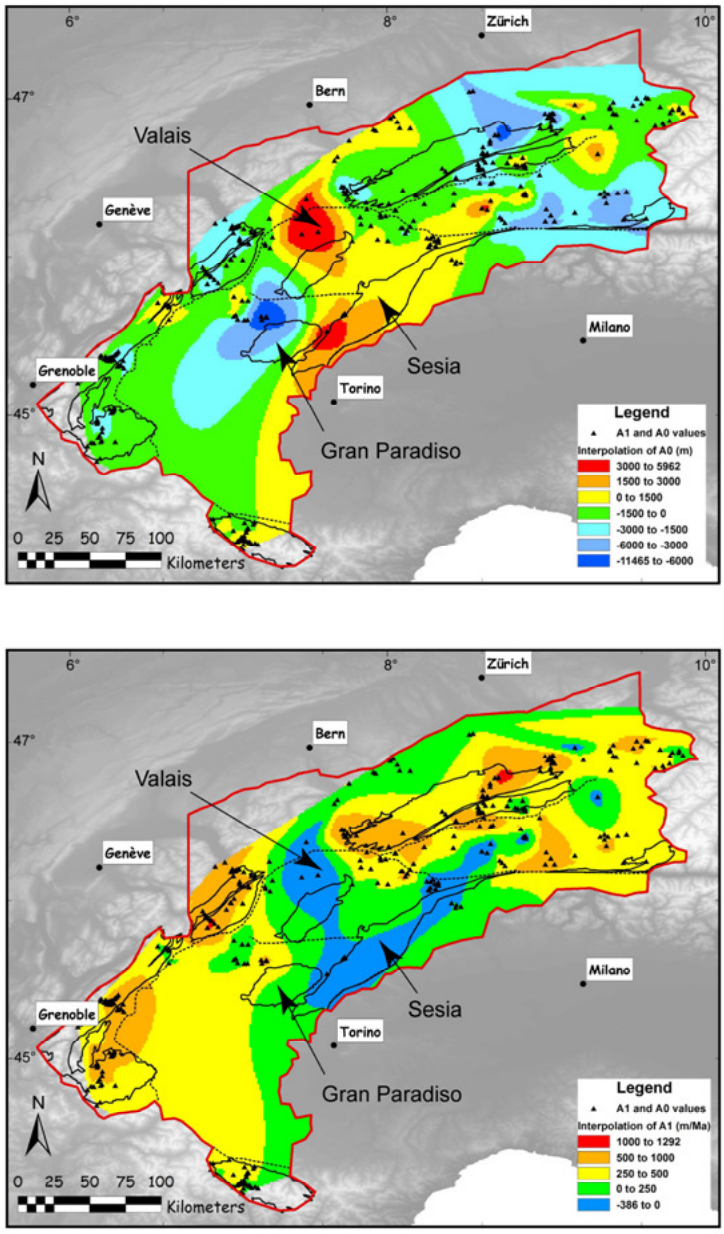

Figure II.3.6. Interpolation of the A1 and A0 values calculated to define the optimum age-elevation relationship in the neighbourhood of each datapoint, such as $z = A1 \times t + A0$, where z is the elevation in m above sea level, t the AFT age in Ma, A1 the slope of the age-elevation relationship, and A0 the ordinate at origin, i.e. the projected elevation for zero age according to the AFT ages at outcrop. See Figure II.2.3-a for references to original data.

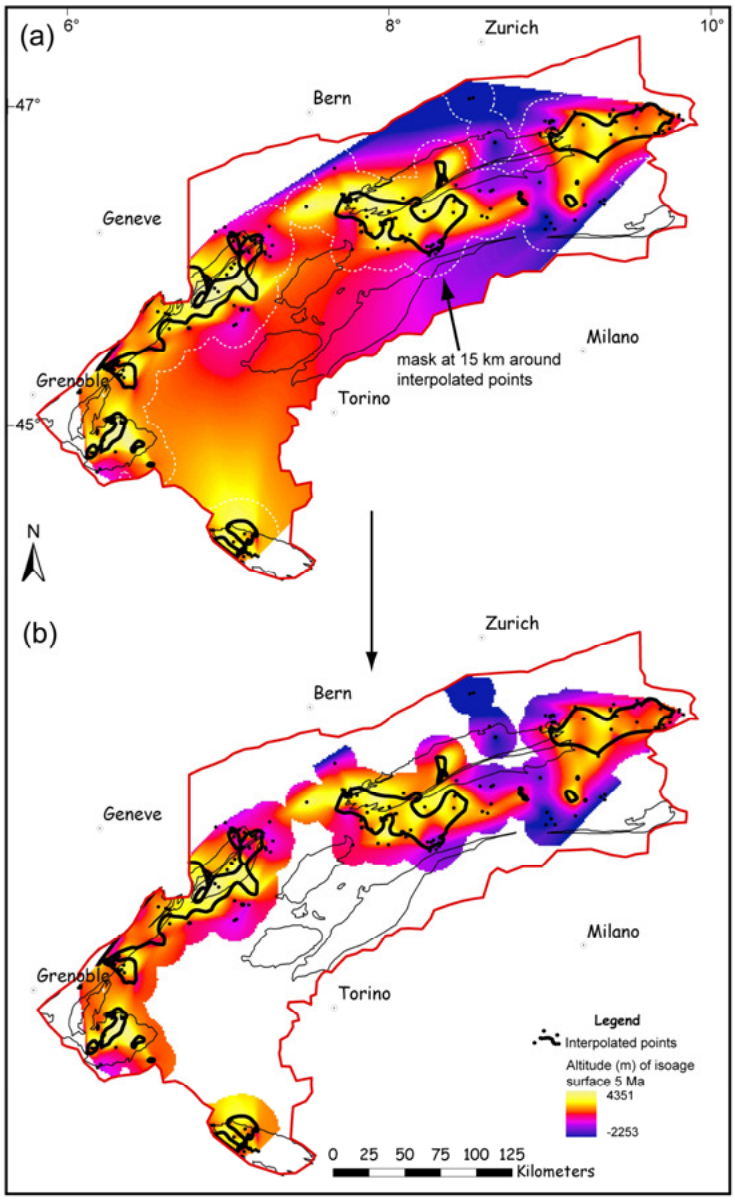

Figure II.3.7. (a) Use of a 15 km mask (white dotted line) to clip a map of isoage surfaces elevation, after interpolation between the datapoints (shown as bold black lines and dots). (b) Final map of isoage surface elevation. See section II.2.4.3 for references to original data.

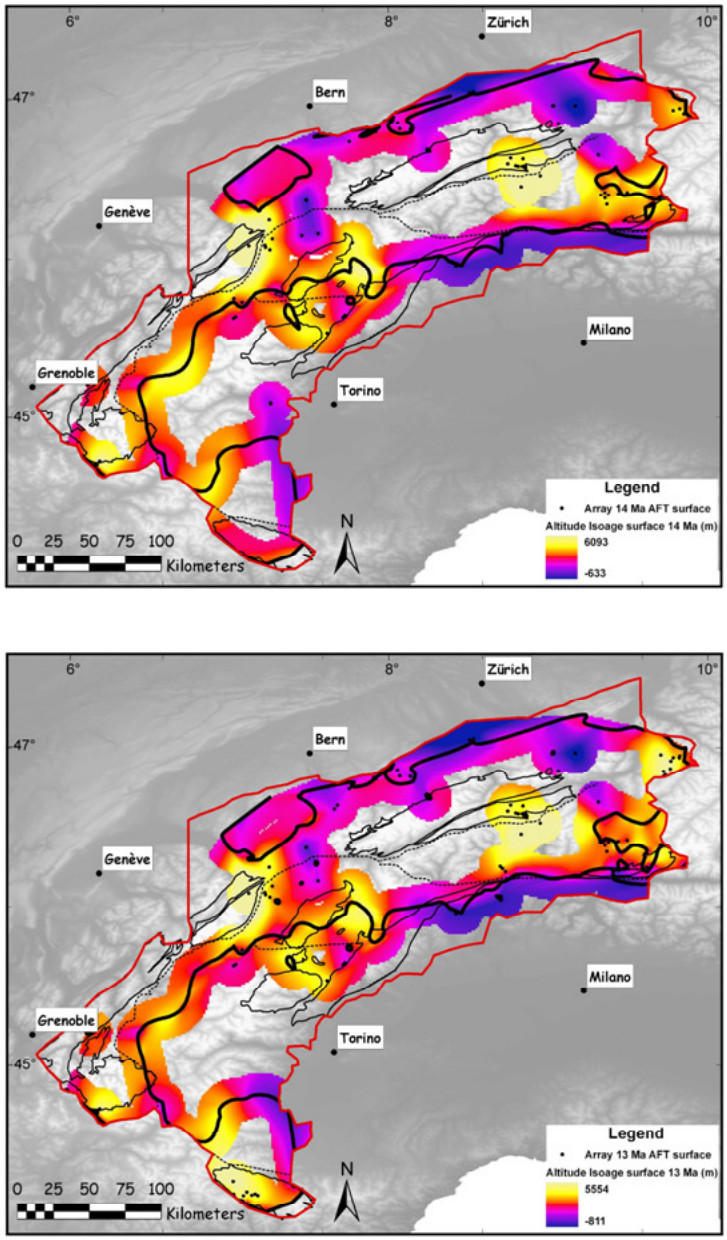

Figure II.3.8. Maps of the elevation of the 13 Ma and the 14 Ma apatite fission-track isoage surface.

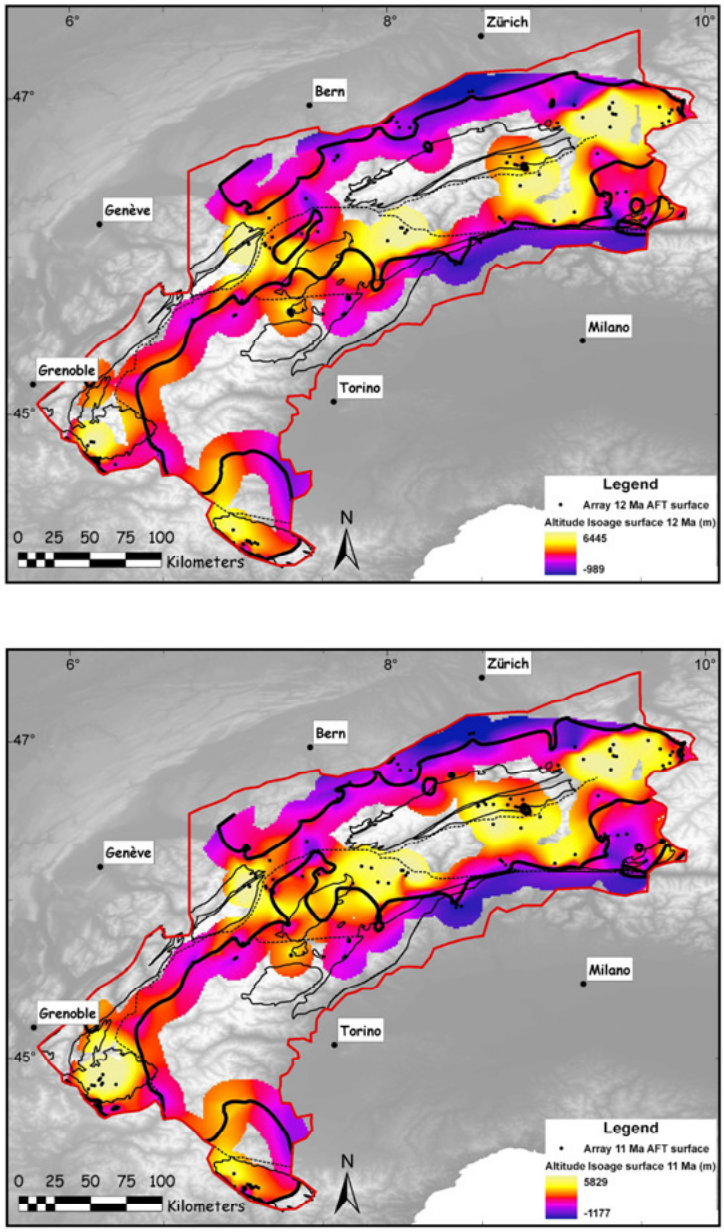

Figure II.3.9. Maps of the elevation of the 11 Ma and the 12 Ma apatite fission-track isoage surface.

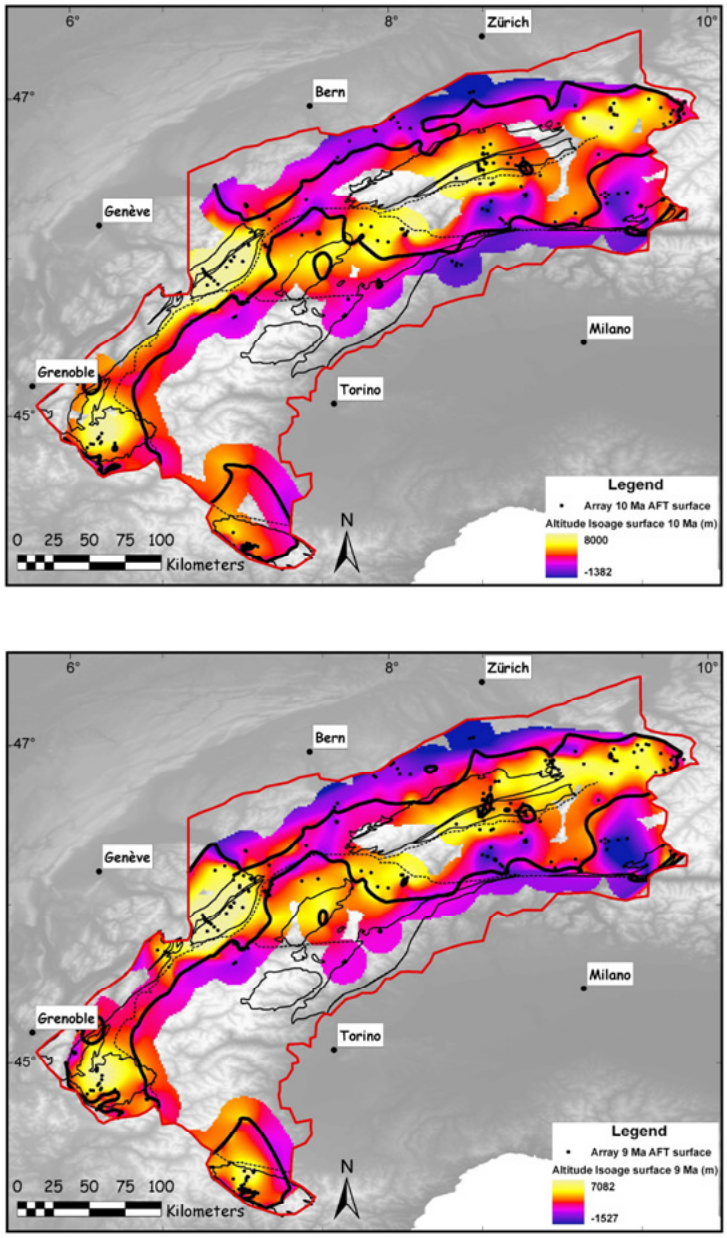

Figure II.3.10. Maps of the elevation of the 9 Ma and the 10 Ma apatite fission-track isoage surface.

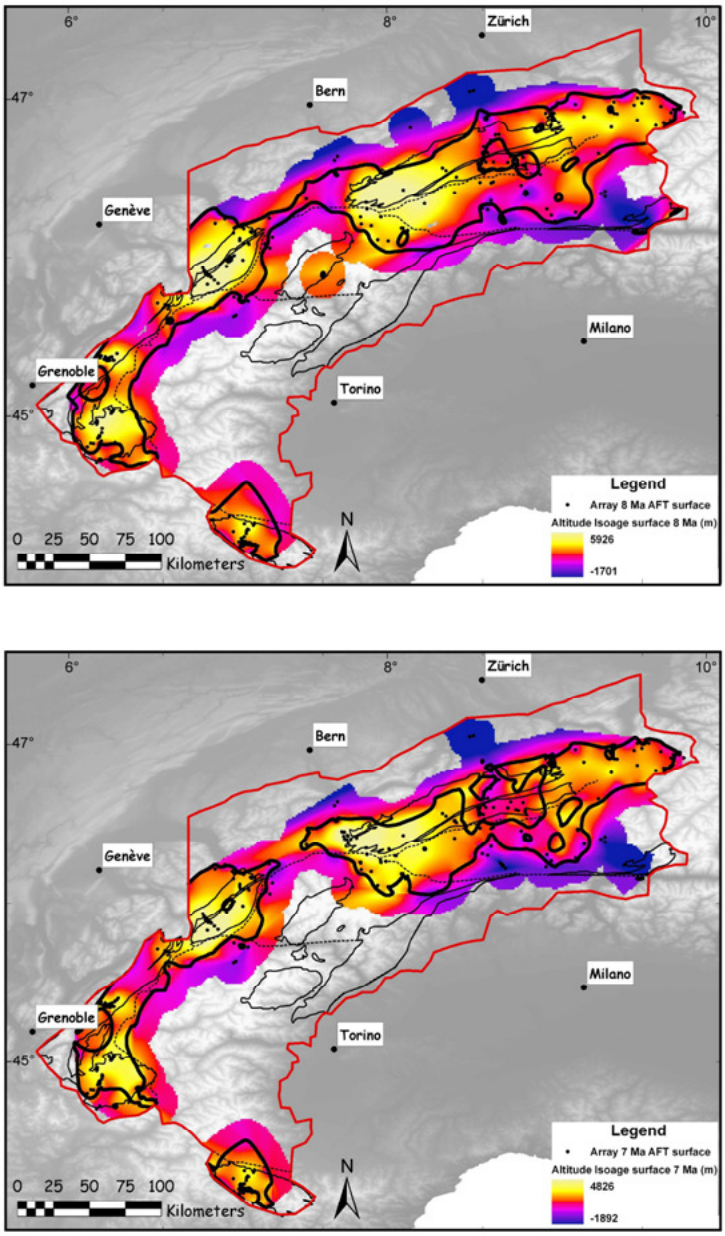

Figure II.3.11. Maps of the elevation of the 7 Ma and the 8 Ma apatite fission-track isoage surface.

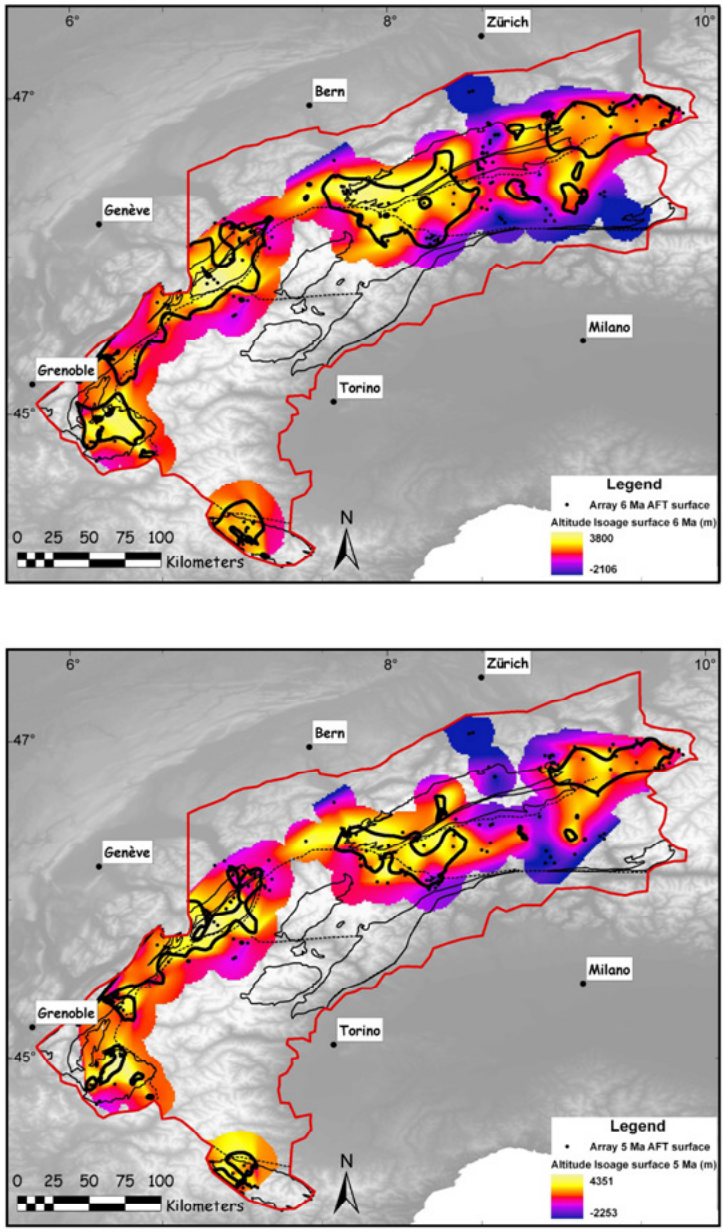

Figure II.3.12. Maps of the elevation of the 5 Ma and the 6 Ma apatite fission-track isoage surface.

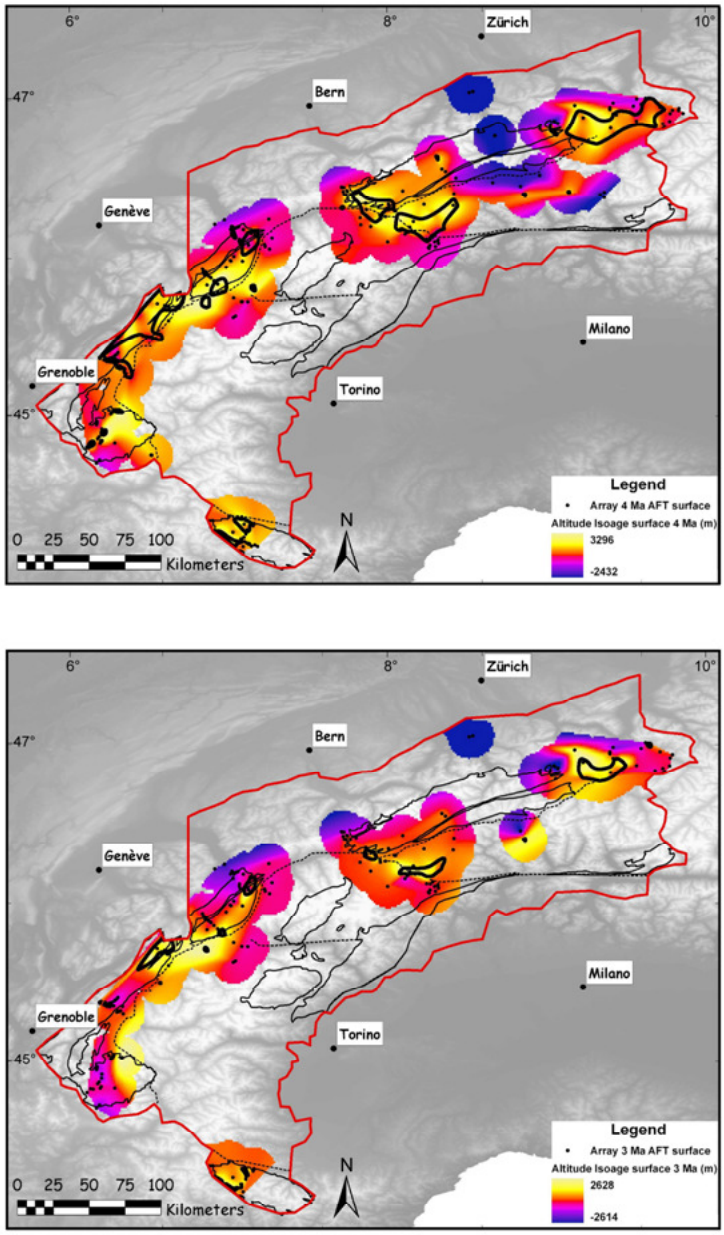

Figure II.3.13. Maps of the elevation of the 3 Ma and the 4 Ma apatite fission-track isoage surface.

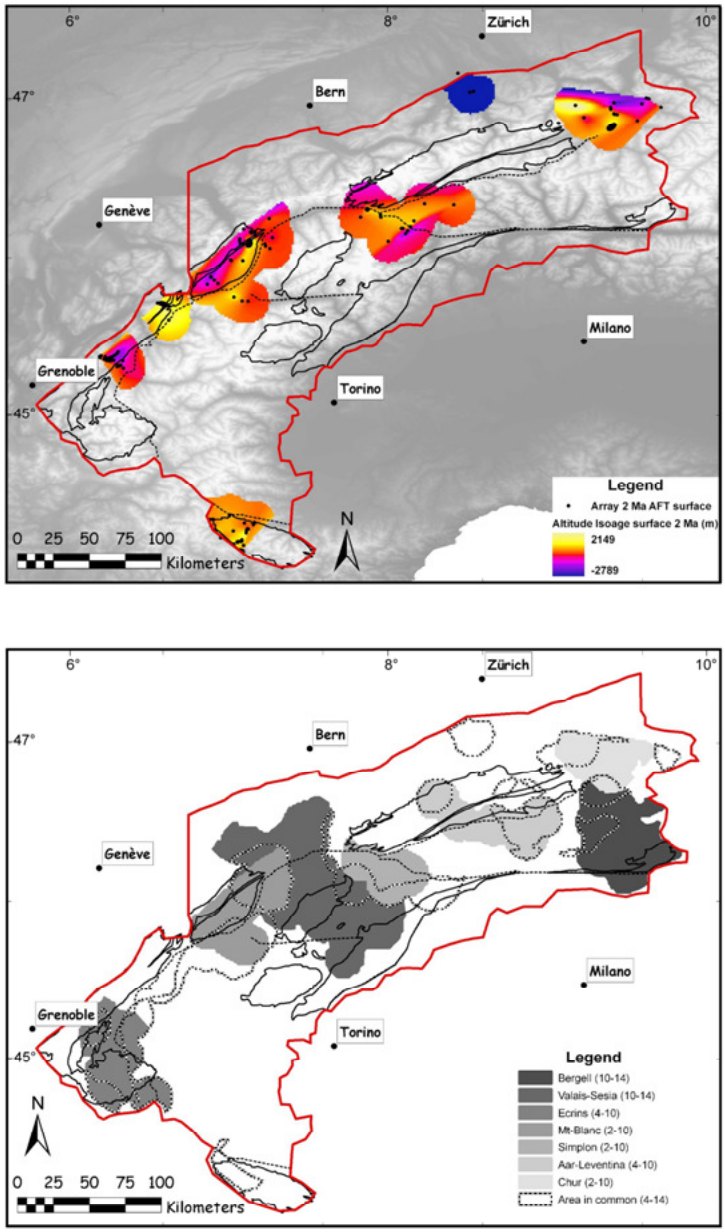

Figure II.3.14. (Upper) Map of the elevation of the 2 Ma apatite fission-track isoage surface. (Lower) Map of the eight areas of continuous isoage surface coverage used in long-term exhumation rate estimations (the extent of time coverage for each area is specified in the legend).

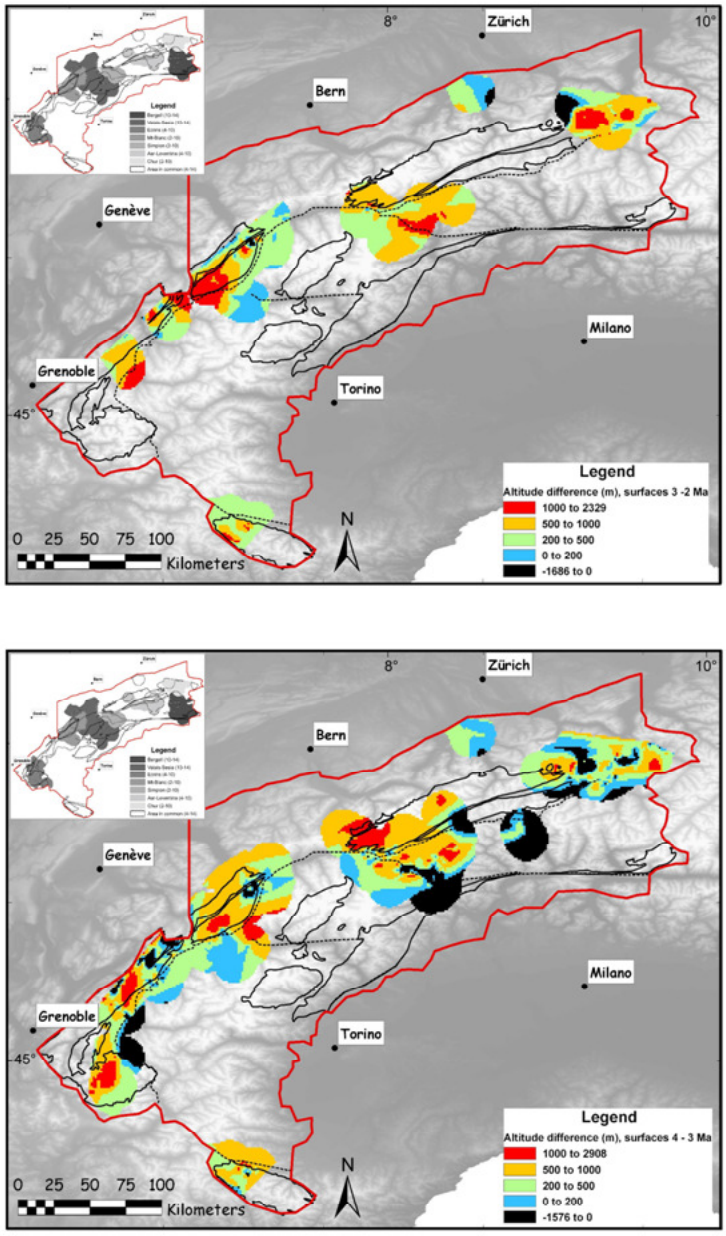

Figure II.3.15. Elevation difference between the 3-2 Ma and the 4-3 Ma apatite fission-track isoage surfaces. The inset map in the upper left hand corner is a copy of Figure II.3.14 (lower) and serves as a reminder of the location of the eight sub-areas of study where isoage surfaces are available over several Myr.

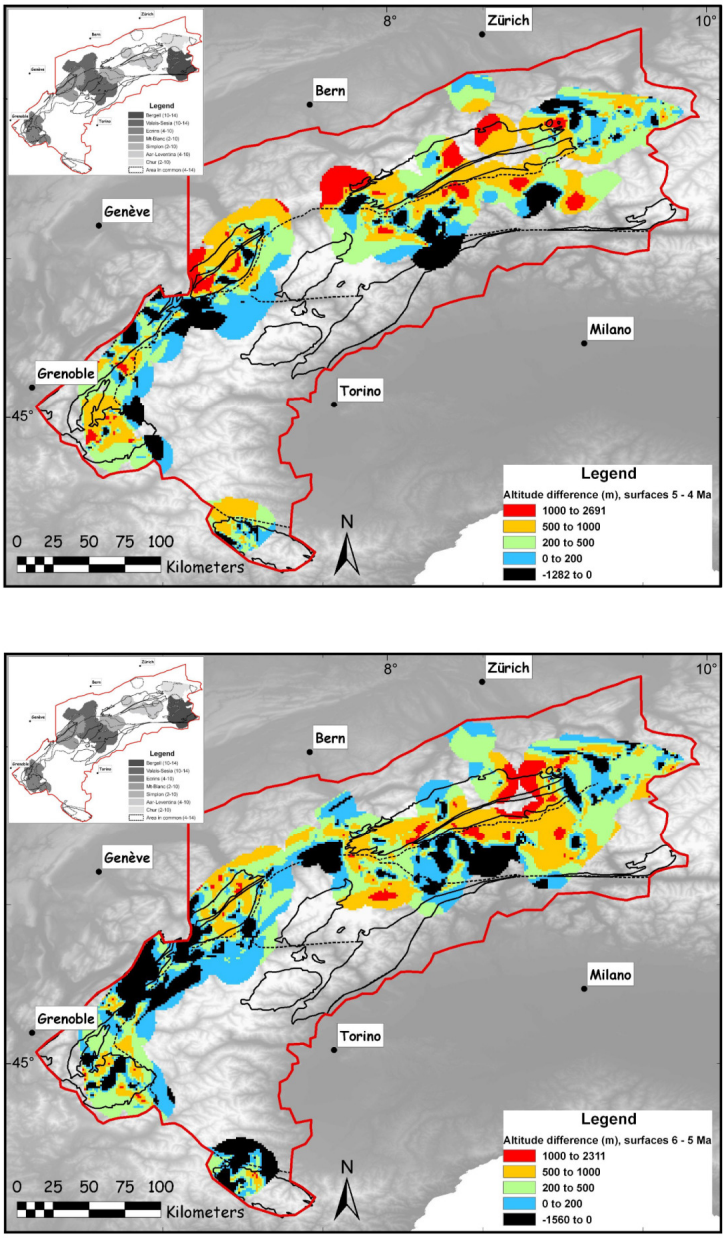

Figure II.3.16. Elevation difference between the 5-4 Ma and the 6-5 Ma apatite fission-track isoage surfaces.

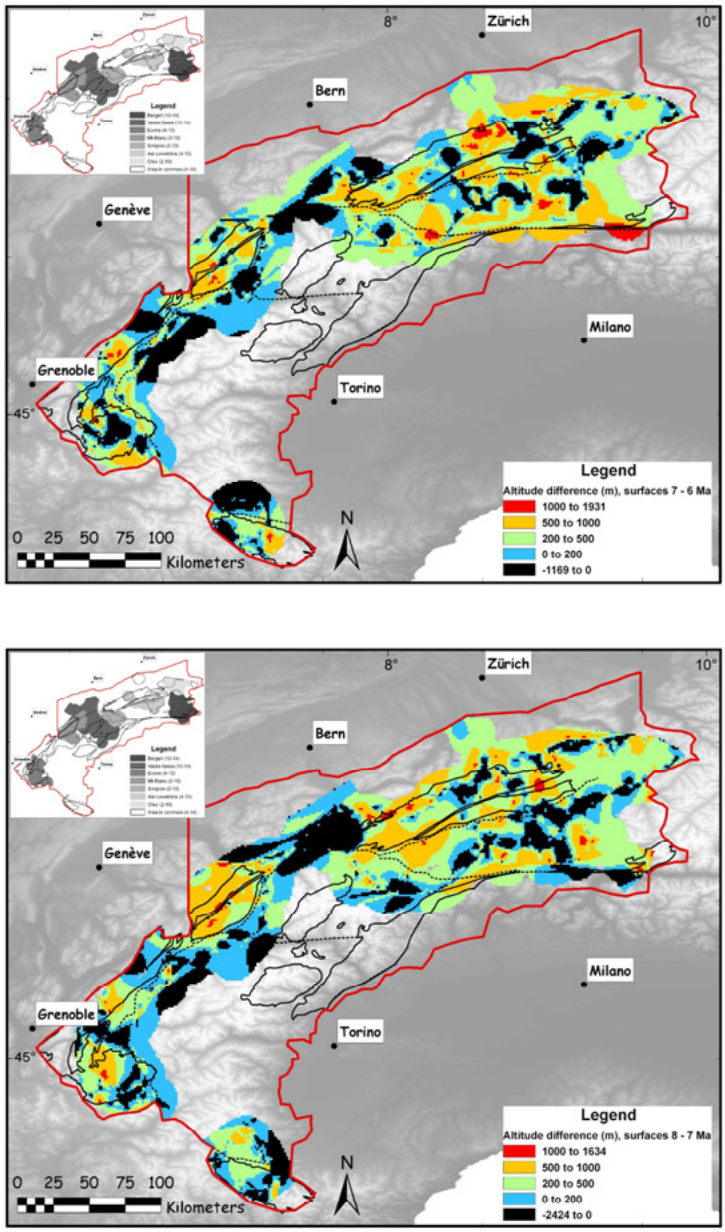

Figure II.3.17. Elevation difference between the 7-6 Ma and the 8-7 Ma apatite fission-track isoage surfaces.

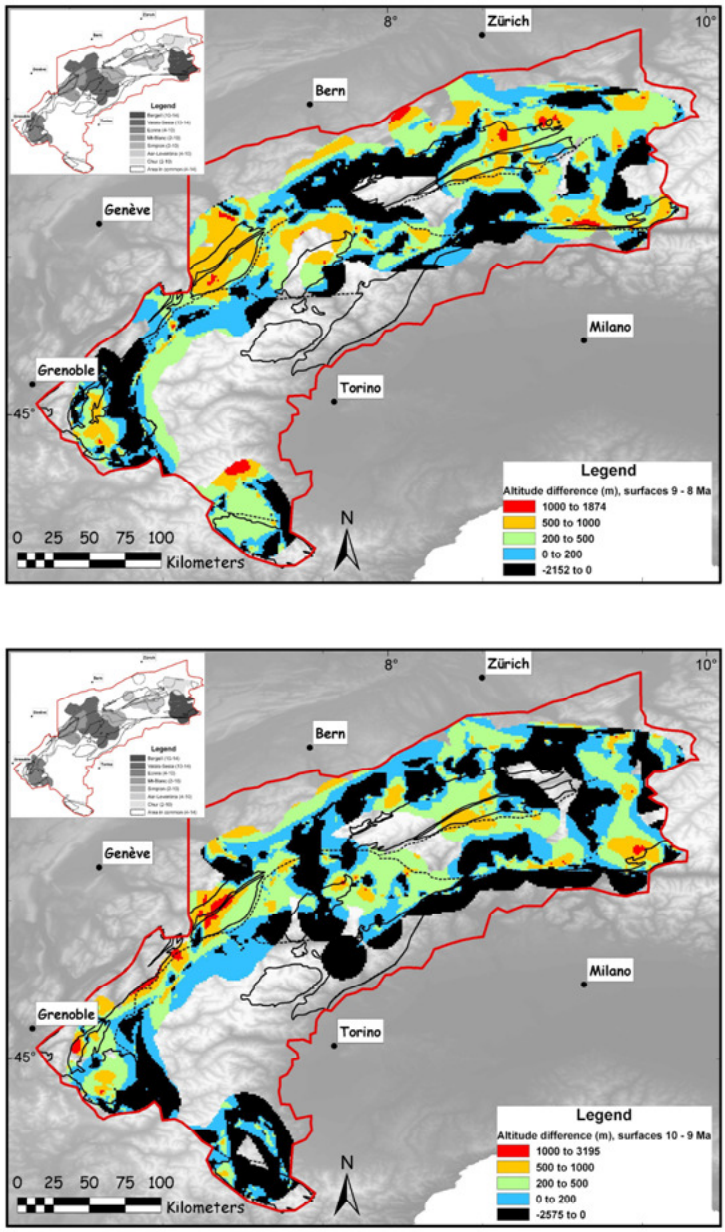

Figure II.3.18. Elevation difference between the 9-8 Ma and the 10-9 Ma apatite fission-track isoage surfaces.

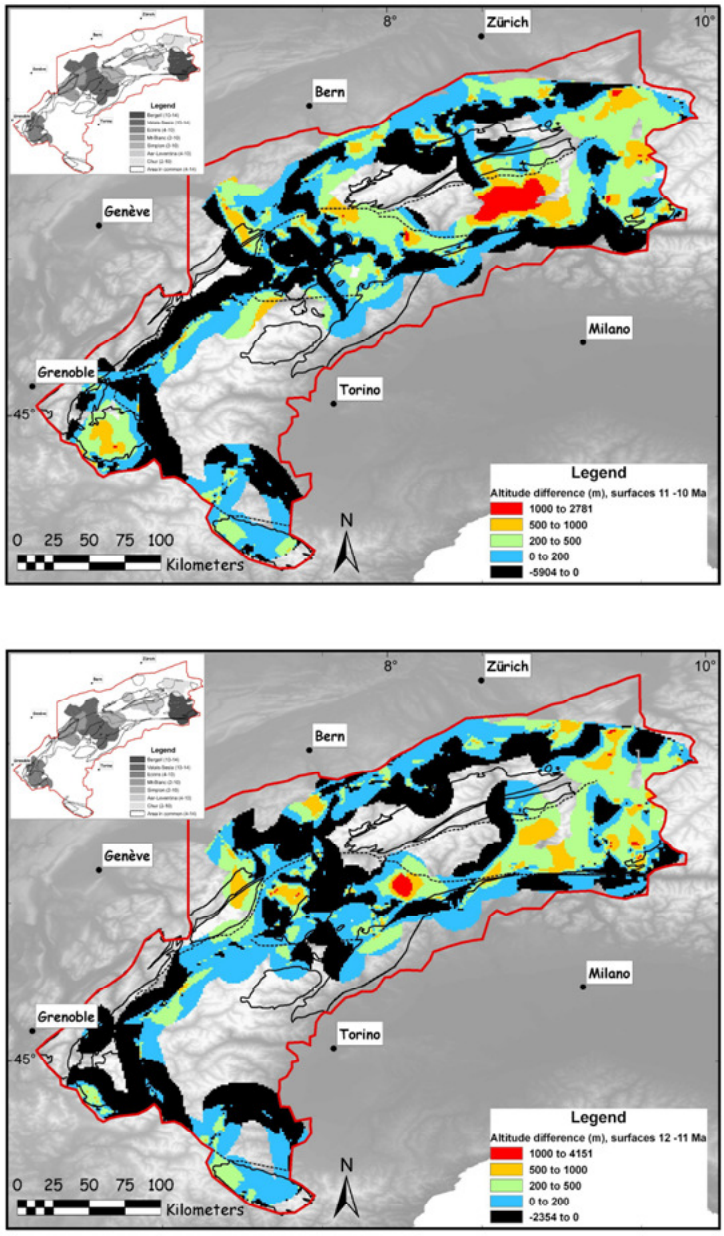

Figure II.3.19. Elevation difference between the 11-10 Ma and the 12-11 Ma apatite fission-track isoage surfaces.

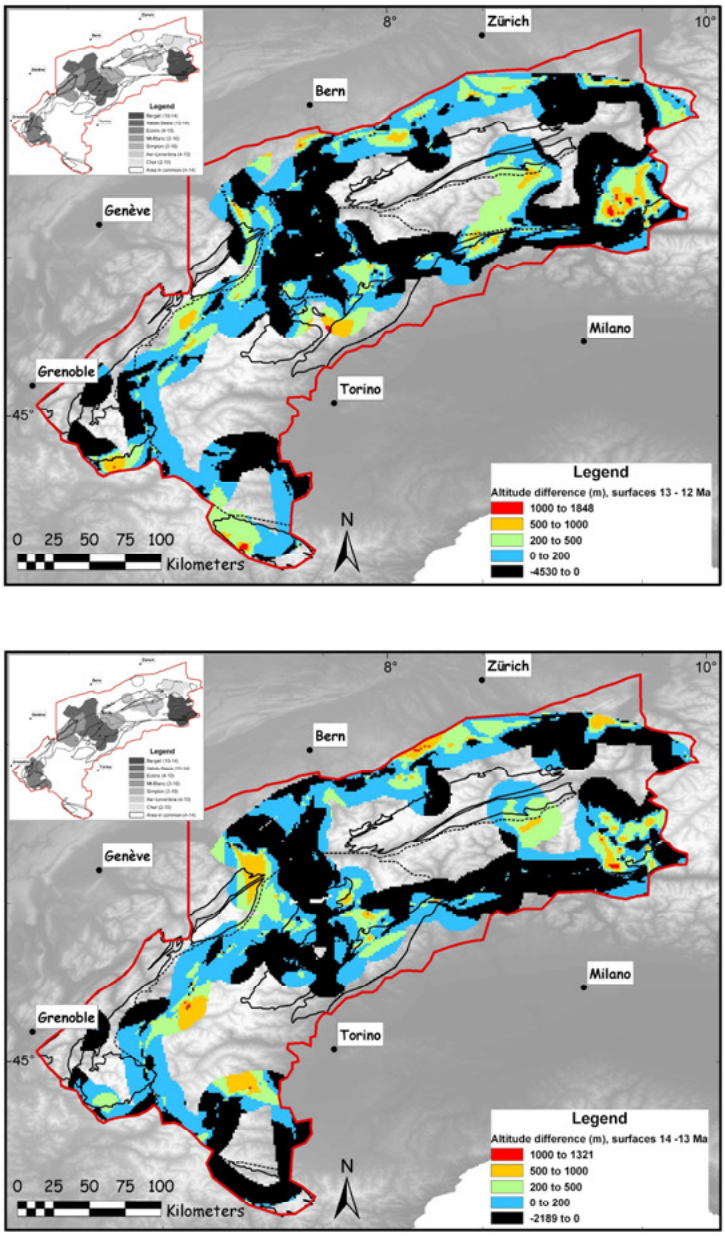

Figure II.3.20. Elevation difference between the 13-12 Ma and the 14-13 Ma apatite fission-track isoage surfaces.

A series of 13 maps of isoage surface elevations between 14 and 2 Ma were computed (Figures 8 to 14). As each map has a different areal coverage, it is necessary to define areas with a continuous coverage over several Myr in order to follow the evolution of exhumation rates during a substantial period. Eight areas have been identified for this study (Figure II.3.14, lower)

II.3.2.3. Calculation of exhumation rates using isoage surfaces

The difference in elevation between successive isoage surfaces is used as a proxy to estimate the amount of exhumation during the corresponding time-period. The maps of elevation difference between two successive AFT isoage surfaces are presented in Figures 15 to 20. Areas in black correspond to negative elevation difference occurring when two computed isoage surfaces cross each other, which is the sign of either locally high error on isoage surface elevation, or a real local negative age-elevation relationship, as identified in section II.3.2.1 above.

After extracting the values of isoage surface elevation difference in each map presented in Figures 15 to 20 over the eight study areas defined in Figure II.3.14 (lower), I used the distribution of pixel values to estimate the average exhumation rate in the area during the corresponding time period. The graphs presented in Figures 21 to 28 show pixel value distributions for each of the eight study areas. Hollow symbols show the entire pixel value distribution, while black symbols show the distribution of positive pixel values (i.e. after discarding the negative values – in black on the maps in Figures 15 to 20) that were used to estimate local average exhumation rates reported in Figure II.2.10.

Several factors can explain the error on isoage surface elevation, leading to negative elevation differences that are easily noticeable (black areas on Figures 15 to 20; negative areas of the histograms on Figures 21 to 28), and more generally to a "family of inaccurate pixels" (Figure II.3.29). These include locally negative A1 values (see Figure II.3.6) and the vagaries of the projection of isoage contours on the topography, when an older contour is accidentally projected over a valley while a younger contour is projected over a ridge. Close to such areas, the interpolated isoage surfaces will cross each other, generating inaccurate values for elevation differences: both negative pixels close to the wrong data points, and positive but inaccurate pixels at a greater distance.

Figure II.3.29 shows a schematic histogram of pixel-value distribution extracted from a map of difference in AFT isoage surface elevations. The skewed pattern chosen for this example is often observed in frequency histograms (e.g. Figure II.3.21), suggesting that it may be composed of two superposed families of pixels values: a minor population with low or negative values (family of inaccurate pixels, in pink) and a major population with positive values (family of accurate pixels, in yellow). The average elevation difference for the entire histogram (X1) is significantly underestimated compared to the average elevation difference for accurate pixels X3. The average value X2 calculated after discarding negative pixels is closer to X3, even though the positive inaccurate pixels could not be discarded.

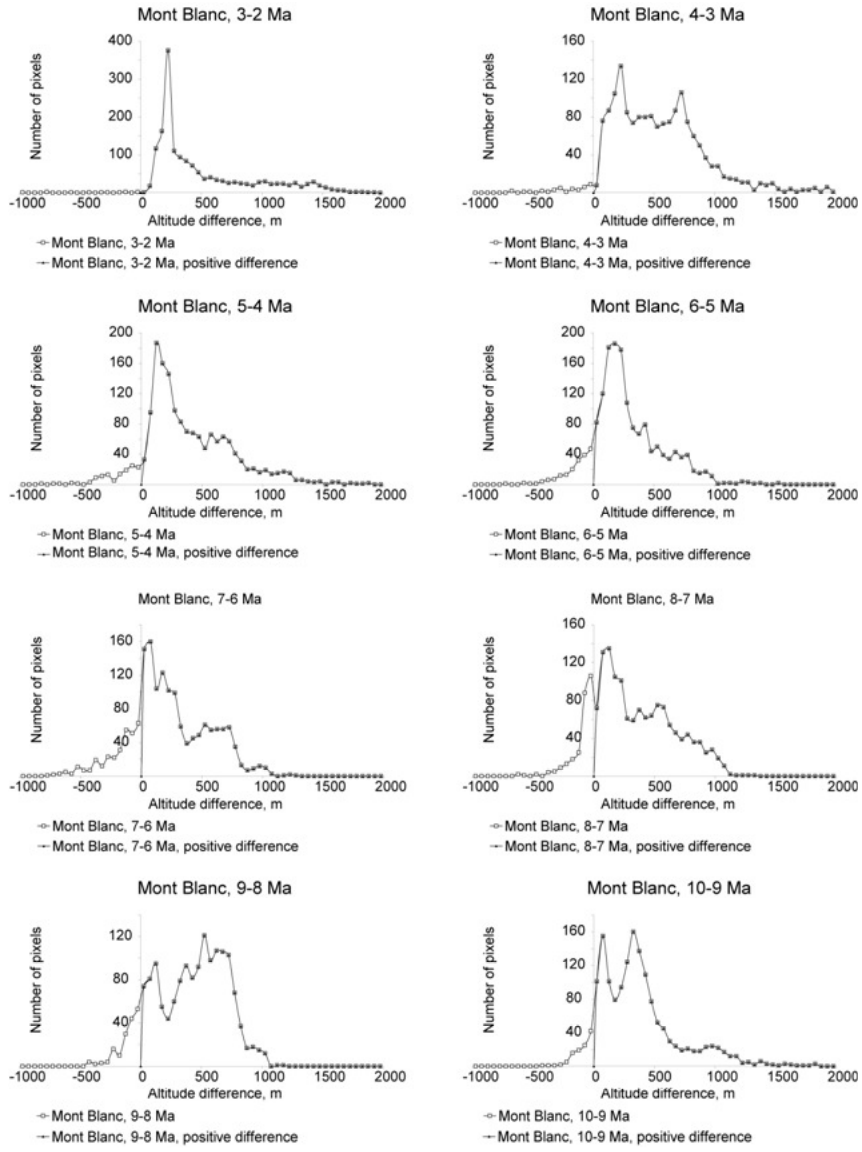

Figure II.3.21. Elevation difference between AFT isoage surfaces in the Mont-Blanc area between 10 and 2 Ma.

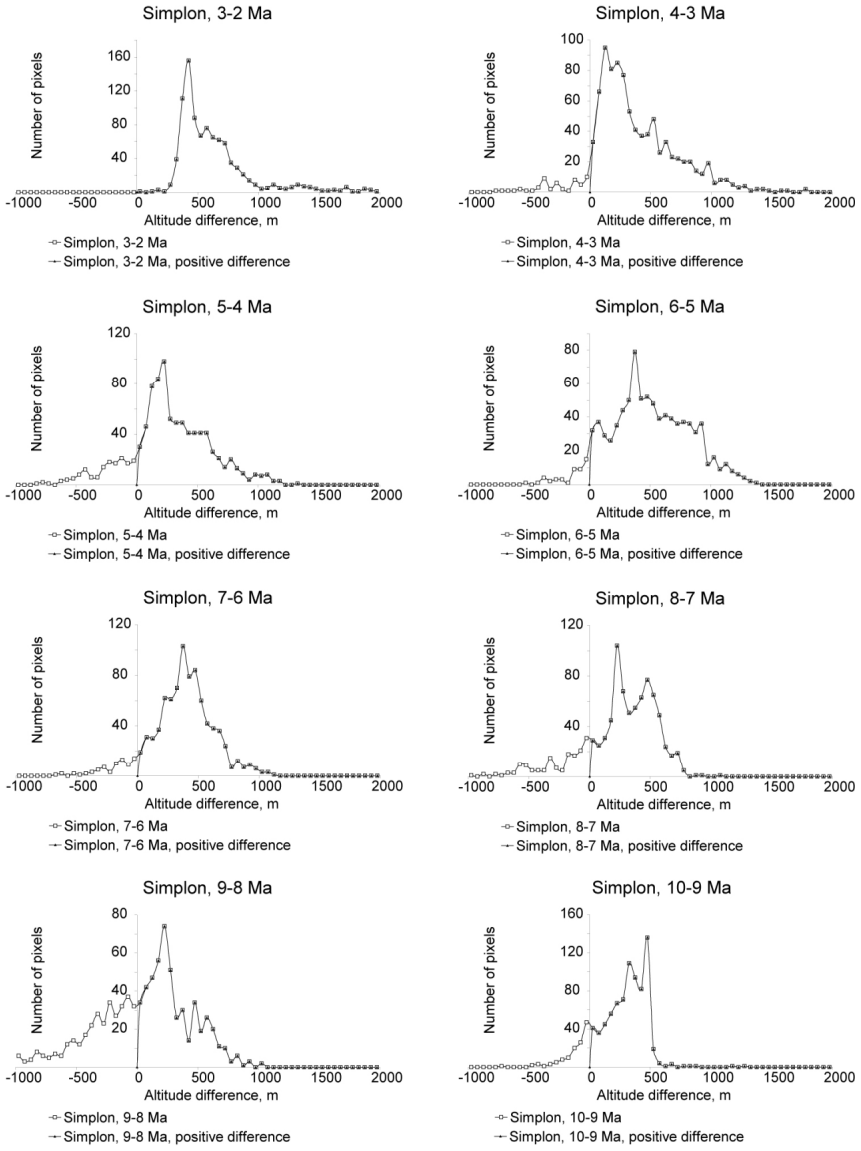

Figure II.3.22. Elevation difference between AFT isoage surfaces in the Simplon area between 10 and 2 Ma.

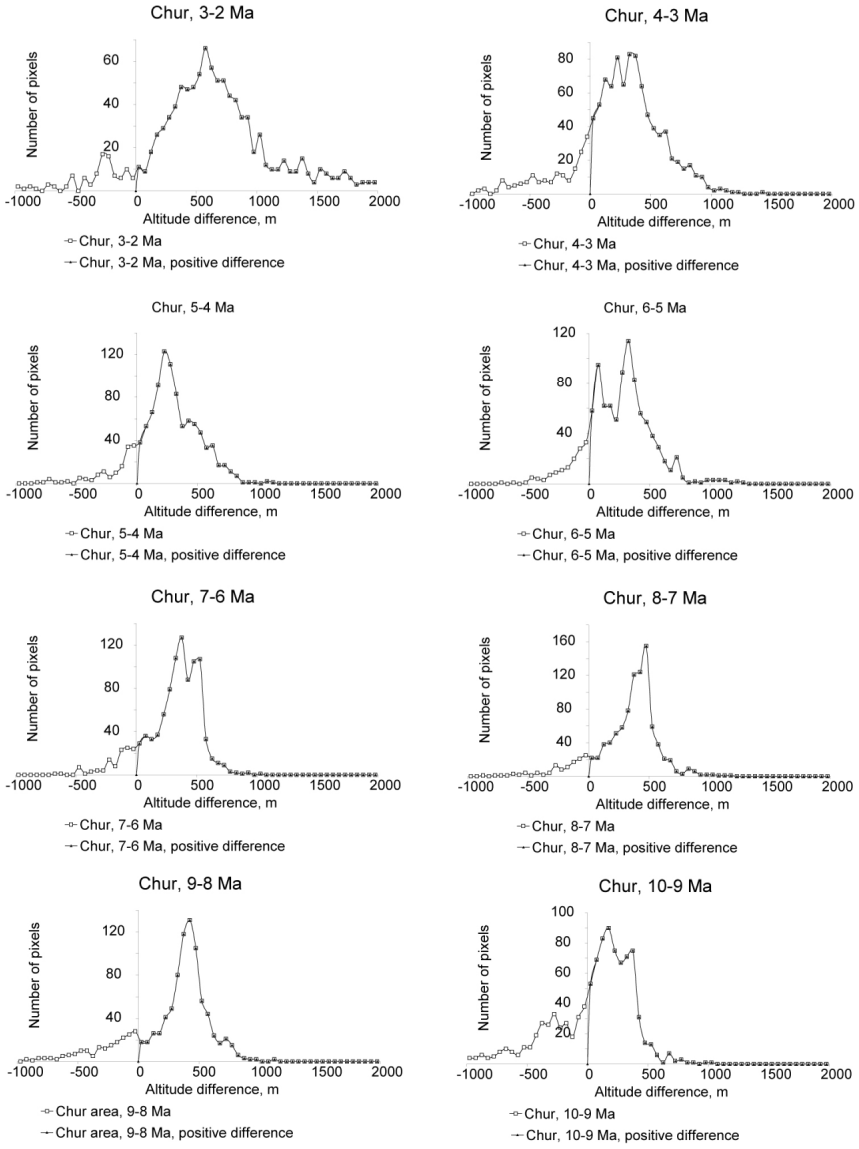

Figure II.3.23. Elevation difference between AFT isoage surfaces in the Chur area between 10 and 2 Ma.

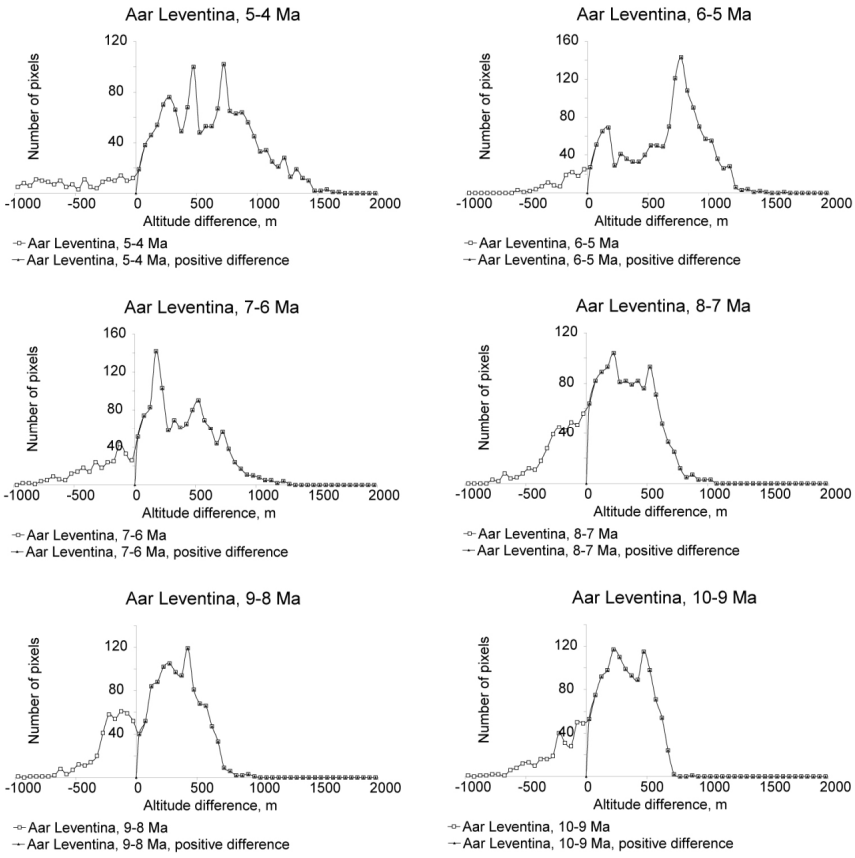

Figure II.3.24. Elevation difference between AFT isoage surfaces in the Aar-Leventina area between 10 and 4 Ma.

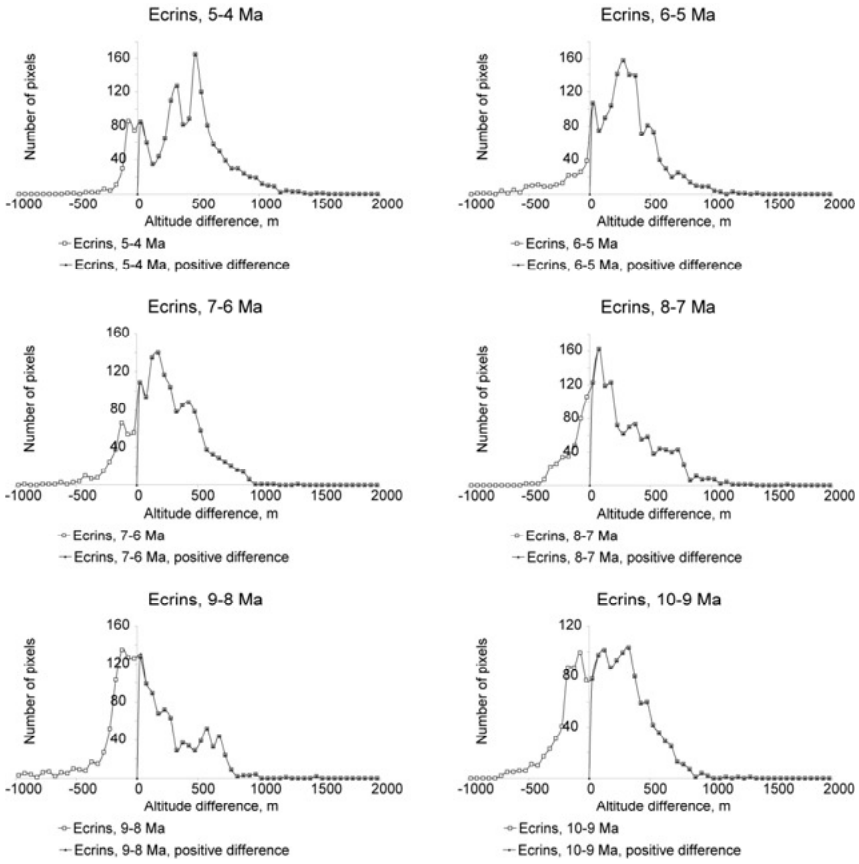

Figure II.3.25. Elevation difference between AFT isoage surfaces in the Ecrins area between 10 and 4 Ma.

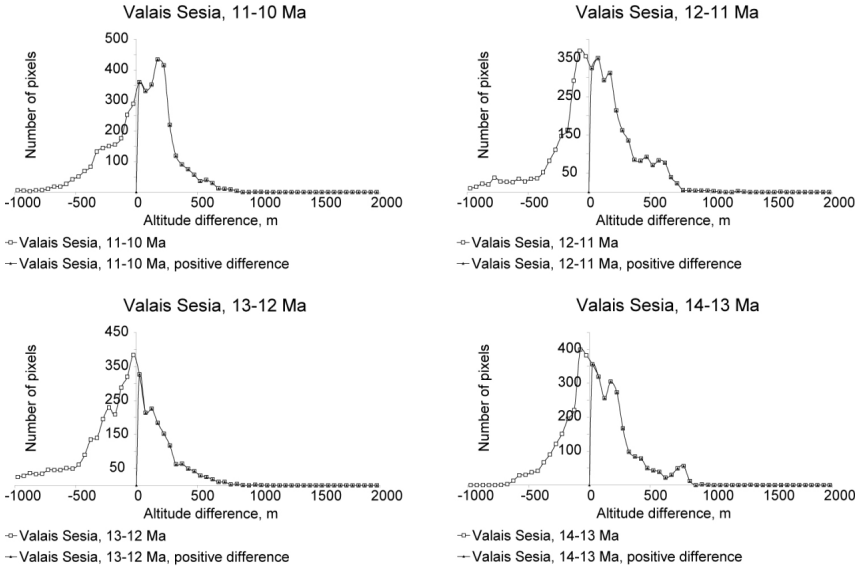

Figure II.3.26. Elevation difference between AFT isoage surfaces in the Valais-Sesia area between 14 and 10 Ma.

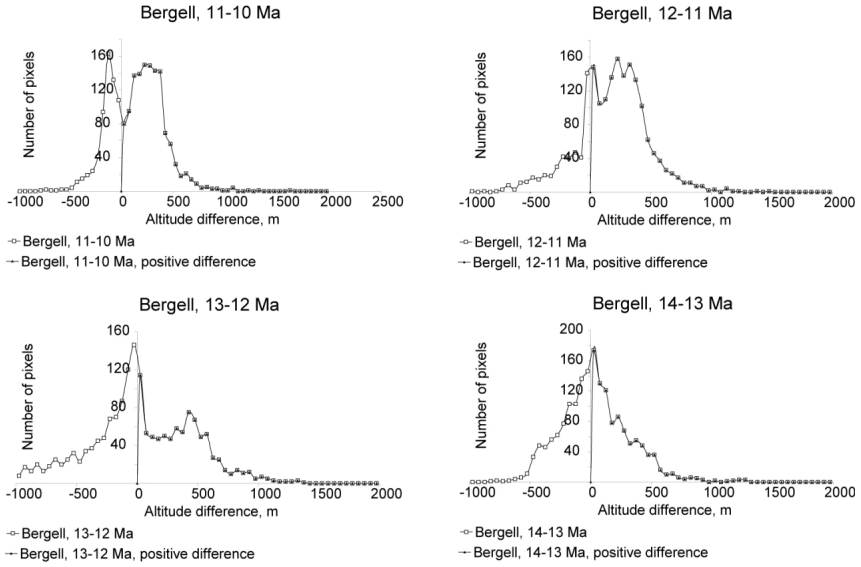

Figure II.3.27. Elevation difference between AFT isoage surfaces in the Bergell area between 14 and 10 Ma.

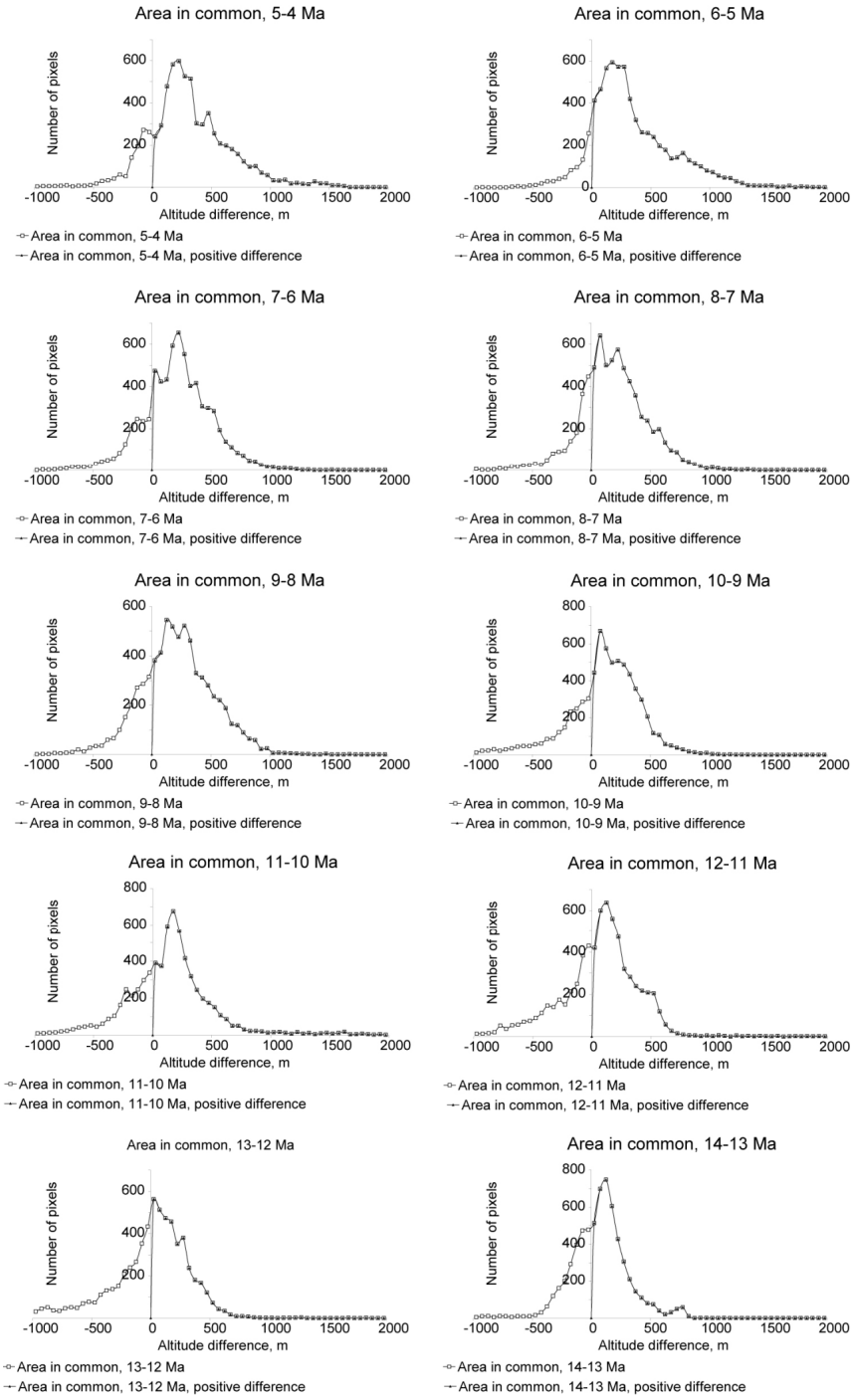

Figure II.3.28. Elevation difference between AFT isoage surfaces in the area of longest continuous coverage, between 14 and 4 Ma.

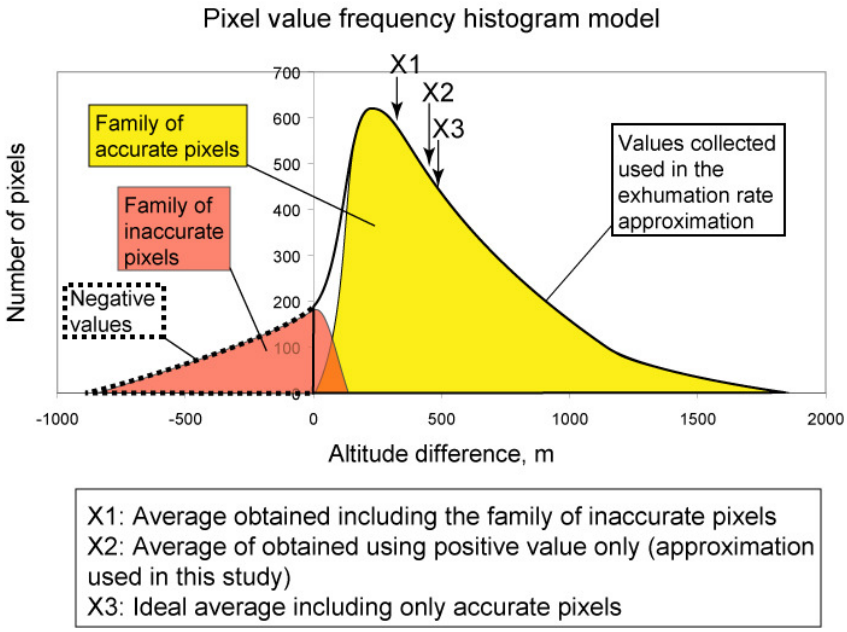

Figure II.3.29. Example of pixel-value frequency histogram showing the elevation difference between two apatite fission-track isoage surfaces.

II.3.2.4. Assessing the use of average distance between isoage surfaces as a proxy for exhumation rate

In order to assess the quality of our dataset of isoage surface elevations, I use the average value and the standard deviation of the histograms presented in Figures 21 to 28, as markers of their morphology, and compare "entire" histograms with "positive" ones, obtained after discarding negative pixels.

Figure II.3.30 (upper) shows an increasing value for the average distance between two isoage surfaces toward the present, while the standard deviation is higher in both the oldest and the youngest histograms studied. The trend of higher standard deviation (i.e. wider histograms) toward the present is confirmed after discarding negative pixels, on Figure II.3.31, upper diagram. In addition, the lower diagram on Figure II.3.31 shows that standard deviation and average distance are well correlated. These two observations could possibly denote a bias in the estimates of exhumation rate, if the rejection of negative pixels on histograms with the highest standard deviation coincides with higher average distance on positive pixel value distribution simply because of a geometrical effect (if two histograms, a narrow and a wide one are centred on the value zero, the average of the positive part will be higher for the widest histogram). However, a similar relationship already exists between standard deviation and average distance on entire histograms (lower graph on Figure II.3.30), demonstrating that

entire histograms with the largest values of average distance are also the widest, probably because of a higher uncertainty in the determination of isoage surface elevation. In addition, Figure II.3.32 shows that the proportion of positive pixels for elevated values of average distance (above 400 m) is very high (upper graph); and that the proportion of positive pixels is also very high for elevation differences calculated after 7 Ma (lower graph). I conclude that the higher values of exhumation rates observed in the upper diagram of Figure II.3.31, and Figure II.2.10 are not an artefact due to the rejection of negative pixels on histograms of elevation difference between isoage surfaces, but reflect a real late Neogene increase in exhumation of the Western Alps

II.3.2.5. Cumulated exhumation rates

The curves of exhumation rate through time (Figure II.2.10) can be used to estimate the cumulative amount of denudation over the study period (Figure II.3.33), which is of direct interest to compare with results of numerical modeling based on thermochronology (section IV.2) or with the amount of denudation involved in the isostatic rebound of the Molasse Basin (Cederbom et al., 2004). The cumulated denudation between 10 and 2 Ma is reported with plain colour lines, and reaches over 3000 m (arrow a). The cumulated denudation between 5 and 2 Ma reaches 1000-1500 m (arrow b).

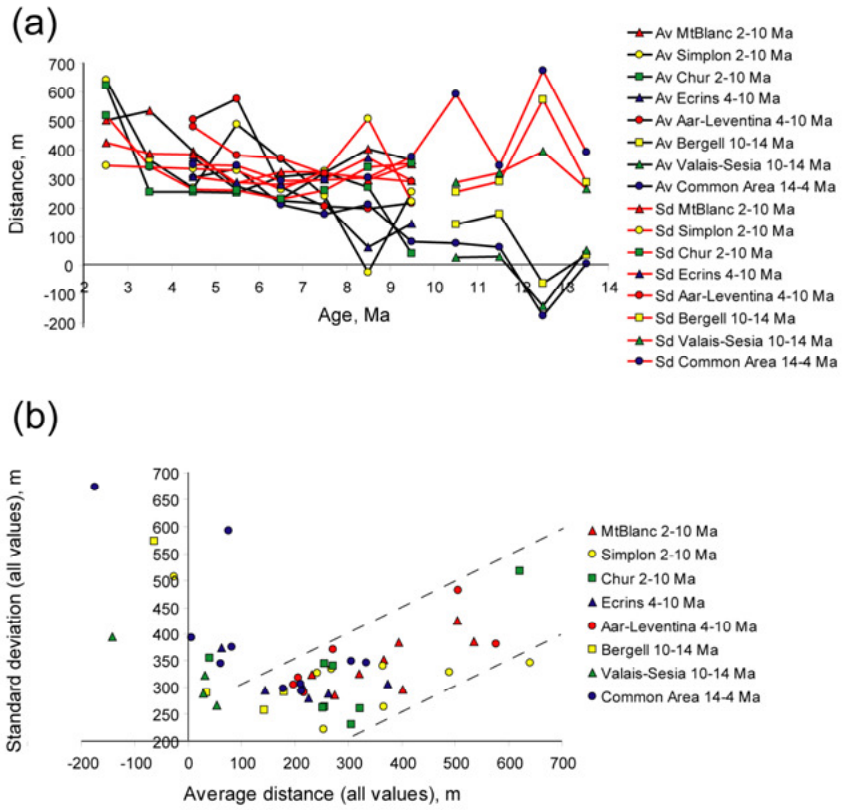

Figure II.3.30. (a) Average distance (Av) and standard deviation (Sd) between isoage surfaces on entire histograms of pixels value distribution: description of the "entire" histograms of pixel-value frequency presented in Figures 21 to 28. Black lines show the average distance between isoage surfaces (Av), and red ones show the standard deviation (Sd) of the histograms, for each of the eight study areas. (b) Standard deviation (Sd) versus average distance (Av) on entire histograms of pixels value distribution, for each time step studied over the eight study areas. Dashed lines highlight the relationship between Sd and Av.

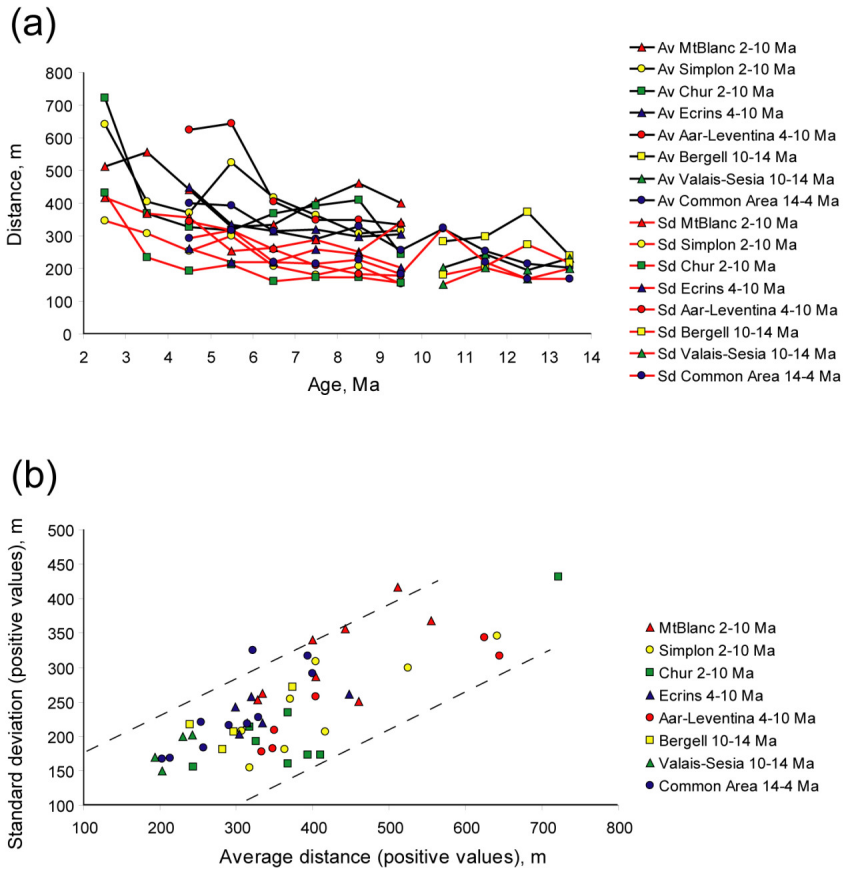

Figure II.3.31. (a) Average distance (Av) and standard deviation (Sd) between isoage surfaces on histograms of positive pixels value distribution: description of the "positive" histograms of pixel-value frequency on each histogram presented in Figures 21 to 28. Black lines show the average distance between isoage surfaces (Av), and red ones show the standard deviation (Sd) of the histograms, for each of the eight study areas. (b) Standard deviation (Sd) versus average distance (Av) on histograms of positive pixels value distribution, for each time step studied over the eight study areas. Dashed lines highlight the relationship between Sd and Av.

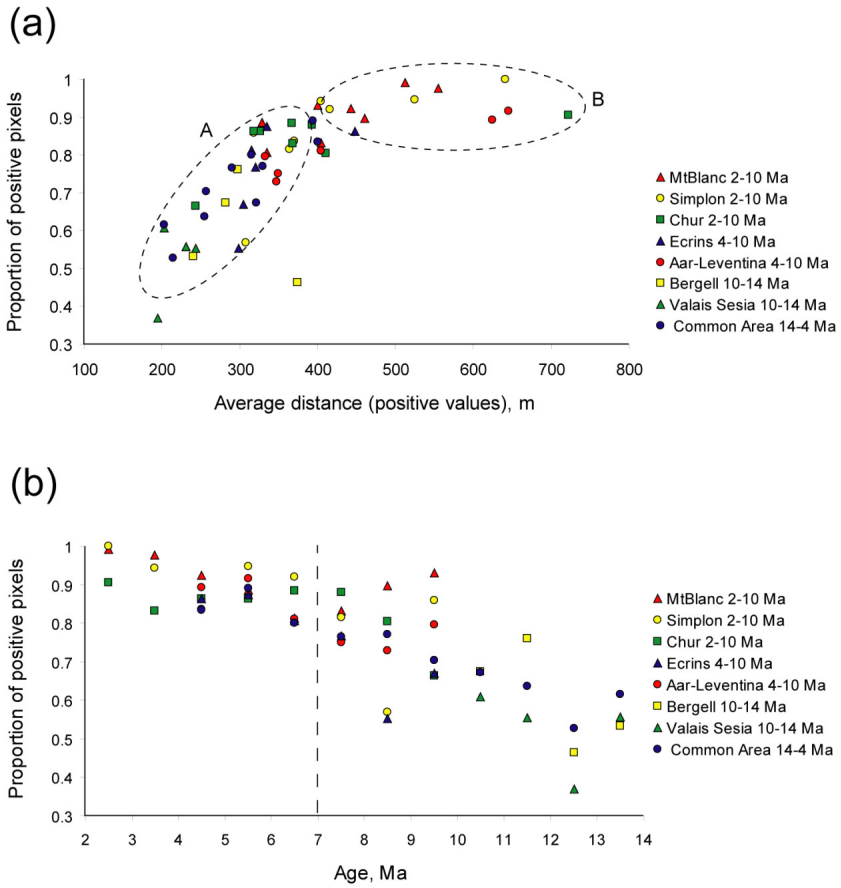

Figure II.3.32. (a) Proportion of positive pixels on each histogram presented in Figures 21 to 28, versus average distance calculated on "positive" histograms. Ellipses A and B underline two groups of dots: (A) the proportion of positive pixels is linked to the average distance calculated on the positive part of the histograms, under 400 m; (B) histograms for which the average distance calculated on the positive part of the histogram is above 400 m have high proportions of positive pixels. (b) Proportion of positive pixels on each histogram presented in Figures 21 to 28, versus age. All histograms for isoage surfaces < 7 Ma have high proportions of positive pixel values.

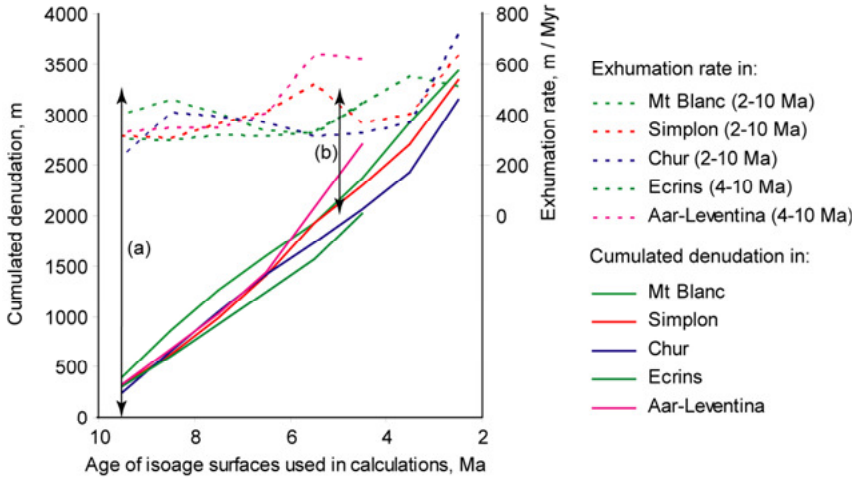

Figure II.3.33. Exhumation rate and cumulated denudation. The exhumation rates in five study areas (dotted coloured lines) estimated between 10 and 2 Ma using isoage surfaces (see locations on the lower Figure II.3.8 and original data in Figure II.2.10) allow us to estimate cumulated denudation (plain coloured lines) through time.

Chapter III

Spatial correlation between long-term exhumation rates and present-day forcing parameters in the western European Alps

III.1. Chapter overview

III.1.1. Publication:

This chapter presents a paper submitted to *Geology* on April 25th 2008, under revision at the time of thesis defense.

III.1.2. Presentation at international meetings:

- December 2007, American Geophysical Union, Fall meeting San Francisco (USA):
Vernon, A.J., **van der Beek**, P.A., Sinclair, H.D., Rahn, M.K. Tectonic vs. climatic controls on accelerated Mio-Pliocene denudation of the western European Alps. *Eos Transactions AGU, 88(52)*, Fall Meeting Supplement, Abstract T14C-07.

III.1.3. Contributors to Chapter III

Ciaran Beggan and Benoît Dubacq provided invaluable help with writing of Matlab™ code, which I used to automate the calculation of correlation coefficients from the database.

III.2. Spatial correlation between long-term exhumation rates and present-day forcing parameters in the western European Alps

Antoine J. Vernon[1,2], Peter A. van der Beek[2], Hugh D. Sinclair[1]

[1]School of Geosciences, Grant Institute, University of Edinburgh, Edinburgh EH9-3JW, United-Kingdom

[2]Laboratoire de Géodynamique des Chaînes Alpines, Université Joseph Fourier, 38400 Grenoble, France

* Corresponding author: vernon.antoine@gmail.com

Abstract

Observations that suggest a significant increase in denudation rates in the western European Alps over the last few million years, coinciding with a decrease in tectonic activity, have led to increased speculation concerning the nature of tectonic-climate interactions in this mountain belt. We address this question by quantitatively correlating the spatial pattern of long-term exhumation rates with those of potential short-term tectonic, climatic and morphologic variables. We find that present-day rock uplift and mean elevation are well correlated with long-term exhumation rates; whereas relief, present-day precipitation, discharge, stream power and released seismic energy are not or only weakly correlated. We attribute the lack of correlation between long-term exhumation and climate to a strong temporal variability in climate and erosional processes during Plio-Pleistocene times. The correlation between present-day rock uplift and long-term exhumation suggests that the rock uplift signal is sustained on geological timescales and points to either long-term steady-state exhumation in an active mountain belt, or isostatic response to crustal unloading. Given the lack of correlation between the patterns of released seismic energy, rock uplift and long-term exhumation, we favor the latter explanation. A quantitative comparison of exhumation and rock uplift rates remains necessary, however, to determine whether isostatic rebound alone is sufficient to explain the observed rock uplift pattern in the Western Alps.

Keywords: European Alps, exhumation, thermochronology, tectonics, climate, morphology

III.2.1. Introduction

The topographic and denudation histories of mountain belts result from an interplay between tectonic and climatic processes. The relative importance of potential climatic, tectonic or morphologic controlling parameters has been discussed by several authors (e.g., Burbank et al., 2003; Dadson et al., 2003; Reiners et al., 2003; Wobus et al., 2003) who have reached

contrasting conclusions. An inherent problem in these kinds of studies relates to the different timescales addressed: whereas geologically meaningful denudation rates inferred by low-temperature thermochronology are measured on 10^6 yr timescales, records of controlling parameters (e.g. precipitation, runoff, released seismic energy, current deformation as measured by GPS, etc.) rarely exceed a few tens of years.

Recent studies of the Western Alps (Figure III.2.1) yield a seemingly paradoxical suite of observations: whereas the expected outcome of the extensional collapse of the orogen core from Late Miocene times onward, substantiated by geodetic, geologic and seismologic data (e.g., Selverstone, 2005; Sue et al., 2007b and references therein), would be a decrease in sediment production, the sedimentary record instead shows a dramatic increase in sediment flux from the Alps since ~5 Ma (Kuhlemann et al., 2002). The latter finding has recently been corroborated by Vernon et al. (2008), who show from a compilation of thermochronological data that exhumation rates have at least doubled since this time in the Western Alps. Similarly, geodetic measurements attest to ongoing rock uplift within most parts of the belt (e.g., Schlatter et al., 2005). Moreover, whereas convergence is still active in the east but has ceased in the west (Serpelloni et al., 2005), the Western Alps show significantly higher mean topography and relief than the eastern Alps.

Several different mechanisms have been proposed to explain the enigmatic present-day exhumation and uplift rate patterns in the Western Alps. These include both tectonic (Persaud and Pfiffner, 2004) and deep-seated geodynamic (Kuhlemann, 2007; Lyon-Caen and Molnar, 1989) processes. However, climatically-induced processes have also been proposed; in particular, the spatial coincidence of highest rock uplift rates with areas of most deeply incised valleys has been used to infer that a significant part of the uplift signal results from isostatic response to focused erosion of the mountain belt (Champagnac et al., 2007; Schlunegger and Hinderer, 2001).

Here we study the spatial correlation between present-day climatic and tectonic forcing parameters with long-term exhumation rates, as inferred from a fission-track thermochronology database (Vernon et al., 2008). Our aim is to establish what may be driving present-day rock uplift and exhumation in the Western Alps. Although we are fully aware that any potential spatial correlation does not imply a causal relationship because of the different timescales involved, we are encouraged by the recent findings of Wittmann et al. (2007), who showed a strong spatial correlation between denudation rates on millennial time-scales

recorded by cosmogenic isotope abundances in river sediments on the one hand, and both relief characteristics (which presumably reflect long-term landscape dynamics; e.g., Whipple, 2001) and present-day rock uplift rate on the other.

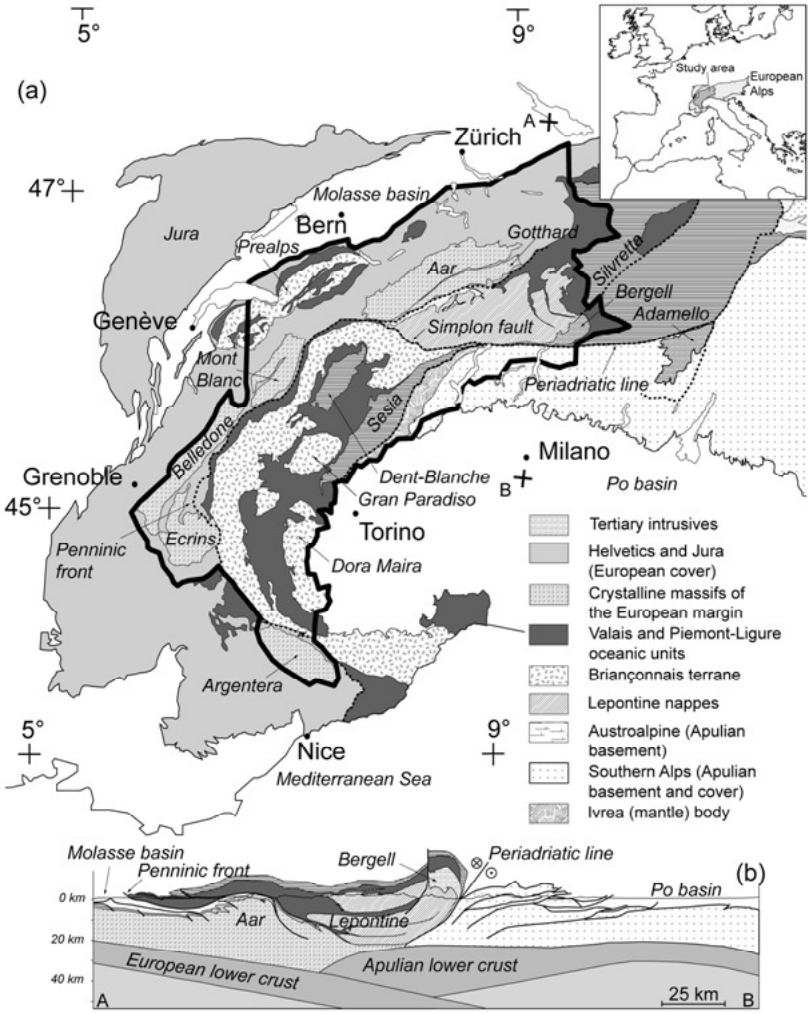

Figure III.2.1. Geological map of the Western Alps (after Schmid et al., 2004) and crustal cross-section along the NFP20-East seismic line (Schmid et al., 2004; AB on map). Inset shows location in Europe. Thick black line contours the study area.

Such correlations lead us to assume that the present-day spatial patterns of forcing parameters are representative of the long term, and that the parameters are linked, either directly or through a common factor.

III.2.2. Data and methods

We extract parameters characterizing long-term exhumation rates from an apatite fission-track (AFT) database recently compiled by Vernon et al. (2008). We use the map of interpolated

AFT ages and the elevation of "isoage" surfaces linking points with equal AFT ages, which record the amount of exhumation more directly (Vernon et al., 2008).

We compare the spatial distribution of long-term exhumation rates with that of tectonic, climatic and geomorphologic forcing parameters. Morphologic parameters are extracted from the 3 arc-second (~90 m) resolution Shuttle Radar Topography Mission (SRTM) Digital Elevation Model (DEM) available from the CGIAR-CSI database (http://srtm.csi.cgiar.org). They include elevation averaged over a 1.4 km radius and relief within a 5-km radius. Rock uplift values are from the Swiss Federal Office of Topography (SwissTopo) geodetic database (Schlatter, 2007). We also mapped the spatial variation in seismic energy released between 1959 and 2000 using the database compiled by Delacou et al. (2004). Although this database only contains earthquakes for which reliable focal mechanisms are available, causing under-representation of events with local magnitude $M_l < 3$, the available record represents > 95 % of the total seismic energy released during that time interval (Sue et al., 2007a). We quantified the released seismic energy (Se) from the local magnitudes using the classical relationship log Se [J] = 1.5 M_l + 4.8 (Gutenberg and Richter, 1954). Values were cumulated in a sliding 25-km radius window cropped at 25 km around data points.

Potential climatic controls were inferred from the Swiss Federal Office of Meteorology and Climatology (MeteoSwiss) 1971-1990 precipitation database (Frei and Schär, 1998; Schwarb et al., 2001). Precipitation values were interpolated from rain-gauge measurements by Schwarb et al. (2001) using the PRISM model of Daly et al. (1994), which models the orographic control on precipitation. Cumulated flow in streams is estimated by integrating the amount of annual precipitation over the upstream drainage area. Unit stream power (SP) is calculated from the annual cumulated flow (Q) and local slope (S), obtained from the SRTM DEM, using the relationship SP ~$Q^{0.5}$ S, based on the assumptions that channel width is proportional to $Q^{0.5}$ and that runoff equals upstream precipitation, thus neglecting the effect of evapo-transpiration and local water recycling.

All data sets were re-sampled on a common 3 arc-second grid clipped at a distance of 15-25 km around each data point, to remove unconstrained interpolated values. Therefore, due to the uneven resolution of the original data, the coverage of the study area is not complete for every

map. Maps of the most relevant variables are shown in Figure III.2.2; all maps are presented in Figures III.2.4 to III.2.17 of the data repository.[7]

The grids were sampled along the fluvial network draining more than 1.5 km^2 for the analysis of spatial correlation. We calculated Kendall τ-b rank correlation coefficients for every association of two variables[8]. The use of the non-parametric Kendall τ-b test (Noether, 1981) is justified by the unknown Gaussian nature of each data field, the presence of outlier points which would bias a correlation calculation based on values, and the possibility to normalize the value of correlation strength τ using the number of data pairs considered minus the number of tied pairs. In addition, values of Kendall τ-b can be easily translated into comprehensible probabilities of concordance or discordance for a given pair of variables (Noether, 1981). We also show a N-S cross-section across these datasets in Figure III.2.3, in order to better visualize potential (anti-)correlations between the different variables[9].

III.2.3. Correlation results

Table III.2.1 reports the Kendall τ-b rank correlation coefficients for pairs of controlling parameters and different measures of long-term exhumation rates. Note that the notion of "controlling parameters" is a simplification here, as it neglects feed-back effects. Rock uplift, for instance, may control exhumation rates but will also be controlled by them through the isostatic response to denudation. Also, some of the parameters are not fully independent: stream power, for instance, is tied to both precipitation and topography. Tables III.2.2 and III.2.3 in the data repository report the correlation coefficients between the different control parameters and the different measures of long-term exhumation. Measures of long-term exhumation rates are fairly to very strongly correlated between themselves, suggesting they are relevant and measure a significant quantity.

[7] The data depository contains documents joined to the article submitted to *Geology*.
[8] A few examples of plots showing value distribution for two variables are given in Figure III.3.1.
[9] This cross-section is described in more details in section III.3.3 anf figures therein, together with a second cross-section perpendicular to the Simplon fault.

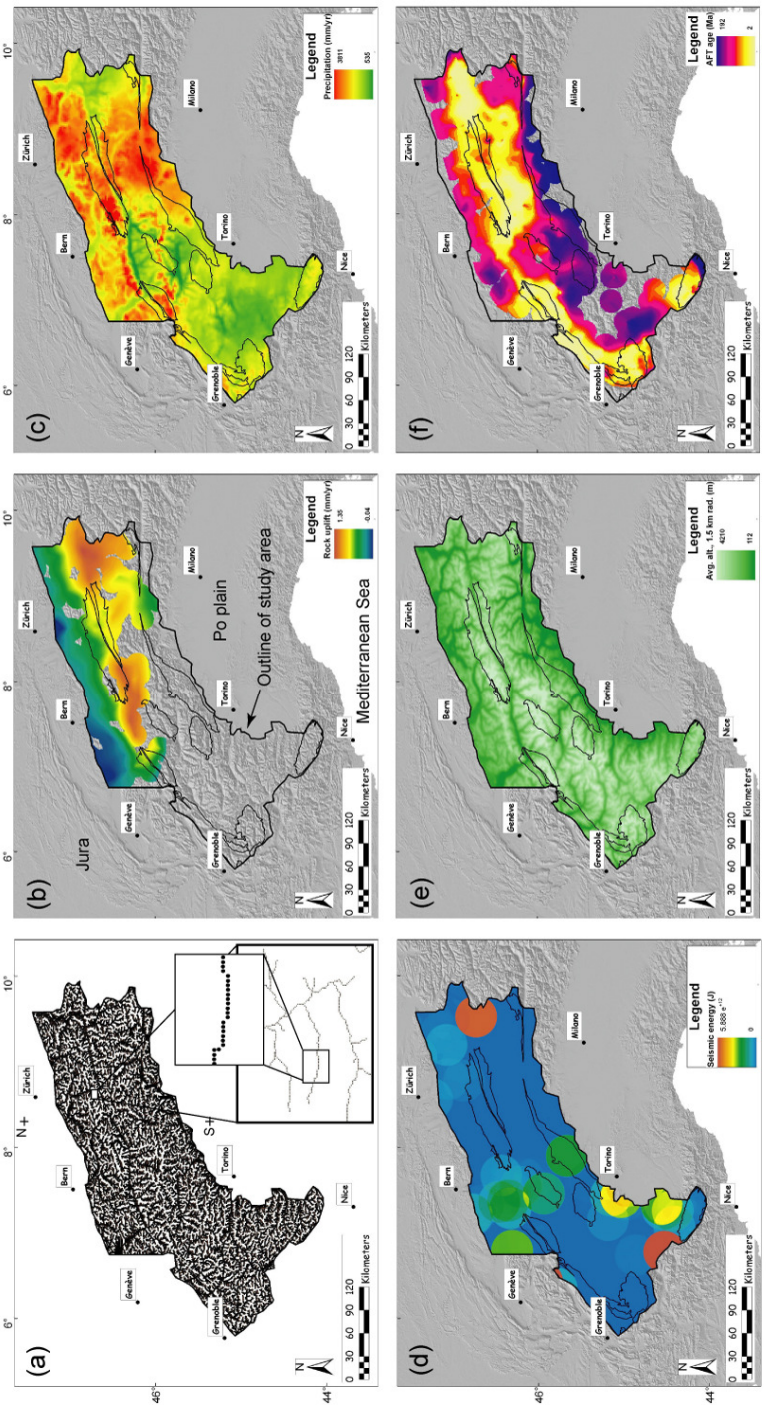

Figure III.2.2. Maps of selected control parameters and sampling grid: (a) Sampling pattern, based on the river network draining at least 1.5 km^2 (inset shows a detail). The sampling mesh is based on the 3 arc-second DEM resolution, for a maximum of 258,311 pixels over the study area. N-S: location of cross-section shown in Figure III.2.3; (b) Rock uplift rate (after Schlatter, 2007). Thin black lines contour major tectonic units detailed in Figure III.2.1; (c) Annual precipitation (Frei and Schär, 1998; Schwarb et al., 2001); (d) Seismic energy released (after Delacou et al., 2004 and Sue et al., 2007a); (e) Average elevation within a radius of 1.4 km; (f) Interpolated AFT age (Vernon et al., 2008).

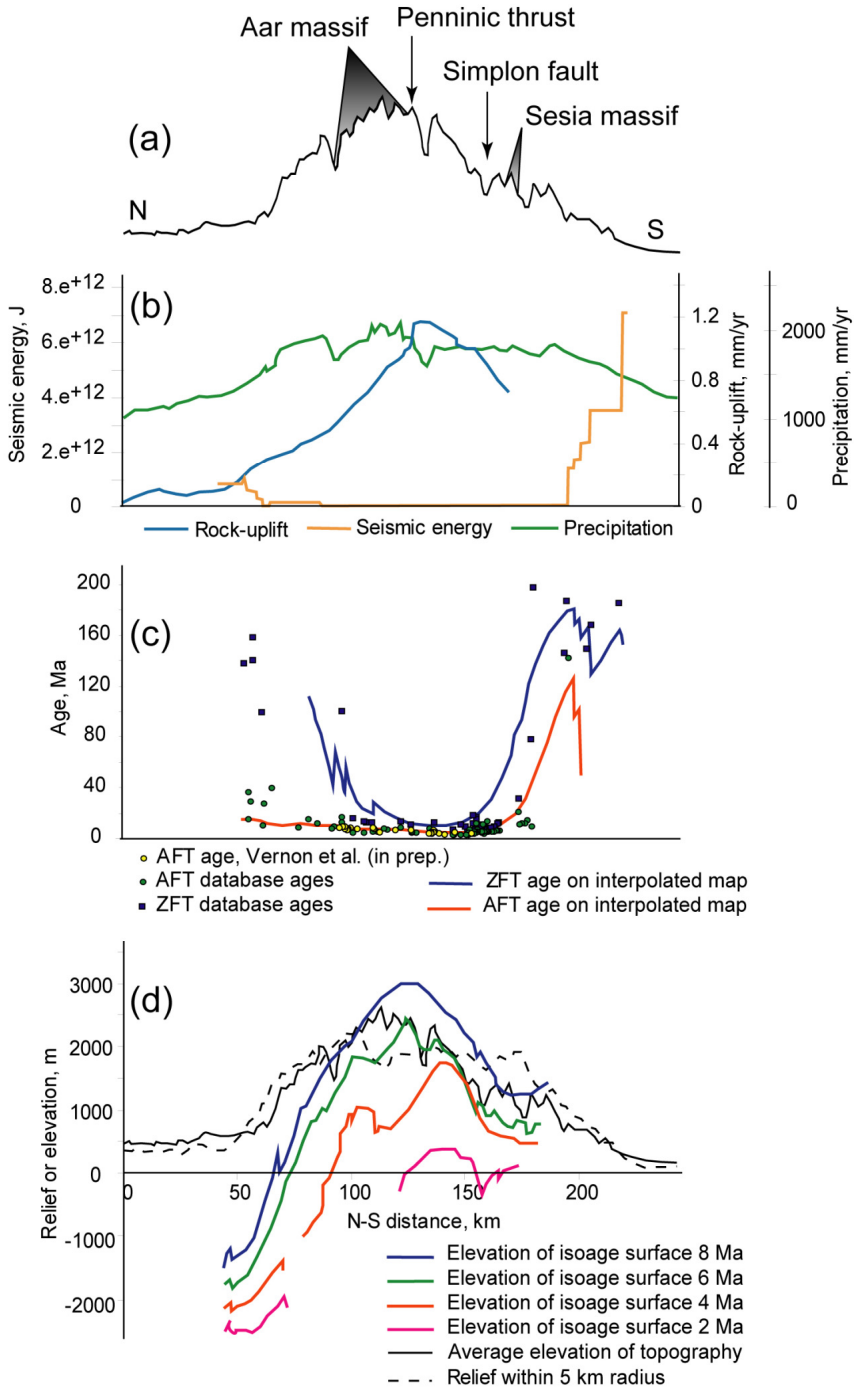

Figure III.2.3. N-S cross-section showing the value of parameters averaged over five sections made parallel to the profile line drawn in Figure III.2.2-a, and separated by 34 km. (a) Major tectonic units projected over the simplified topography; (b) present-day rock uplift, precipitation and seismic energy released; (c) Apatite (AFT) and Zircon (ZFT) fission-track ages indicating long-term exhumation rates, from the database compiled in Vernon et al. (2008) or unpublished (Vernon et al., manuscript in preparation); (d) mean topography and relief within a 5-km radius, and the elevation of four different AFT isoage surfaces. The maps used to extract information on this transect are provided with references in Figures III.2.4 to III.2.17 of the data repository.

	Rock uplift	Precipitation	Cumulated flow	Stream power	Seismic energy	Relief (5 km)	Mean Elevation
AFT age	-0.4242	-0.1267	-0.0464	-0.0933	0.0667	-0.1433	-0.0515
2 Ma isoage surface elevation	0.3891	-0.0837	-0.0056	0.1044	0.0247	0.0547	0.1815
4 Ma isoage surface elevation	0.4116	-0.1512	-0.0353	0.037	0.0331	0.0494	0.1891
Distance between 4-2 Ma isoage surfaces	0.1788	0.1713	-0.0229	0.0529	-0.1314	0.1437	0.2652

Table III.2.1. Kendall τ-b correlation coefficients between different potential control parameters and measures of long-term exhumation.

Our results show that present-day rock uplift and mean elevation are well correlated to long-term exhumation rates (taking τ-b > 0.15 as an arbitrary cut-off). The same parameters appeared to correlate strongly with millennial-scale catchment-wide erosion rates from cosmogenic data (Wittmann et al., 2007); our results thus support these findings and suggest they can be extrapolated toward long-term exhumation rates.

In contrast, precipitation and relief correlate only weakly with measures of long-term exhumation and neither cumulated flow, stream power, nor released seismic energy correlate with any of them. The cross-section in Figure III.2.3 shows how these variables are distributed across the Alps: whereas present-day rock uplift and long-term exhumation rates peak in the central, highest and most dissected part of the belt, precipitation appears more widely distributed and seismic energy is currently mostly released toward the interior edge of the belt; with the exception of an area between the Mont-Blanc and the Aar Massifs (Figure III.2.2).

III.2.4. Discussion and conclusions

The lack of strong correlation between precipitation rate, cumulated flow, stream power and released seismic energy with measures of long-term exhumation suggests either that the short-term records of these parameters are not representative of their long-term action, or that they have not exercised an important control on exhumation in the Western Alps.

The spatial pattern of precipitation has been shown to vary significantly between glacial and interglacial times (e.g., Florineth and Schlüchter, 2000). Thus the 20-year precipitation record cannot be considered representative of long-term precipitation in the Alps. Moreover, the

climatic parameters tested here are mostly relevant for fluvial incision, whereas glacial erosion must have been the dominant mechanism during most of the Quaternary in the Alps. A similar situation has been demonstrated recently for the central Nepal Himalaya, where long-term exhumation rates appear independent of present-day precipitation patterns (Burbank et al., 2003), due to glacial erosion, but short-term erosion rates do scale with both precipitation and runoff (Gabet et al., 2008). Similarly, the lack of correlation between stream power and long-term exhumation results from the transient nature of the post-glacial Alpine landscape (Brocard et al., 2003; Schlunegger and Hinderer, 2003), which causes a strong short-wavelength spatial variability of the stream-power signal. The weak correlation between relief and long-term exhumation may be explained by the widespread occurrence of threshold hill-slopes.

The record of seismic energy release also spans only 41 years, significantly shorter than the return period of major earthquakes in the Alps. Consequently, the pattern of released seismic energy may be locally underestimated. However, the pattern of present-day seismicity has been shown to be consistent with paleo-stress measurements throughout the western Alpine arc (Sue et al., 2007b and references therein). Moreover, the pattern of released seismic energy also does not correlate with present-day rock uplift, measured over a comparable time interval. Therefore, it appears that present-day rock uplift, as well as long-term exhumation are not coupled to seismicity, casting doubts on models in which exhumation is a direct response to active tectonics (e.g., Persaud and Pfiffner, 2004) or in which the Alps respond to increased exhumation by focused deformation within a brittle deforming critical wedge (e.g., Willett et al., 2006).

The strong spatial correlation between elevation, rock uplift and long-term exhumation can be interpreted as either pointing to long-term steady state between rock uplift and exhumation in an active orogenic wedge, or to isostatic response to focused denudation of a post-orogenic mountain belt. However, the lack of correlation between long-term exhumation and released seismic energy argues against an active orogenic wedge, as denudation rates appear to be strongly controlled by seismicity in such settings (Dadson et al., 2003). If the rock uplift pattern was to be explained by the isostatic response to focused denudation only, it should not exceed ~80 % of exhumation rates in the case of local isostasy and significantly less for flexural rebound. We are currently not able to answer this question due to the lack of paleo-elevation markers, but Champagnac et al. (2008; 2007) have recently used mass-balance calculations to propose that the isostatic response to denudation can account for ~50 % of the

observed rock uplift, suggesting that the rest should be due to either shorter-term response to glacial unloading or long-term, long-wavelength geodynamic forcing.

Our results demonstrate that regions with sustained exhumation for the past 4 Myr in the Alps correlate with present-day rock uplift and mean elevation. The simplest interpretation for these data is that they record late- to post-orogenic isostatic adjustment to localized erosion, possibly in addition to some long-wavelength geodynamic signal.

Acknowledgements

SwissTopo created and provided the rock uplift rate data and ETH Zurich provided the precipitation data. We thank Christian Sue for providing the seismicity data and for advice on how to use and interpret these. Ciaran Beggan and Benoit Dubacq are thanked for invaluable help in data handling. This study was supported by an INSU-CNRS "Reliefs de la Terre" program grant to PvdB, a University of Edinburgh PhD teaching studentship and an international student mobility (MIRA) grant of the Rhône-Alpes region to AV.

III.2.5. Data repository

III.2.5.1. Additional tables of Kendall τ-b values in the Western Alps

	Rock uplift	Precipitation	Cumulated flow	Stream power	Seismic energy	Relief (5 km)
Precipitation	-0.2065					
Cumulated flow	0.0036	0.0447				
Stream power	0.192	0.016	0.3351			
Seismic energy	-0.0669	-0.2511	-0.0485	-0.0612		
Relief (5 km)	0.3971	-0.0563	-0.0223	0.219	-0.0825	
Mean elevation	0.2481	-0.0355	-0.1908	0.0758	-0.0134	0.284

Table III.2.2. Kendall τ-b correlation coefficients between different potential control parameters and measures of long-term exhumation.

	AFT Age	2 Ma isoage surface elevation	4 Ma isoage surface elevation
2 Ma isoage surface elevation	-0.1525		
4 Ma isoage surface elevation	-0.3173	0.406	
Distance between 4-2 Ma isoage surfaces	-0.3253	-0.0599	0.5348

Table III.2.3. Kendall τ-b correlation coefficients between different potential control parameters and measures of long-term exhumation.

III.2.5.2. Maps used in the study of correlations between long-term exhumation trends and present-day forcing parameters

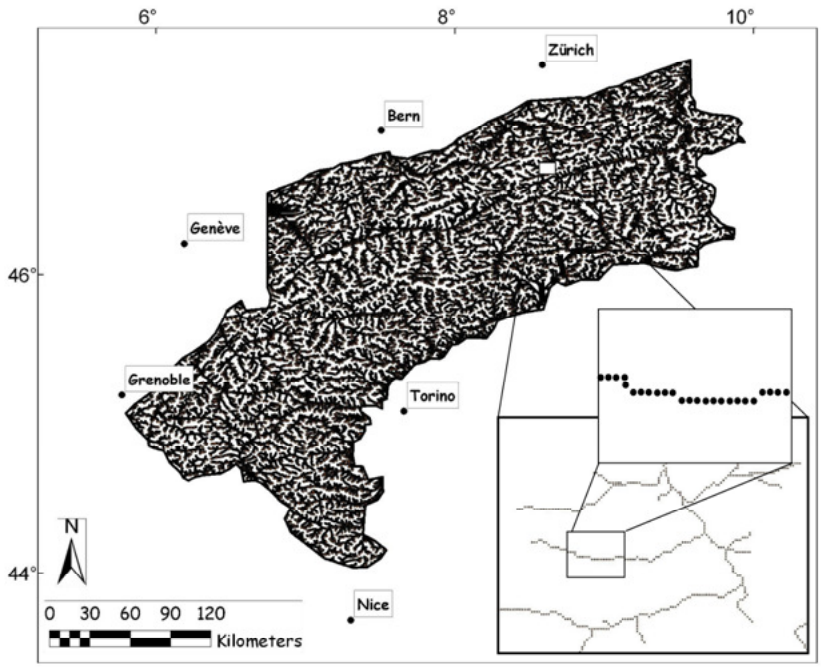

Figure III.2.4. Sampling grid.

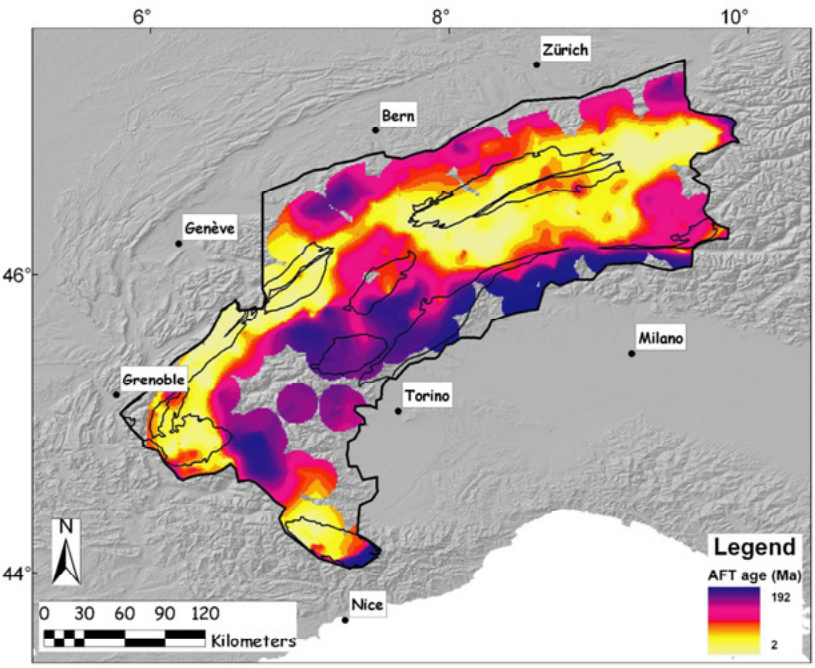

Figure III.2.5. Interpolated apatite fission track (AFT) age, after Vernon et al. (2008).

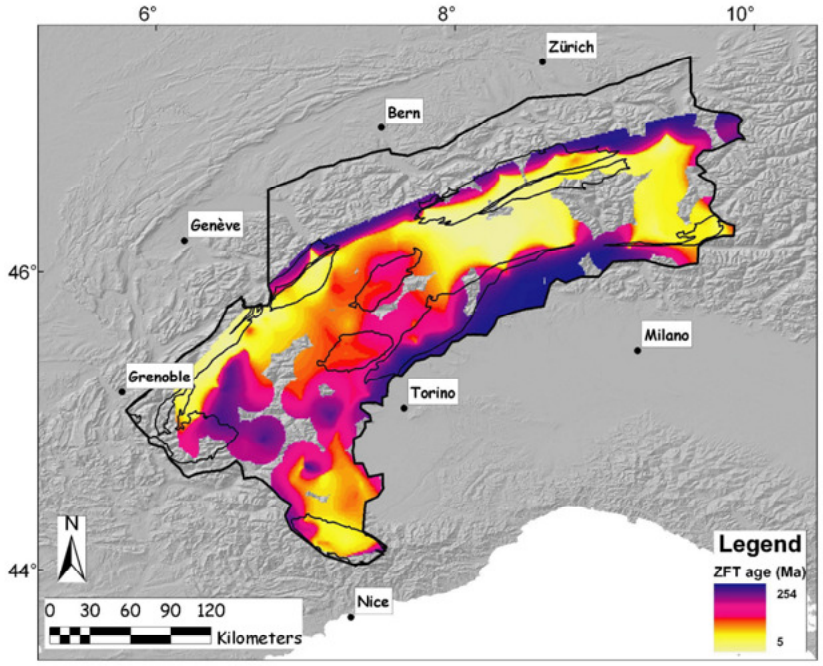

Figure III.2.6. Interpolated zircon fission track (ZFT) age after Vernon et al. (2008).

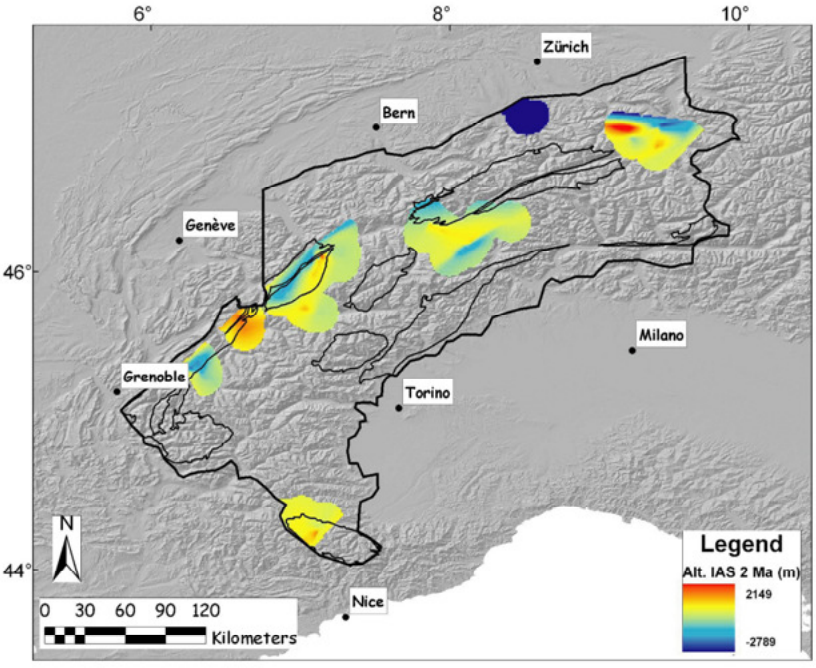

Figure III.2.7. Elevation of the 2 Ma isoage surface, after Vernon et al. (2008).

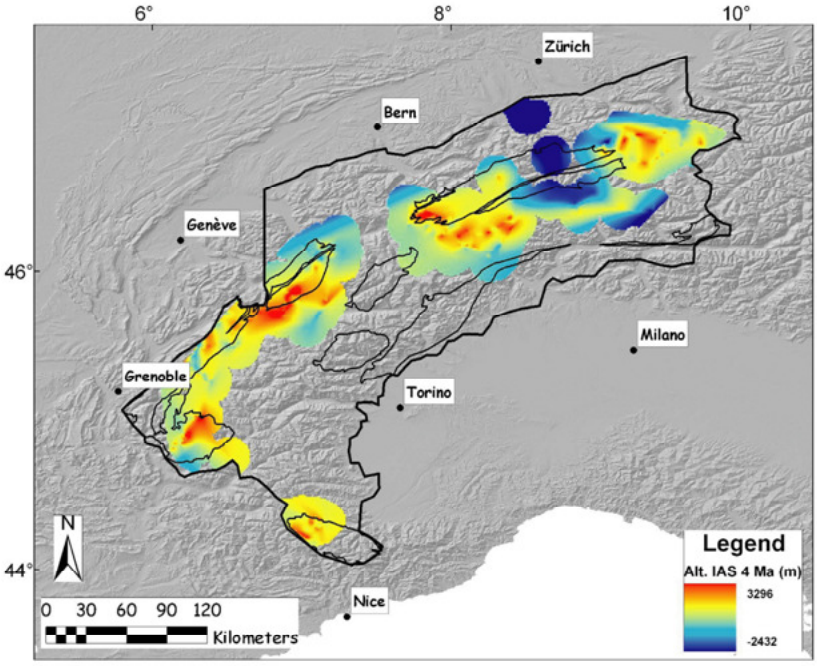

Figure III.2.8. Elevation of the 4 Ma isoage surface, after Vernon et al. (2008).

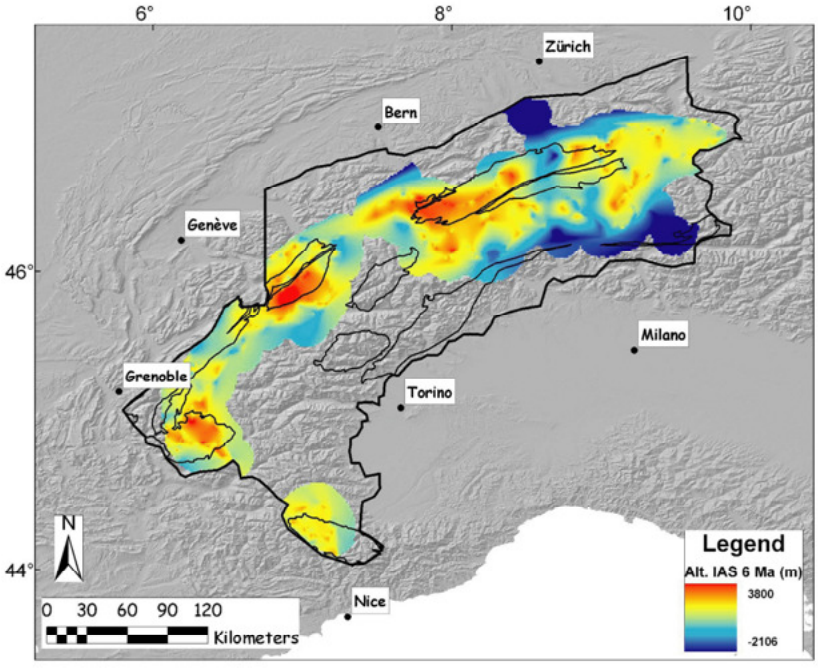

Figure III.2.9. Elevation of the 6 Ma isoage surface, after Vernon et al. (2008).

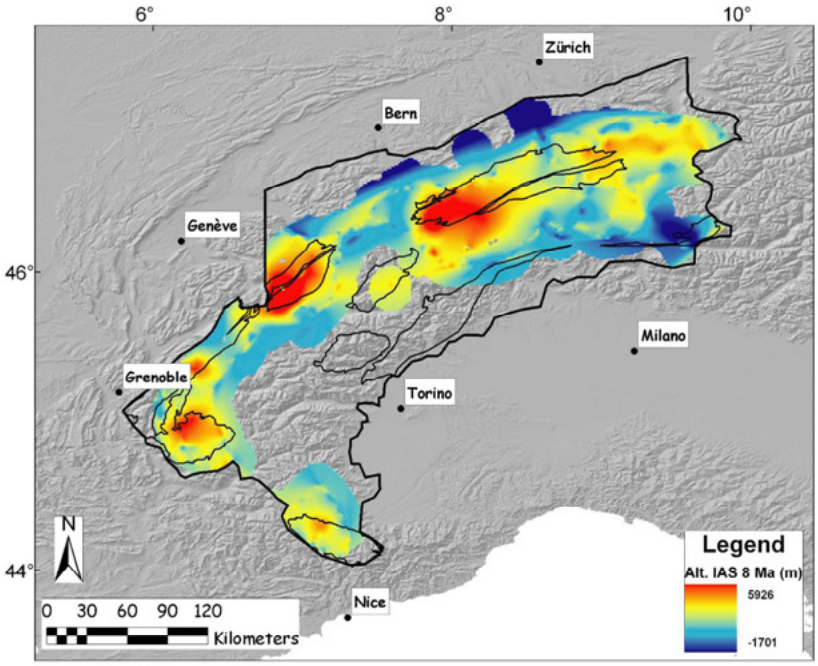

Figure III.2.10. Elevation of the 8 Ma isoage surface, after Vernon et al. (2008).

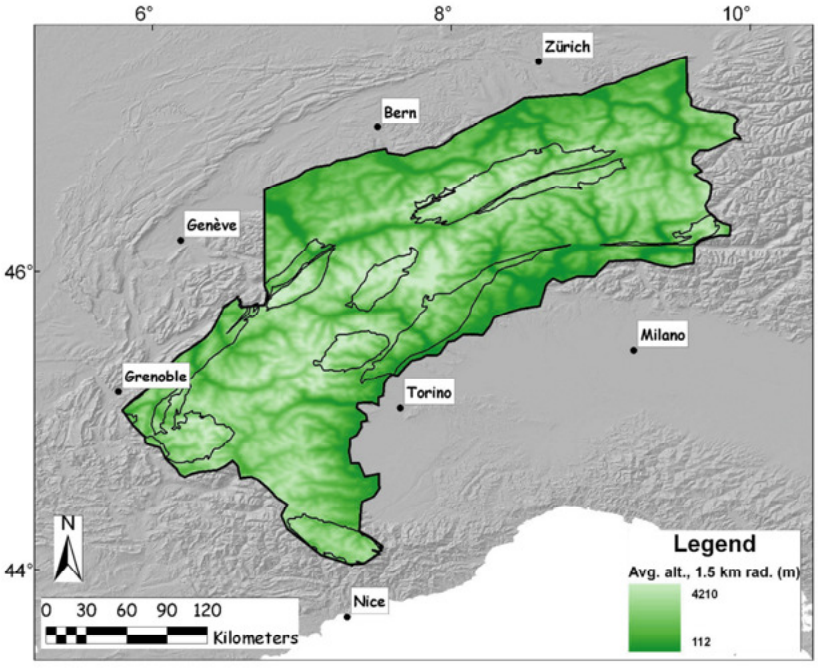

Figure III.2.11. Mean elevation in a 1.4 km radius, calculated using the DEM obtained from the CGIAR-CSI SRTM 3-arc second resolution database (http://srtm.csi.cgiar.org).

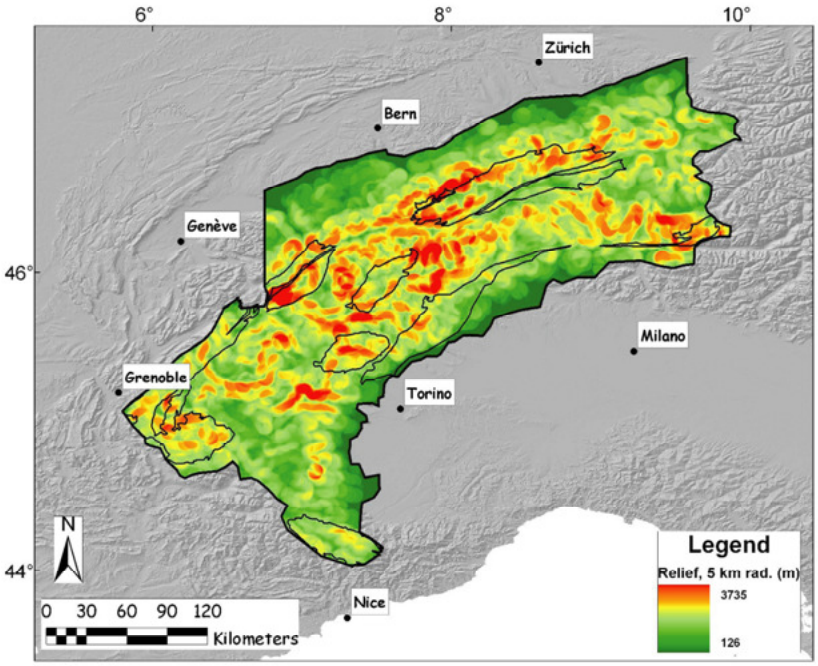

Figure III.2.12. Relief (difference between maximum and minimum elevation) in a 5-km radius, calculated using the DEM obtained from the CGIAR-CSI SRTM 3-arc second resolution database (http://srtm.csi.cgiar.org).

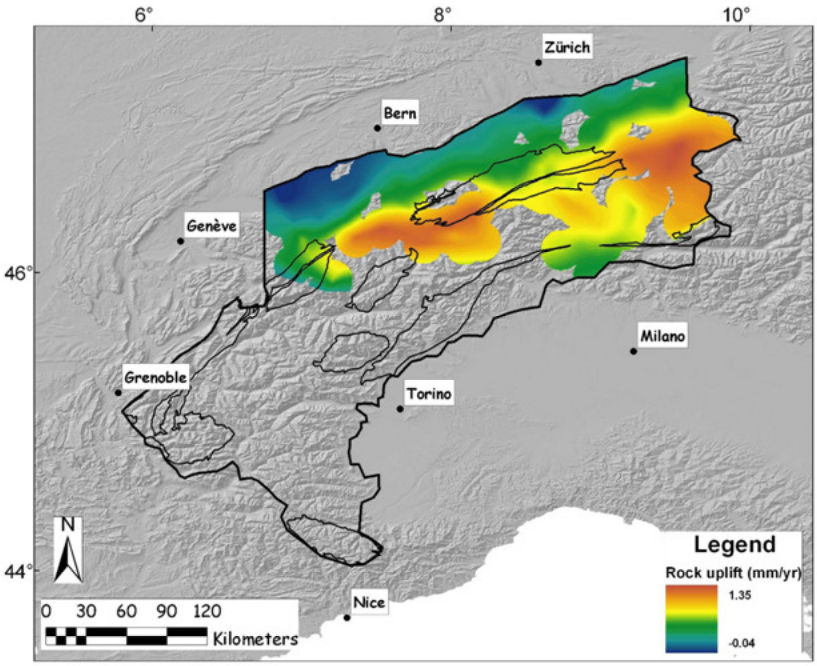

Figure III.2.13. Annual uplift rate measured by geodesy, from the Swiss Federal Office of Topography (SwissTopo) geodetic database (Schlatter, 2007).

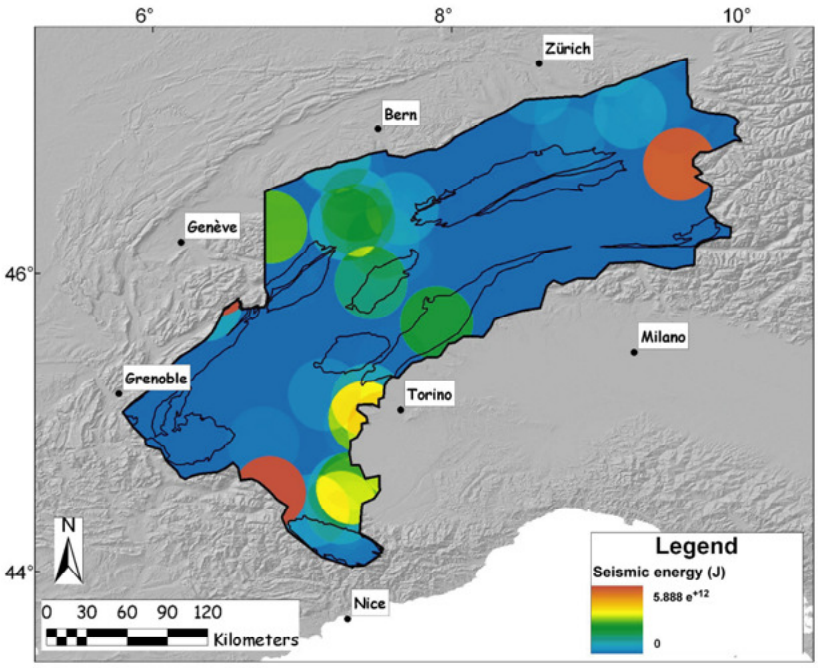

Figure III.2.14. Cumulated seismic energy released, using the earthquake database in Delacou et al. (2004), for the record over the 1959-2000 period for which the focal mechanism is known.

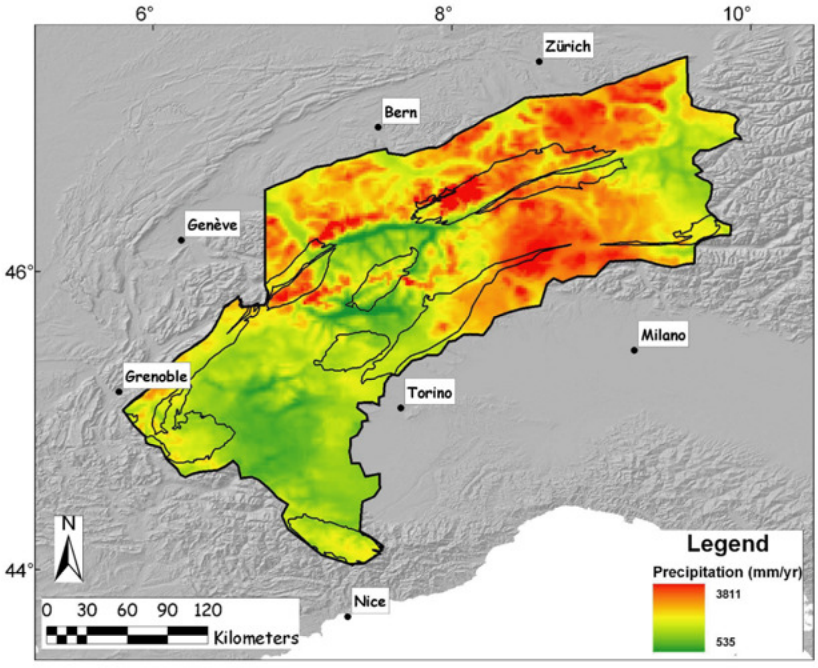

Figure III.2.15. Yearly precipitation derived from interpolated rain-gauge data available at the Swiss Federal Office of Meteorology and Climatology (MeteoSwiss) 1971-1990 precipitation database (Frei and Schär, 1998; Schwarb et al., 2001).

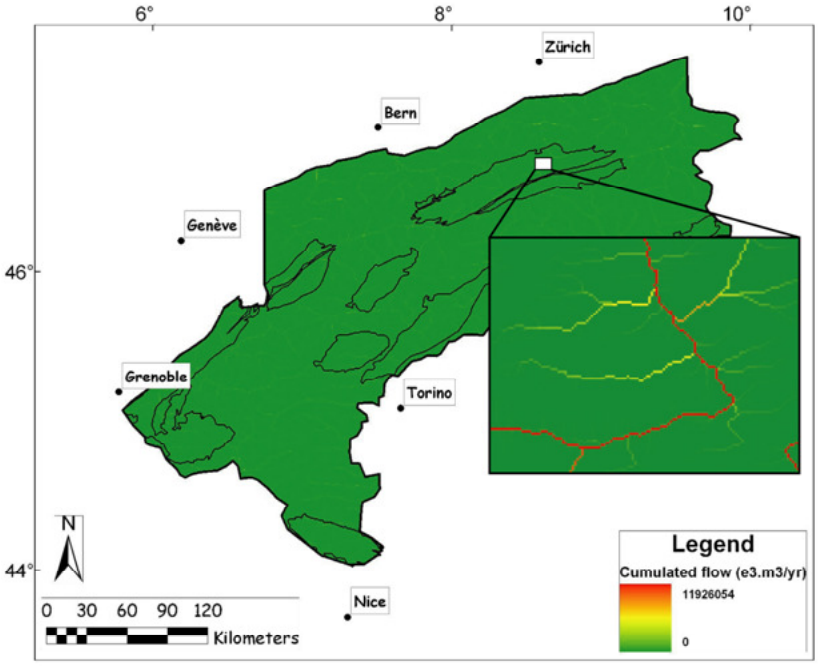

Figure III.2.16. Annual cumulated flow derived from the precipitation record (Figure III.2.15) and the river network. This calculation neglects the effect of local precipitation recycling due to evapo-transpiration.

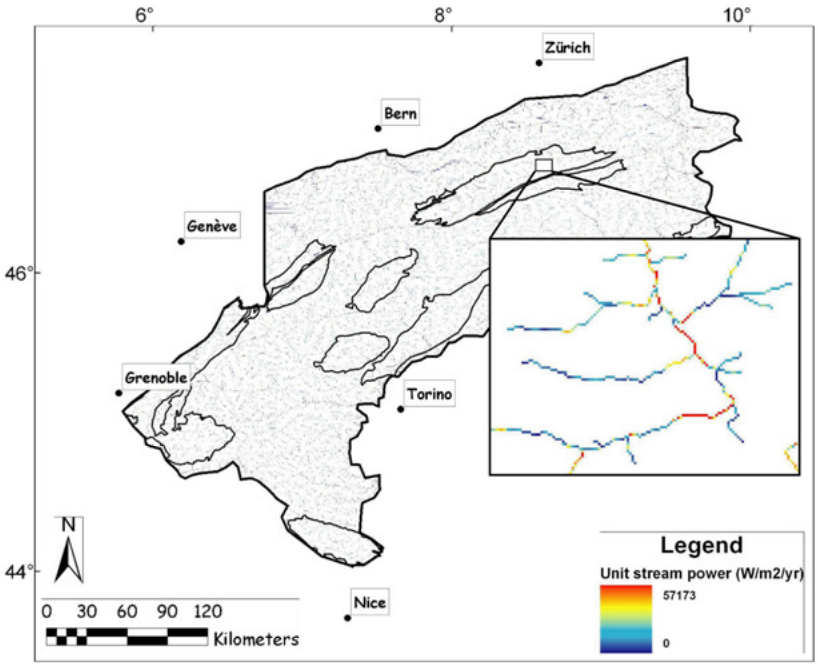

Figure III.2.17. Average annual unit stream power, calculated from the annual cumulated flow (Figure III.2.16) and the local DEM slope.

III.3. Appendix to Chapter III

In section III.2, I presented the results of a correlation study between markers of long-term exhumation and present-day forcing parameters in the Western Alps. The observations are based on map representations of the different parameters, compared spatially through rank-correlation statistics on pixel values; and a cross-section through these maps along a N-S transect through the Aar Massif and Lepontine Dome (central Alps). Here, I report detailed tables of Kendall τ-b values calculated over the Western Alps and over five smaller study areas where I outline the relationship between parameters studied. I provide additional cross-sections to describe past and present exhumation over the Aar Massif-Lepontine Dome transect, and over the extensional Simplon fault, located at the south-western boundary of the Lepontine Dome.

III.3.1. Correlation study

Figure III.3.1 presents a few examples of the plots used to determine the degree of correlation between various parameters sampled over the Western Alps (see section III.2.2 for details on the method). Each pixel sampled on the maps is shown by a red dot. The two black lines on each graph represent two regression lines calculated assuming that one of the two parameters is dependent of the other. In a perfect correlation, these two lines are superposed, whereas they are perpendicular when there is no correlation. As the maps used in correlation studies do not overlap entirely (see Figures III.2.5 to III.2.17), the number of pixels involved in the correlation test of different pairs of parameters may differ (see for instance, Table III.3.1). This is also the reason why the range of value of one parameter may differ between two correlation tests, such as the range in uplift rate on Figures III.3.1-c and -d.

III.3.2. Study areas: Western Alps versus five sub-areas

Beyond the rank correlation study over the entire Western Alps presented in section III.2, I delimited five smaller study areas in the Queyras, Ecrins, Mont Blanc and Aar Massifs, and the Lepontine Alps, located on Figure III.3.2. The aim was to determine whether the conclusions on the control of long-term exhumation apply at all scales, or follow regionally varying patterns. Although Kendall τ-b values are normalised to the number of points used in the calculation, I provide in Tables III.3.1 to III.3.12 the number of points n together with τ-b values, as a means to assess the trustworthiness and significance of the Kendall τ-b values with regard to the area studied. Each table is composed of three parts showing the values calculated for each combination of two parameters selected among: rock uplift, precipitation,

cumulated annual flow, unit stream power, seismic energy released, relief in a 5 km radius, mean elevation (grouped under the name "input" parameters), or AFT age, elevation of the isoage surface at 4 or 2 Ma, distance between the isoage surfaces ages 4 and 2 Ma (grouped under the name "output" parameters).

III.3.2.1. Western Alps

Results for the entire Western Alps have already been presented in a synthetic way in section III.2. Here, I provide in Table III.3.1 the number of points on which each Kendall τ-b value has been calculated for each association of two parameters, as well as Kendall τ-b values as a reminder in Table III.3.2.

III.3.2.2. Queyras area

Although showing no correlation at the scale of the Western Alps, precipitation is here strongly negatively correlated to AFT age, which is expected in the case of a control of exhumation by precipitation. The trend of correlation between relief and AFT age is negative(tentatively compatible with the hypothesis of a recent incision of valleys). Mean elevation is inversely correlated with hydrological proxies (precipitation, cumulated flow, stream power), suggesting no primary control of the location of precipitation by rain-shadow effects. Rock uplift data is not available for the French part of the Western Alps.

III.3.2.3. Ecrins area

Seismic energy is positively correlated with with AFT age, suggesting a negative correlation between seismicity and exhumation. This would not be expected in the case of thrust-related seismicity and exhumation occurring in a compressive belt. However, the Ecrins area comprises the Penninic thrust which is seismically active and shows a large jump in AFT ages, suggesting extensional deformation taking place (Tricart et al., 2007). Just like in Queyras, precipitation is negatively correlated with AFT ages. The negative correlation between seismic energy and precipitation suggests that the former is not controlled by the latter. The relief is positively correlated with precipitation and stream power, highlighting a possible local rain-shadow control on the location of precipitation.

III.3.2.4. Mont Blanc area

Contrarily to the Western Alps and the Queyras areas, the precipitation is here strongly correlated with mean elevation highlighting, like in the Ecrins area, a possible local rain-shadow control on the location of precipitation.

III.3.2.5. Lepontine area

Rock uplift is here positively correlated with the mean elevation and positively correlated with the elevation of 4 and 2 Ma isoage surfaces, as well as the 4-2 Ma exhumation rate. The uplift rate is negatively correlated with AFT age, which in turn is positively correlated with precipitation. This suggests that the present-day uplift pattern is closer to the 4 Ma average than the present-day precipitation pattern is, or at least that variations in precipitation rate over the study area do not play a role in controlling long-term exhumation. In this regard, the Lepontine area is comforting the observations made at the scale of the Western Alps.

III.3.2.6. Aar area

The uplift rate is strongly negatively correlated with AFT age, highlighting a long-term pattern of rock uplift coupled to denudation. In contrast to the trend observed in the entire Western Alps, the uplift rate is here positively correlated with precipitation. The negative correlation between seismic energy and uplift demonstrates that the two are not caused by the same tectonic process. Precipitation is strongly positively correlated with mean elevation, and negatively correlated with AFT age.

Although the Kendall τ-b correlation test applied on the entire Western Alps (section III.2) does not show correlation between precipitation and elevation, such a correlation does appear in two of the sub-areas (the Aar and Mont-Blanc Massifs). However, this may be affected by the way rain-gauge data was interpolated to produce a precipitation map (Schwarb et al., 2001). Although precipitation is not linked to the uplift rate in the Western Alps, the data do not rule out a climatic control on uplift in the Aar Massif, and on long-term exhumation in the Queyras and the Ecrins Massifs (young AFT ages coincide with high precipitation). The study of correlation trends between exhumation proxies in sub-areas of the Western Alps gives hint that regional trends may exist. However, these trends are smoothed in the study of the Western Alps, which is the relevant scale to understand controls at the orogen scale involved in peri-alpine sedimentation pattern (Kuhlemann, 2000) or the uplift of the foreland basin (Cederbom et al., 2004).

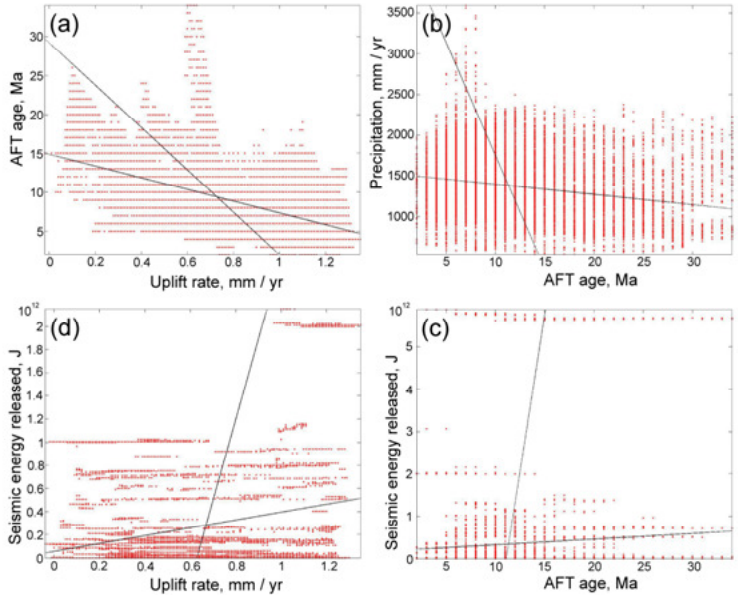

Figure III.3.1. Examples of 4 plots used in the search for correlation in the parameters space: (a) example of a "strong" correlation (AFT age vs. uplift rate), (b) "weak" correlation (AFT age vs. precipitation), and (c, d) no correlation (Uplift rate and AFT age vs. seismic energy released).

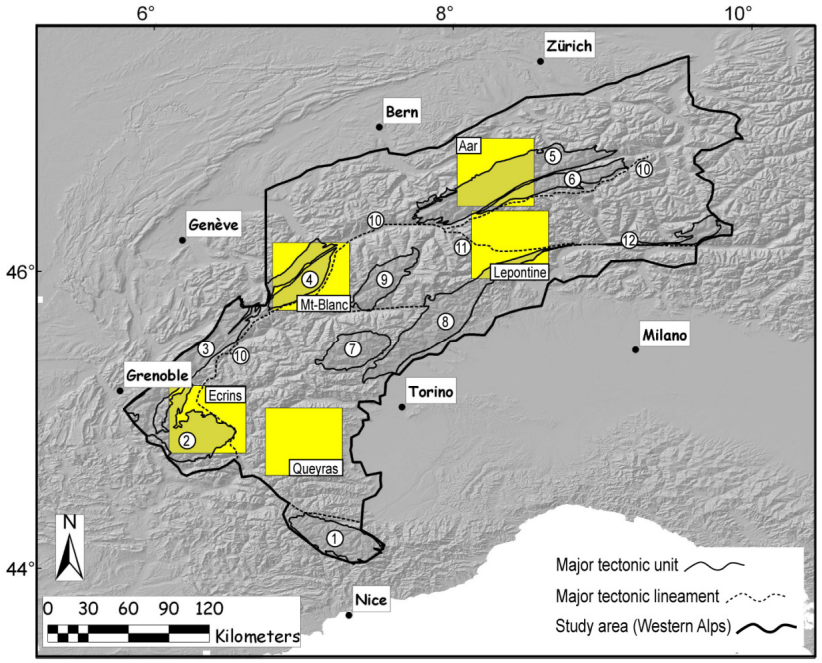

Figure III.3.2. Location of the main study area in the Western Alps (thick black contour), and the five sub-areas (yellow rectangles). The numbers refer to tectonic units or structures: 1) Argentera Massif, 2) Ecrins Massif, 3) Belledonne Massif, 4) Mont Blanc Massif, 5) Aar and 6) Gotthard Massifs, 7) Gran Paradiso Massif, 8) Sesia and 9) Dent Blanche Massifs, 10) Penninic thrust, 11) Simplon fault, 12) Peri-Adriatic fault.

Input vs. output

	Rock uplift	Precipitation	Cumulated flow	Stream power	Seismic energy	Relief (5 km)	Mean Elevation
AFT age	102350	204630	204630	204630	204630	204630	204630
2 Ma isoage surface elevation	26296	46606	46606	46606	46606	46606	46606
4 Ma isoage surface elevation	56519	100277	100277	100277	100277	100277	100277
Distance between 4-2 Ma isoage surfaces	26146	46367	46367	46367	46367	46367	46367

Input vs. input

	Rock uplift	Precipitation	Cumulated flow	Stream power	Seismic energy	Relief (5 km)
Precipitation	120180					
Cumulated flow	120180	258311				
Stream power	120180	258311	258311			
Seismic energy	120180	258311	258311	258311		
Relief (5 km)	120180	258311	258311	258311	258311	
Mean elevation	120180	258311	258311	258311	258311	258311

Output vs. output

	AFT Age	2 Ma isoage surface elevation	4 Ma isoage surface elevation
2 Ma isoage surface elevation	45282		
4 Ma isoage surface elevation	98567	46367	
Distance between 4-2 Ma isoage surfaces	45151	46367	46367

Table III.3.1. Number of points used in the calculation of correlation coefficients between each pair of parameters in the Western Alps study area. Total amount of points: 258311.

Input vs. output

	Rock uplift	Precipitation	Cumulated flow	Stream power	Seismic energy	Relief (5 km)	Mean Elevation
AFT age	-0.4242	-0.1267	-0.0464	-0.0933	0.0667	-0.1433	-0.0515
2 Ma isoage surface elevation	0.3891	-0.0837	-0.0056	0.1044	0.0247	0.0547	0.1815
4 Ma isoage surface elevation	0.4116	-0.1512	-0.0353	0.037	0.0331	0.0494	0.1891
Distance between 4-2 Ma isoage surfaces	0.1788	0.1713	-0.0229	0.0529	-0.1314	0.1437	0.2652

Input vs. input

	Rock uplift	Precipitation	Cumulated flow	Stream power	Seismic energy	Relief (5 km)
Precipitation	-0.2065					
Cumulated flow	0.0036	0.0447				
Stream power	0.192	0.016	0.3351			
Seismic energy	-0.0669	-0.2511	-0.0485	-0.0612		
Relief (5 km)	0.3971	-0.0563	-0.0223	0.219	-0.0825	
Mean elevation	0.2481	-0.0355	-0.1908	0.0758	-0.0134	0.284

Output vs. output

	AFT Age	2 Ma isoage surface elevation	4 Ma isoage surface elevation
2 Ma isoage surface elevation	-0.1525		
4 Ma isoage surface elevation	-0.3173	0.406	
Distance between 4-2 Ma isoage surfaces	-0.3253	-0.0599	0.5348

Table III.3.2. Kendal τ-b parameters calculated for every combination of two parameters in the Western Alps study area.

Input vs. output

	Rock uplift	Precipitation	Cumulated flow	Stream power	Seismic energy	Relief (5 km)	Mean Elevation
AFT age	0	6080	6080	6080	6080	.	6080
2 Ma isoage surface elevation	0	0	0	0	0	0	0
4 Ma isoage surface elevation	0	0	0	0	0	0	0
Distance between 4-2 Ma isoage surfaces	0	0	0	0	0	0	0

Input vs. input

	Rock uplift	Precipitation	Cumulated flow	Stream power	Seismic energy	Relief (5 km)
Precipitation	0					
Cumulated flow	0	9921				
Stream power	0	9921	9921			
Seismic energy	0	9921	9921	9921		
Relief (5 km)	0	9921	9921	9921	9921	
Mean elevation	0	9921	9921	9921	9921	9921

Output vs. output

	AFT Age	2 Ma isoage surface elevation	4 Ma isoage surface elevation
2 Ma isoage surface elevation	0		
4 Ma isoage surface elevation	0	0	
Distance between 4-2 Ma isoage surfaces	0	0	0

Table III.3.3. Number of points used in the calculation of correlation coefficients between each pair of parameters in the Queyras study area. Total amount of points: 9921.

Input vs. output

	Rock uplift	Precipitation	Cumulated flow	Stream power	Seismic energy	Relief (5 km)	Mean Elevation
AFT age		-0.4544	0.0775	0.0235	0.1504	-0.1753	-0.1155
2 Ma isoage surface elevation							
4 Ma isoage surface elevation							
Distance between 4-2 Ma isoage surfaces							

Input vs. input

	Rock uplift	Precipitation	Cumulated flow	Stream power	Seismic energy	Relief (5 km)
Precipitation						
Cumulated flow		-0.0278				
Stream power		0.0228	0.3655			
Seismic energy		0.0539	0.0344	-0.0238		
Relief (5 km)		0.1346	-0.0663	0.0758	-0.1725	
Mean elevation		-0.225	-0.2755	-0.2091	-0.0163	-0.0722

Output vs. output

	AFT Age	2 Ma isoage surface elevation	4 Ma isoage surface elevation
2 Ma isoage surface elevation			
4 Ma isoage surface elevation			
Distance between 4-2 Ma isoage surfaces			

Table III.3.4. Kendal τ-b parameters calculated for every combination of two parameters in the Queyras study area. Empty cells correspond to no data (n = 0 in Table III.3.3).

Input vs. output

	Rock uplift	Precipitation	Cumulated flow	Stream power	Seismic energy	Relief (5 km)	Mean Elevation
AFT age	0	9619	9619	9619	9619	9619	9619
2 Ma isoage surface elevation	0	303	303	303	303	303	303
4 Ma isoage surface elevation	0	7547	7547	7547	7547	7547	7547
Distance between 4-2 Ma isoage surfaces	0	303	303	303	303	303	303

Input vs. input

	Rock uplift	Precipitation	Cumulated flow	Stream power	Seismic energy	Relief (5 km)
Precipitation	0					
Cumulated flow	0	9803				
Stream power	0	9803	9803			
Seismic energy	0	9803	9803	9803		
Relief (5 km)	0	9803	9803	9803	9803	
Mean elevation	0	9803	9803	9803	9803	9803

Output vs. output

	AFT Age	2 Ma isoage surface elevation	4 Ma isoage surface elevation
2 Ma isoage surface elevation	303		
4 Ma isoage surface elevation	7547	303	
Distance between 4-2 Ma isoage surfaces	303	303	303

Table III.3.5. Number of points used in the calculation of correlation coefficients between each pair of parameters in the Ecrins study area. Total amount of points: 9803.

Input vs. output

	Rock uplift	Precipitation	Cumulated flow	Stream power	Seismic energy	Relief (5 km)	Mean Elevation
AFT age		-0.3919	-0.0457	-0.1234	0.5934	-0.3676	-0.1191
2 Ma isoage surface elevation		0.7187	0.0541	-0.0442	-0.696	0.1185	0.0842
4 Ma isoage surface elevation		-0.307	-0.0385	-0.1185	0.2698	-0.073	0.2376
Distance between 4-2 Ma isoage surfaces		-0.2023	0.0128	-0.043	0.301	0.1005	-0.2541

Input vs. input

	Rock uplift	Precipitation	Cumulated flow	Stream power	Seismic energy	Relief (5 km)
Precipitation						
Cumulated flow		0.0054				
Stream power		0.1023	0.4087			
Seismic energy		-0.5788	-0.051	-0.1448		
Relief (5 km)		0.2382	0.0842	0.212	-0.2508	
Mean elevation		0.0711	-0.362	-0.283	-0.0348	-0.0742

Output vs. output

	AFT Age	2 Ma isoage surface elevation	4 Ma isoage surface elevation
2 Ma isoage surface elevation	-0.6142		
4 Ma isoage surface elevation	-0.1174	0.5935	
Distance between 4-2 Ma isoage surfaces	0.1042	-0.3299	0.091

Table III.3.6. Kendal τ-b parameters calculated for every combination of two parameters in the Ecrins study area. Empty cells correspond to no data (n = 0 in Table III.3.5).

Input vs. output

	Rock uplift	Precipitation	Cumulated flow	Stream power	Seismic energy	Relief (5 km)	Mean Elevation
AFT age	5357	10001	10001	10001	10001	10001	10001
2 Ma isoage surface elevation	3970	7618	7618	7618	7618	7618	7618
4 Ma isoage surface elevation	5241	9564	9564	9564	9564	9564	9564
Distance between 4-2 Ma isoage surfaces	3970	7618	7618	7618	7618	7618	7618

Input vs. input

	Rock uplift	Precipitation	Cumulated flow	Stream power	Seismic energy	Relief (5 km)
Precipitation	5484					
Cumulated flow	5484	10202				
Stream power	5484	10202	10202			
Seismic energy	5484	10202	10202	10202		
Relief (5 km)	5484	10202	10202	10202	10202	
Mean elevation	5484	10202	10202	10202	10202	10202

Output vs. output

	AFT Age	2 Ma isoage surface elevation	4 Ma isoage surface elevation
2 Ma isoage surface elevation	7618		
4 Ma isoage surface elevation	9540	7618	
Distance between 4-2 Ma isoage surfaces	7618	7618	7618

Table III.3.7. Number of points used in the calculation of correlation coefficients between each pair of parameters in the Mont Blanc study area. Total amount of points: 10202.

Input vs. output

	Rock uplift	Precipitation	Cumulated flow	Stream power	Seismic energy	Relief (5 km)	Mean Elevation
AFT age	-0.1362	-0.0955	-0.0832	0.0425	0.1061	0.0165	0.1523
2 Ma isoage surface elevation	0.0547	-0.1102	0.0136	0.0305	-0.1861	-0.2064	-0.0036
4 Ma isoage surface elevation	-0.2909	0.3124	-0.0268	-0.017	-0.2052	0.0355	0.4134
Distance between 4-2 Ma isoage surfaces	-0.6153	0.5679	-0.0405	-0.0132	-0.0691	0.1485	0.4193

Input vs. input

	Rock uplift	Precipitation	Cumulated flow	Stream power	Seismic energy	Relief (5 km)
Precipitation	-0.544					
Cumulated flow	0.0661	-0.1174				
Stream power	0.0498	-0.0457	0.3693			
Seismic energy	-0.1577	0.0859	-0.0352	-0.0446		
Relief (5 km)	0.0131	0.0936	-0.0047	0.0738	0.1116	
Mean elevation	-0.3775	0.5133	-0.2334	-0.0981	0.0109	0.1093

Output vs. output

	AFT Age	2 Ma isoage surface elevation	4 Ma isoage surface elevation
2 Ma isoage surface elevation	0.0437		
4 Ma isoage surface elevation	-0.0922	0.1301	
Distance between 4-2 Ma isoage surfaces	-0.1861	-0.2411	0.6298

Table III.3.8. Kendal τ-b parameters calculated for every combination of two parameters in the Mont Blanc study area.

Input vs. output

	Rock uplift	Precipitation	Cumulated flow	Stream power	Seismic energy	Relief (5 km)	Mean Elevation
AFT age	2949	10287	10287	10287	10287	10287	10287
2 Ma isoage surface elevation	2277	4281	4281	4281	4281	4281	4281
4 Ma isoage surface elevation	2758	7773	7773	7773	7773	7773	7773
Distance between 4-2 Ma isoage surfaces	2277	4281	4281	4281	4281	4281	4281

Input vs. input

	Rock uplift	Precipitation	Cumulated flow	Stream power	Seismic energy	Relief (5 km)
Precipitation	2949					
Cumulated flow	2949	10623				
Stream power	2949	10623	10623			
Seismic energy	2949	10623	10623	10623		
Relief (5 km)	2949	10623	10623	10623	10623	
Mean elevation	2949	10623	10623	10623	10623	10623

Output vs. output

	AFT Age	2 Ma isoage surface elevation	4 Ma isoage surface elevation
2 Ma isoage surface elevation	4281		
4 Ma isoage surface elevation	7773	4281	
Distance between 4-2 Ma isoage surfaces	4281	4281	4281

Table III.3.9. Number of points used in the calculation of correlation coefficients between each pair of parameters in the Lepontine study area. Total amount of points: 10623.

Input vs. output

	Rock uplift	Precipitation	Cumulated flow	Stream power	Seismic energy	Relief (5 km)	Mean Elevation
AFT age	-0.1022	0.3621	0.0221	-0.0178	-0.0772	-0.3435	-0.25
2 Ma isoage surface elevation	0.2918	0.1435	-0.0565	-0.1213	-0.1441	0.0767	0.3098
4 Ma isoage surface elevation	0.4892	-0.167	-0.0789	0.0635	0.1094	0.3105	0.4628
Distance between 4-2 Ma isoage surfaces	0.1742	0.0544	-0.0239	-0.0103	-0.137	0.0405	0.0319

Input vs. input

	Rock uplift	Precipitation	Cumulated flow	Stream power	Seismic energy	Relief (5 km)
Precipitation	-0.3739					
Cumulated flow	-0.0136	-0.0071				
Stream power	0.028	0.0019	0.367			
Seismic energy	0.0971	-0.3694	-0.0188	0.0273		
Relief (5 km)	0.1549	-0.3453	-0.0398	0.1117	0.2064	
Mean elevation	0.4319	-0.0644	-0.2709	-0.0521	0.1229	0.1836

Output vs. output

	AFT Age	2 Ma isoage surface elevation	4 Ma isoage surface elevation
2 Ma isoage surface elevation	0.0803		
4 Ma isoage surface elevation	-0.5337	0.2415	
Distance between 4-2 Ma isoage surfaces	-0.4222	-0.1334	0.627

Table III.3.10. Kendal τ-b parameters calculated for every combination of two parameters in the Lepontine study area.

Input vs. output

	Rock uplift	Precipitation	Cumulated flow	Stream power	Seismic energy	Relief (5 km)	Mean Elevation
AFT age	9814	10501	10501	10501	10501	10501	10501
2 Ma isoage surface elevation	336	366	366	366	0	366	366
4 Ma isoage surface elevation	5184	5408	5408	5408	5408	5408	5408
Distance between 4-2 Ma isoage surfaces	336	366	366	366	366	366	366

Input vs. input

	Rock uplift	Precipitation	Cumulated flow	Stream power	Seismic energy	Relief (5 km)
Precipitation	9994					
Cumulated flow	9994	10823				
Stream power	9994	10823	10823			
Seismic energy	9994	10823	10823	10823		
Relief (5 km)	9994	10823	10823	10823	10823	
Mean elevation	9994	10823	10823	10823	10823	10823

Output vs. output

	AFT Age	2 Ma isoage surface elevation	4 Ma isoage surface elevation
2 Ma isoage surface elevation	366		
4 Ma isoage surface elevation	5401	366	
Distance between 4-2 Ma isoage surfaces	366	366	366

Table III.3.11. Number of points used in the calculation of correlation coefficients between each pair of parameters in the Aar study area. Total amount of points: 10823.

Input vs. output

	Rock uplift	Precipitation	Cumulated flow	Stream power	Seismic energy	Relief (5 km)	Mean Elevation
AFT age	-0.6612	-0.2035	-0.0427	-0.0991	0.3506	-0.0712	-0.4447
2 Ma isoage surface elevation	-0.2363	0.2865	-0.2358	-0.284	NaN	-0.17	0.2884
4 Ma isoage surface elevation	0.4371	0.0424	0.043	-0.0367	-0.1587	0.0629	0.1321
Distance between 4-2 Ma isoage surfaces	0.3065	-0.3984	0.258	0.2719	NaN	0.3312	-0.3613

Input vs. input

	Rock uplift	Precipitation	Cumulated flow	Stream power	Seismic energy	Relief (5 km)
Precipitation	0.2171					
Cumulated flow	0.0813	-0.1072				
Stream power	0.1052	-0.0077	0.25			
Seismic energy	-0.4702	-0.0748	-0.0182	0.0185		
Relief (5 km)	0.1867	0.0915	0.0089	0.1538	0.0215	
Mean elevation	0.502	0.6023	-0.1029	-0.0014	-0.25	0.1213

Output vs. output

	AFT Age	2 Ma isoage surface elevation	4 Ma isoage surface elevation
2 Ma isoage surface elevation	0.071		
4 Ma isoage surface elevation	-0.4862	-0.1605	
Distance between 4-2 Ma isoage surfaces	-0.1815	-0.6725	0.511

Table III.3.12. Kendal τ-b parameters calculated for every combination of two parameters in the Aar study area.

III.3.3. Cross-sections through the raster maps and age database

To complement the cross-sections presented in Figure III.2.3, I provide here additional data on the Aar-Lepontine section, as well as an axial (Simplon) section passing through the Aar Massif, the Simplon fault, the Dent-Blanche, Sesia and Gran Paradiso Massifs (Figure III.3.3). The data presented in these cross-sections are taken from the maps on Figures III.2.5 to III.2.17, as well as AFT and ZFT ages from the database presented in section II.2 and new ages detailed in section IV.2.

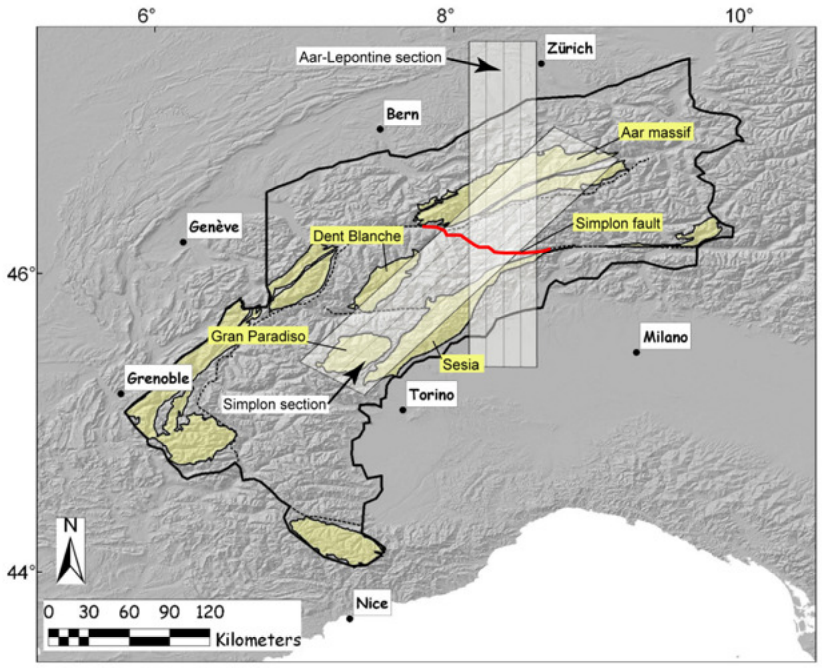

Figure III.3.3. Location of the two cross-sections

III.3.3.1. Aar-Lepontine section

The Aar-Lepontine section (see location on Figure III.3.3) crosses the Western Alps between the Swiss Molasse foreland basin and the Po plain, and was constructed by averaging five 242-km long parallel transects separated by 8.5 km along a N-0.5 °W strike. Its aim is to study the exhumation history of the central Alps, on a transect approximately perpendicular to their strike.

Figures III.3.4 and III.3.5 enable to compare the pattern of rock uplift with AFT and ZFT ages. All AFT ages exhibit alpine cooling ages (i.e. younger than ca. 35 Ma) and a pattern where younger ages are found in the axial region of the orogen. ZFT ages show a similar age pattern across the orogen, although only the most central segment of the transect shows an alpine age reset. In both cases, the pattern of present-day rock uplift is consistent with the

long-term exhumation trend evidenced by fission track ages, with the highest uplift rates in locations with youngest ages.

The 8 to 2 Ma AFT isoage surfaces in the central panel of Figure III.3.6 present an imbricated pattern, younging downward as required by definition (Vernon et al., 2008). The lower graph in Figure III.3.6 shows that the distance between isoage surfaces is noticeably greater between 6-4 and 4-2 Ma than between 8-6 Ma, confirming a change in exhumation rate after 6 Ma. Two central AFT ages from boreholes in the Swiss Molasse foreland basin (3.6 and 4.7 Ma) are added on Figure III.3.6 central panel. These samples are the deepest dated in each borehole reported in Cederbom et al. (2004), and their age was totally reset before the exhumation phase dated around 4 Ma by Cederbom et al. (2004).

It must be noted, however, that if these two samples belong to an uplifted paleo-partial annealing zone (PAZ), they cannot be overlain by older isoage surfaces (contrarily to the appearance on Figure III.3.6) because the AFT ages on detrital apatites located higher in the sedimentary pile have not been reset, as illustrated on the sketches of Figure III.3.7. The reasons why isoage surfaces shown in cross-section on Figure III.3.6 are extrapolated as far north as the location of the two dated borehole samples in the foreland basin, is that the maps of isoage surfaces are cropped by a 15 km mask (section II.2) around datapoints, thus leaving ill-defined pixels in the external border of maps. In addition, the cross-section presented in Figure III.3.6 results from the averaging of five sections separated by 8.5 km, which are slightly oblique to the Aar Massif northern boundary, so it is not possible to locate precisely the boundary between axial chain bedrock and foreland basin deposits on the section.

The apex of the uplift curve (Figure III.3.6, lower panel) fits with the apexes of AFT isoage surfaces at 4 and 2 Ma, but is shifted toward south of the apexes of the two upper isoage surfaces presented, aged 6 and 8 Ma, suggesting a modification in the exhumation pattern after 6 Ma. In addition, using the fragmentary data available on the lower panel of Figure III.3.6, I propose that the denudation between 8 and 6 Ma (green curve) is not greater close to the chain axis, whereas the denudation between 6 and 4 Ma and between 4 and 2 Ma (red and pink curves) seem more variable and higher close to the chain axis than at its borders. The apexes of the 6-4 and 4-2 Ma curves, estimated from the general trends of available data, are located respectively further north than, and at the same latitude as the apex of the rock uplift curve. These observations confirm that the exhumation pattern of the chain changed later than

6 Ma, and more precisely that the present-day pattern of rock uplift might be as old as 4 Ma, because of its agreement with the 4-2 Ma exhumation pattern,.

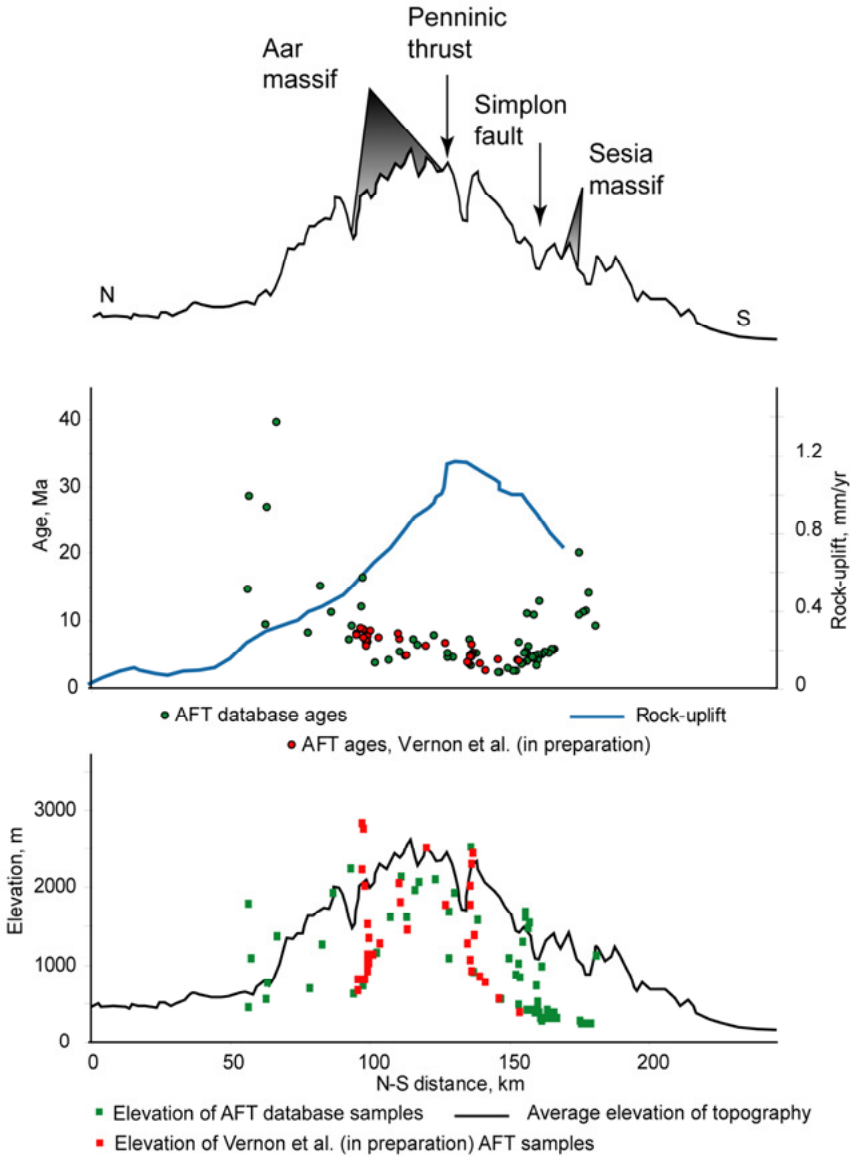

Figure III.3.4. AFT ages across the Aar-Lepontine section, compared to present-day rock uplift rates. "AFT database ages" are described in section II.2, "rock uplift" in section III.2 and "AFT ages, Vernon et al. (in preparation)" in section IV.2. The lower panel presents the elevation of samples dated, superposed to the curve of average elevation of the topography.

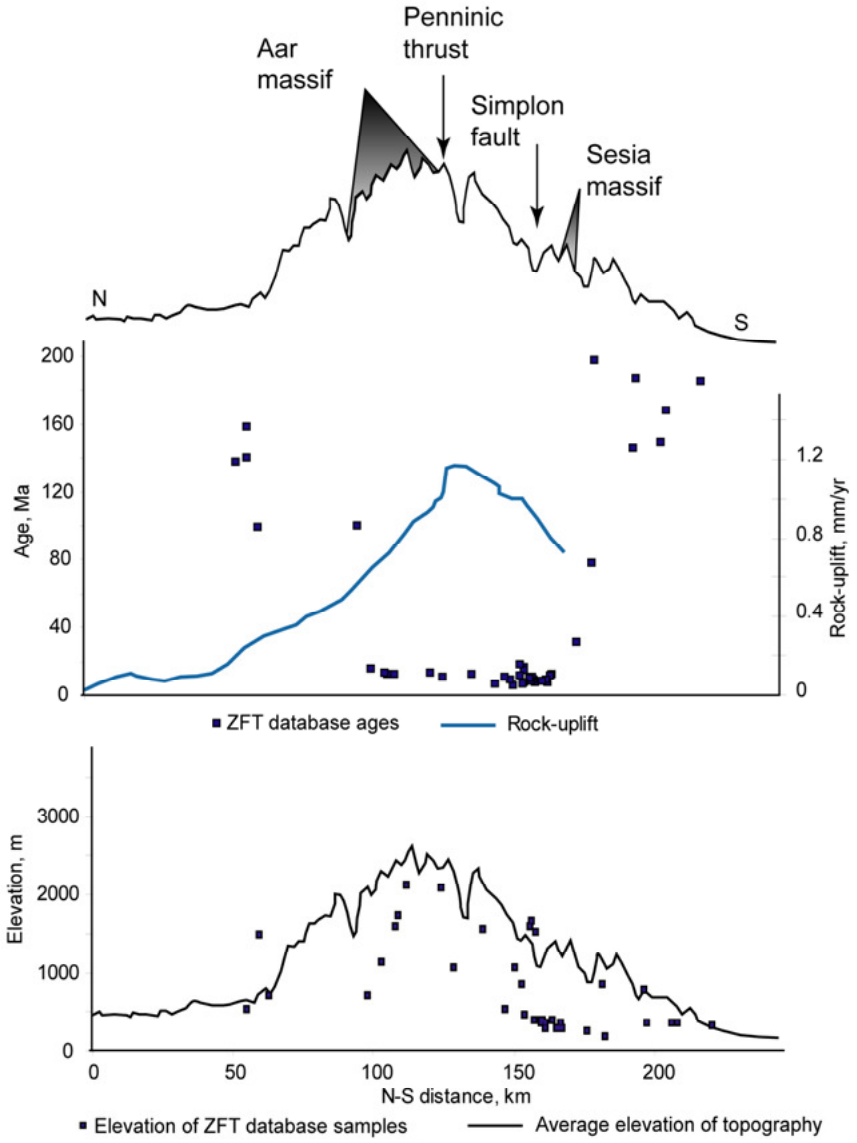

Figure III.3.5. ZFT ages across the Aar-Lepontine section. "ZFT database ages" are described in section II.2, and "rock uplift" in section III.2. The lower panel presents the elevation of samples dated, superposed on the average topography.

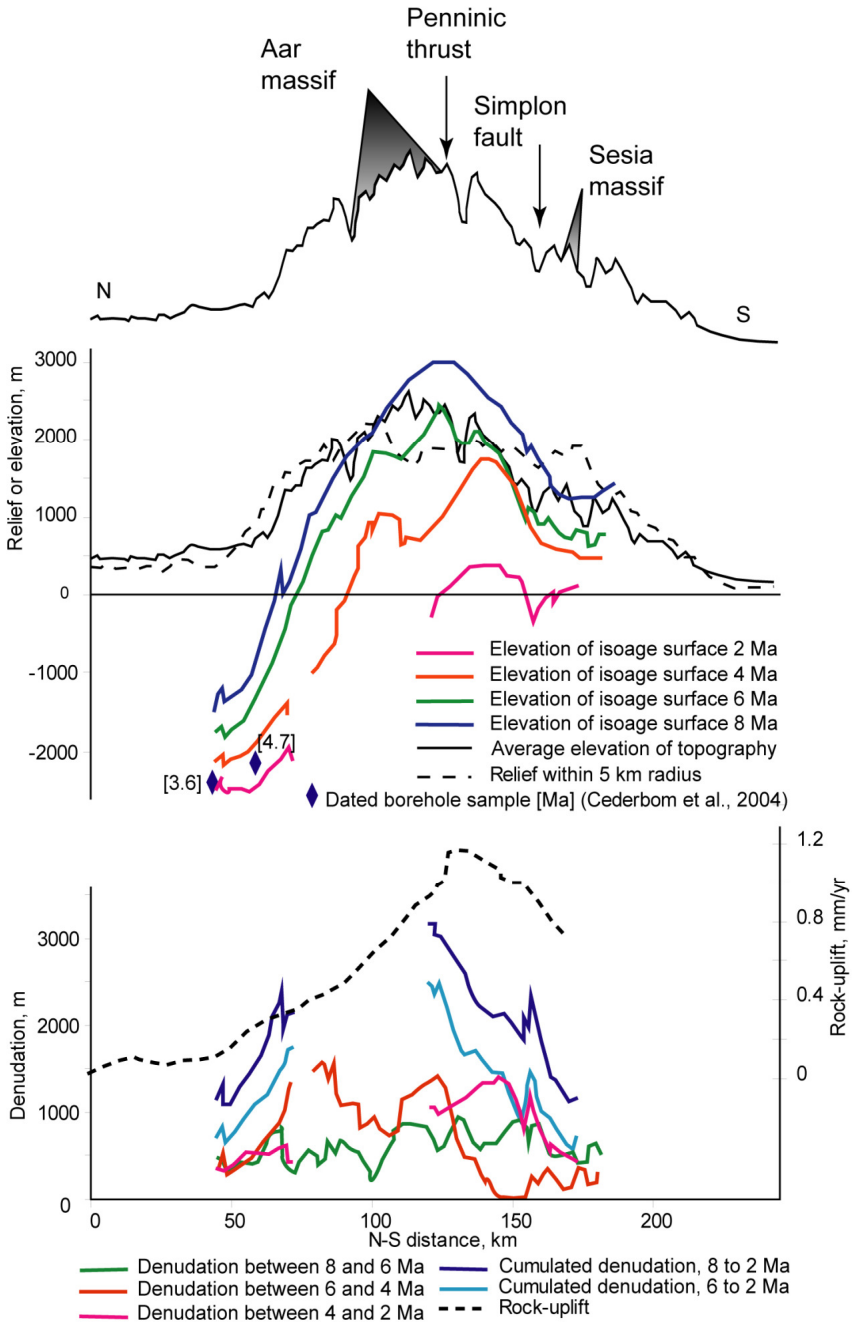

Figure III.3.6. Isoage surface elevation and derived amount of exhumation during the 8-2 Ma time period. The original data is from section II.2.

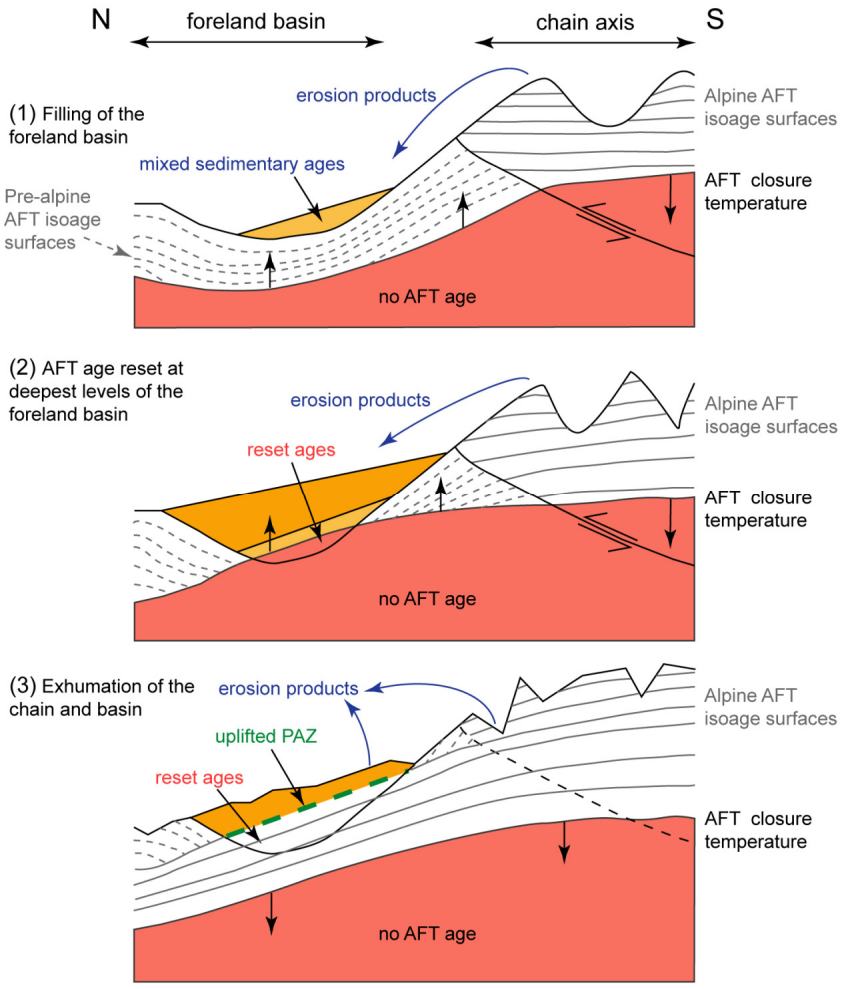

Figure III.3.7. Evolution of AFT isoage surfaces at the orogen scale (viewed in a foreland basin to chain axis section with a strong vertical exageration). (1) At early stages, exhumation takes place in the chain along active thrusts, while the foreland basin is infilled by sedimentation, causing the "tilting" of the surface of AFT closure temperature. Black arrows underline how this surface moves upward relative to a fixed point in the foreland basin, and downward relative to a fixed point under the chain axis. (2) The increase in temperature in the foreland basin sediments triggers the reset of detrital AFT ages at depth, as well as the reset of Pre-alpine AFT isoage surfaces (dashed gray lines). (3) When the convergence rate decreases and the chain is passively exhumed, a paleo-partial annealing zone is exhumed in the basin (dotted green line), with Alpine AFT isoage surfaces present underneath. Above the paleo-partial annealing zone, the AFT ages in the sediments are partially or non reset and therefore AFT isoage surfaces do not exist. The "tilting" of the AFT closure temperature isotherm (used here as an approximation to the partial annealing zone) described in panel (1) explains how Alpine AFT isoage surfaces can erase Pre-alpine ones and thus give the impression of surfaces crossing each other.

III.3.3.2. Simplon section

The second cross-section reported in this chapter is the Simplon section (see location on Figure III.3.3), perpendicular to the Simplon fault. It was constructed by averaging five 206 km long parallel transects separated by 10.5 km along a N-38 °E strike. Its aim is to compare the history of exhumation on both sides of the normal fault which is dipping to the south-west and has been reported to be affected by late Neogene extension (Grosjean et al., 2004).

Figures III.3.8 and III.3.9 compare AFT and ZFT ages with present-day uplift rate. As this transect is more or less superposed to the chain axis, most of the AFT and ZFT ages exhibit alpine cooling ages (i.e. younger than ca. 35 Ma). The elevation of dated samples (Figure III.3.8 and III.3.9) does not vary along the cross-section, demonstrating that the age variation observed along the transect is not controlled by a sampling bias. The patterns of zircon and apatite fission-track ages show a similar trend: older ages in the south-west, and younger ages in the north-east with a concave-up pattern of both AFT and ZFT ages younger than 10 Ma in the vicinity of the Simplon fault (see areas F1 and F2 on Figures III.3.8 and III.3.9 respectively). The record of rock uplift is only available in the north-eastern half of the transect, but is consistent with the age pattern (young fission track ages are observed in regions of high uplift rate). The pattern of AFT ages confirms the hypothesis of Zwingmann and Mancktelow (2004) according to whom K / Ar ages on fault-gauge illite demonstrate that the Simplon fault was still active at ca. 5 Ma. Furthermore, the pattern of uplift rate suggests that the upward flexure of the footwall (the south-western Lepontine Dome), synchronous of extension, is still taking place.

Figure III.3.10 presents a summary of the data available along the Simplon transect to describe long-term exhumation and its potential present-day forcing. Central panel: rock uplift rates are only available in Switzerland, east of the Simplon fault, but do not appear correlated either with seismic energy released or precipitation, as has been described extensively in section III.2. Lowest panel: as already shown in Figures III.3.8 and III.3.9, the patterns of AFT and ZFT ages mirror the present-day uplift-rate, and the area of highest recent exhumation (youngest fission-track ages) corresponds to the vicinity of the Simplon fault. Figure III.3.11 shows a sharp increase from ca. 1000 m of denudation between 8-6 Ma to slightly less than 2000 m between 6 and 4 Ma in the Aar Massif (red curve on lower panel), highlighting a likely increase in denudation rate in this area since 6 Ma.

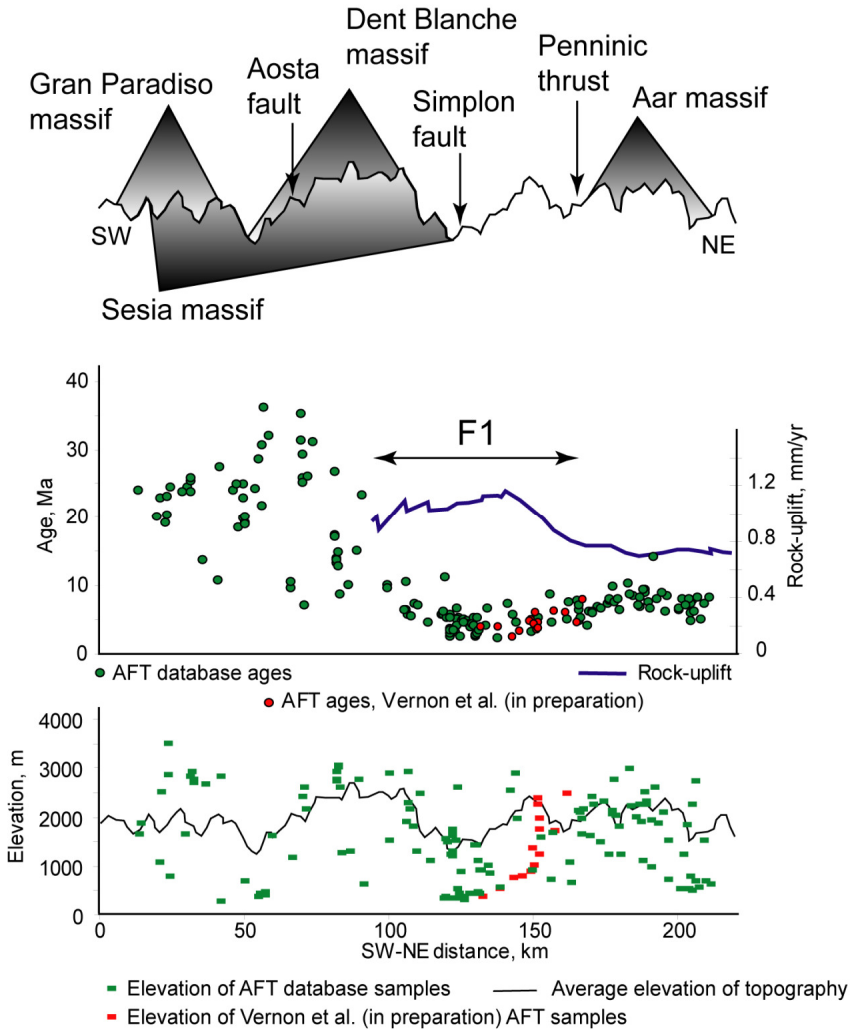

Figure III.3.8. Cross section showing AFT ages over the Simplon fault. "AFT database ages" are described in section II.2., "rock uplift" in section III.2. and "AFT ages, Vernon et al. (in preparation)" in section IV.2. The extent of the "F1" arrow underlines the flexure pattern of AFT ages younger than 10 Ma, which indicates recent differential exhumation in this area. The lower panel presents the elevation of dated samples, superposed on the average topography.

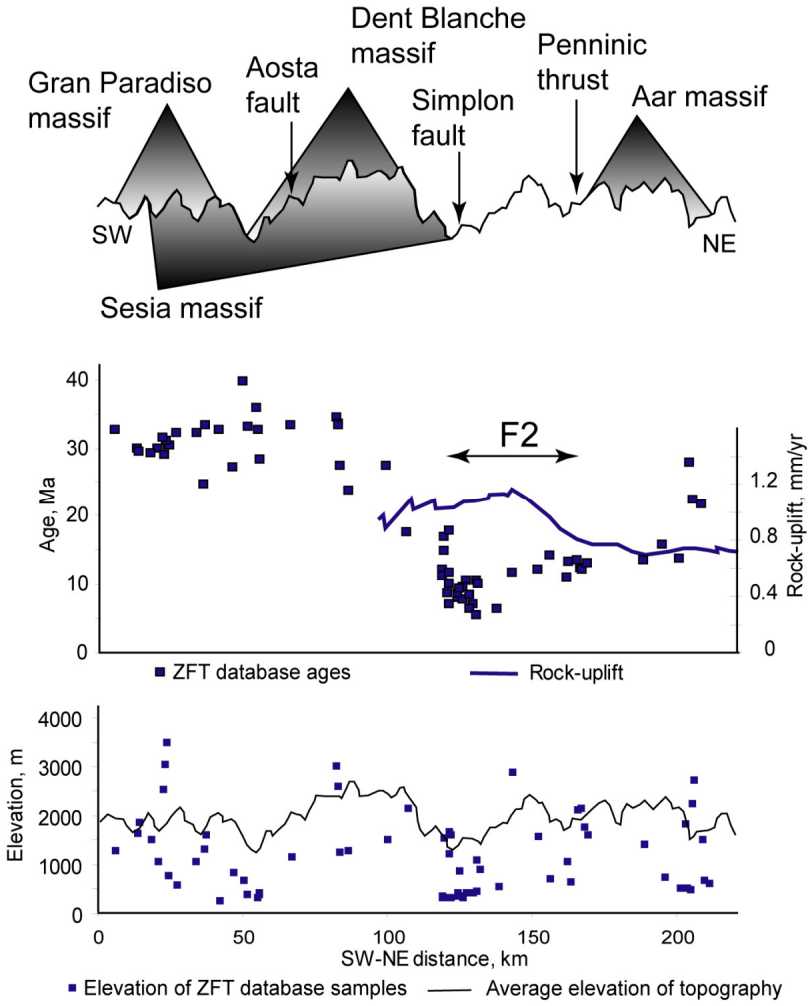

Figure III.3.9. Cross section showing ZFT ages over the Simplon fault. "ZFT database ages" are described in section II.2. and "rock uplift" in section III.2. The extent of the "F2" arrow underlines the flexure of the pattern of ZFT ages younger than 15 Ma, which indicates recent differential exhumation in this area. The lower panel presents the elevation of dated samples, superposed on the average topography.

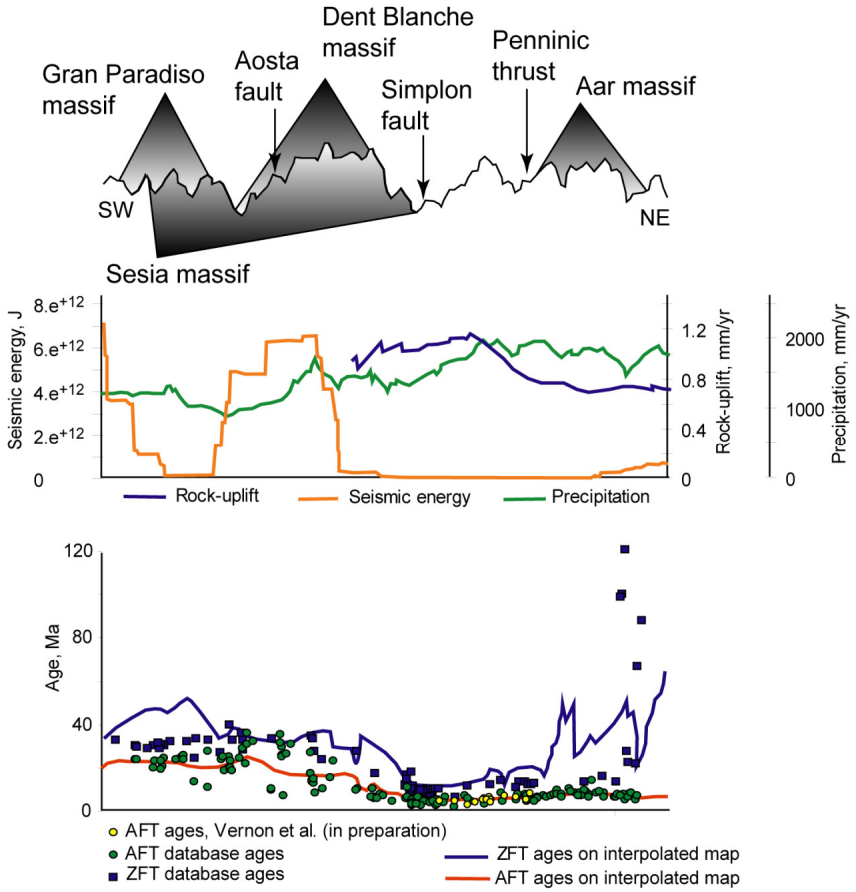

Figure III.3.10. Cross section over the Simplon fault. Rock uplift, seismic energy and precipitation data are described in section III.2. AFT and ZFT databases and interpolated maps are from section II.2. The remaining AFT ages (Vernon et al., in preparation) are from section IV.2.

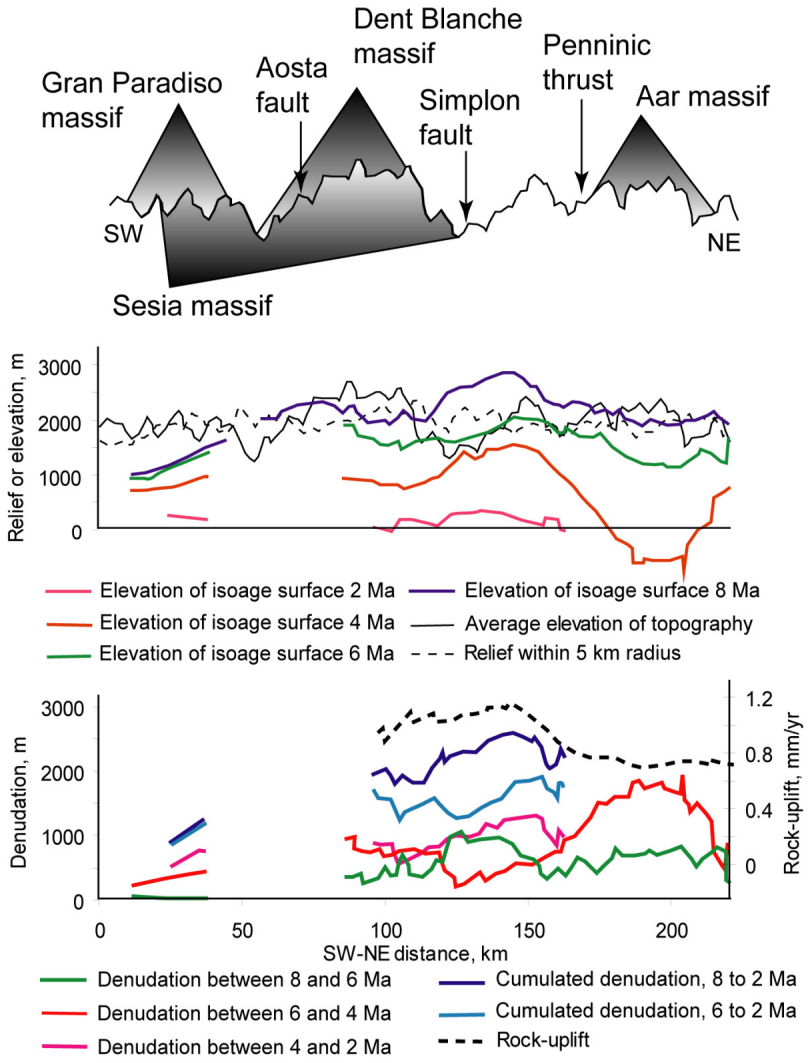

Figure III.3.11. Isoage surfaces elevation and exhumation rates over the Simplon fault. AFT isoage surfaces are from section II.2.5.3.

Chapter IV

Late Neogene exhumation of the central European Alps: low-temperature thermochronology from the Aar Massif (Switzerland) and the Lepontine Dome (Italy)

IV.1. Chapter overview

IV.1.1 Publication

This chapter comprises the material for a paper submitted to *Tectonics* on August 30th 2008.

IV.1.2. Presentation in international meetings

- **April 2008**, European Geological Union Vienna (Austria):

Vernon, A.J., van der Beek, P.A., Sinclair, H.D., Persano, C., Stuart, F.M. Mechanisms of late Neogene exhumation of the Alps: Insights from AFT and AHe vertical profiles in the Aar Massif (Switzerland) and the Lepontine Alps (Italy). *Geophysical Research Abstracts, 10*, SRef-ID: 1607-7962/gra/EGU2008-A-10428.

IV.1.3. Contributors to Chapter IV

François Senebier realized apatite separation from grinded samples. Erika Labrin, Bardhyl Muceku and Cristina Persano taught me the AFT method; Jurgen Foeken and Fin Stuart the He extraction (AHe dating) and Valerie Olive and Cristina Persano the U-Th separation (AHe dating). Valerie Olive realized the ICP-MS quantification of U-Th concentration. Peter van der Beek wrote a Fortran code associating *Pecube* (Braun, 2003) to thermal models of fission-track annealing and helium diffusion. He also provided help in the calculation of the uncertainty of weighted regression lines.

IV.2. Late Neogene exhumation of the central European Alps: low-temperature thermochronology from the Aar Massif (Switzerland) and the Lepontine Dome (Italy)

Antoine J. Vernon[1,2*], Peter A. van der Beek[1], Hugh D. Sinclair[2], Cristina Persano[3], Jurgen Foeken[4], Finlay M. Stuart[4]

[1]L.G.C.A., Maison des Géosciences, Université Joseph Fourier, 38041 Grenoble Cedex, France

[2]Grant Institute, The University of Edinburgh, Edinburgh EH9-3JW, U.K.

[3]Department of Geographical and Earth Sciences, University of Glasgow, Glasgow G12-8QQ, U.K.

[4]Isotope Geosciences Unit, Scottish Universities Environmental Research Centre, East-Kilbride G75-0QF, U.K.

*Corresponding author, vernon.antoine@gmail.com

Abstract

The increase in exhumation rate since 5-4 Ma predicted in the western European Alps from quantification of sediment volumes (Kuhlemann, 2000) and the rebound and denudation of the Swiss Molasse foreland basin (Cederbom et al., 2004), was recently confirmed by a synthetic study of apatite fission track (AFT) ages over the entire Western Alps (Vernon et al., 2008). However, these authors underlined the potential regional variation of this signal in both age of onset and intensity. In order to assess regional differences in exhumation histories that are superimposed on the general trend, we present new apatite fission-track (AFT) and apatite Uranium-Thorium / Helium (AHe) ages from two elevation profiles in the central Aar Massif (Guttannen area, Switzerland) and the western Lepontine Dome (Formazza area, Italy). We describe the evolution of late Neogene exhumation rates firstly by qualitative description of age elevation relationships, and secondly by thermo-chronometric modeling. Based on the 3-D heat-equation solver *Pecube* (Braun, 2003), we predict AFT and AHe ages for a range of tested exhumation histories and pin-point scenarios where predicted ages fit closely to measured ages. A qualitative interpretation of the two sets of AFT and AHe ages suggested a two-phase (9-7 and 5-3 Ma) exhumation scenario affecting the central Alps, with a stronger expression of the Pliocene signal in the Formazza area. The best-fit exhumation scenarios tested with *Pecube* give support to this interpretation, but also highlight the existence of several other likely scenarios. Among the set of 122 scenarios tested in the Formazza area, the two best-fit age prediction models corresponds to either a continuous denudation rate of ca. 0.75 km / Myr with no evidence for relief change, or a one step exhumation rate change from 0.3 to 1 km / Myr at 5 Ma, with decreasing relief. Best predicted

models among the 125 scenarios tested in the Guttannen area occur for two pulses of exhumation (0.3 to 0.7 km / Myr exhumation increase repeatedly at 9-7 and at 5-3 Ma), or a continuous denudation rate of ca. 0.4 km / Myr; both cases with relief increase. The total exhumation for the last 5 Myr calculated using any of these models is significantly lower than the 6.5 km of denudation predicted by Cederbom et al. (2004) in the axial part of the belt. Contingent upon further flexural modeling, the exhumation recorded in the axial region of the Alps since 5 Ma does not appear sufficient to explain the denudation in the Swiss Molasse foreland basin by simple isostatic rebound.

IV.2.1. Introduction

Late Neogene sediment volumes from around the globe record an increase in sediment accumulation rates during Pliocene times (Davies et al., 1977; Zhang et al., 2001; Molnar 2004); this is supported by data from the European Alps (Kuhlemann, 2000). This observation, together with the documented exhumation of the Swiss Molasse foreland basin since ca. 5-4 Ma led Cederbom et al. (2004) and Champagnac et al. (2007) to propose that the bulk of the Alps experienced accelerated exhumation and isostatic rebound since this time. Evidence of tectonic deformation during the same period is not compelling, and therefore a climatic change has been proposed as the driving mechanism for increased erosion rates. Consequently, it is predicted that a denudation signal of Mio-Pliocene age should be present throughout the axial Alpine crystalline massifs. The uniquely dense apatite fission-track (AFT) record in the western European Alps has been used to reconstruct regional isoage AFT surfaces, from which exhumation rates have been derived for the 13.5 to 2.5 Ma period (Vernon et al., 2008). In addition to supporting the hypothesis of accelerated denudation and sedimentation after ~5 Ma, Vernon et al. (2008) indicated a spatial diachroneity in exhumation on a 50-100 km wavelength, with accelerations starting between 6.5 Ma and 2.5 Ma or later. Such heterogeneity would be difficult to explain in terms of simple isostatic rebound on the wavelength of lithospheric support of the topographic load, and so is important to resolve by further analysis.

Here, we test for regional variations in late Neogene exhumation histories along a profile perpendicular to the central Alps using AFT and AHe ages sampled up elevation profiles, linked by horizontal sampling. The sample sites are from the Aar Massif (Guttannen) and the Lepontine Dome (Formazza; Figure IV.2.1).

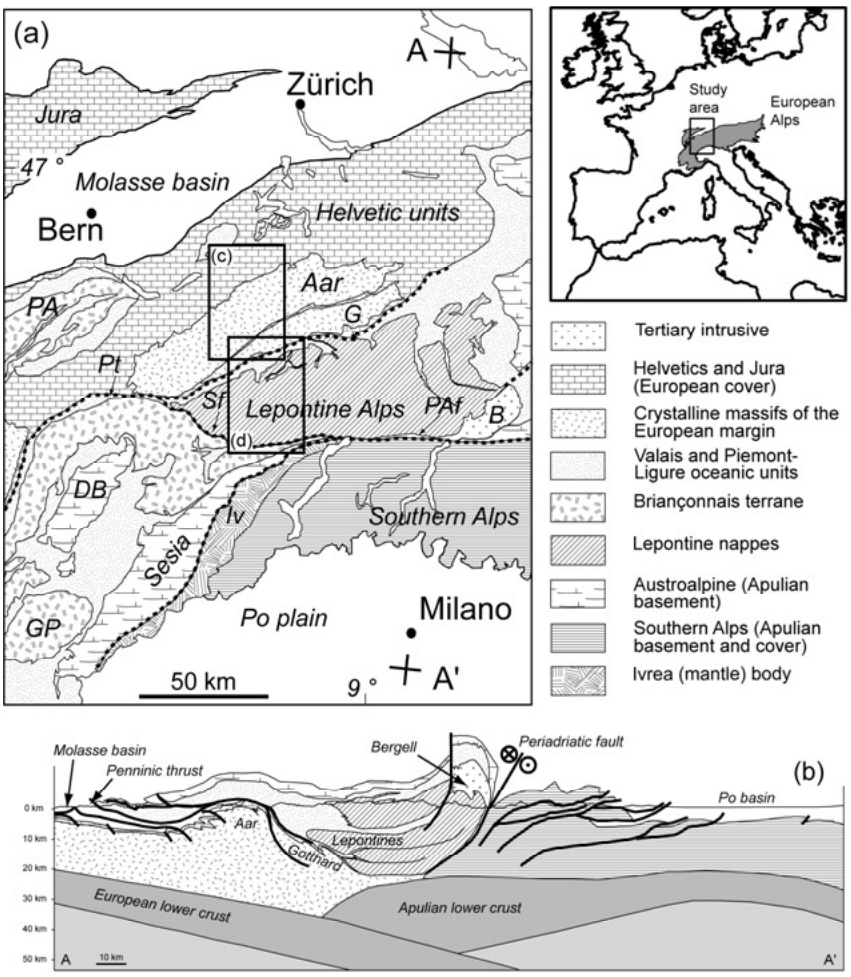

Figure IV.2.1. (a) Simplified geological map of the study area, after Schmid et al., 2004. B: Bergell; DB: Dent Blanche Massif; G: Gotthard Massif; GP: Gran Paradiso Massif; Iv: Ivrea body, PA: Prealps; PAf: Periadriatic fault; Pt: Peninnic thrust; Sf: Simplon fault. (b) Crustal-scale geological cross-section along the NFP20-East seismic line (A-A' in a), showing the relationship between the main geological units (after Schmid et al., 1996). (c) and (d) respectively represent the Guttannen (Switzerland) and the Formazza (Italy) areas used in *Pecube* models.

The profile projects into the mountain belt from the well data of the Swiss Molasse foreland basin studied by Cederbom et al. (2004). These data will rigorously test the hypothesis of a spatially smoothed exhumation history since 5 Ma, as would be predicted for simple isostatic rebound of a dead mountain belt, versus a history of localized exhumation that may be linked to late stages of plate convergence as suggested by Vernon et al. (2008). We test several exhumation scenarios with a numerical model (*Pecube*) capable of exploring the role of evolving thermal and topographic parameters (Braun, 2003) in order to determine sets of conditions that are able to explain measured AFT and AHe ages. The best-fit exhumation histories will be compared to those required by the erosion history of the foreland basin (Cederbom et al., 2004), assuming a simple model of flexural isostatic rebound in response to accelerated erosional unloading of the axial zones.

After describing the sampling, dating methods and results, we consider the effect of apatite U and Th zonation on AHe alpha-ejection corrected ages and propose that it may constitute an explanation for samples where corrected AHe ages are older than AFT ages. We then qualitatively interpret the AFT and AHe data from the elevation profiles in Guttannen and Formazza. Finally, we test the qualitative exhumation scenarios by numerical modeling and propose most likely exhumation histories.

IV.2.2. Geological setting

The study area includes the central Aar Massif (Switzerland) and the western part of the Lepontine Dome (Italy, Switzerland). This area is commonly described as belonging to the Western Alps, as defined by the boundary of the Austroalpine Silvretta unit located to the East of the Lepontine Dome (Kuhlemann, 2000). It is bordered to the North by the Préalpes klippen, Helvetic units and peri-alpine sediments of the Swiss Molasse foreland Basin (Homewood et al., 1986). To the South, the study area is bordered by the Peri-Adriatic line, the Southern Alps units and the Po plain (Schmid et al., 2004; Fantoni et al., 2004). Whereas the Swiss Molasse foreland basin has been exhuming since 5-4 Ma (Cederbom et al., 2004), the Po Basin accumulated post-Messinian sediments lying unconformably over the southernmost South Alpine thrusts (Fantoni et al., 2004; Scardia et al., 2006).

The Aar-Gotthard Massif is one of the alpine external crystalline massifs, belonging to the former European margin. It comprises pre-Variscan and Variscan sub-units of meta-sediments, anatectic migmatites, metasedimentary and granitic gneisses, and volcanoclastic sediments (Abrecht, 1994; von Raumer et al., 1999); these sub-units strike approximately parallel to the Alps. The Massifs have experienced Variscan amphibolite facies metamorphism followed by retrograde metamorphism in greenschist facies (Abrecht, 1994). Alpine strain is recorded in the Aar-Gotthard Massifs by the development of ductile shear fabrics, composed of broadly vertical and N60 degree bearing foliations and associated shear-zones delimiting lenses of less deformed material (Choukroune and Gapais, 1983; Marquer and Gapais, 1985; Marquer and Burkhard, 1992).

The Lepontine Dome records extensive Tertiary amphibolite facies metamorphism, delimited in the south by the Peri-Adriatic line. To the north, metamorphic grade reduces gradually over the Penninic front, and reaches greenschist facies in the Gotthard and the Aar Massifs (Frey and Ferreiro Maehlmann, 1999). The Lepontine Dome is bound to the west and east by two

outward-dipping normal faults, the Simplon and Forcola faults respectively. The structure of the Lepontine area is that of a pile of nappes of gneissic and meta-sedimentary composition, respectively pre-Triassic and Mesozoic in age (Frey and Ferreiro Maehlmann, 1999). The peak of metamorphism post-dates nappe emplacement, as isograds cross-cut structural boundaries (Frey and Ferreiro Maehlmann, 1999).

IV.2.3. Thermochronology dating

IV.2.3.1 Sample collection and preparation

The Aar-Gotthard Massifs and the Lepontine Dome are the sites of many of the earliest alpine apatite fission-track analyses, which provided ages ranging from mid-Miocene to Pliocene (e.g. Wagner and Reimer, 1972; Schär et al., 1975; Hurford, 1986; Michalski and Soom, 1990). However, the early AFT studies that estimated exhumation rates plotted sample elevation against age along transects that either followed the valleys, or that were widely dispersed. In such configurations, the slope of the apparent AER may be severely overestimated or even inverse as a consequence of the fact that the closure temperature isotherms are not horizontal planes (Braun, 2002). This effect is strongest for low-temperature thermochronometers (AHe) in a scenario of steady or reducing relief.

Existing AFT ages were used to locate suitable sampling areas in the Western Alps, where the AFT and AHe ages measured along elevation profiles could be expected to frame the period of suspected change in exhumation dynamics around 5 Ma. Rock samples were collected across a north-south profile between the Aar Massif (upper Aar valley, Switzerland) and the Lepontine Alps (Toce valley, Italy), completed by two altitudinal profiles located in Formazza (Lepontines) and Guttannen (Aar Massif) spanning respectively 1400 and 1800 m of vertical relief (Figure IV.2.2, Table IV.2.1). These altitudinal profiles were sampled perpendicular to the main valley, with the intention of comparing age with elevation on a subset of the database. Careful assessment of the landscape and regional foliations of the sampled exposures ensured that samples were from in place bedrock and not from large deep-seated landslides. A standard sample preparation procedure was applied. Following grinding, apatites were extracted from the 80-250 µm fraction by standard heavy liquid and magnetic techniques[10].

[10] Additional details on sampling can be found in section IV.3.1.

IV.2.3.2 Apatite fission track (AFT) dating

AFT dating was performed following the method described in Tricart et al. (2007). For each sample, 120 apatite crystals were handpicked under binocular lenses and moulded in araldite resin, before being polished and chemically etched for 20 seconds in a 4.5 M HNO_3 solution at 20 °C. A sheet of natural low-U mica used as the induced-track detector was tightly applied against the polished surface before irradiation at the ORPHEE reactor in Saclay (France). NBS-962 dosimeter glasses (National Bureau of Standards, Gaithersburg, MD, USA) with [U] = 12.3 ppm were included in the irradiation batch in order to calculate the neutron fluence. Several mineral standards (Durango and Fish Canyon) were also included in order to calculate a Zeta value (Hurford and Green, 1983). Mica detectors were etched for 40 minutes in a 40 % HF solution at room temperature. A total of 14 Zeta measurements on Durango, Fish Canyon and Mont Dromedary standards from several irradiations in Grenoble and Glasgow Universities were used to calculate a weighted average Zeta value at 325 ± 25[11]. We counted spontaneous and induced tracks using a Zeiss Axioplan Fission Track microscope, under 1250x magnification, with the help of reflected light to distinguish between tracks and crystal dislocations or inclusions. Provided a sufficient number of good quality apatites were present, we counted ca. 20 crystals per sample, some of them without spontaneous tracks.

IV.2.3.3. Apatite Uranium-Thorium / Helium (AHe) dating

AHe dating was performed following the method described in Foeken et al. (2006) on replicates of single apatite grains carefully picked in clove oil to reduce the risk of U-Th or He rich inclusion. The length and width of each crystal was measured under a binocular microscope under a magnification of 258x before packing it closely in a disposable Pt capsule. The Helium content of single grains was extracted by heating at circa 600 °C (based on a Pt color chart) using a 25 W, 808 nm diode laser, for 2 minutes, purified in an ultra-high vacuum line and measured with an electron multiplier in a Hiden HAL3F quadrupole mass spectrometer operated in static mode. Absolute He concentrations were calculated from peak height comparison against a known volume of ^4He injected into the line. The volume of blank He (extracted from empty Pt capsules) was subtracted from each sample measurement. The same laser degassing process was repeated two or three times until reaching blank-level He, unless a continuously high amount of gas extracted suggested the presence of an unnoticed inclusion.

[11] Additional details on AFT age calculation and Zeta value can be found in section IV.3.2.1 and Figure IV.3.2.

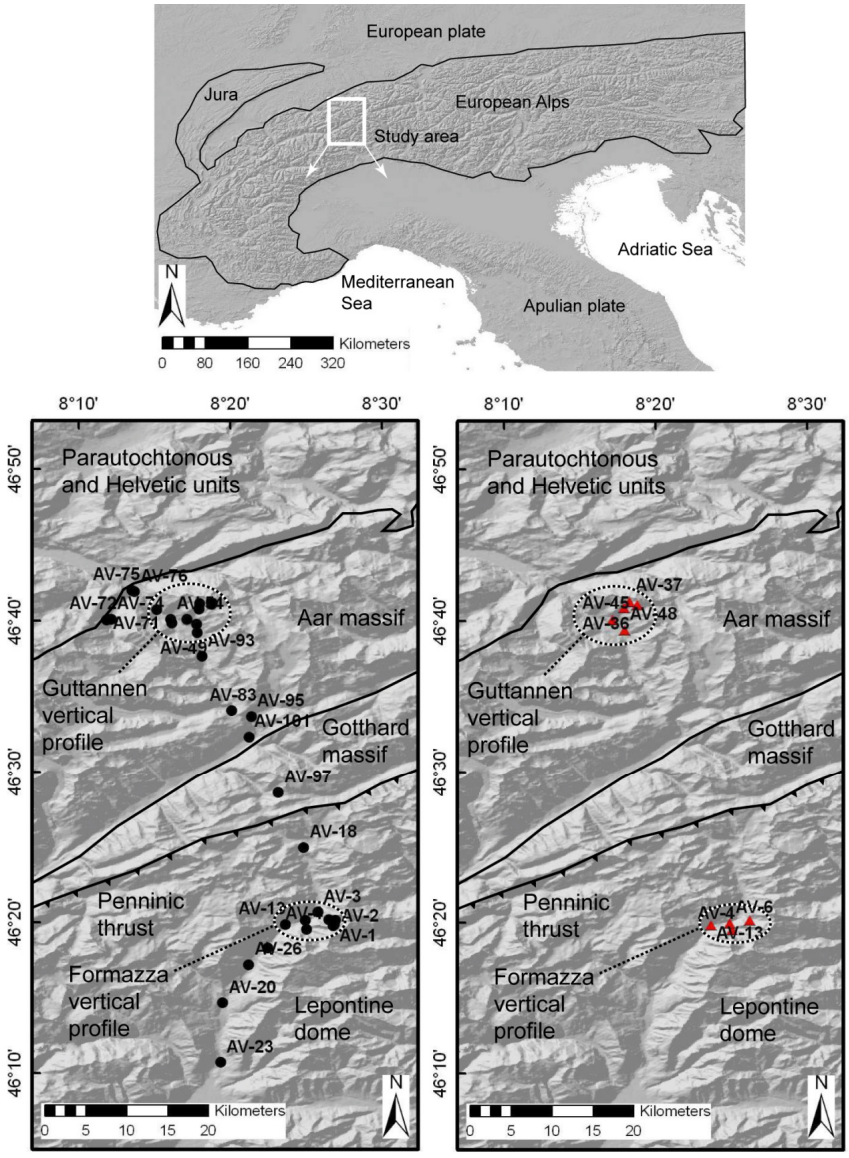

Figure IV.2.2. Map of AFT (left) and AHe (right) sampling.

U and Th were measured by isotopic dilution with inductively coupled plasma mass spectrometry (ICP-MS). An average of 0.15 ± 0.009 ng of ^{230}Th and 0.06 ± 0.003 ng of ^{235}U were added as spike to the dissolving 5 M HNO_3 solution and left overnight at 100 °C. Due to scale instability at the time of measurement, the weight of spike used in the age calculation was approximated by averaging the 120 last measurements in the lab and using the standard deviation of the distribution as the spike weight uncertainty. ICP-MS mass fractionation was accounted for through the repeated measurement of a U-500 standard. Blank measurements of nitric acid and spike were used to correct the measured isotopic ratios. The total amounts of U

and Th were determined using the formula in Evans et al. (2005), and final AHe ages were obtained using the non-iterative formula proposed by Meesters and Dunai (2005).[12]

Name	Latitude	Longitude	Elevation	Location	Lithology
Guttannen area					
AV29	8.314113	46.68528	2800	Furtwangstock	K-Feldspar orthogneiss
AV28	8.313765	46.68393	2720	Furtwangstock	Orthogneiss
AV37	8.305003	46.68782	2460	Wannis lake	Orthogneiss
AV35	8.300052	46.68471	2200	Wannis lake	Orthogneiss
AV36	8.29868	46.68068	2103	Wannis lake	Orthogneiss
AV39	8.299301	46.67865	2000	Wannis lake	Orthogneiss
AV70	8.253222	46.67831	780	Boden	Muscovite granitoid
AV45	8.286386	46.66772	1505	Wysstanni	Orthogneiss
AV47	8.296753	46.66225	1303	Wysstanni	Micaschist
AV48	8.29927	46.65616	1210	Guttannen, Vorses	Biotite orthogneiss
AV49	8.297264	46.65325	1095	Furen	Quartzite, with epidote
AV50	8.269657	46.66335	1000	Boden	Orthogneiss
AV54	8.26842	46.66786	900	Boden	Porphyroid orthogneiss
Formazza area					
AV1	8.447009	46.32905	2400	Fondovalle	Biotite and garnet micaschist
AV10	8.448012	46.33062	2280	Fondovalle	Paragneiss
AV2	8.449394	46.3351	1993	Fondovalle	Micaschist
AV11	8.441943	46.33607	1740	Fondovalle	Porphyroid orthogneiss
AV12	8.437074	46.33611	1625	Fondovalle, Rido	Orthogneiss
AV4	8.4174	46.32549	1365	Foppiano, Alpe Croce	Deformed granitoid
AV3	8.430079	46.34427	1240	Fondovalle dorf	Deformed granitoid
AV6	8.415249	46.33226	1095	Foppiano	Paragneiss
AV14	8.416279	46.33539	1020	Alpe Cneila, new tunnel	Deformed granitoid
AV13	8.394115	46.33064	895	Chioso	Orthogneiss
N-S transect					
AV75	8.225759	46.69964	640	Innertkirchen	Deformed granitoid
AV76	8.228674	46.69782	770	Bim Chapel	Biotite orthogneiss
AV72	8.200137	46.66766	1005	Urbach Tal	Granitoid
AV74	8.203077	46.66764	905	Urbach Tal	Micaschist
AV71	8.198168	46.667	1110	Urbach Tal	Orthogneiss
AV93	8.302725	46.62712	1240	Grimsel, Schwarzbrunnenbrig	Orthogneiss
AV83	8.335357	46.56727	2005	Grimselpass	Porphyroid orthogneiss
AV95	8.357095	46.5608	1790	Gletsch	Porphyroid orthogneiss
AV101	8.354433	46.53833	1405	Oberwald, St Niklaus	Orthogneiss
AV97	8.386597	46.47666	2485	Nufenenpass	Biotite orthogneiss
AV18	8.41447	46.41548	1720	La Frua, Alpe Stafel	Micaschist
AV16	8.375162	46.30471	805	San Rocco	Orthogneiss
AV26	8.354082	46.28621	760	Cadarese	Porphyroid orthogneiss
AV20	8.325497	46.24416	520	Verampio	Granitoid
AV23	8.323134	46.1785	370	Ponte Maglio	Orthogneiss

Table IV.2.1. Sampling details. Samples ranked from north to south in each location.

IV.2.4. Results

IV.2.4.1. AFT ages

AFT central ages were calculated using the software *Trackkey* 4.2g (Dunkl, 2002); the complementary use of the peak-age analysis software *Binomfit* (Brandon, 1992; 1996) enabled the detection of outlier grains that may have an important effect on central age calculations, and so were discarded. These results are reported in Table IV.2.2 and Figure

[12] Additional details on AHe age calculation can be found in section IV.3.3; followed by a series of tests aimed at assessing the quality of the data: volume of Helium obtained in a second heating step (section IV.3.3.1 and Figure IV.3.6), age measured on standard Durango apatite fragments (Figure IV.3.7.a), effect of He volume, U and Th concentrations, Ft correction on the age of single grain replicates (section IV.3.3.2 and Figures IV.3.7.b to IV.3.9), and finally comparison between the ages of single grain replicates dated for each sample (section IV.3.3.3 and Figure IV.3.10).

IV.2.3[13]. In a few instances, binomial-peak fitting performed by *Binomfit* recorded two individual grain age populations, the smallest one accounting for ≥ 30 % of the counted apatites (samples AV01, -54, -70, -75). Among these samples, one is located at the top of the Formazza profile (AV01; Table IV.2.2) and two others at the base of the Guttannen profile (AV54, -70; Table IV.2.2). The last sample in this case, AV75, is located at a lower altitude than the Guttannen elevation profile *sensu stricto*, further down in the valley. All samples are from basement rock having undergone a stage of alpine metamorphism in greenschist or higher facies, which affected most parts of the Aar and Lepontine Massifs (Hunziker et al., 1992; Challandes, 2001). Although these conditions must have reset all low-temperature thermochronometers, the apatite composition in meta-sediments may vary from grain to grain, which affects the closure temperature, thus leading to several groups of grain-ages within a single sample. This effect is stronger in the case of extended stay in the partial annealing zone temperature range. Unfortunately, the overall low numbers of spontaneous tracks in the analysed apatites rendered the quantification of track-length distributions and subsequent modeling of the cooling histories impossible.

AFT ages from samples of the Guttannen and Formazza elevation profiles are plotted in Figures IV.2.4, after discarding the ages with two individual grains age populations. The ages used are either the central age, or the main peak age (P1 age in Table IV.2.2) in case of the presence of a few outlier grains. Error weighted regression lines and 95 % confidence intervals are added on the diagrams, along with the slope of the regression line, which corresponds to the apparent exhumation rate. We performed the age-elevation regression with none of the parameters considered as independent, following the method in Williamson (1968). The errors used for AFT ages are the 1-σ error on central age or main peak age.

Central ages in the Guttannen elevation profile show a positive correlation with elevation (Figure IV.2.4), with ages varying from 6.7 ± 0.6 Ma at 1303 m (AV47) to 8.7 ± 0.8 Ma at 2800 m elevation (AV29). The regression relationship is very steep, with an apparent exhumation rate of 1028 ± 459 m / Myr, based an error-weighted regression calculation with R^2 of 0.43.

[13] Details on the different ways to express average AFT ages, and the use of AFT radial plots are provided in section IV.3.2.2. Radial plots drawn with *Trackkey* 4.2g (Dunkl, 2002) are reported in Figure IV.3.3. A quick assessment of data quality is reported in section IV.3.2.3 and Figure IV.3.4, where the central age is checked against a relationship with the number of grains counted, the mean concentration in uranium, and the 1-σ error on central age is checked against a relationship with the concentration in Uranium.

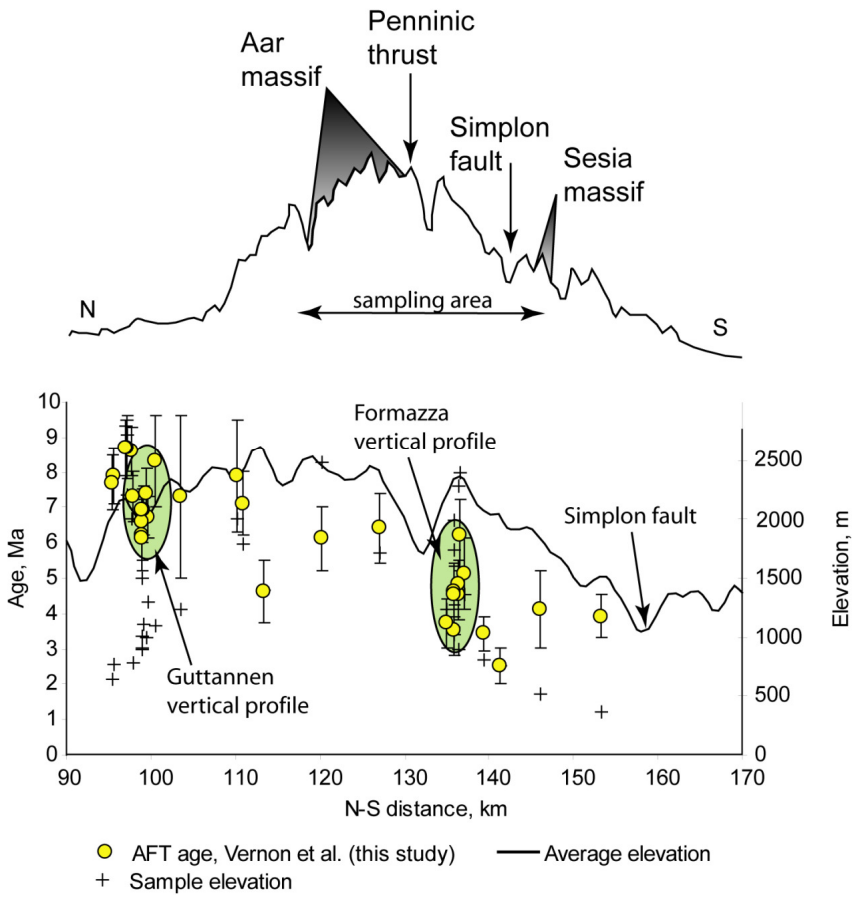

Figure IV.2.3. Longitudinal profile of AFT ages: plot of central AFT ages obtained in this study (Table IV.2.2) on a north-south cross-section joining the Guttannen elevation profile (Switzerland) to the Formazza elevation profile (Italy). Vertical error bars show the 1 σ error on central ages. AFT central ages are sensibly younger on the Formazza elevation profile than on the Guttannen one.

Central ages in the Formazza elevation profile are inversely correlated with elevation (Figure IV.2.4) and vary between 3.5 ± 0.7 (AV11) and 5.1 ± 1.0 (AV4) Ma, i.e.significantly younger than in the Guttannen profile. The relatively ill-constrained AER of 1966 ± 2309 m / Myr remains consistent with apparent positive exhumation rates up to > 350 m / Myr at the 95 % confidence level, however such negative age-elevation relationships can occur when the topographic slope is modified by relief reduction, becomes less steep than the AFT closure surface (Braun, 2002), or when local tilting of the profile has occurred since closure (Rahn and Grasemann, 1999).

A horizontal profile of AFT central ages along a N-S transect (Figure IV.2.3) illustrates a pattern of older ages over the Aar Massif (Guttannen elevation profile) than over the Lepontine Alps (Formazza profile), with ages around 8-7 Ma and 5-4 Ma, respectively. The ages on the horizontal transect are in agreement with existing data from Keller et al (2005) in the western Lepontine Alps or Schär et al. (1975) and Rahn and Grasemann (1999) in the

north-eastern Aar and Gotthard Massifs. AFT ages published by Michalski and Soom (1990) for the upper Aar valley upstream and downstream of our elevation profile (12 ± 0.9 Ma at 720 m, 4.2 ± 1.1 Ma at 1586 m and 5.3 ± 1.1 Ma at 2160 m) differ significantly from our measurements; however part of the difference may be explained by the very low number of spontaneous tracks counted in both studies, and by the lack of good-quality apatites.

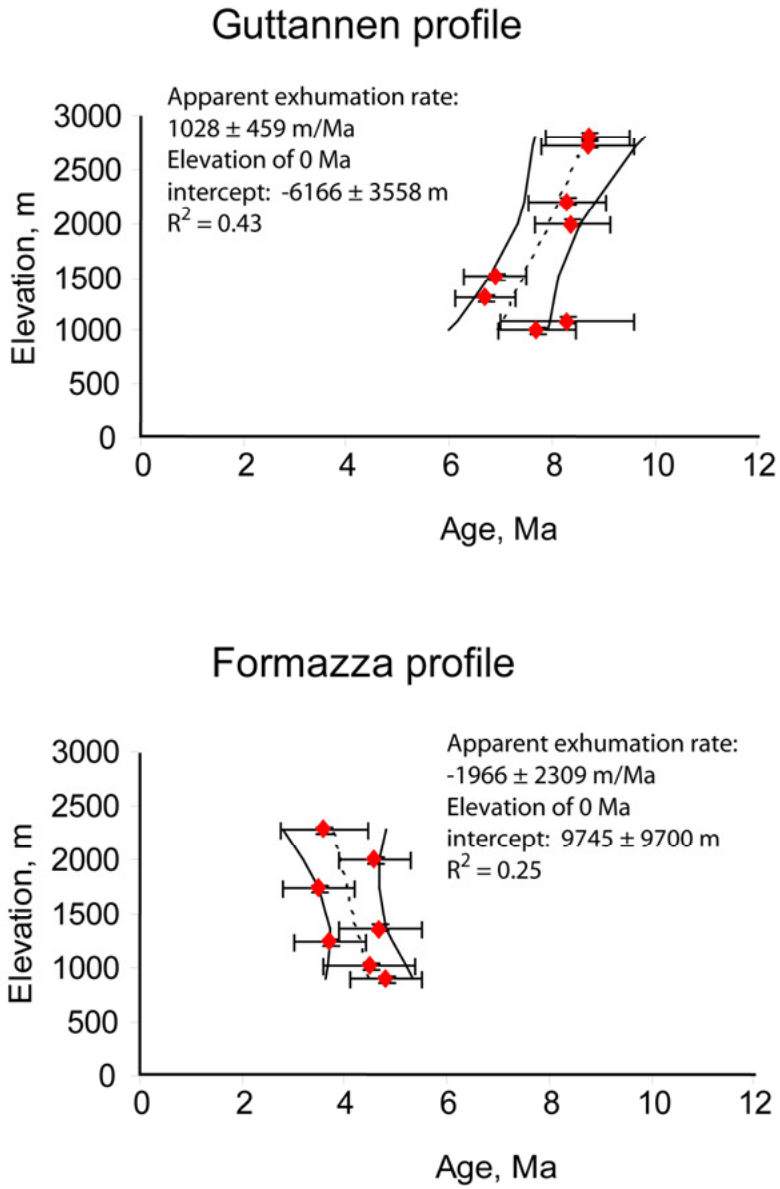

Figure IV.2.4. AFT age-elevation profiles and weighted regression relationship (dashed line: regression line; bold lines: 95% confidence interval) for the Guttannen and Formazza areas. Central ages or main age-peak of the AFT age population are plotted, excluding samples with a second age-peak population comprising more than 30% of the grains counted (AV1, AV54 and AV70).

Name	N	ρs	*Ns*	ρi	*Ni*	ρd	Nd	P (χ^{2}) (%)	D (%)	**C age**	1 σ	**P1 age**	1 σ	P1 %	**P2 age**	1 σ	P2 %	[U]	Δ[U]
Guttannen section																			
AV29	22	3.244	*463*	31.933	*4558*	5.302	9317	68.6	0	**8.7**	0.8	**8.7**	0.8	100				74	29
AV28	22	1.348	*246*	13.89	*2534*	5.492	7546	58.2	6	**8.7**	0.9	**8.7**	0.85	100				33	61
AV35	22	4.793	*919*	49.493	*9490*	5.491	7546	0.2	16	**8.7**	0.8	**8.3**	0.75	93.2	**14.6**	4.1	6.8	112	31
AV39	22	5.03	*937*	51.888	*9666*	5.491	7546	17.3	7	**8.6**	0.7	**8.4**	0.75	93.3	**12.9**	3.1	.7	116	18
AV45	21	4.442	*586*	54.968	*7252*	5.24	7463	72.1	0	**6.9**	0.6	**6.9**	0.6	100				129	22
AV47	22	3.974	*438*	52.6	*5797*	5.49	7546	65.9	0	**6.7**	0.6	**6.7**	0.65	100				118	23
AV49	7	1.211	*63*	13.057	*679*	5.49	7546	81.4	0	**8.3**	1.3	**8.3**	1.3	100				29	27
AV50	22	3.895	*511*	49.664	*6515*	5.81	9647	51.6	8	**7.4**	0.7	**7.7**	0.75	93.3	**4.7**	1.25	6.7	103	28
AV54§	21	2.777	*320*	41.444	*4776*	5.489	7546	3.7	18	**6.1**	0.6	**7.1**	1.2	61	**4.7**	1	39	91	25
AV70§	19	4.376	*465*	54.559	*5797*	5.489	7546	4.6	16	**7.3**	0.7	**8.2**	0.95	70	**5.4**	0.85	30	123	42
Formazza section																			
AV1§	23	0.479	*68*	6.749	*959*	5.31	9317	19.3	30	**6.2**	1	**7.7**	2.15	69.4	**3.2**	2.1	30.6	16	31
AV10	22	0.448	*66*	9.075	*1338*	5.495	7546	16.3	28	**4.5**	0.7	**3.6**	0.85	80.5	**8.4**	4.3	19.5	21	56
AV2	21	0.425	*60*	8.332	*1175*	5.496	7546	53.0	3	**4.6**	0.7	**4.6**	0.7	100				18	38
AV11	16	0.42	*32*	11.223	*855*	5.813	9647	65.1	11	**3.5**	0.7	**3.5**	0.7	100				23	63
AV4	21	0.373	*55*	6.624	*976*	5.496	7546	0.2	50	**5.1**	1	**4.7**	0.8	95.5	**46.9**	40.95	4.5	14	65
AV3	20	0.335	*42*	8.02	*1004*	5.496	7546	65.7	2	**3.7**	0.7	**3.7**	0.65	100				17	41
AV14	20	0.381	*34*	8.012	*715*	5.812	9647	66.2	3	**4.5**	0.9	**4.5**	0.9	100				17	42
AV13	21	0.413	*59*	7.632	*1091*	5.495	7546	76.1	0	**4.8**	0.7	**4.8**	0.75	100				18	46
N-S transect																			
AV75§	20	1.847	*316*	22.656	*3876*	5.81	9647	13.3	15	**7.7**	0.8	**6.8**	1.1	67.1	**9.6**	2.25	32.9	48	21
AV76	20	5.291	*655*	57.577	*7128*	5.27	7463	0.1	9	**7.9**	0.8	**7.6**	0.7	80.1	**11.9**	1.75	14.7	133	36
AV72	6	2.307	*59*	31.83	*814*	5.286	7463	30.9	6	**6.2**	1	**6.2**	0.95	100				71	36
AV74	21	2.162	*322*	30.696	*4572*	5.81	9647	57.4	2	**6.6**	0.6	**6.6**	0.65	100				65	25
AV71	19	3.632	*368*	44.824	*4542*	5.278	9317	45.6	4	**6.9**	0.7	**6.8**	0.7	94	**10.3**	4.7	6	113	43
AV93	6	0.443	*12*	5.245	*142*	5.317	7463	52.3	0	**7.3**	2.3	**7.3**	2.3	100				12	38
AV83	10	0.656	*33*	7.139	*359*	5.301	7463	95.8	0	**7.9**	1.6	**7.9**	1.55	100				20	70
AV95	17	1.123	*102*	14.85	*1349*	5.811	9647	72.4	2	**7.1**	0.9	**7.1**	0.95	100				31	47
AV101	15	2.76	*88*	55.479	*1769*	5.378	7463	0.3	49	**4.6**	0.9	**3.6**	0.65	86	**11**	4.05	14	112	59
AV97	25	0.413	*77*	5.867	*1093*	5.332	7463	6.7	6	**6.1**	0.9	**6**	1	97.9	**20.7**	58	2.1	13	48
AV18	20	0.442	*58*	6.157	*807*	5.494	7546	58.8	0	**6.4**	1	**6.4**	1	100				13	64
AV16	17	0.491	*62*	12.854	*1623*	5.494	7546	94.2	0	**3.4**	0.5	**3.4**	0.55	100				28	50
AV26	23	0.188	*29*	6.785	*1049*	5.492	7546	7.0	37	**2.5**	0.5	**3.1**	1	79.9	**0.3**	9.2	20.1	15	54
AV20	21	0.123	*21*	2.622	*446*	5.493	7546	45.0	51	**4.1**	1.1	**3**	1.1	85.8	**10.2**	6.55	14.2	6	72
AV23	25	0.235	*57*	5.435	*1320*	5.492	7546	81.0	2	**3.9**	0.6	**3.9**	3.9	100				12	34

Table IV.2.2. AFT dating results. Name §: sample with suspected double-peak age. N: number of apatite grains counted; ρs: density of spontaneous tracks (10^6 cm^{-2}); Ns: number of spontaneous tracks; ρi: density of induced tracks (10^6 cm^{-2}); Ni: number of induced tracks; ρd: density of tracks on irradiation fluence dosimeters (10^6 cm^{-2}); Nd: number of tracks counted on irradiation fluence dosimeters; P(χ^2) (%):probability that the single grain ages represent one population; D (%): age dispersion; C-age: Central Age; 1 σ: error on central age; P1 age: major age component in grain-age peak analysis; P1%: percentage of total number of grains in main age-peak; P2 age: minor age component in grain-age peak analysis; P2%: percentage of total number of grains in minor age-peak; [U]: Uranium concentration in ppm; Δ[U]: uncertainty on Uranium concentration, %. Samples are ranked in decreasing elevation order within the first two sections of the table, and from north to south in the last section.

IV.2.4.2. AHe ages

IV.2.4.2.1. Criteria of selection among replicates

The results for the three to five crystals (replicates) dated individually for each sample are reported in Table IV.2.3. However, we discarded results of several replicates (see details in legend of Table IV.2.3) prior to the calculation of average ages using the relative error (analytical error / age) as weight (Figure IV.2.5).

In our study, analytical errors of around 8 % are larger than usually reported, due to the relatively high uncertainty in the weight of U and Th spike added before the quantification of these elements. The errors on AHe ages used in the rest of this study are either the average analytical error on replicates, or the weighted 1-σ value, whichever is largest. Four Durango standard apatite fragments were dated in order to assess the reliability of the dating process, and all but one are within the age range (31.1 to 33.4 Ma) accepted by Boyce and Hodges (2005).

The age-elevation relationship of un-corrected AHe ages in the Guttannen and the Formazza elevation profiles are presented in Figure IV.2.6 with the same method of regression line calculation as described in section IV.2.4.1. The Guttannen profile displays a strongly correlated relationship with elevation (R^2 = 0.88) with weighted average ages ranging from 5.2 ± 0.5 Ma at 1505 m elevation (AV45) to 9.0 ± 1.3 Ma at 2720 m (AV28), and an apparent exhumation rate of 486 ± 135 m / Myr (Figure IV.2.6). In Formazza, the age-elevation relationship is steeper (apparent exhumation rate of 675 ± 539 m / Myr) but less well constrained (R^2 = 0.5). Weighted average AHe ages are also younger, ranging from 2.6 ± 0.2 at 895 m elevation (AV13) to 5.2 ± 2.5 Ma at 1625 m (AV12).

IV.2.4.2.2. Alpha-ejection correction

In samples with U and Th homogeneously scattered in the grain, a significant amount of He is lost by radioactive decay of atoms situated close to the crystal border. The proportion of He loss out of the crystal during the emission of alpha particles decreases from 50 % on the grain surface to zero when the emission point is located more than 20 µm from the surface (Farley et al., 1996, Farley, 2002). A correction factor (Ft) based on crystal shape and Th / U ratio therefore needs to be applied to un-zoned grains following the method in Farley (2002) in order to make up for the lost He and avoid age underestimation. However, the determination of the grain surface / volume ratio is imprecise and the error on the correction factor Ft is particularly important for small grains (Farley et al., 1996).

Name-§	^{232}Th	1 σ	^{238}U	1 σ	^{4}He	1 σ	TA err	*Raw age*	*Raw err*	L	W	Tr	Ft	*Corr age*	*Corr err*	#
Guttannen section																
AV28-1	0.035	0.002	0.106	0.006	1.15 E-10	6.15 E-13	8.6	*8.3*	*0.7*	235	150	2	0.81	*10.3*	*0.9*	**a**
AV28-2	0.022	0.002	0.124	0.007	2.38 E-10	1.30 E-12	8.7	*15.1*	*1.3*	245	135	2	0.79	*19*	*1.7*	**a, b**
AV28-3	0.071	0.005	0.116	0.007	1.23 E-10	4.74 E-13	8.5	*7.6*	*0.7*	200	160	1	0.82	*9.3*	*0.8*	
AV28-4	0.019	0.001	0.111	0.007	1.21 E-10	4.57 E-13	9.1	*8.6*	*0.8*	225	145	1	0.81	*10.6*	*1*	
AV28-5	0.024	0.002	0.110	0.006	1.51 E-10	5.94 E-13	8.5	*10.7*	*0.9*	225	150	2	0.80	*13.3*	*1.1*	
Weighted age AV28								**9.0**	**1.3**					**11.1**	**1.7**	
AV37-1	0.024	0.002	0.468	0.026	4.99 E-10	1.85 E-12	8.8	*8.7*	*0.8*	185	175	0	0.84	*10.3*	*0.9*	
AV37-2	0.007	0.001	0.199	0.011	1.87 E-10	7.09 E-13	9.4	*7.7*	*0.7*	200	150	1	0.82	*9.4*	*0.9*	
AV37-3	0.038	0.002	0.168	0.009	1.57 E-10	5.85 E-13	8.3	*7.3*	*0.6*	195	135	2	0.78	*9.4*	*0.8*	
AV37-4	0.013	0.001	0.252	0.016	2.64 E-10	1.02 E-12	9.5	*8.5*	*0.8*	220	155	1	0.82	*10.3*	*1*	
Weighted age AV37								**8.0**	**0.7**					**9.8**	**0.9**	
AV36-1	0.048	0.003	0.102	0.006	1.05 E-10	4.57 E-13	8.6	*7.6*	*0.7*	265	125	2	0.78	*9.8*	*0.8*	
AV36-2	0.047	0.003	0.059	0.004	5.38 E-11	2.15 E-13	9.5	*6.3*	*0.6*	140	65	1	0.62	*10.2*	*1*	
AV36-3	0.026	0.002	0.073	0.005	6.75 E-11	2.69 E-13	9.3	*7.0*	*0.7*	170	125	2	0.76	*9.2*	*0.9*	
AV36-4	0.040	0.002	0.056	0.003	5.64 E-11	2.25 E-13	8.3	*7.1*	*0.6*	160	130	2	0.76	*9.3*	*0.8*	
AV36-5	0.140	0.008	0.109	0.006	3.27 E-10	1.31 E-12	8.2	*18.9*	*1.6*	215	130	2	0.78	*24.4*	*2*	**b**
Weighted age AV36								**7.1**	**0.6**					**9.6**	**0.9**	
AV45-1	0.009	0.001	0.228	0.013	1.39 E-10	5.55 E-13	8.8	*5.0*	*0.4*	155	105	2	0.73	*6.8*	*0.6*	
AV45-2	0.013	0.001	0.259	0.015	1.70 E-10	7.41 E-13	10.0	*5.3*	*0.5*	150	100	1	0.74	*7.2*	*0.7*	
AV45-3	0.010	0.001	0.213	0.011	1.26 E-10	5.59 E-13	9.1	*4.8*	*0.4*	215	70	0	0.67	*7.2*	*0.7*	
AV45-4	0.013	0.001	0.182	0.010	1.03 E-10	4.55 E-13	9.9	*4.6*	*0.5*	150	75	0	0.68	*6.7*	*0.7*	
AV45-5	0.018	0.001	0.256	0.014	1.92 E-10	7.57 E-13	9.1	*6.1*	*0.6*	175	100	1	0.74	*8.2*	*0.7*	
Weighted age AV45								**5.2**	**0.5**					**7.2**	**0.7**	
AV48-1	0.016	0.001	1.086	0.058	8.48 E-10	3.18 E-12	9.1	*6.4*	*0.6*	200	150	2	0.80	*8*	*0.7*	
AV48-2	0.007	0.001	0.664	0.035	4.59 E-10	1.80 E-12	8.8	*5.7*	*0.5*	185	125	2	0.77	*7.4*	*0.7*	
AV48-3	0.006	0.000	0.407	0.023	2.68 E-10	1.07 E-12	9.0	*5.4*	*0.5*	190	125	1	0.79	*6.9*	*0.6*	
AV48-4	0.011	0.001	0.870	0.050	6.56 E-10	2.61 E-12	9.3	*6.2*	*0.6*	210	170	0	0.84	*7.3*	*0.7*	
AV48-5	0.026	0.002	0.312	0.018	1.63 E-10	6.51 E-13	8.9	*4.2*	*0.4*	190	155	1	0.82	*5.1*	*0.5*	
Weighted age AV48								**5.9**	**0.5**					**7.4**	**0.7**	
Formazza section																
AV12-1	0.016	0.001	0.275	0.016	5.72 E-12	2.64 E-14	8.7	*0.2*	*0.0*	240	150	2	0.81	*0.2*	*0*	**b**
AV12-2	0.005	0.000	0.005	0.001	9.73 E-13	4.49 E-15	15.2	*1.2*	*0.2*	180	100	2	0.72	*1.7*	*0.3*	**c, d**
AV12-3	0.000	0.000	0.005	0.001	4.82 E-12	2.22 E-14	32.1	*7.4*	*2.4*	225	140	2	0.80	*9.3*	*3*	**d**
AV12-4	0.032	0.002	0.033	0.002	1.47 E-11	7.02 E-14	10.0	*3.0*	*0.3*	220	150	1	0.81	*3.7*	*0.4*	
AV12-5	0.013	0.001	0.014	0.001	1.67 E-11	6.80 E-14	11.2	*8.0*	*0.9*	165	110	1	0.75	*10.6*	*1.2*	
Weighted age AV12								**5.2**	**2.4**					**6.7**	**3.4**	
AV4-1	0.121	0.007	0.108	0.007	5.84 E-11	2.68 E-13	8.6	*3.5*	*0.3*	160	115	1	0.76	*4.6*	*0.4*	
AV4-2	0.042	0.003	0.049	0.003	2.23 E-11	1.02 E-13	9.6	*3.1*	*0.3*	260	185	2	0.84	*3.8*	*0.4*	
AV4-3	0.054	0.004	0.054	0.003	2.01 E-11	9.23 E-14	8.7	*2.5*	*0.2*	235	155	2	0.81	*3.1*	*0.3*	
AV4-4	0.024	0.002	0.018	0.001	7.47 E-12	3.46 E-14	9.0	*2.6*	*0.2*	200	160	2	0.80	*3.2*	*0.3*	
AV4-5	0.031	0.002	0.030	0.002	1.74 E-11	8.05 E-14	9.2	*3.9*	*0.4*	275	175	1	0.84	*4.6*	*0.4*	
Weighted age AV4								**3.1**	**0.5**					**3.9**	**0.7**	
AV6-1	0.094	0.006	0.039	0.002	3.38 E-11	1.54 E-13	9.0	*4.6*	*0.4*	200	120	1	0.77	*6*	*0.5*	
AV6-2	0.044	0.003	0.039	0.002	1.57 E-11	7.22 E-14	9.1	*2.6*	*0.2*	205	165	2	0.81	*3.3*	*0.3*	
AV6-3	0.055	0.004	0.045	0.003	4.10 E-11	1.87 E-13	9.6	*5.8*	*0.6*	230	150	2	0.80	*7.3*	*0.7*	
Weighted age AV6								**4.3**	**1.3**					**5.4**	**1.7**	
AV13-1	0.039	0.003	0.021	0.001	9.66 E-12	4.43 E-14	9.7	*2.6*	*0.3*	195	175	0	0.84	*3.1*	*0.3*	
AV13-2	0.002	0.000	0.001	0.000	2.52 E-13	1.16 E-15	23.1	*1.1*	*0.2*	250	105	0	0.76	*1.4*	*0.3*	**c, d**
AV13-3	0.028	0.002	0.010	0.001	2.86 E-11	8.58 E-14	8.9	*14.5*	*1.3*	240	165	0	0.83	*17.4*	*1.6*	**a, d**
AV13-4	0.129	0.008	0.068	0.004	3.09 E-11	1.41 E-13	8.9	*2.6*	*0.2*	260	85	2	0.69	*3.7*	*0.3*	
Weighted age AV13								**2.6**	**0.2**					**3.4**	**0.3**	

Table IV.2.3. AHe dating results. Name-§: sample name (replicate §); ^{232}Th, ^{238}U: mass of Th and U in the grain (ng); ^{4}He: volume of He extracted, in standard laboratory conditions (cc); TA err: Total Analytical Error (%); Raw age: grain age before applying the FT alpha-ejection correction factor (Ma); Raw err: analytical error (Ma) on raw age; L and W: length and width of crystal, µm; Tr: number of intact crystal terminations; Ft: alpha correction factor (Reiners, 2002); Corr age: grain age after applying the Ft alpha ejection correction factor (Ma); Corr err: analytical error (Ma), on corrected age; #: reason for discarding the replicate before error-weighted age calculation. These reasons include: (a) He extraction at second heating amounting to more than 5 % of the extraction at first heating (suggesting the presence of He rich inclusion), (b) very high [U] concentration (suggesting the presence of a U-rich inclusion) and / or absurd replicate age (such as 0.2 Ma or 20 Ma in samples otherwise dated ca. 5 Ma), (c) blank-level He extraction at first heating, (d) ICP-MS counting of isotopic counts per second smaller than our limit of quantification (10 times the number of counts per second measured with ultra-pure 5 M HNO_3 blank); Weighted ages (calculated using the non-discarded replicates): analytical error-weighted raw or corrected age (Ma); followed by the weighted standard deviation or average analytical error, whichever highest, on weighted raw or corrected age (Ma). Samples are ranked in decreasing elevation order within the first two sections of the table, and from north to south in the last section.

Name-§	^{232}Th	1 σ	^{238}U	1 σ	^{4}He	1 σ	TA err	*Raw age*	*Raw err*	L	W	Tr	Ft	*Corr age*	*Corr err*	#
Durango standards																
DU-1	3.469	0.209	0.187	0.010	3.95 E-09	1.75 E-11	8.0	**32.3**	**2.6**							
DU-2	3.222	0.691	0.158	0.010	3.32 E-09	1.34 E-11	22.3	**29.8**	**6.6**							
DU-3	1.736	0.103	0.096	0.005	2.01 E-09	9.27 E-12	8.0	**32.7**	**2.6**							
DU-4	3.248	0.196	0.180	0.010	3.81 E-09	1.57 E-11	8.2	**33.1**	**2.7**							

Table IV.2.3. (Continued for Durango standard).

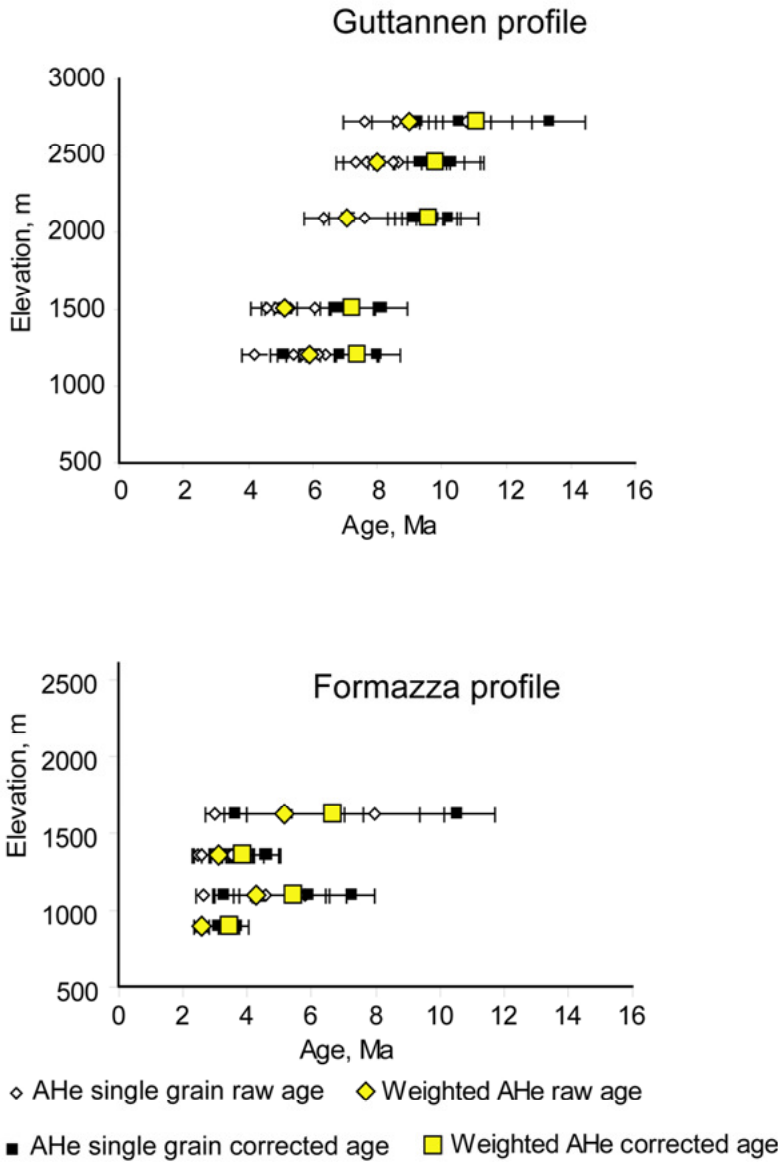

Figure IV.2.5. Single grain and error-weighted AHe ages in the Guttannen and the Formazza elevation profiles. Alpha-ejection corrected ages are illustrated with a square symbol.

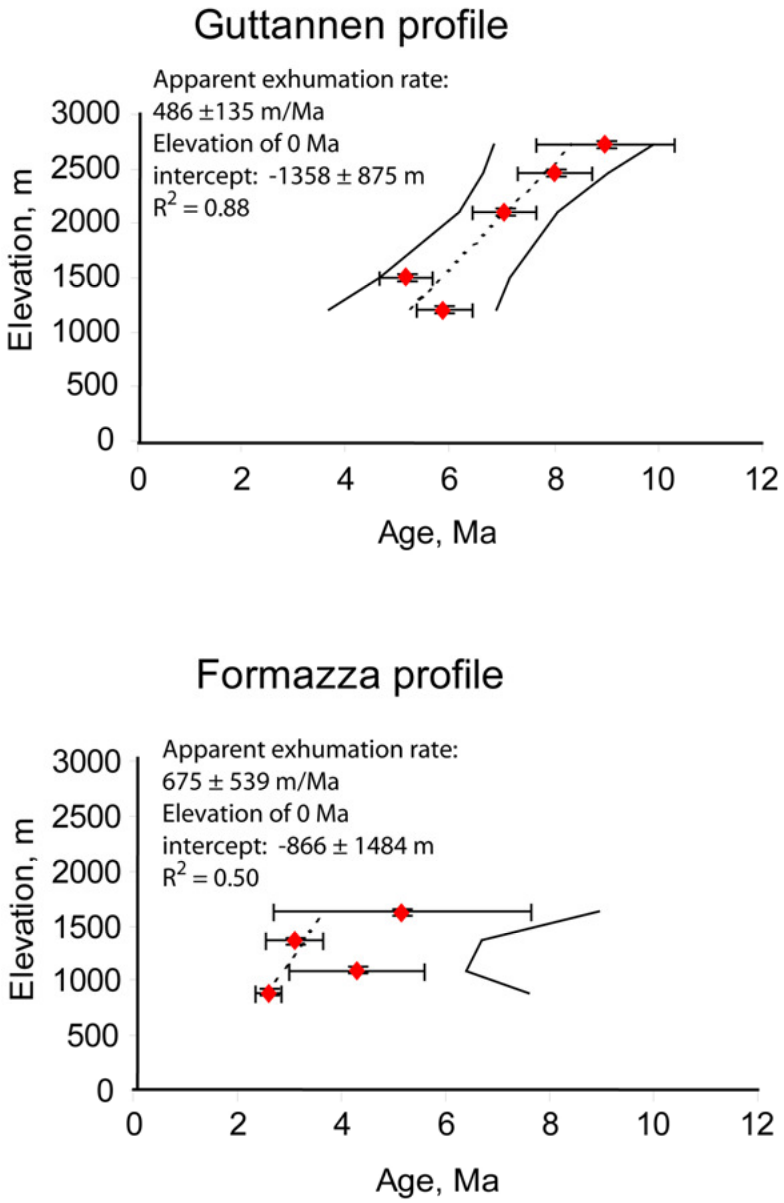

Figure IV.2.6. AHe age-elevation profiles and weighted regression relationship (dashed line: regression line; bold lines: 95% confidence interval) for the Guttannen and the Formazza areas. Non alpha-ejection corrected AHe ages are used.

IV.2.4.3. Modeling the role of apatite zoning on AHe age

The distinctive closure temperatures usually considered for the AFT and AHe thermochronometers (120-90 °C and 80-55 °C respectively; Reiners et al., 2005), lead us to expect AFT ages to be older than AHe ages at a given location. However, several of our corrected AHe ages overlap or are older than the AFT ages of the same samples (e.g. AV28 and AV45), or samples located at similar elevations on an elevation profile (cf. Figure IV.2.7). Various factors such as the underestimation of fission-track annealing (e.g. Hendricks and Redfield, 2005), or the overestimation of He diffusion associated with radiation damage (Green et al., 2006, Shuster et al., 2006) may explain age overlap, particularly in U-rich or old samples. Neither condition, however, is met by our samples. An alternative explanation could be the over-correction of AHe ages by the Ft alpha-ejection parameter in case of strong U and Th apatite zoning (Boyce and Hodges, 2005, Hourigan et al., 2005). The amount of correction applied to a crystal can be underestimated if U and Th are more concentrated at the rim (external zoning), or overestimated if the core is more concentrated (internal zoning). Additionally, the Ft correction assumes that the minerals surrounding the apatite grain are devoid of U and Th, whereas in natural rocks several minerals, such as micas, have U and Th concentrations equal or larger than apatite, which may lead to He-implantation in the outer 20 µm of the grain (Spencer et al., 2004).

A strong zoning in track density was observed in most of the polished sections of apatite grains for several AFT samples. For instance, samples AV4 and AV13 (see Table IV.2.2) strikingly displayed prints of induced tracks smaller than the crystal size, suggesting an internal zoning (U+Th more concentrated in the core than the rim of the apatites). In these conditions, the real age of a crystal would lie between the raw and the corrected values using a standard alpha ejection calculation (Farley et al., 1996). No alpha-ejection correction is needed if the crystal displays a ≥ 20 µm rim that is totally depleted in U and Th, although some helium is still lost by diffusion, a process which is taken into account by the *Decomp* AHe age prediction program.

Decomp (Meesters and Dunai, 2002; Dunai, 2005) is a forward model that tests the effect of cooling history and U-Th zonation on the AHe ages before α-ejection correction. The algorithm takes into consideration α-ejection happening in the external part of the crystals and He diffusion out of the grains, both of which strongly depend on U and Th zonation. In order to assess the extent to which the age variation measured in several replicates could be due to

zonation, we modeled the effect of zonation on ages in several realistic cooling-history scenarios with rates between 8 and 25 °C / Myr (Figure IV.2.8).

Although the drastic degree of zonation tested (Figure IV.2.8) may be unrealistic in nature, the range of AHe ages modeled by *Decomp* illustrates the very strong dependency on U-Th zonation compared to the effect of the details of cooling history. In the conditions tested, the apparent age of zoned apatites varies between - 30.8 % and + 49.7 % of the age calculated for un-zoned apatites (Table IV.2.4; Figure IV.2.8). The model confirms that apatites with a strong internal zonation of U and Th (cases D and E) may have apparent un-corrected ages that are much older than under the assumption of no zonation, and therefore do not require application of a Ft alpha-ejection correction to the volume of He extracted.

	A	B (% A)	C (% A)	D (% A)	E (% A)
Steady cooling rate	6.8	4.8 (-29.8)	6.1 (-10.6)	9.7 (+41.7)	8.8 (+28.4)
Faster cooling at 8 Ma	6.3	4.5 (-28.4)	5.7 (-9.7)	8.6 (+37.1)	8.0 (+27.1)
Faster cooling at 4 Ma	5.0	3.4 (-30.8)	4.4 (-11.7)	7.4 (+49.7)	6.4 (+29.3)
Faster cooling at 8 and 4 Ma	6.5	4.7 (-28.7)	5.9 (-9.9)	9.0 (+38.2)	8.3 (+27.4)

Table IV.2.4. Comparison between modeled AHe ages for different cooling scenarios (first column). Each period of faster cooling last for 1 Myr, centered on the age indicated (see Figure IV.2.8). A (Ma): apparent age for non-zoned apatites (Ma), B and C: apparent age and age difference (in % of age A) in two cases of external zonation, D and E: apparent age and age difference (in % of A) in two cases of internal zonation. Details on B-E zonation are given in the caption of Figure IV.2.8.

IV.2.4.4. Age-elevation relationships in the Guttannen and the Formazza elevation profiles

All AFT and AHe ages obtained on the Guttannen and the Formazza elevation profiles are plotted in age / elevation diagrams in Figure IV.2.7, including AFT samples with several grains age populations. The comparison between AFT central ages, raw and alpha-ejection corrected AHe ages in the Guttannen elevation profile (Figure IV.2.7) shows that un-corrected AHe ages are generally slightly younger than AFT ages, but corrected AHe ages are older. The closeness between AFT and AHe ages and the steepness of age-elevation relationships in the Guttanen profile (Figure IV.2.7) suggests rapid cooling / exhumation at 9-7 Ma. The presence of two samples at the base of the profile (Figure IV.2.7) with two age-peaks gathering more than 30 % of the dated grains each (green circles) may be the result of a longer stay of this region in the partial annealing zone after 7 Ma, dispersing the age of individual grains.

The elevation of the AFT zero-age intersect of the AFT age-elevation regression line lies at 6166 m below sea level (Figure IV.2.4), i.e. at least 7150 m below the valley bottom. The

temperature at this depth may reach 140 to 210 °C, assuming a 20 to 30 °C / km geothermal gradient, which is clearly above the closure temperature for the AFT system. Therefore, we interpret this slope as requiring slowing in the exhumation rate of the Aar Massif after 7 Ma, which is the approximate AFT age of the lowest samples displaying a single age population in the profile.

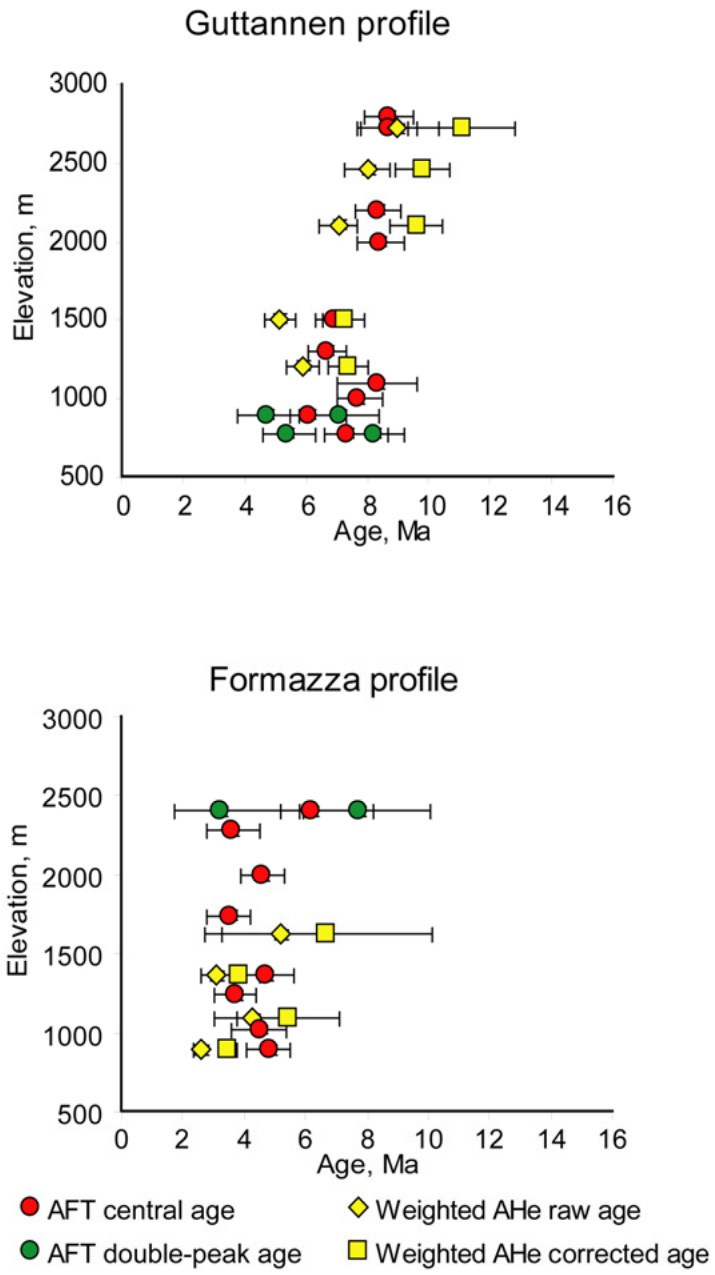

Figure IV.2.7. Comparison between AFT ages, un-corrected and alpha-ejection corrected AHe ages obtained in the Guttannen and the Formazza elevation profiles. Green dots are used in addition to the red symbol showing central age, in samples where single grain ages are very dispersed and can be characterized as belonging to several age populations grouping at least 30 % of dated grains.

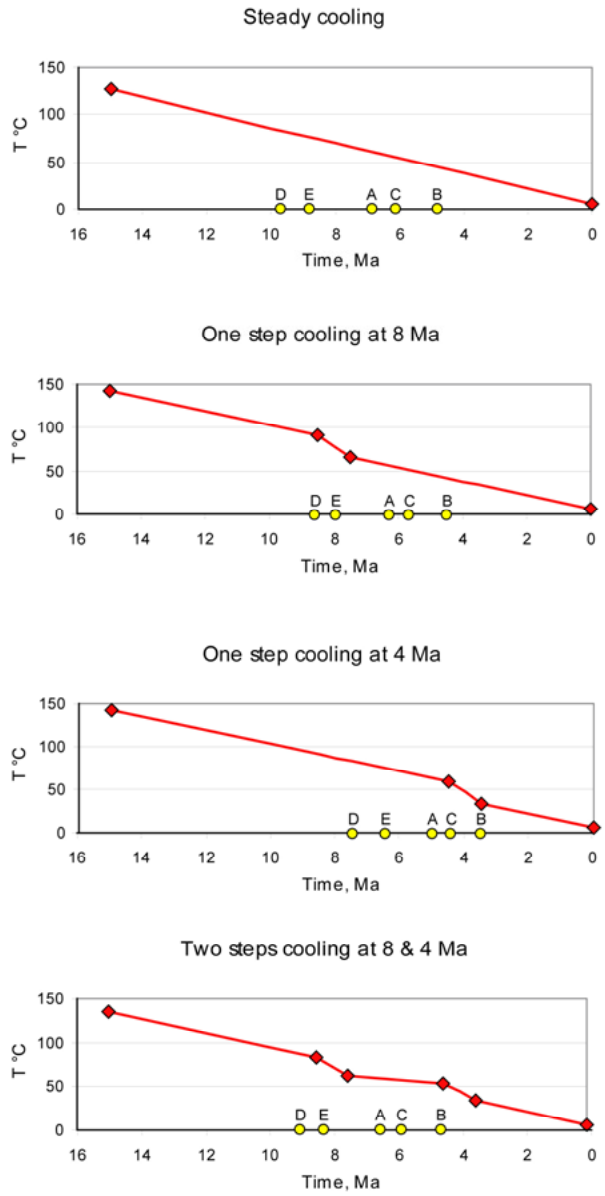

Figure IV.2.8. Effect of U and Th zonation on modeled AHe ages using *Decomp*, for four different cooling scenarios (see curves). In each case, the total cooling is approximately 130 °C in the last 15 Myr, with times of cooling-rate change underlined by a diamond symbol. The model apatite used is a sphere of 75 µm radius, which corresponds to the mean surface / volume ratio observed in the crystals we dated in this study. The emission distance was set at 20 µm, and the software default values were used for other parameters. The yellow circles illustrate the range of theoretical AHe ages obtained for five different distributions of the U and Th in the model spherical apatite. A: non zoned apatite, B: externally zoned apatite with U and Th concentrated in the outer 15 µm, C: externally zoned apatite with U and Th concentrated in the outer 30 µm, D: internally zoned apatite with U and Th concentrated in the inner 30 µm, E: internally zoned apatite with U and Th concentrated in the inner 60 µm.

The AHe age-elevation relationship shows a zero-age intercept at 1358 m below sea level, i.e. at least 2350 m below the valley bottom, which we expect to be temperature of 45-70 °C, corresponding to the partial retention zone of helium in apatites. This second thermochronometer therefore does not require a change in exhumation rate since 9 Ma (the highest AHe age in the elevation profile), in contrast to the AFT data above. None of these observations based on the regression line calculated for samples dated in the Guttannen elevation profiles appears to support a local acceleration in exhumation at 5 Ma, as was predicted by Cederbom et al. (2004).

Our observations in the Formazza elevation profile are different. The low number of points in the AHe profile does not enable us to use the regression line with confidence. However, a comparison between AFT central ages, and both raw and alpha-ejection corrected AHe ages in the Formazza elevation profile (Figure IV.2.7) shows that uncorrected AHe ages are generally of the same age as AFT, but corrected AHe ages are older. In a similar way as in the Guttannen profile, the observation of a sample with a double age peak at the top of the profile may result from a longer stay in the partial annealing zone prior to 6 Ma, having caused individual apatite ages to disperse.

The overlapping AFT and AHe ages in Formazza, joined to the observation of an AFT age with dispersed individual grain-age at the top of the profile might result from a period of fast exhumation around 5-4 Ma, following a period of slower passage through the AFT partial annealing zone at 6 Ma.

The combination of observations in the Guttannen and the Formazza profiles suggests a common period of slow exhumation centered on 6 Ma, with a period of fast exhumation before (documented in Guttannen) and after (documented in Formazza). In the lack of higher-temperature thermochronometer data (such as zircon U-Th / He) in Formazza, we cannot assess the evidence for a similar period of rapid exhumation prior to 6 Ma in Formazza. Given the generally younger ages outcropping in the Italian profile, it is clear that the average exhumation rate since 6 Ma has been higher there than in the Swiss profile (Figure IV.2.3). Our qualitative analysis of AFT and AHe data on two elevation profiles along a N-S transect linking the Aar Massif to the Lepontine Dome thus lead us to propose the following scenario for late Neogene exhumation: a period of fast exhumation (9-7 Ma) was followed by 2 Myrs of slow cooling (7-5 Ma). Subsequently, exhumation increased again (5-4 Ma), but more intensely on the southern flank of the orogen, exemplified by the Formazza profile.

If we assume that the AFT age at the top of the Formazza profile (ca. 2400 m) and the two AFT ages at the bottom of the Guttannen profile (ca. 840 m) remained for a longer time than other samples in the partial annealing zone between 7 and 5 Ma (Figure IV.2.7), and if the elevation of the partial annealing zone was comparable in both areas at the time of closure, then we infer a minimal additional exhumation of ca. 1560 m during the last 5 Ma in Formazza compared to the Guttannen area. This estimate is minimal, as it does not integrate the thickness of the partial annealing zone between its base (corresponding to the samples in Formazza) and its summit (corresponding to the samples in Guttannen).

IV.2.5. Interpreting exhumation histories using *Pecube*

In previous studies, age-elevation profiles have often been directly interpreted in terms of exhumation rates (Michalski and Soom, 1990, Lihou et al., 1995, Rahn et al., 1997) even though the slopes of age-elevation relationships might be overestimated (see section 1). The program *Pecube* (Braun, 2003) solves equations for the thermal structure of the crust and the cooling history of rocks that are currently at the surface, taking into account varying denudation rates and the isostatic response to relief variation. It enables the assessment of the effects of a range of exhumation histories and relief change scenarios on cooling histories, and then uses these to predict AFT and AHe ages at the surface.

As *Pecube* can only be used over limited areas, where geothermal gradient, exhumation history and rock thermal diffusivity are relatively homogeneous, we limited our study to two regions of 37 x 38 km centered on the Guttannen and the Formazza profiles (locations c and d on Figure IV.2.1), using a coarse version (1 km pixel size) of the DEM available from the CGIAR-CSI SRTM 90 m database (http://srtm.csi.cgiar.org). During the more than 120 different exhumation and relief change histories tested in each area, we kept the thermal parameters of the crust constant, as well as the values of plate flexure parameters used to include the effect of isostatic rebound following relief change, as detailed in Table IV.2.5. We calculated AFT and AHe ages for each surface grid node from the predicted cooling histories, using the forward model of Green et al. (1989) with the modified annealing parameters of Stephenson et al. (2006) for AFT ages; and the model and parameters of Farley (2000) for AHe ages.

Parameters for thermal calculation	
Model crustal thickness C	50 km (Stampfli et al., 1998)
Number of nodes in the vertical (z) direction nz	21
Thermal diffusivity κ	25 $km^2.Myr^{-1}$ (Braun and Robert, 2005)
Temperature at the base of the model T_{max}	650 °C (Bousquet et al., 1997)
Temperature at sea level T_0	15 °C
Atmospheric lapse rate G	6 $°C.km^{-1}$
Crustal heat production H	8 $°C.Myr^{-1}$ (Braun and Robert, 2005)
Erosional response time τ	1000 Myr
Parameters for plate flexure	
Crustal density, ρ_c	2700 $kg.m^{-3}$
Sublithospheric mantle density, ρ_m	3200 $kg.m^{-3}$
Young's modulus, Y	10^{+11} Pa
Poisson ratio ν	0.25
Equivalent elastic thickness Te	20 km (Burov and Diament, 1996)

Table IV.2.5. Values of parameters of crustal thermal variation and plate flexure used in every *Pecube* run.

We then calculated a value of cumulated misfit (μ) between measured and predicted ages in order to quantify their closeness and assess the likelihood of each set of parameters tested (Figure IV.2.9):

$$\mu = \sqrt{\sum_{i=1}^{n} \left(\frac{age_{obs} - age_{pred}}{\sigma_{age_{obs}}} \right)^2} \qquad \text{(IV.2.1)}$$

where age_{obs} and age_{pred} are the observed and predicted ages, respectively and σ is the age error. Central AFT age were used in the misfit calculation, or the main age-peak component in cases where it included more than 70 % of the grains counted (see Table IV.2.2); otherwise the age was not used. The AHe ages used in the model were not corrected for alpha-ejection, due to presumed U and Th zonation susceptible to cause the overestimation of the correction factor.

The series of *Pecube* runs were aimed at finding best-fit exhumation and relief change scenarios by tuning these parameters and comparing AFT and AHe ages predicted from the resulting thermal history, with measured ages. We report the values of misfit obtained in Figures IV.2.10 to IV.2.13.

Our first set of runs tests different values of steady exhumation rate (Figure IV.2.10). In the Formazza area, the best-fitting scenario (cumulated misfit: μ = 4.4) is obtained for 0.75 km /

Myr (insensitive to relief change), and in the Guttannen area (cumulated misfit: $\mu = 7.4$) for 0.4 km / Myr (with increasing relief). However, some of the other scenarios tested provided slightly better misfit values in Guttannen.

We subsequently tested models including a single exhumation event of 2 Myr duration, centered at either 8 or at 4 Ma (Figure IV.2.11). The three sets on abscissa axis of Figure IV.2.11 show different scenarios of exhumation rate variation (moderate, strong, extreme). In Guttannen, the best results are obtained for a pulse in exhumation rate centered at 4 Ma (yellow symbols), with steadily or temporarily increasing relief (triangle or circle symbols respectively). The scenarios with a sharp exhumation pulse (0.1 to 1 km / Myr) illustrate the extreme role played by relief change when the background exhumation rate is very low (0.1 km / Myr). In Formazza, we observe a broadly similar pattern although the scarcity of AFT and AHe ages older than 6 Ma in this profile do not allow to test accurately models involving an exhumation pulse centered at 8 Ma. In both areas, relatively high best misfit values ($\mu = 8.4$ and 16.2 respectively) lead to discard the one exhumation pulse scenario.

Thirdly, we tested models that included two exhumation pulses, both lasting for 2 Myr and centered at 8 and 4 Ma respectively (Figure IV.2.12). These models quantify the qualitative interpretation of age-elevation relationships detailed in section IV.2.4.3. The first three exhumation scenarios tested involve two exhumation pulses of equal importance, whereas the two last scenarios test exhumation pulses that differ in intensity. In Guttannen, the best-fitting scenario (cumulated misfit $\mu = 7.2$) is obtained for moderate exhumation rate increase (0.3 to 0.7 km / Myr) during two periods (9-7 and 5-3 Ma), in a context of increasing relief. However, another scenario with steady relief and a stronger exhumation rate contrast (0.25 to 1 km / Myr) yields an almost equally good misfit value ($\mu = 7.4$); underlining the low resolution we have to quantify precisely exhumation rate variations. In contrast, relief change can have a strong effect, such that relief decrease (square symbol) or periodic increase during exhumation pulses (circle) yield very high misfit values. The best scenario modeled in Guttannen (case C in Figures IV.2.12 and IV.2.14) constitute a validation by quantitative means of the observations made qualitatively on AFT and AHe elevation profiles in Guttannen and Formazza (Figure IV.2.7). Interestingly, this shows that a significant pulse of exhumation must have taken place after closure of the AFT and AHe systems and thus not directly recorded by them (as few ages in the Guttannen profile cover the 5 to 3 Ma period). Though high values of misfit ($\mu \geq 10$) are obtained in Formazza for models with two

exhumation periods, they do not lead to temperate the previous observation due to the distribution of ages in this profile.

Finally, we tested a single-step change in exhumation rate, lasting until present (Figure IV.2.13). Here, the misfit values obtained in Guttannen are above values obtained in other scenarios ($\mu \geq 9.7$). In Formazza, however, a low misfit value ($\mu = 4.8$) is obtained for an increase in exhumation rate from 0.3 to 1 km / Myr at ~5 Ma, with little effect of tested relief changes. The two best-fits scenarios in the Guttannen and the Formazza areas are illustrated in Figure IV.2.14, where the predicted and measured AFT and AHe ages are compared.

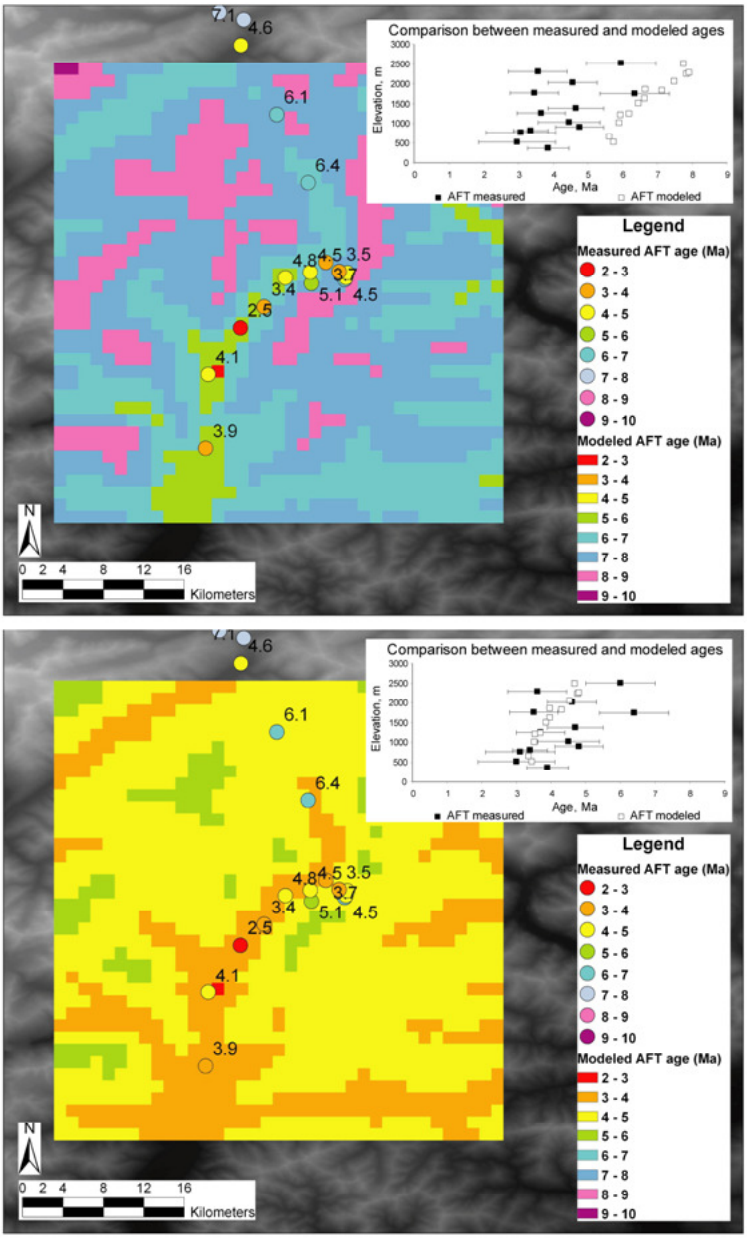

Figure IV.2.9. Comparison between two AFT age predictions in the Formazza area, with either a high total misfit value of 13.3 (upper map), or a low misfit value of 4.2 (lower map). The color scale on the maps correspond to predicted age on 1 by 1 km pixels, while the dots show measured AFT ages, with the same age-scale color code. The two plots represent elevation versus age for the measured AFT ages (black squares) and the ages predicted at the same locations after the thermal histories modeled by *Pecube* (hollow squares).

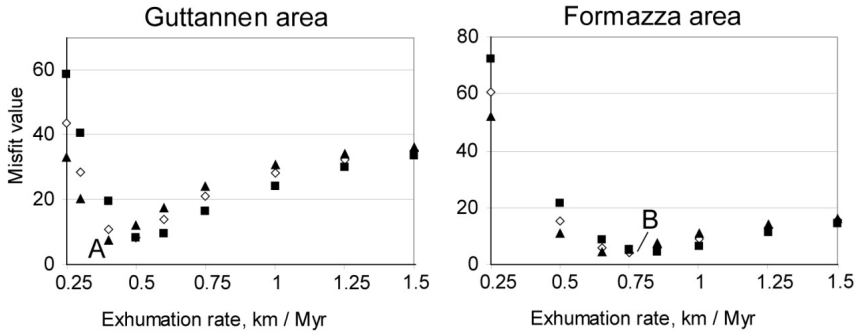

Figure IV.2.10. Values of cumulated misfit between predicted and measured ages in the Guttannen and the Formazza study areas, for different scenarios of steady exhumation rate (plotted on x-axis). Symbols shape represents the relief variation tested, with hollow diamonds for a steady relief (similar to the present one), squares for a decrease from 160 % to the present relief (100 %) during the exhumation of the last 6 km of material, and triangles for an increase from 40 % to the present relief (100 %) during the same period. A (μ = 7.4) and B (μ = 4.4) refer to examples A and B on Figure IV.2.14.

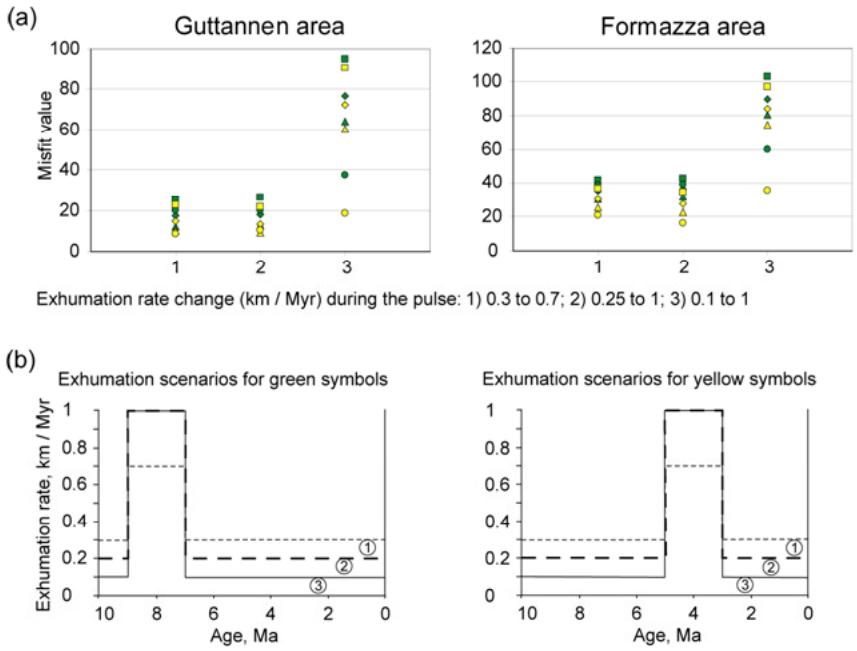

Figure IV.2.11. (a) Values of cumulated misfit between predicted and measured ages in the Guttannen and the Formazza study areas, for different scenarios of 2 Myr long exhumation pulses centered at either 8 or 4 Ma (b). The horizontal axis on (a) enables to differentiate between three scenarios of exhumation rate change (see numbers on curves of graphs b). The color code represents the age of the exhumation pulse centered at either 8 (green) or 4 Ma (yellow), and the symbol pattern indicates whether relief remained steady during the exhumation of the last 6 km (diamond), increased from 50 % of the present-day relief (triangle), decreased from 150 % of the present-day relief, or increased temporarily to one and a half the present-day relief during exhumation pulses (circle).

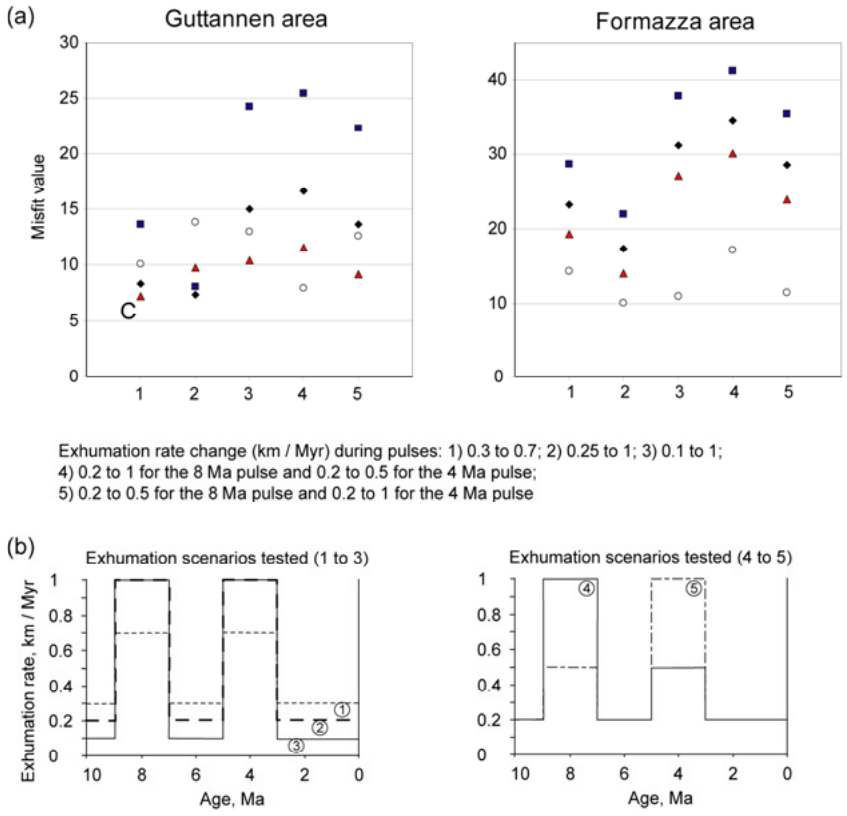

Figure IV.2.12. Values of cumulated misfit between predicted and measured ages in the Guttannen and the Formazza study areas (a), for different scenarios of two 2 Myr long exhumation pulses centered at 8 and 4 Ma (b). The horizontal axis on (a) enables to differentiate between five scenarios of exhumation rate change. (see numbers on curves of graphs b). The symbol patterns indicate whether relief remained steady during the exhumation of the last 6 km (diamond), increased from 50 % of the present-day relief (triangle), decreased from 150 % of the present-day relief, or increased temporarily to one and a half the present-day relief during exhumation pulses (circle). C (μ = 7.2) refers to example C on Figure IV.2.14.

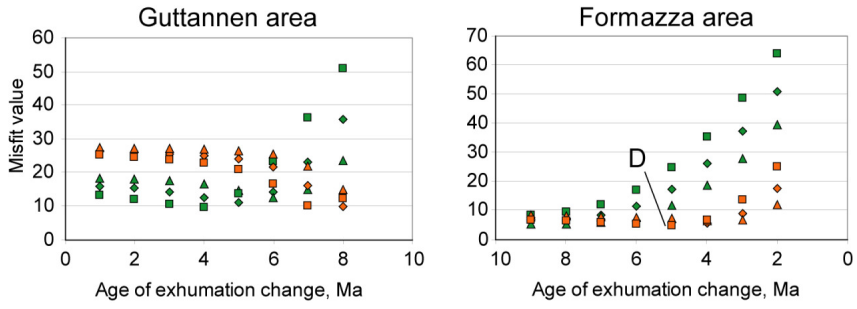

Figure IV.2.13. Values of cumulated misfit between predicted and measured ages in the Guttannen and the Formazza study areas for different scenarios of single-step exhumation rate increase starting at the age on x-axis. The color code represents two different scenarios of exhumation rate change: either from 0.2 to 0.7 km / Myr (green), or from 0.3 to 1 km / Myr (orange). The symbol patterns indicate whether relief remained steady (diamond), increased from 70 % to the present-day relief since the exhumation increase (triangle) or decreased from 130 % to the present-day relief the exhumation increase (square). D (μ = 4.8) refers to example D on Figure IV.2.14.

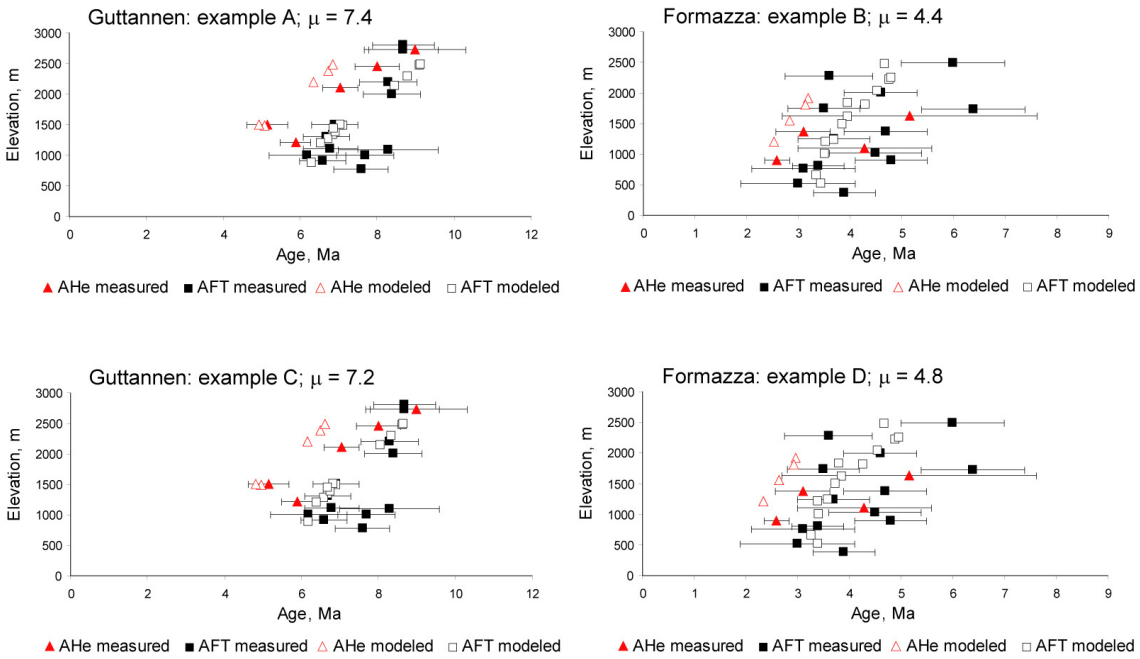

Figure IV.2.14. Comparison between measured AHe and AFT ages, and predicted ages using *Pecube* modeling. μ is the value of cumulated misfit used to quantify the gap between measured and predicted ages (see equation IV.2.1). Examples A and C correspond to the two best models in Guttannen, (see Figures IV.2.10 and IV.2.12), and examples B and C to the best models in Formazza (see Figures IV.2.10 and IV.2.13).

IV.2.6. Discussion and conclusions

AFT dating along a N-S profile stretching from the Aar Massif to the western Lepontine Dome area displays significantly older ages in the northern Alps than in the southern Alps (ca. 7 Ma versus 4 Ma; Figure IV.2.3). In both the Guttannen (Aar Massif) and the Formazza (Lepontine Dome) areas, the closeness or even the superposition between AFT ages and alpha-ejection corrected AHe ages suggests rapid exhumation around the ages of these two thermochronometers. Internal zoning of U and Th may lead to an overestimation of the Ft correction factor, which was confirmed qualitatively by observations of the external detectors during AFT dating.

The qualitative interpretation of age-elevation relationships led us to propose that late Neogene alpine denudation is characterized by two distinct episodes of high exhumation rate, the first one between 9-7 Ma (recorded in the Aar Massif), and the second one between 5 and 3 Ma (recorded in the Lepontine Alps). Similar times of rapid exhumation have been recently proposed from qualitative inspection of age-elevation relationships for the western Aar Massif (Aramowicz et al., 2007) and the Mont Blanc Massif (Glotzbach et al., 2008) respectively. AFT and AHe ages interpreted to result from slow passage through the partial annealing and partial retention zones between 7 and 5 Ma in both study areas, enabled us to formulate the

hypothesis that the whole alpine section studied shares major exhumation features. This qualitative interpretation was confirmed by a quantitative assessment of exhumation histories using the *Pecube* thermal model. However, several contradictory likely scenarios stand out among the cases tested.

In Formazza, the models favor either steady 0.75 km / Myr exhumation, or an exhumation rate increasing from 0.3 to 1 km / Myr around 5 Ma and steady since then, with little effect of relief change. The former scenario is in agreement with detrital FT data that have been argued to show exhumational steady state in the Lepontine area since at least 20 Ma at rates of ~0.7 km / Myr (Bernet et al., 2001; Garzanti and Malusa, 2008). The contradiction between these two scenarios may partially arise from the lack of thermochronometer data for ages older than 6 Ma (such as zircon (U-Th) / He or zircon fission track would supposedly provide). In Guttannen, the two best-fitting scenarios are difficult to conciliate as well: either an increase of the exhumation rates from 0.3 to 0.7 km / Myr at 9-7 Ma, followed by a second pulse at 5-3 Ma, or a steady 0.4 km / Myr exhumation rate; both with relief increase.

Although the scenario with lowest misfit value in Guttannen (case C in Figures IV.2.12 and IV.2.14) supports the qualitative interpretation of elevation profiles (section IV.2.4.4), other scenarios retained impair our ability to draw out the late Neogene exhumation rate history in the Guttannen and the Formazza areas unambiguously, based on available AFT and AHe ages. A higher number of age data spanning a longer period (possibly including higher temperature thermochronometers), combined with a refined scanning of parameters space would enable to determine the best-fit scenarios with more accuracy. Indeed, we infer that the scenarios tested may have overlooked local misfit minima in the parameters space. The use of inversion methods offers promising perspectives to test randomly several thousands of parameter value combinations, and thus solve this problem.

These observations only give partial support to Cederbom et al.'s (2004) hypothesis of a major pulse of exhumation in the axial chain since 5 Ma, facilitated by climatic factors. Although our conclusions do not rule out a temporal signal of increased exhumation since ca. 5 Ma, the amount of exhumation calculated as necessary to trigger more than 1.4 km of flexural isostasy uplift and denudation in the foreland basin is not reached. The predicted exhumation of 6.5 km in about 5 Ma is significantly higher than the amount corresponding to our best-fit model in Guttannen, which do not exceed 2.3 km. Possible reasons for the discrepancy between denudation in the Molasse basin and the axial chain include the use of an underestimated

effective elastic thickness in the calculation of flexural isostatic rebound (Cederbom et al., 2004); or a deep-seated controlling factor, such as the delamination of thickened lithospheric mantle which would provide long-wavelength rock uplift of the orogen and its foreland without requiring denudation of the orogen core (Platt and England, 1993).

This study highlights partial agreement between qualitative interpretations of low-temperature thermochronometer age-elevation relationships and inferences from quantitative numerical modeling of these data. It underlines that the understanding of exhumation history greatly benefits from thermal modeling to go beyong alluring age-elevation relationships plots, and stresses out the rich potential for methods enabling the testing of randomly chosen sets of exhumation, thermal and flexural parameters.

Acknowledgements

Meinert Rahn contributed to sampling strategy. We thank Charlotte Cederbom and Jean-Daniel Champagnac for insightful discussions on alpine uplift and exhumation. Erika Labrin, Bardhyl Muceku, Francois Senebier (in alphabetical order) provided invaluable help in preparing samples and teaching techniques to AV. Valerie Olive run the ICP-MS analyses in East-Kilbride. This study was supported by an INSU-CNRS "Reliefs de la Terre" program grant to PvdB, a University of Edinburgh PhD teaching studentship and an international student mobility (MIRA) grant of the Rhône-Alpes region to AV.

IV.3. Appendix to Chapter IV

The main findings of our thermochronological study, based on the interpretation of AFT and AHe ages-elevation relationships and thermal modeling were exposed in section IV.2. Here, I will provide additional details on sampling, AFT and AHe dating methods and the assessment of data quality. I will complete the chapter by the description of a thrust observed in the northern front of the Aar massif, in the upper Aar valley, and discuss the AFT ages obtained on the foot- and the hangingwall in the perspective of dating the deformation in frontal Aar massif.

IV.3.1. Sampling

Sampling for the thermochronology study was performed during four weeks at the end of summer 2005. Two elevation profiles constitute the cornerstone of this study. These two profiles are named "Guttannen" (in the Aar massif, Switzerland) and "Formazza" (in the Antigorio massif, Italy) after the closest villages. Samples from a third profile along the Siedelhorn summit (west of Grimsel pass; southern Aar massif) did not provide a sufficient amount of apatites. I completed the two elevation profiles with samples from a longitudinal profile extending between Innertkirchen (northern Aar) and Crevoladossola (close to the Peri-Adriatic line; southern Alps).

The north-south profile extends over 50 km across the Western Alps at the longitude 8° 20' E. It stretches from north to south across the Helvetic units, separating the Swiss molasse basin and the Aar external crystalline massif in Switzerland, to the area of the Peri-Adriatic fault, which forms the boundary between the Lepontine Dome to the north and the Southern Alps and Po foreland basin to the south. This profiles follows two major alpine valleys perpendicular to the drainage divide: the upper Aar valley flowing northward across the Aar massif and draining to the Rhine, and the Toce valley flowing southwards across the Antigorio unit of the Lepontine Alps and draining to the Po.

The detailed location of sampling was conditioned by avoiding areas of forest where fallen blocks could not be differenciated from bedrock, and avoiding faulted areas with a double purpose: limiting the risk of post AFT-closure displacement along the course of an elevation profile, and limiting the risk of apatite reheating by fault-drained fluid circulation.

IV.3.2. Apatite fission-track dating

Technical details given in this section are only meant to introduce the documents making up this appendix. More complete information can be found in section IV.2, or in the synthesis paper by Gallagher et al. (1998). The location, name and central age of samples dated using the AFT technique are presented in Figure IV.3.1.

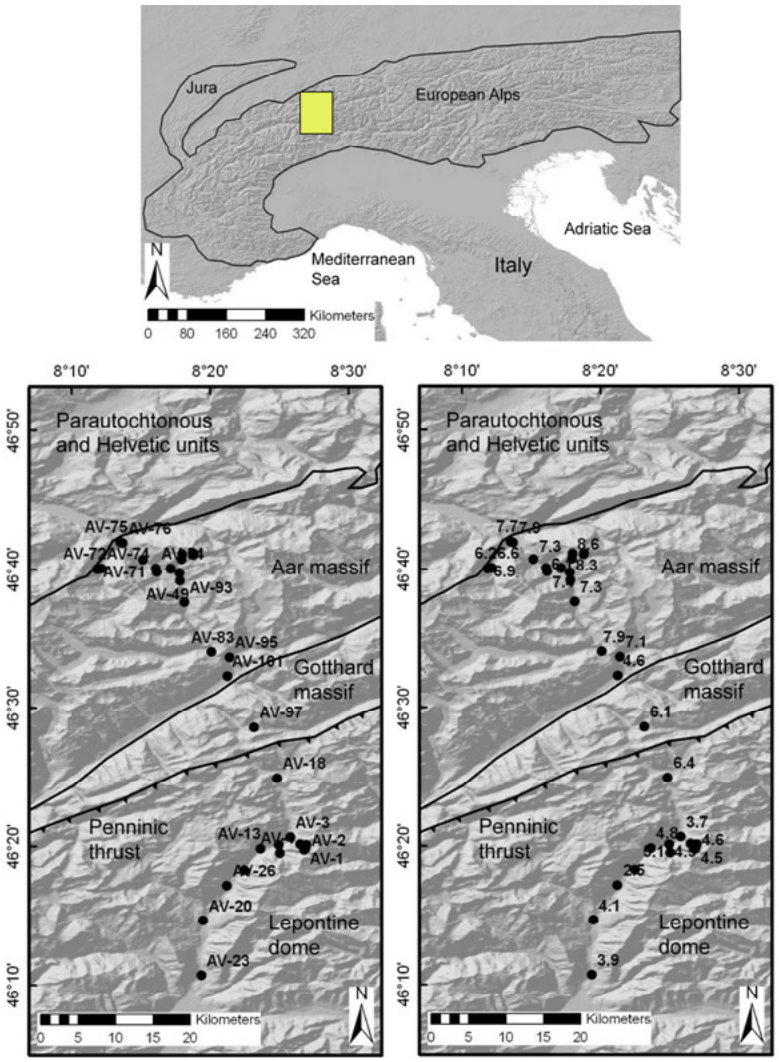

Figure IV.3.1. Sample names and central AFT ages in map view. The yellow rectangle shows the location of the study area.

IV.3.2.1. Determination of Zeta value

The "Zeta" calibration used with the external detector method enables to take in account systematic errors in counting, proper to each fission-track operator, which depend on personal experience, the quality of samples and the Uranium concentration of the glass dosimeter used to monitor the irradiation fluence. The fission-track age equation, using the Zeta approach is

given in Gallagher et al. (1998), along with a review on the history of the method and technical procedures:

$$t = (1 / \lambda_d) \, Ln(1 + (\rho_s / \rho_i) \, \rho_d \, \lambda_d \, \zeta \, g) \qquad (IV.3.1)$$

Where t is the age; λ_d the α decay constant of ^{238}U ($1.55.10^{-10}$ yr^{-1}); ρ_s, ρ_i and ρ_d the track density in cm^{-2} in the apatite (spontaneous tracks), the mica detector (induced tracks) and the dosimeter respectively; ρ_d being an indirect measure of the neutron irradiation fluence for a U-enriched glass dosimeter of known concentration. ζ, the Zeta value in $yr.cm^2$, is calculated for each operator by dating mineral standards of known age; it integrates the experience of the operator, the ill-constrained spontaneous fission decay constant λ_f for ^{238}U, the neutron fluence Φ of the irradiation batch, the ill-constrained Uranium fission radius σ_f and the ^{235}U / ^{238}U concentration ratio I. The geometrical factor g is set at 0.5, since the polished apatites are cut in half along their c axis, hence the volume of Uranium-bearing apatite available to produce induced tracks in the mica detector is half the volume responsible for the spontaneous tracks observed on the polished internal surface of the apatite (Gallagher et al., 1998; Galbraith, 2005).

The Zeta value (Hurford and Green, 1983) is obtained by comparing track density measured on apatite standard of known ages, and external detectors (Gallagher, 1998). In this study, Zeta was calibrated by counting sixteen Fish-Canyon, Durango and Mt Dromedary mineral standards, irradiated in 4 different batches of known neutron fluence. All samples have been irradiated with NBS-962 glasses (U content: 12.3 ppm); however some of the Zeta calibrations were done on batches irradiated with IRMM 540R glasses (U content: 15 ppm). In Figure IV.3.2, I compare these Zeta values, normalising all to the U-content of NBS-962 glass. Although counted during three periods separated by several months, the Zeta values show relatively steady values. I calculated the error-weighted average Zeta value and its uncertainty after removing the first two values, which were anomalously low.

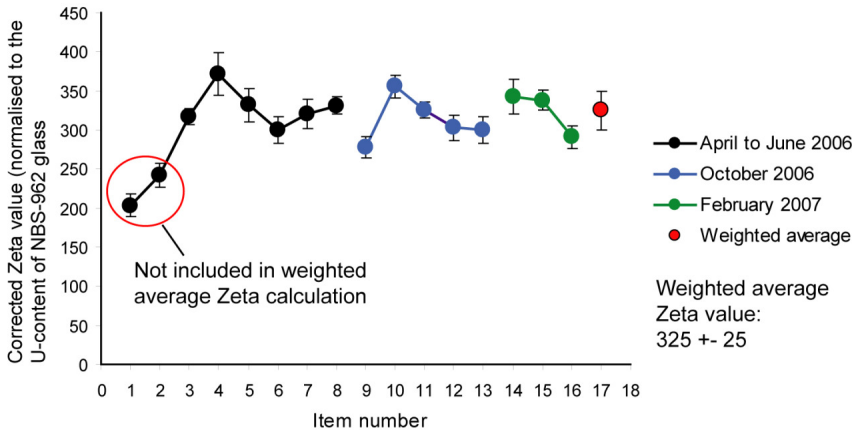

Figure IV.3.2. Zeta calibration. 16 Zeta measurements were realised, using three types of apatite mineral standards irradiated in four different batches. Two values were discarded and the weighted average was calculated over 14 remaining values (red dot).

IV.3.2.2. AFT radial plots

The average AFT age of a sample can be expressed in three ways: as "pooled", "mean" and "central" ages, which yield similar results when the probability distribution of spontaneous and induced tracks among the set of apatites selected follows a Poissonian distribution (see Gallagher et al., 1998, for explanation). The pooled age is obtained by adding all spontaneous and all induced tracks for a single age calculation per sample. The mean age is the arithmetic average of individual grain ages, which allows the final age to reflect the presence of outliers grains. The central age is more sophisticated, as it is the weighted mean of the log normal distribution of single grain age (Galbraith and Laslett, 1993). I report central ages in the present study, as it is more robust to outlier grains (Gallagher et al., 1998).

Radial plots constitute a synthetic way to represent visually the inter-grain age scattering and the different types of error associated with AFT ages (see detailed explanations in Galbraith, 2005). The detail of each sample dated is presented in Figure IV.3.3. On each radial plot, the dots represent the age of an individual apatite grain (function of the number of spontaneous and induced tracks). The dots are placed on an "age line" joining the "0" on y-axis, to the age on the log-scaled graduated arc-circle to the right, which represents individual grain ages. The position of each dot along the "age-line" is defined by the x-axis value, which corresponds to the standard error of the single grain age, defined by the total number of tracks (spontaneous plus induced tracks) counted for the grain (Galbraith, 2005). Dots located closest to the arc-circle therefore have the highest reliability, because their age is defined by more counted tracks. The y-axis on the left represents the width of the single grain age-distribution, the values 1 and -1 corresponding to 1σ and -1σ bracketing the mean grain age. Thus, the smaller the scale on y-axis, the less dispersed the single-grain ages are. A corollary of this

observation, is that samples in which all grains are within a [+2 : -2] band defined on the y-axis are consistent with the hypothesis of a single age-population.

A few samples are characterized by a low number of grains counted (AV49, -72, -83 and -93, with respectively 7, 6, 10 and 6 grains). Although the optimum number of grains counted to maximize the age accuracy is ordinarily 20 or more (Gallagher et al., 1998), the higher uncertainty of ages obtained with 10 grains or less is expressed by a higher error (see the error on central ages on the radial plots Figure IV.3.3) which enabled us to include these samples in further studies (section IV.2.).

IV.3.2.3. Quality of AFT dating

The Figure IV.3.4 represents a qualitative assessment of possible biases on 33 AFT central age and age error due to the number of grains counted, or the U concentration. The three graphs present values of central age, its 1-σ error, and the average U concentration in each sample, obtained by comparing the induced-track density on irradiated apatites and glass dosimeters of known U concentration. The upper diagram shows that the number of grains counted does not influence directly the central age, although a low number of grains counted (and low U concentration) is expected to lead to underestimated age because of "zero-age grains"; apatites with no spontaneous tracks on the polished surface. However, samples with less than 10 grains counted exhibit a larger 1-σ error. The two lower diagrams do not show a linear relationship between central age and error, and U concentration. Instead, they exhibit two populations of samples: (1) a first population with less than 50 ppm U, varying ages and errors, and (2) a second population with 50 to 140 ppm U, old central ages and low errors. These two apparent populations among the 33 samples dated may be linked to the geological history of sampling areas, or be due to experimental biases. Only a precise measurement of U concentration in samples by independent techniques, and the production of an apatite U concentration map covering the study area could resolve this.

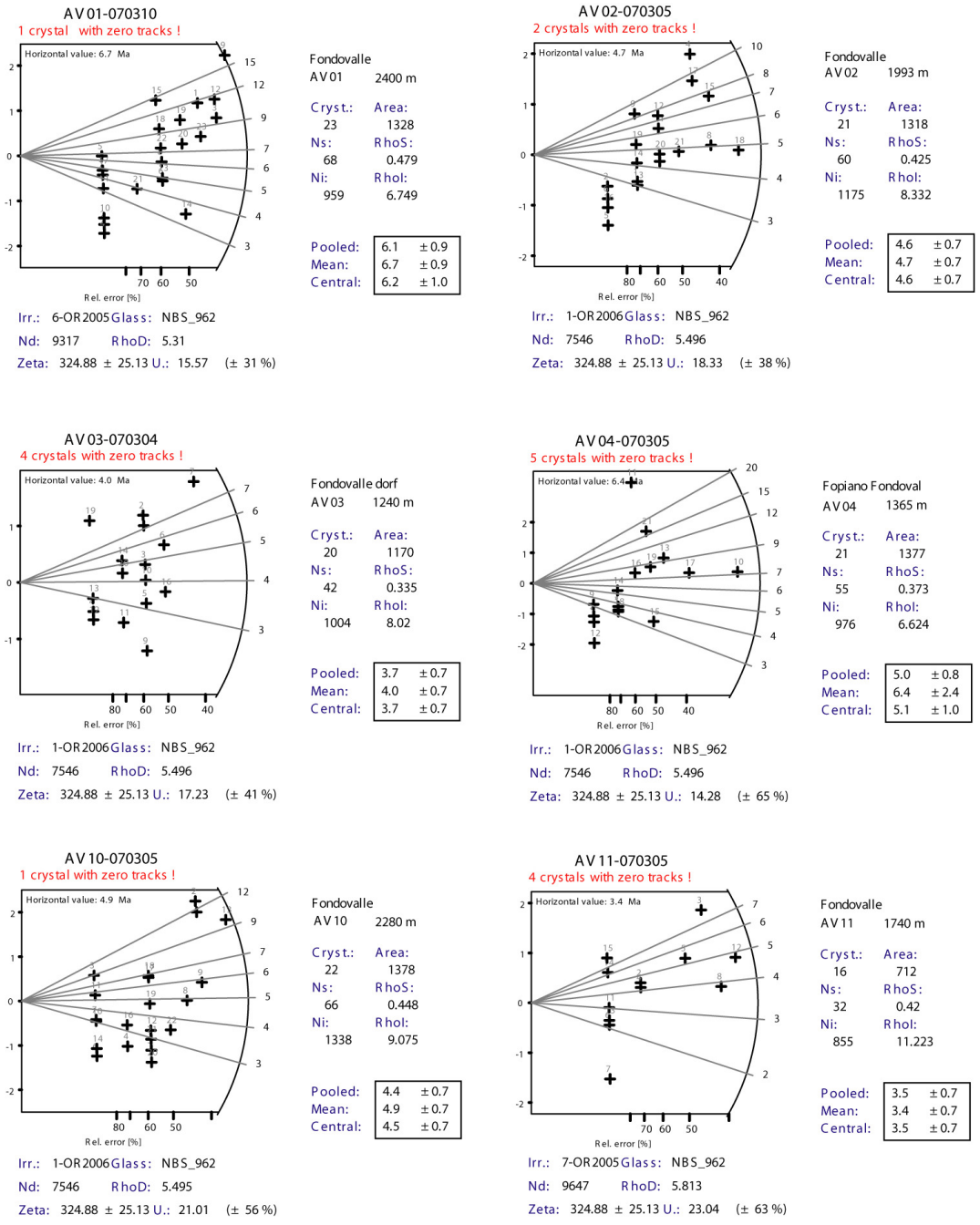

Figure IV.3.3. Radial plot of AFT age calculation as provided by *Trackkey* 4.2g (Dunkl, 2002). The title of each plot is composed of the sample name and the date of track counting (e.g. sample AV01 was counted on March 10th, 2007).

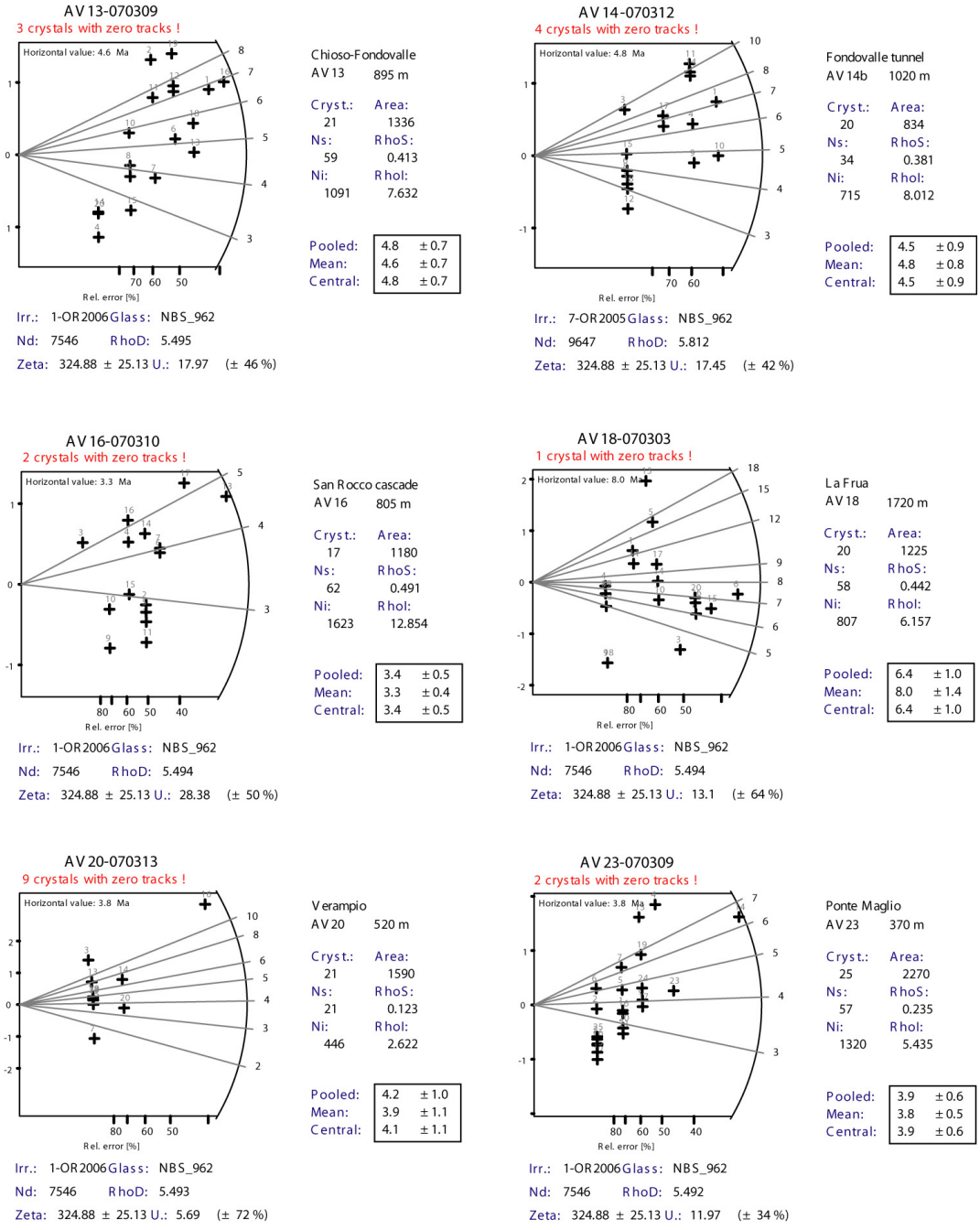

Figure IV.3.3. (continued).

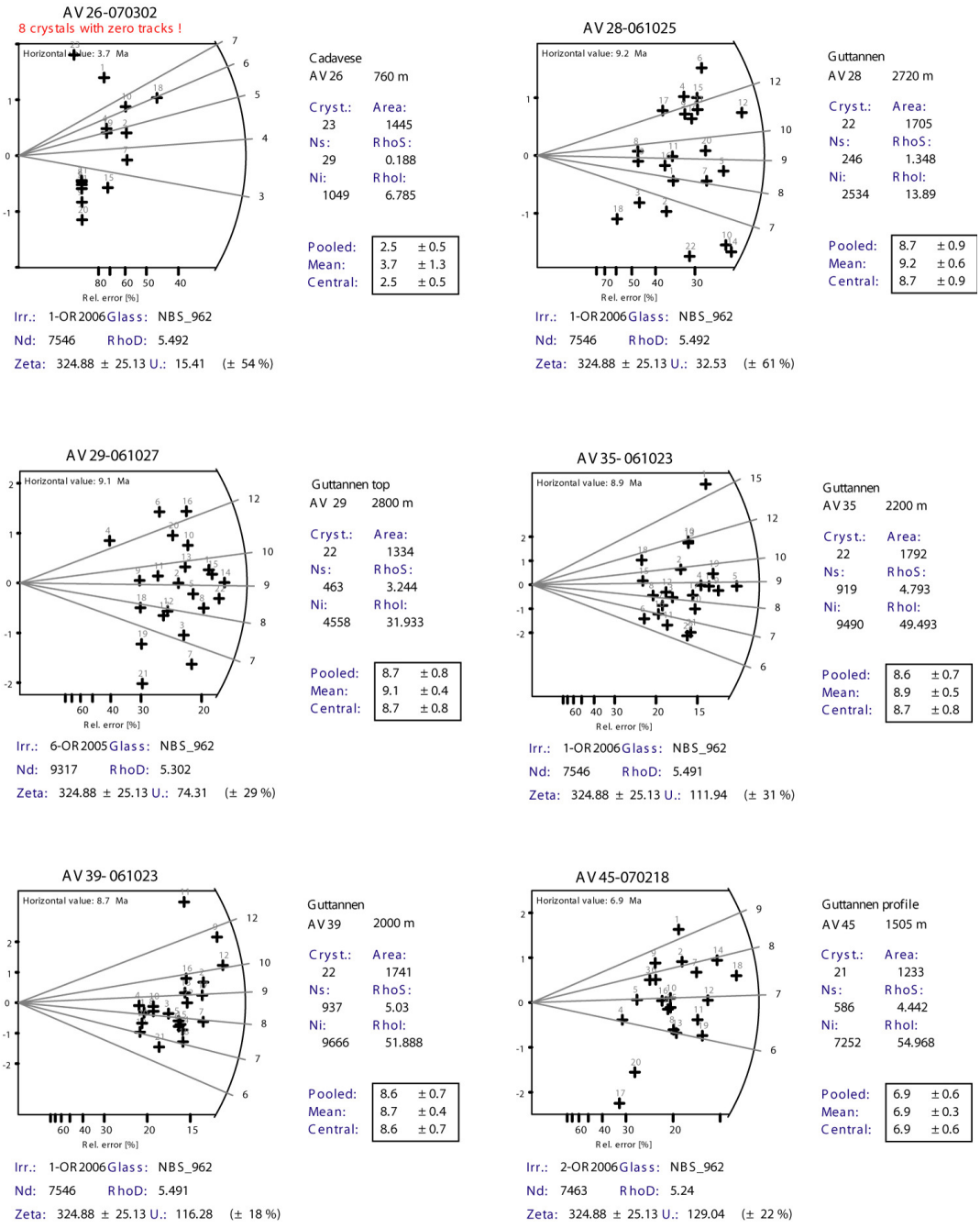

Figure IV.3.3. (continued).

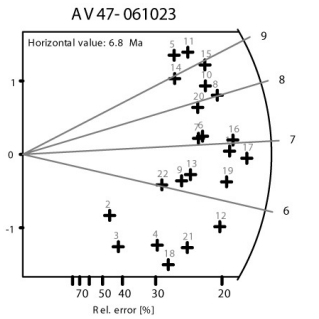

Guttannen
AV47 1303 m

Cryst.:	Area:
22	1030
Ns:	RhoS:
438	3.974
Ni:	Rhol:
5797	52.6

Pooled:	6.7	± 0.6
Mean:	6.8	± 0.4
Central:	6.7	± 0.6

Irr.: 1-OR2006 Glass: NBS_962
Nd: 7546 RhoD: 5.49
Zeta: 324.88 ± 25.13 U.: 117.87 (± 23 %)

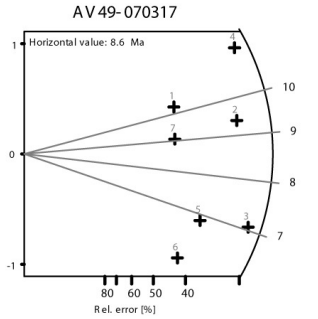

Guttannen Furen
AV49 1095 m

Cryst.:	Area:
7	486
Ns:	RhoS:
63	1.211
Ni:	Rhol:
679	13.057

Pooled:	8.3	± 1.3
Mean:	8.6	± 0.8
Central:	8.3	± 1.3

Irr.: 1-OR2006 Glass: NBS_962
Nd: 7546 RhoD: 5.49
Zeta: 324.88 ± 25.13 U.: 28.82 (± 27 %)

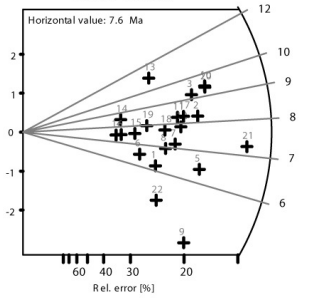

Guttannen
AV50 1000 m

Cryst.:	Area:
22	1226
Ns:	RhoS:
511	3.895
Ni:	Rhol:
6515	49.664

Pooled:	7.4	± 0.7
Mean:	7.6	± 0.3
Central:	7.4	± 0.7

Irr.: 7-OR2005 Glass: NBS_962
Nd: 9647 RhoD: 5.81
Zeta: 324.88 ± 25.13 U.: 103.36 (± 28 %)

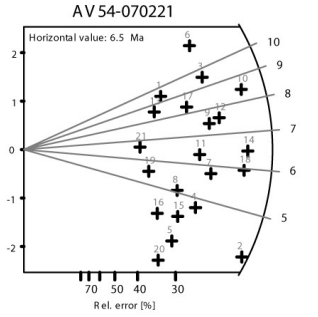

Boden, bend
AV54 900 m

Cryst.:	Area:
21	1077
Ns:	RhoS:
320	2.777
Ni:	Rhol:
4776	41.444

Pooled:	6.0	± 0.6
Mean:	6.5	± 0.5
Central:	6.1	± 0.6

Irr.: 1-OR2006 Glass: NBS_962
Nd: 7546 RhoD: 5.489
Zeta: 324.88 ± 25.13 U.: 90.94 (± 25 %)

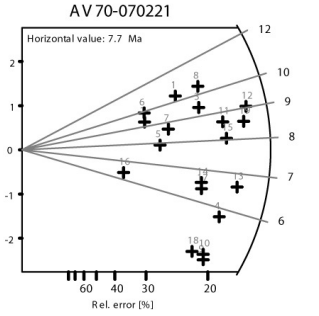

Hotel footwall
AV70 780 m

Cryst.:	Area:
19	993
Ns:	RhoS:
465	4.376
Ni:	Rhol:
5797	54.559

Pooled:	7.1	± 0.7
Mean:	7.7	± 0.4
Central:	7.3	± 0.7

Irr.: 1-OR2006 Glass: NBS_962
Nd: 7546 RhoD: 5.489
Zeta: 324.88 ± 25.13 U.: 123.44 (± 42 %)

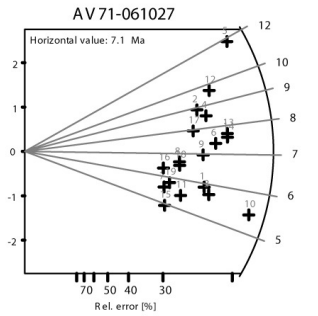

Urbach top
AV71 1110 m

Cryst.:	Area:
19	947
Ns:	RhoS:
368	3.632
Ni:	Rhol:
4542	44.824

Pooled:	6.9	± 0.7
Mean:	7.1	± 0.4
Central:	6.9	± 0.7

Irr.: 6-OR2005 Glass: NBS_962
Nd: 9317 RhoD: 5.278
Zeta: 324.88 ± 25.13 U.: 113.28 (± 43 %)

Figure IV.3.3. (continued).

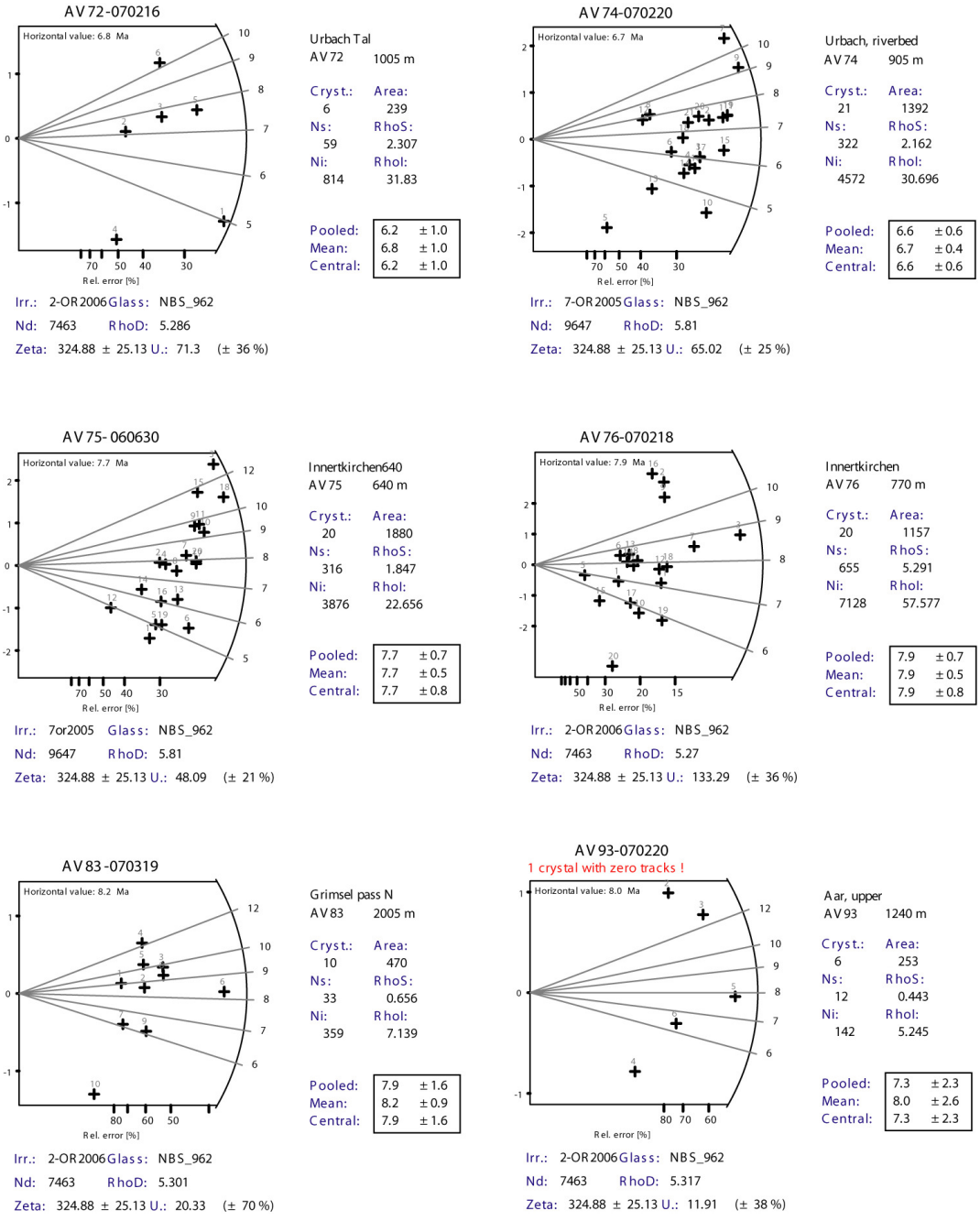

Figure IV.3.3. (continued).

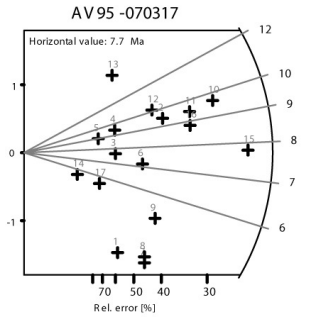

Gletsch Aar
AV95C 1790 m

Cryst.:	Area:
17	849
Ns:	RhoS:
102	1.123
Ni:	Rhol:
1349	14.85

Pooled:	7.1	± 0.9
Mean:	7.7	± 0.7
Central:	7.1	± 0.9

Irr.: 7-OR2005 Glass: NBS_962
Nd: 9647 RhoD: 5.811
Zeta: 324.88 ± 25.13 U.: 31.08 (± 47 %)

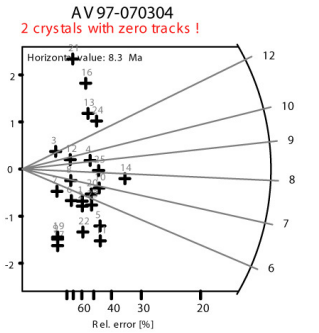

Nufenen pass
AV97 2485 m

Cryst.:	Area:
25	1741
Ns:	RhoS:
77	0.413
Ni:	Rhol:
1093	5.867

Pooled:	6.1	± 0.9
Mean:	8.3	± 1.8
Central:	6.1	± 0.9

Irr.: 2-OR2006 Glass: NBS_962
Nd: 7463 RhoD: 5.332
Zeta: 324.88 ± 25.13 U.: 13.01 (± 48 %)

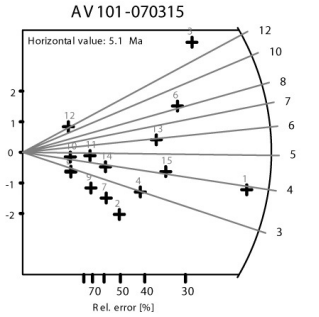

Oberwald mill
AV101S 1405 m

Cryst.:	Area:
15	298
Ns:	RhoS:
88	2.76
Ni:	Rhol:
1769	55.479

Pooled:	4.3	± 0.6
Mean:	5.1	± 1.0
Central:	4.6	± 0.9

Irr.: 2-OR2006 Glass: NBS_962
Nd: 7463 RhoD: 5.378
Zeta: 324.88 ± 25.13 U.: 111.75 (± 59 %)

Figure IV.3.3. (continued).

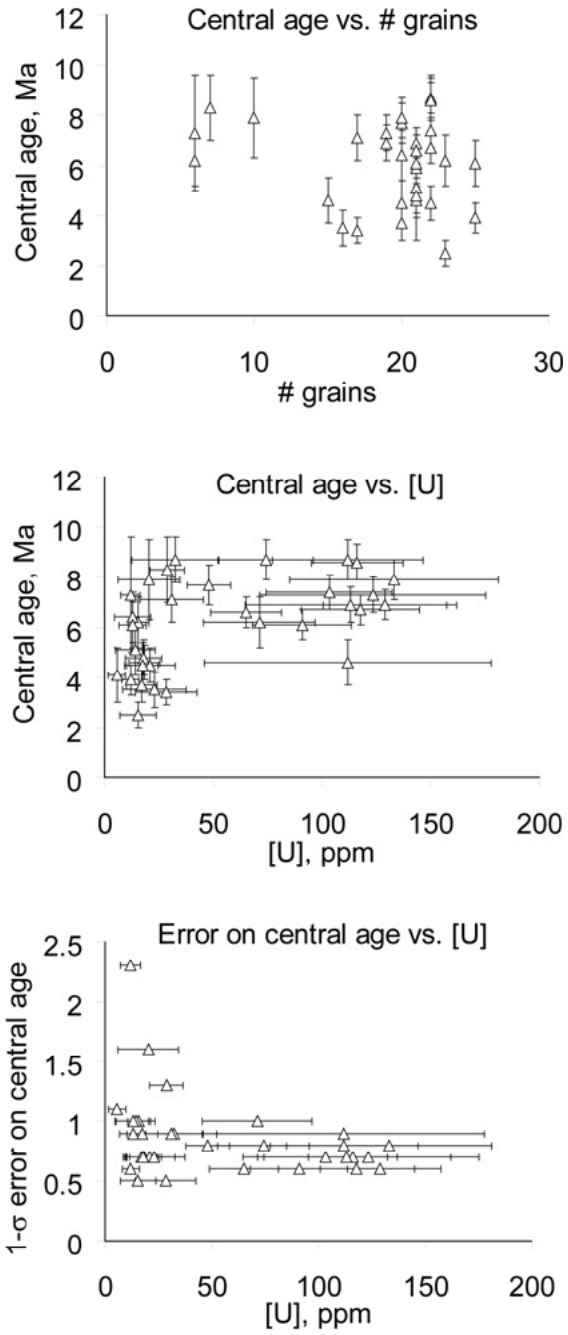

Figure IV.3.4. Central AFT age and 1σ age error plotted against the number of grains counted and the average Uranium concentration in apatite. Error bars show 1-σ errors on central age or U concentration.

IV.3.3. Apatite (U-Th) / He dating

Technical details given in this section are only meant to introduce the documents detailed in this appendix. More complete information can be found in section IV.2., in Braun et al. (2006), or Farley, (2002). The low-temperature thermochronometer based on the ratio between concentrations of radiogenic ^{4}He (α particles) and radioactive ^{238}U, ^{235}U and ^{232}Th relies on two main analytical procedures. After careful picking under a binocular lense, apatites visually free of inclusions were packed individually in a minute Pt tube (in order to ease heating and subsequent manipulations of the grain) before introduction in the laser chamber, where they were heated with a laser-beam, and the amount of He extracted from the crystals was measured in a quadrupole mass-spectrometer. In the next step, the degased apatites were dissolved in nitric acid and U and Th concentrations measured in an ICP-MS using the spike dilution technique. Finally, the age t is obtained by the relationship:

$$^{4}He = (8 \times {}^{238}U) \times (e^{\lambda_{238}t} - 1) + (7 \times {}^{238}U / 137.88) \times (e^{\lambda_{235}t} - 1) + (6 \times {}^{232}Th) \times (e^{\lambda_{232}t} - 1) \quad \text{(IV.3.2)}$$

Where ^{4}He, ^{238}U, and ^{232}Th are number of atoms, 8, 7 and 6 stand for the number of Helium atoms released by the disintegration of an atom of ^{238}U, ^{235}U and ^{232}Th respectively, 1 / 137.88 represents the constant ratio of the ^{235}U / ^{238}U isotopes, and $\lambda_{238,}$ λ_{235}, λ_{232} represent the decay constants of the three isotopes, respectively 1.55 10^{-10} yr^{-1}; 9.85 10^{-10} yr^{-1} and 4.94 10^{-11} yr^{-1} (Farley, 2002). Another parent element which may be a source for significant input of He is ^{147}Sm. However, the decay constant of ^{147}Sm is very low compared to the decay constants for the U and Th isotopes considered (Farley and Stockli, 2002) so the role of this isotope can only be significant in apatites with very low U-Th concentrations.

The stopping-distance of Helium atoms ejected during radioactive decay varies as a function of the crystal density, and reaches ca. 20 µm in apatite (Farley, 2002). A certain amount of Helium is therefore lost out of the crystal during alpha-emission. To compensate for this problem causing age underestimation, Farley (1996) developed a correction factor Ft based on the size and geometry of each crystal. Indeed, large, almost spherical crystals need far less correction than thin, needle-shape crystals as the proportion of material located at less than 20 µm of the crystal surface is smaller. Using this alpha-ejection correction factor, the AHe age become:

$$\text{(Corrected AHe)} = \text{(Raw AHe)} / Ft \quad \text{(IV.3.3)}$$

The raw and corrected AHe ages are presented in Table 3 of section IV.2. The location, names and uncorrected apatite (U-Th) / He ages ("raw" ages; meaning not corrected from alpha-ejection He loss) of samples dated using the AHe technique are presented in Figure IV.3.5.

IV.3.3.1. He yield in laser reheating of single grains

The efficiency of apatite laser heating, used to extract Helium by diffusion, yields varying results depending on factors such a crystal size, or the beam angle. In order to make sure that the entire volume of gas was extracted, I systematically performed a second heating step for each crystal, and quantified the second heating / first heating ratio of gas volume. The Figure IV.3.6 presents these ratios for each replicate of each sample. It was expected that a strong relationship between single-grain age and the ratio of He yield between the second and the first heating may indicate the measuring abnormal He concentrations due to un-noticed He-rich inclusions (such as zircons) releasing their He slowly at temperatures used to degas apatites. However, our samples generally did not express such a pattern, giving us confidence in the lack of inclusions in the crystal used. A few notable exception are may occur in some grains of samples AV6, -13 and to a lesser extend -45.

IV.3.3.2. Quality of AHe dating

The upper graph on Figure IV.3.7 presents the ages of four Durango standards versus Th / U that are routinely measured, intercalated with samples of interest, in order to check age calculations against standards. Our measurements (yellow squares) are comprised within intra-laboratory variability, the natural variation in U and Th concentration within Durango apatite (Boyce and Hodges, 2005) explaining part of the age scattering. The error-bars on our dated Durango fragment are larger than other ages in the laboratory record, because of a larger uncertainty during spike weight measurement.

The lower graph in Figure IV.3.7 shows He volume and U and Th weights in each dated crystal, versus the age difference between single-grain raw age and the error-weighted raw age of each sample (x-axis) obtained after discarding replicates with suspicious values (see details in Table 3 of section IV.2.). Therefore, some of the grains presented on this plot were finally not used in the calculation of weighted age reported in section IV.2.

This study was aimed at assuring that there was no bias in single-grain age caused by extreme amounts of He, U or Th. The fact that most dots are aligned with age-difference values close

to zero simply expresses that single-grain ages are generally close to the weighted mean (at least when taken all together; it will be clear in plates presented later on that some samples have very dispersed single-grain ages). I do not observe a relationship between extreme age differences and the He, U or Th contents, thus not evidencing any analytical bias.

Figure IV.3.8 is complementary to Figure IV.3.7, as it again represents the age difference between single grain raw age and the weighted-average raw age of each sample on the x-axis, while the y-axis now represents the Th / U ratio (upper graph) and the length and diameter of each crystal (lower graph). The upper graph in Figure IV.3.8 does not enable to distinguish a bias on single grain age due to the Th / U ratio, except in two crystals (at the upper right hand corner of the plot), for which a Th / U ratio of about 3 coincides with very old single grain age (more than 10 Ma older than the weighted age). No relationship between crystal size and age difference is identified either (lower graph).

Figure IV.3.9 describes the use of the Ft parameter enabling to correct raw AHe ages for alpha-ejection loss of Helium (Farley, 1996). the upper graph shows a strong positive relationship between crystal diameter and Ft value, whereas the crystal length does not exhibit such a large effect. This relationship illustrates the importance to chose apatites with a large diameter in order to avoid using a high Ft correction factor and the associated error. The lower graph represents single-grain corrected AHe age versus raw AHe age and illustrates the correction of age underestimation performed by dividing raw AHe age by the Ft correction factor. The absolute importance of ejection correction is proportional to the grain age, reaching more than 5 Ma in the case of our oldest single grain.

IV.3.3.3. Comparison between single grain replicate AHe ages

The AHe age of the nine samples reported on Figure IV.3.10 was calculated using three to five single-grain replicates. The light-grey bars illustrate how alpha-ejection corrected ages are older than raw ages, in a varying degree (compare replicate AV6-2 with AV45-5) function of the crystal shape and age. The replicates dated in some samples may exhibit very similar ages (e.g. samples AV-37, -45, -48) or in the contrary very different ones (AV-12, -13). The decision to discard some of the replicates was made following objective criteria (see caption of Table 3, section IV.2.), disregarding an apparent age anomaly, but it appears that many of the outlying replicate ages were not included in the weighted age calculation (the symbol * beside replicate names in Figure IV.3.10 indicates that it was rejected).

IV.3.4. Comparison between AFT and AHe ages

I observed in Figure IV.2.7, that corrected AHe ages can be older than AFT ages, even though the temperature of closure of the latter is higher. In section IV.2.4.3, I used *Decomp* models (Meesters and Dunai, 2002; Dunai, 2005) to illustrate the possible role of U and Th internal zoning, in overestimating the Ft alpha-ejection correction factor. Table IV.3.1 provides a qualitative and non-exhaustive list of other factors, due to geological conditions or experimental procedures, that are likely to cause the under- or overestimation of AFT and AHe dating.

AFT underestimation	AFT overestimation	AHe overestimation	AHe underestimation
Spontaneous tracks are too dense and some are missed.	Induced tracks are too dense and some are missed.	Presence of He from fluid inclusions, or He implantation from neighbouring U-rich minerals.	Crack in the apatite crystal causing He loss by diffusion.
Poor-quality apatite polishing, masking spontaneous tracks	Dislocations in apatite crystals may be counted as spontaneous tracks.	Samples poor in U and Th, but rich in un-accounted radioactive ^{147}Sm	Th contamination may happen on the wall of the beaker used for apatite dissolution.
U and Th internally zoned lead to overestimate the counting of induced tracks.	Mica external detectors may have a lose contact with the apatite polished surface, lowering the density of induced tracks.	The α-ejection correction is too high / unnecessary if U-Th is internally zoned. U-rich crystals in contact with the apatite may cause He implantation.	
Fluor-rich apatites have a lower closure temperature.	The neutron fluence is overestimated when the mica external detectors applied on glass dosimeters are "pitted".	U-Th may be lost during laser heating at too high temperature.	

Table IV.3.1. Factors susceptible to cause the under- or overestimation of AFT and AHe ages.

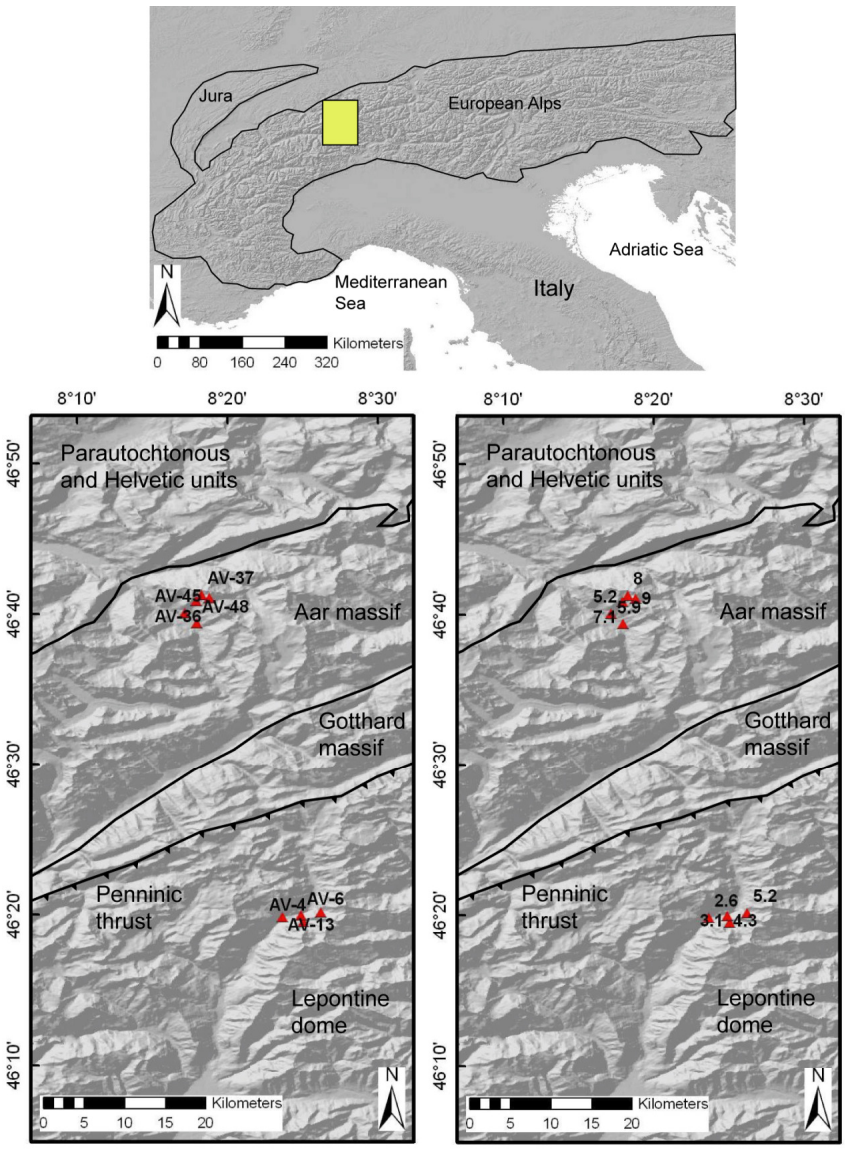

Figure IV.3.5. Sample names and uncorrected AHe ages in map view. The yellow rectangle shows the location of the study area.

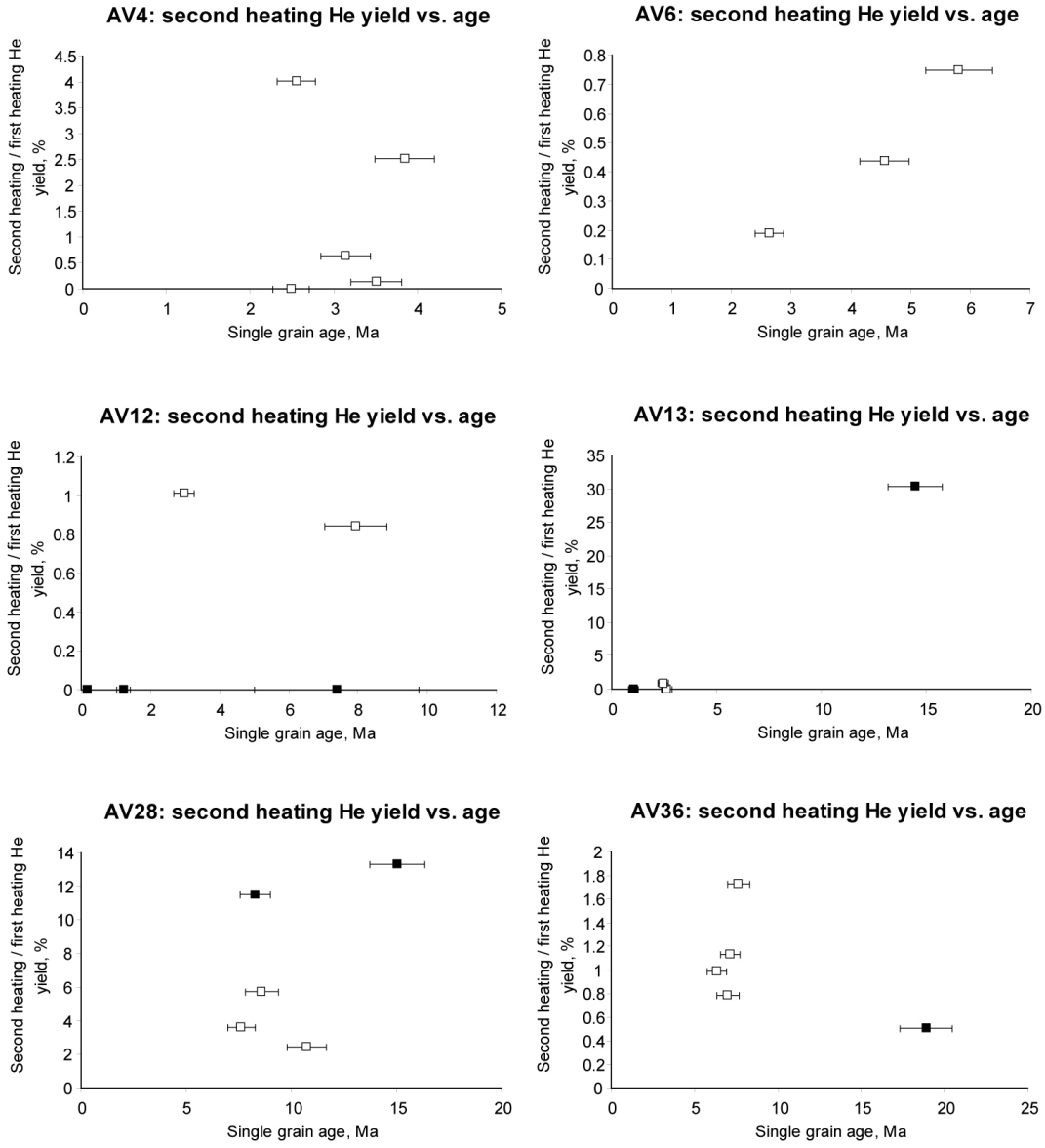

Figure IV.3.6. Comparison between the ratio of He extraction yield brought by a second versus first laser heating, and the uncorrected grain age. All grains are presented here, even those that have been discarded before the calculation of a weighted average age (for reasons detailed in Table IV.2.3; discarded grains are shown by a black square symbol on the plots). For each sample, grains with oldest apparent age, which also exhibit a high proportion of He released during the second heating, are suspected to contain an unnoticed He-rich inclusion leading to overestimate the crystal age.

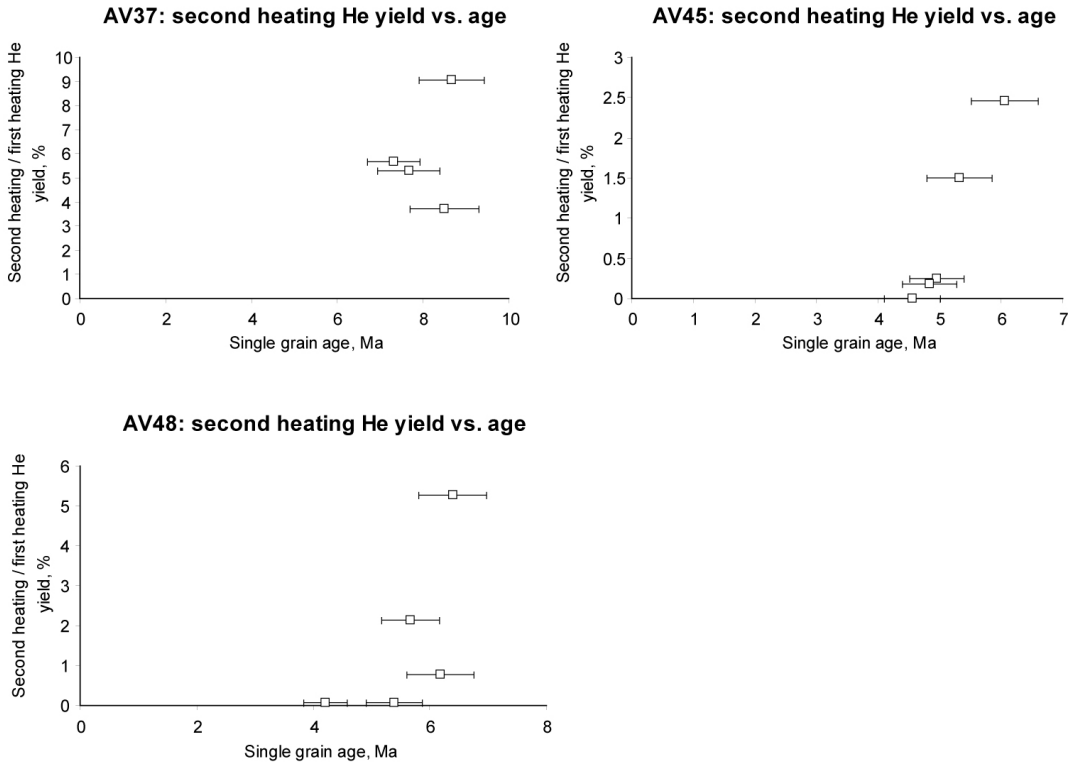

Figure IV.3.6. (continued)

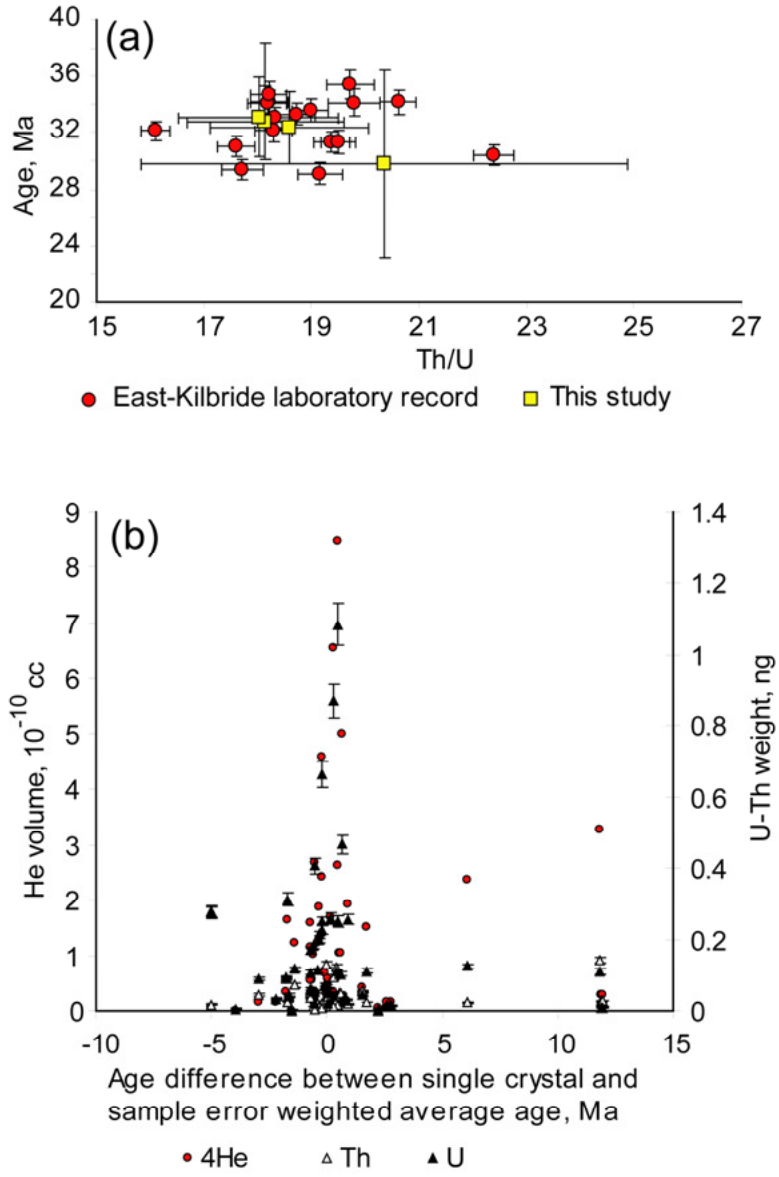

Figure IV.3.7. (a) Durango apatite (U-Th) / He ages (details on Table IV.2.3). Comparison between the fragments of Durango apatite used as an age standard, dated during this study among alpine samples, and the record of Durango ages measured in the lab for the last months. (b) Plot of the He volume and the U and Th masses in each dated grain, versus the age difference between single grain and weighted average age.

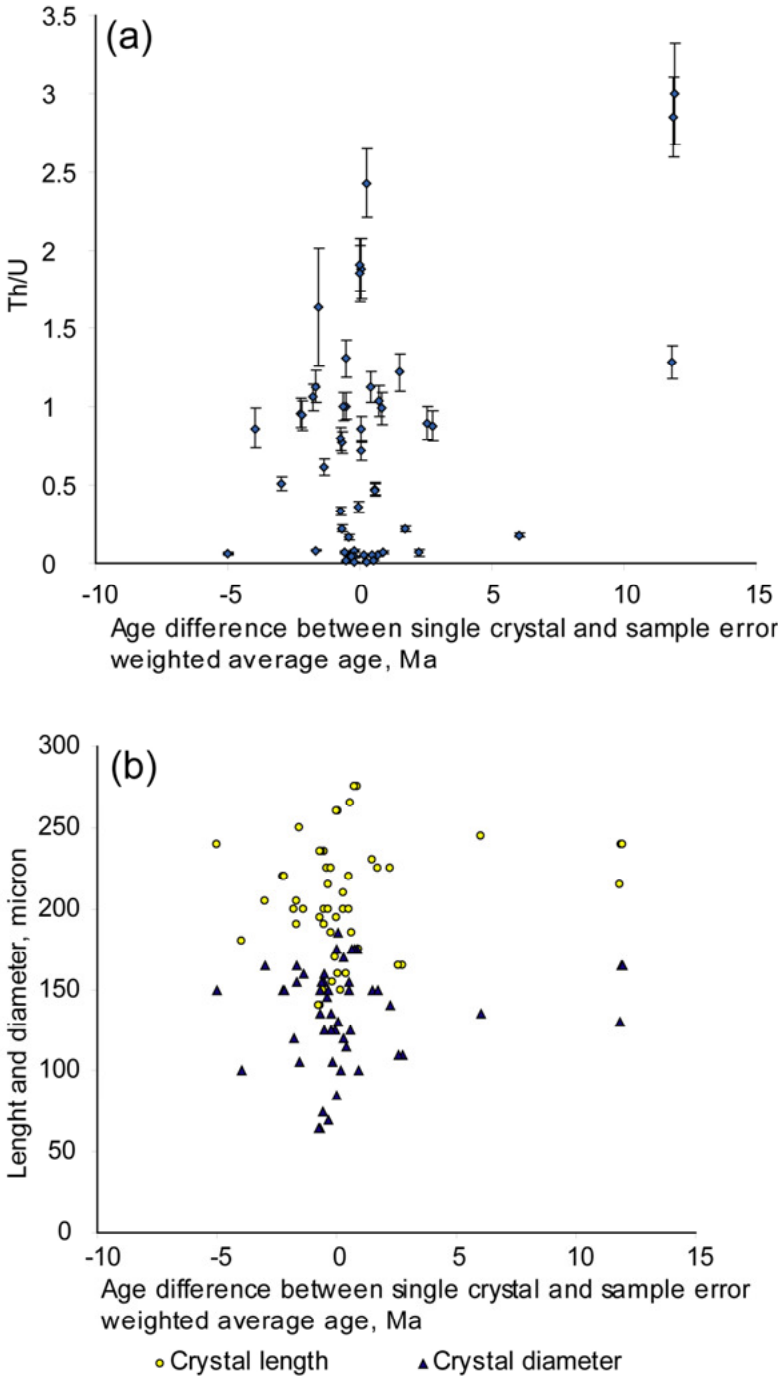

Figure IV.3.8. (a) Plot of the Th / U ratio in each dated grain versus the age difference between single-grain and weighted average age. (b) Plot of the grain dimensions versus the age difference between single-grain and weighted average age.

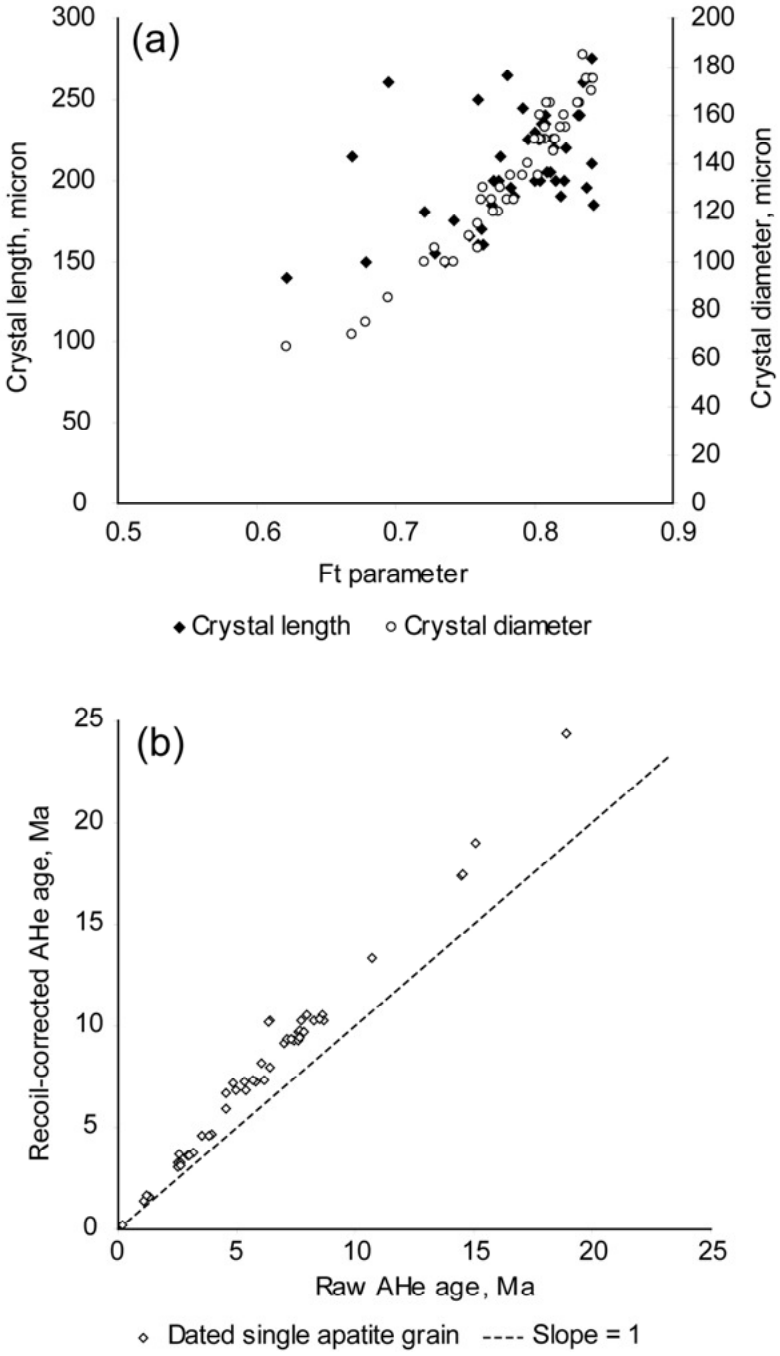

Figure IV.3.9. (a) Plot of diameter and length versus alpha-ejection correction factor Ft for dated apatites. This graph shows the role of crystal diameter on the value of Ft. (b) Plot of corrected versus raw AHe ages. Dashed line has a slope of one and corresponds to a hypothetical case of Ft = 1 where corrected age equates raw age.

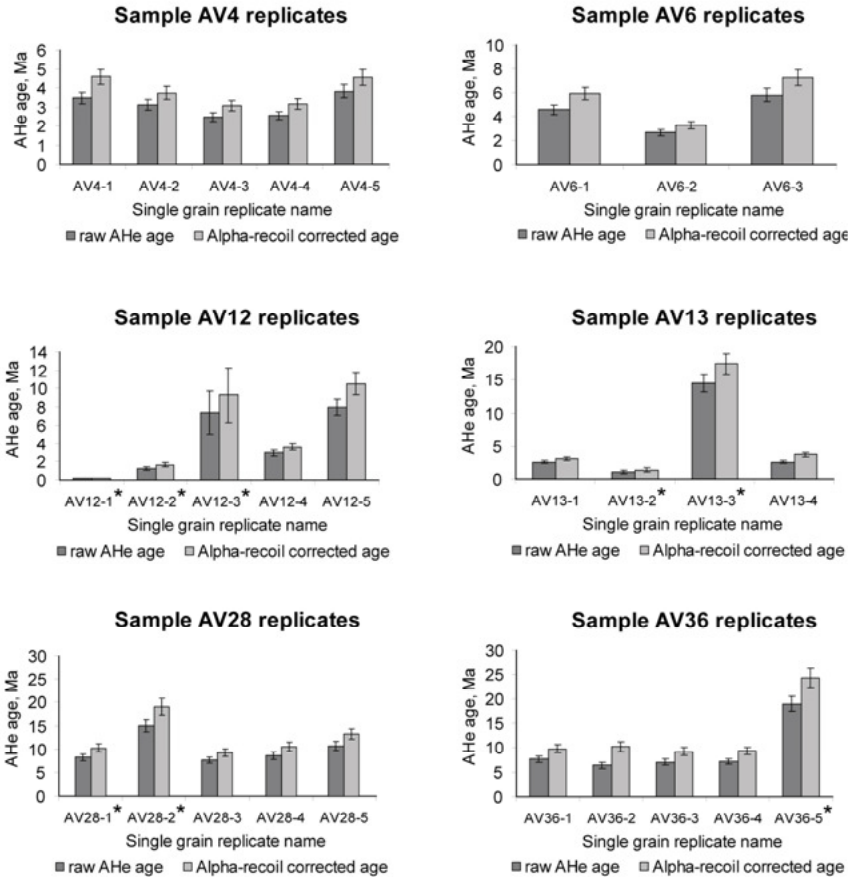

Figure IV.3.10. Comparison of the raw and alpha-ejection corrected AHe ages of the three to five replicates dated for each sample. The replicates marked with an (*) have been discarded for the reason detailed in Table 3 of section IV.2., before calculation of the error-weighted average AHe age.

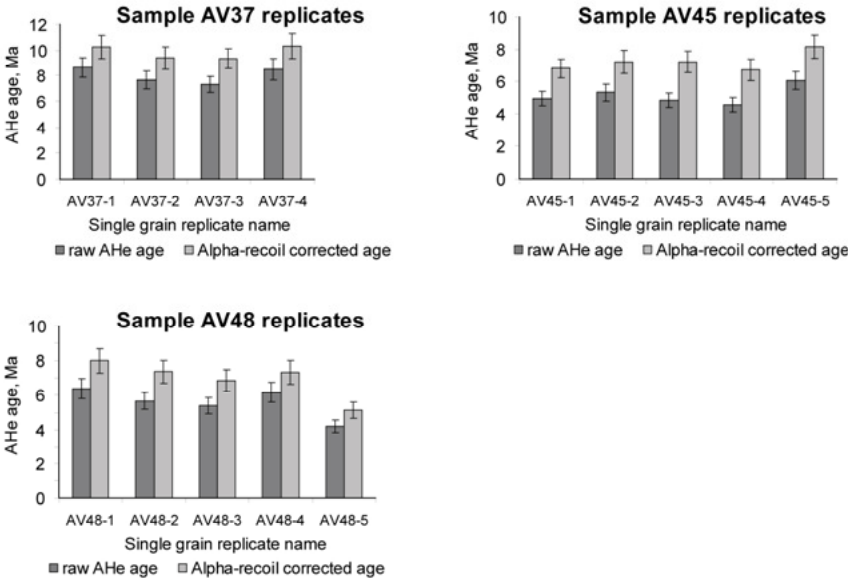

Figure IV.3.10. (continued)

IV.3.5. Dating deformation in the Aar massif

I concluded in section IV.2. that the late Neogene exhumation histories of the Lepontine Dome and the Aar massif differ significantly. In agreement with the predictions in Cederbom et al. (2004), I bring new evidence for an increase in exhumation rate since ca. 4 Ma in the Aar massif. Here, I describe the general steep foliation measured along a S-N transect in the upper Aar valley of the Aar massif (F1), and how the superposition of a series of shallower, north verging foliation planes (F2) at the northern front of the massif, joined to structural arguments, defines one of the frontal thrust of the massif such as described in Pfiffner, 1986. In order to understand the low-temperature deformation of the Aar massif, and to date the deformation along the frontal thrust, which constitutes a major landscape feature, I sampled on both walls of the thrust for AFT dating.Those samples have already been included among the "N-S transect" points of Table IV.2.2, but I will now present them with a focus on their position relative to the thrust.

IV.3.5.1. Foliation in the Aar massif

The contact between Mesozoic sediments of the Helvetic Unit and the northern front of the crystalline Aar massif has been described by Schmid et al. (1996) as a stack of north-verging, low-offset thrusts. According to Persaud and Pfiffner (2004), the orthogonal projection of well-located earthquakes suggests these fault planes are still active. Schmid and Kissling (2000), Schmid et al. (2004) and Rahn and Grasemann (1999) present a section of the northern Aar, with multiple thrusts of low offset. Although the description of several thrusts relies on seismic reflection data along the profile NFP 20-EAST, at least one of these thrusts can be seen outcropping in the northern part of our central Aar massif study area. In the southern part of the massif, the deformation is dominated by ductile shear-zones delimiting lense-shaped volumes of weakly foliated rock. This gneissification process was conducted by bulk heterogeneous shortening affecting the crystalline massif in a single deformation period (eg. Choukroune and Gapais, 1983; Gapais, 1985).

In the upper Aar valley (see location on Figure IV.3.11), I observed and measured foliation F1 across the entire massif, often marked by deformed porphyroid feldspars. Foliation F2 is present in the northern part of the massif only, and becomes increasingly concentrated northwards, changing from discrete planes separated by several cm, to a fully penetrative deformation. Relative to F1 foliation, the F2 foliation is recognized as more localised, and significantly shallower than the steep F1 planes.

Figure IV.3.12 presents measurements of the F1 foliation averaged at each outcrop. F1 foliation planes are characterized by a dip of approximately 61° towards N 143 °E (according to the value of mean vector calculated from the plane poles in Figure IV.3.11). F1 foliation is observed across the whole section of the Aar massif, however much less intensively in the northernmost region (north-west from the "Frontal Aar thrust" on Figure IV.3.12). F1 foliation is characterised by simple-shear deformation, as evidenced by observations of pervasive foliation planes perpendicular to magmatic aplite / coarse ocular gneiss boundaries, causing no offset to it.

Figure IV.3.13 presents measurements of the F2 foliation averaged at each outcrop. F2 foliation planes are characterized by a dip of approximately 26° towards N 128 °E (according to the value of mean vector calculated from the plane poles in Figure IV.3.11). The F2 foliation is not observed in the southern part of the section in the Aar massif. The density of planes increases between Guttannen (see Figure IV.3.13) and the Frontal Aar thrust, which is therefore not a discrete brittle structure. F2 foliation clearly offsets F1 as well as numerous centimeter thick quartz veins, thus postdating the emplacement of both features. I can therefore provide a relative dating of the F2 planes as younger than the F1, which marks bulk heterogeneous shortening affecting the crystalline massif (eg. Choukroune and Gapais, 1983; Gapais, 1985).

IV.3.5.2. AFT dating across the Aar frontal thrust

Figure IV.3.14 shows the Aar frontal thrust seen from the north-east, in the Urbach valley. Five samples were dated with AFT on the footwall of the thrust and compared with ages on the hangingwall, at similar elevations (Figure IV.3.15). The aim was to try and determine the age of deformation relative to AFT age, along with the amount of vertical offset.

I do not observe an age shift between AFT ages sampled on the hanging- or the footwall of the frontal thrust (Figure IV.3.15). This implies that both crossed the AFT partial annealing zone at the same time around 7 Ma, when the thrust had stopped activity. However, an age offset relative to elevation is not easy to evidence as the age-elevation relationship for AFT ages is poorly defined (see the dispersion of AFT ages on the hanging wall, figured by yellow dots). It is therefore possible that some vertical offset happening after AFT closure remains undetected. In addition, hot fluid circulation is likely during and after fault activation, which could contribute to the homogeneisation of AFT ages in the vicinity of a major fault zone.

As a conclusion, it very unlikely that this thrust constitutes a major structure responsible for the late Miocene - early Pliocene exhumation pulse observed in the Aar massif. Therefore, assuming that long-term exhumation recorded by low-temperature thermochronometers in the Aar massif is linked to contemporaneous rock uplift, the latter is likely not controlled by active faulting, but rather by large-scale flexure or regional uplift.

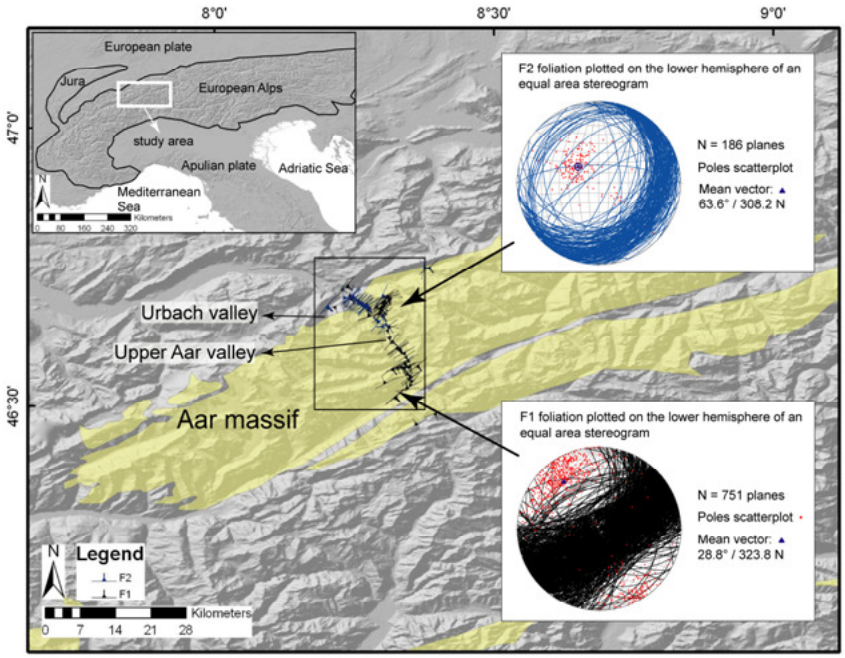

Figure IV.3.11. Study area: structural measurements of two families of foliation planes were performed in the Upper Aar valley, central Alps. The planes recorded are individual measurements that were later averaged at each outcrop (values shown on Figures IV.3.12, IV.3.13 and IV.3.15 are averages) using the "Plot mean vector" function of StereoWin program by R. Allmendinger (Cornell University; 2002), applied on the pole of the foliation planes.

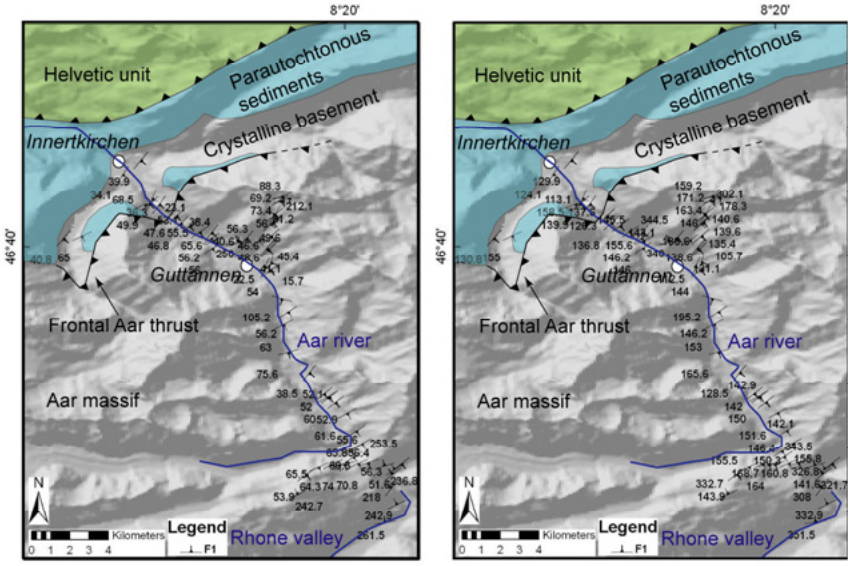

Figure IV.3.12. Detail of measurements of the F1 foliation along the upper Aar valley, upstream of Innertkirchen, Switzerland. (Left) Dip of foliation plane, in degree relative to the horizontal. (Right) Dip direction, in degree relative to north. Main geological units appear in color, and the frontal Aar thrust is highlighted. It is thrusting over the northernmost part of the Aar massif crystalline basement, and locally over the parautochtonous Mesozoic cover of the latter (blue patches between Innertkirchen and Guttannen).

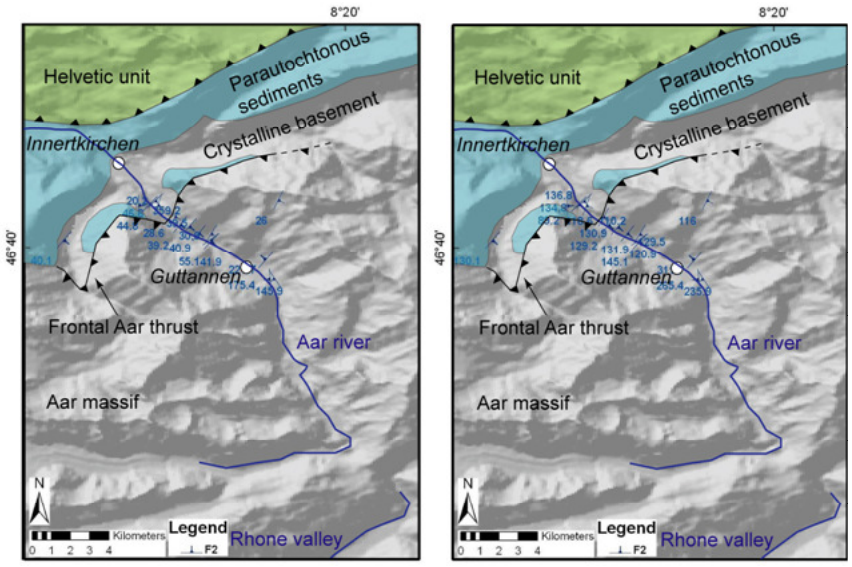

Figure IV.3.13. Same as Figure IV.3.12 for the F2 foliation planes.

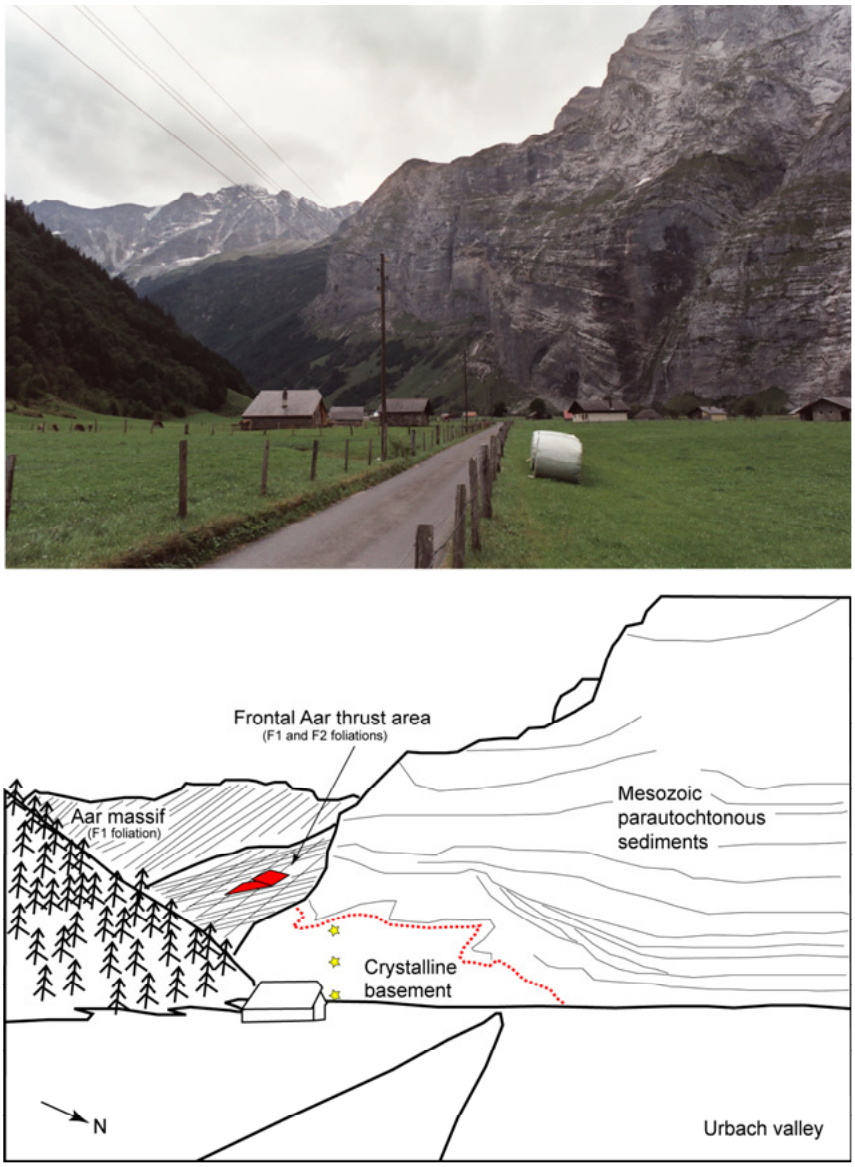

Figure IV.3.14. North verging thrust (see red arrow) at the northern Aar massif boundary, in the Urbach valley (location on Figures IV.3.11 and IV.3.15). The thrust, parallel to the F2 foliation, passes over the crystalline basement covered by Mesozoic sediments (red dotted line shows the discordance). The three yellow stars show the location of three AFT samples separated by approximately 100 m in elevation.

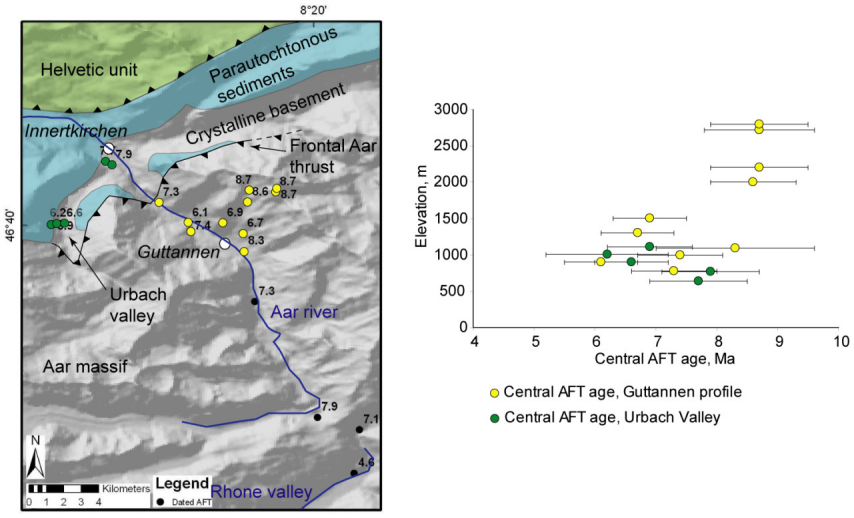

Figure IV.3.15. AFT dating on the footwall (green dots) and the hangingwall (yellow dots) of the frontal Aar thrust. (Left) Localization map showing main geological structures, AFT ages considered in the study of the frontal Aar thrust (coloured dots) and other AFT ages (black dots, see Table. (Right) Age-elevation plot of AFT central ages measured in the Guttannen elevation profile and under the frontal thrust.

Chapter V
Discussion

V.1. Overview and synthesis

This thesis has applied three approaches in order to investigate the hypothesis of a late Neogene increase in exhumation rate of the western European Alps and to assess the regional variability of this trend: (1) An apatite and zircon fission-track database, (2) new apatite fission-track and (U-Th) / He ages on two targeted areas of the Western Alps and (3), a GIS study of the spatial variation in parameters that potentially control exhumation rate.

In this discussion chapter, I will review the results obtained, compare their implications and propose directions for future work.

Chapter II confirms the reality of a signal of increased late Neogene exhumation in the Western Alps and has underlined regional differences in the expression of this signal. In Chapter III, I infer that the present-day patterns of stream power and seismic energy release are unable to explain long-term exhumation and present-day rock uplift, suggesting either that the short-term records of these parameters are not representative of their long-term action, or that they have not exercised an important control on exhumation in the Western Alps. Finally, Chapter IV records contrasting late Neogene exhumation histories for the northern-side (two pulses of higher exhumation rate between 9-7 and 5-3 Ma, or a steady exhumation rate of 0.4 km / Myr) and the southern-side of the mountain chain (steady 0.75 km / Myr exhumation rate or a single step of exhumation rate increase from 0.3 to 1 km / Myr at 5 Ma).

V.2. Description, interpretation and implications of results

V.2.1. Present-day controls on exhumation rates

Much emphasis has been placed on the interplay between climate and topography on the morphology of mountain belts (Montgomery et al., 2001), seismicity and denudation (Dadson et al., 2003) and precipitation and long-term exhumation (Reiners et al., 2003; Burbank et al., 2003).

The long-term exhumation pattern observed in the Western Alps is not correlated with present-day precipitation and stream power; this contrasts with results from the Cascade Mountains, northwest USA (Reiners et al., 2003). Smaller study areas such as the Queyras or

Ecrins, however, do exhibit strong negative correlation between precipitation rate and AFT age, highlighting a potential relationship between long-term exhumation and present-day erosive forcing in these massifs. The complex geometry of the Alps, contributing to potentially significant changes in precipitation gradients through time, and in particular during glaciations, may explain this difference. However, long-term exhumation is spatially correlated with present-day rock uplift rates, implying that the latter is the result of forcing parameters that have been steady for the last 5 Myr at least. These long-term forcing factors may be linked to tectonic deformation or isostatic rebound, but probably not to glacial erosion, as its onset as an efficient erosion agent is too recent (0.87 Ma; Scardia et al., 2006) to explain increased exhumation rates since ~5 Ma. The lack of correlation between released seismic energy and present-day uplift rate is counter to hypotheses involving a thrust-controlled uplift pattern, thus leaving only the orogenic-decay / isostatic-rebound explanation as a driver for the observed exhumation pattern. In contrast, the fact that present-day precipitation does not correlate with long-term exhumation rate does not necessarily imply that I should reject a long-term climate control on the 5 Ma exhumation increase, because the short-term record of precipitation does not necessarily reflect long-term patterns. Our results also demonstrate that seismicity in the Western Alps is not correlated with long-term exhumation, which is in contradiction with qualitative observations by Mosar (1999), Persaud and Pfiffner (2004), or Schlunegger and Hinderer (2001) in the central Alps. I propose that a statistical and larger-scale approach such as presented in section III.2 enables the avoidance of being misled by local high density of small earthquakes that do not contribute much to the total energy released at the orogen scale.

The results presented in section III.2 strongly suggest that present-day rock uplift and exhumation have been coupled for the last several million years, and that models based solely on the localisation of present precipitation or brittle deformation cannot explain the exhumation pattern; implying that rock uplift and exhumation during the late Neogene are controlled either by the passive isostatic response to increased denudation or by deep geodynamic processes.

V.2.2. Late Neogene increase in exhumation rate

In Chapter II, I show that the axial region of the Western Alps contains a record of a broad increase in exhumation rate around 5 Ma, consistent with the peri-alpine sedimentary record (Kuhlemann, 2000). In addition, average exhumation rates since AFT closure age are faster

than average exhumation rates between ZFT and AFT closure ages in the external part of the arc.

One of the questions at the basis of this study was to determine whether the late Neogene exhumation increase happened homogeneously over the Alps, or if some areas were more strongly affected than others. Both the variation in apparent age of onset of exhumation increase, dated in different regions between 6.5 and 2.5 Ma (see Figure II.2.10.), and the study of altitudinal transects using AFT and AHe ages enhanced by numerical modeling of exhumation scenarios (Chapter IV), confirm that regional differences in the exhumation record exist. The increase in exhumation rate at the Mio-Pliocene boundary, and the regional variations of this signal may have several reasons including heterogeneity in rock erodability, variability in the regional precipitation pattern and in tectonic uplift, or localised isostatic uplift in response to denudation, post-glacial unloading, or lithospheric mantle detachment. Although the discussion of potential mechanisms that follows enables consideration of these different parameters, further work is needed to determine the role of internal versus external forcing parameters in the recent exhumation of the Western Alps, as well as the partitioning between local and regional features. The difficulty lies in the fact that we only have access to snapshots of parameters value (such as precipitation, rock uplift, seismic energy released etc.), whereas the objective is to understand phenomena with long equilibrium timescales (Herman and Braun, 2006). Testable hypotheses include the fact that in a critical-wedge model for mountain belts, an increase in tectonic flux produces an increase in both rock uplift rate and relief, whereas an increase in precipitation leads to decreasing relief (Roe et al., 2006).

An important result of this study is that the amount of cumulated exhumation inferred from different approaches is significantly lower than the prediction of > 6.5 km since 5 Ma made by Cederbom et al. (2004), based on a simple crustal flexure model constrained by exhumation observations in the foreland basin. The estimates of axial range cumulated exhumation derived from isoage surfaces reach only 1 to 1.5 km between 5 and 2 Ma (Figure II.3.33), and 2 to 5 km in the last 5 Ma according to results of *Pecube* modeling (Figures IV.2.10 and IV.2.13).

The rejection of a simple isostatic flexural explanation for the exhumation of the molasse foreland basin leads me to review alternative possibilities. A first-order correction that needs to be made is that the observation of 1400 m of exhumation in the foreland basin (according to the elevation of an uplifted apatite fission-track partial annealing zone) does not necessarily

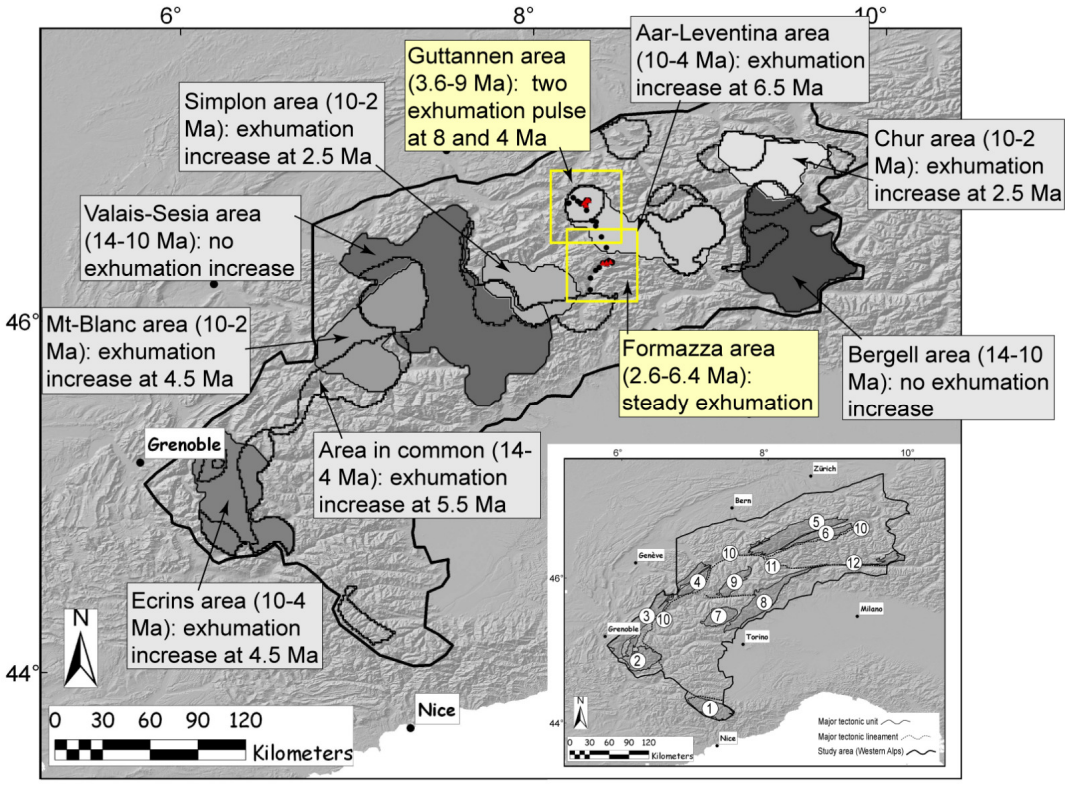

Figure V.2.1. Regional variation of the exhumation signals calculated over the Western Alps using the distance between isoage surfaces (grey boxes; see details in section II.2.) or *Pecube* modeling of AFT and AHe ages (yellow boxes; see details in section IV.2.). Each box contains information on the area name, the time length examined and the local exhumation history documented. The grey-shaded shapes within the Western Alps contour (thickest black line) correspond to the areas of continuous isoage surface coverage (see section II.2.). The yellow squares show the two areas used in *Pecube* modeling (see section IV.2.), with AFT and AHe ages used in the model (black and red dots respectively). The inset map shows the main tectonic features: 1) Argentera massif, 2) Ecrins massif, 3) Belledonne massif, 4) Mont Blanc massif, 5) Aar and 6) Gotthard massifs, 7) Gran Paradiso massif, 8) Sesia and 9) Dent Blanche massifs, 10) Penninic thrust, 11) Simplon fault, 12) Peri-Adriatic fault.

translate into 1400 m of tectonic uplift. A relevant argument against this can be found in nearby alpine foreland deposits of the Chambaran Plateau, where Champagnac et al. (2008) used abandoned Pliocene-Quaternary surfaces to quantify rock uplift: in this situation, exhumation of the surfaces since ~2 Ma is null, and surface uplift equates rock uplift.

Alternative explanations for exhumation of the molasse basin include tectonic underplating (Mosar, 1999) or the convective removal of thickened lithosphere (Lyon-Caen and Molnar, 1989; Genser et al., 2007). Although an event of slab detachment has been argued to have occurred early in the orogen history (Davies and von Blanckenburg, 1995; Sinclair, 1997), tomographic imaging of the upper mantle by Lippitsch et al. (2003) suggested lower lithosphere delamination progressing between the westernmost and the Central Alps. The

regional variation in age of delamination is likely to lead to along-strike variation in vertical motion, in turn explaining part of the regional variability in exhumation rate (Figure V.2.1).

A fall of base level linked to the extensive Messinian sea-level drop in the Mediterranean around 5.6 Ma, which has been argued to play a role on the southern and south-western flanks of the Alps (Clauzon et al., 1996; Foeken et al., 2003; Willett et al., 2006) can be rejected here. In effect, the Messinian erosion surface reached the Bresse graben (North of Lyon, France); but did not contour the Jura Mountains nor affect the Rhine watershed (Loget et al., 2006), so that the base-level of central molasse basin (Cederbom et al.'s study area) was not affected.

Climate change, causing increased erosion efficiency and positive feedback through isostatic response remains among the probable factors of molasse basin exhumation, as the end Miocene is characterised by global warming (Vidal et al., 2002), and likely reorganisation of oceanic circulation following the closure of the Panama straight (Haug and Tiedemann, 1998).

An interesting comparison can be made between our data and those of Gibson et al (2007) for the Pyrenees. These authors describe the Pyrenean exhumation history since 20 Ma as post-orogenic and characterized by a spatially constant but very limited exhumation rate of less than 0.2 km / Myr in average. I report significantly higher values of exhumation rates in sections II.2. and IV.2. in the Western Alps during the last 5 Ma, even though convergence and compressive deformation-controlled uplift were likely decreasing (Calais et al., 2001; this work, section III.2.). While keeping in mind that active deformation in the Alps occurred up to significantly more recently than 20 Ma (see the AFT and ZFT cross-sections perpendicular to the Simplon fault in section II.3.), this difference raises the question of whether two orogens of comparable width and elevation, and located in a similar climatic setting, can have such a different exhumation history without tectonic deformation or deep-seated internal forcing such as lithospheric mantle delamination affecting at least one of them (Lyon-Caen and Molnar, 1989; Platt and England, 1993; Lippitsch et al., 2003).

V.3 Future work

The methods developed and the results obtained in this thesis have raised a series of issues requiring further investigation in order to improve our understanding of late Neogene exhumation of the Alps.

V.3.1. Following on Chapter II

As more studies involving AFT ages in the Alps continue to be published, the update of the AFT database since its completion in 2006 would enable a better resolution in isoage surfaces computation. In particular, adding more boreholes and tunnel data would enable to constrain better the youngest isoage surfaces. It would also enable to lower the age-elevation relationship overestimation (the A1 slope in section II.2.4.3.1) due to surface sampling.

One limitation of the isoage surfaces obtained following the method described in section II.2 is the lack of uncertainty indicator, for the reasons detailed in II.2.6.2. It could be valuable to experiment ways to estimate the uncertainty in isoage surface elevation. One way worth exploring would require automating the process of calculating isoage surface elevation from a set of dated samples. Then, I could assess the degree of variation in the final maps by bootstrapping methods, i.e. testing a random number of age and elevation data taken from the database, as well as the effect of randomly perturbing sample location and density.

V.3.2. Following on Chapter III

The search of correlation between exhumation factors susceptible to control the exhumation rate may be significantly improved by using modified or updated data. For instance, the maps of stream power should be calibrated by river measurements in order to avoid the overestimation of river flow in areas with high evapo-transpiration. The map of rock uplift could provide a better coverage after collecting and rending compatible geodetic and newly available GPS data data over France and Italy. Finally, models of ice-flow could enable to assess the role of Pleistocene glacial erosion on long-term exhumation rates and present-day rock uplift rates. The study of local correlations could be improved by focusing on massif-scale catchments areas, including the available data of sediment transportation and erosion rates from cosmogenic isotopes. Refining the search of parameters correlated with exhumation at smaller scale would enable to determine whether our conclusions are valid at all scales or not.

V.3.3. Following on Chapter IV

The need for alpha-ejection He-loss age correction may be avoided by dating large apatite crystals, abraded in order to remove the external 20 µm rim; although this method introduces an additional error when crystals are zoned in Uranium and Thorium (Farley et al., 1996). The assessment of apatite compositional zonation, by techniques such as cathodo-luminescence, could be a diagnostic tool to decide whether alpha-ejection correction should be performed or not. The assessment of the nature and U-concentration of minerals surrounding the apatites is also suitable in order to take in consideration the implantation of He from a neighbour crystal (for instance, thin-section observation could determine that most apatites are included in biotites, the U-concentration of which could be determined independently).

The measurement of additional thermochronometers on the elevation profiles studied, such as zircon (U-Th) / He which is characterised by a closure temperature of ca. 180 °C (Reiners et al., 2004) would enable to constrain the exhumation history of the regions over a longer period of time, and in particular to test the hypothesis of an 8 Ma pulse of exhumation in the Lepontine Dome.

The use of inversion techniques to test iteratively several thousands of combinations of parameters value in *Pecube* would enable to sample the exhumation and relief-change parameters space a lot more exhaustively than was done in this study (e.g. Braun and Robert, 2005). Doing so would permit better constraints on the conditions that lead to the smallest misfit values between measured and predicted ages, and possibly determine "local optima" in parameters value that may lead to erroneous conclusions when the number of model tested is low.

V.3.4. Understanding the causes and effects of recent exhumation

The prediction of at least 6.5 km of exhumation occurring in the axial part of the belt as a cause for the flexural unloading of the European plate and the observed exhumation in the Swiss Molasse foreland basin (Cederbom et al., 2004) deserves further attention. A reassessment of this prediction would involve quantifying thrust-controlled tectonic uplift along the Jura detachment surface (Becker, 2000; Mosar, 1999), extending the regional coverage of the estimates of denudation in the foreland basin, and testing a range of elastic thicknesses for the European plate.

The spatial variations in late Neogene exhumation rates (Figure V.2.1) observed in Chapter II and IV are yet unexplained. They may result from differential erosion due to local hotspots of precipitation, be localised on the hangingwall of active thrusts or the footwall of normal faults, or respond to local hotspots of rock uplift caused by erosional, glacial or mantle delamination isostatic rebound. Further work is needed to study the lateral extent of areas with different exhumation histories, determine whether they correspond with tectonic units, and ultimately understand if the local rates of denudation were controlled by climate, tectonic uplift or isostatic response to unloading.

The efficiency of glacial vs. fluvial erosion is still a matter of debate. Nevertheless, the quantification of Pleistocene glacial erosion might serve at least two purposes: (1) constrain better the amount of rock uplift accountable to glaciation versus deglaciation. By assuming that the uplift due to deformation can be neglected, and subtracting the uplift due to deglaciation and erosion from the measured uplift rate, it becomes possible to quantify the role of deep-seated processes such as lithospheric mantle delamination. (2) Erosion of the southern Alpine foreland contemporaneous to Messinian base level fall has been advanced by Willett et al. (2006) as a substantial factor in the reorganisation of the deformation field in the Western Alps. However, the relative importance of Messinian fluvial incision and Quaternary glacial erosion in the Great Italian Lakes valleys remains poorly constrained. The age difference between these two processes should enable to discriminate between them using a very low temperature thermochronometer. These two objectives would be fulfilled by dating valley incision using the newly developed ^{4}He / ^{3}He technique (Shuster, 2005). This tool, not yet applied to the study of Alpine geomorphology is likely to provide groundbreaking advances in the understanding of Alpine relief evolution.

Chapter VI
General Conclusions

The main conclusions of this thesis are:

I)

- Based on the reconstruction of AFT isoage surfaces and the quantification of volumes of material separating these surfaces, I confirm a late Neogene increase in exhumation rate in the Western Alps, proposed previously from an analysis of the sedimentary record.
- The consistency between exhumation rate estimates using sediment volumes and AFT isoage surfaces validates the use of both techniques in the case of an orogen characterized by high relief and limited deformation.
- There are likely regional differences in the time of onset of the Plio-Peistocene exhumation pulse from one massif to another.
- Overall, exhumation rates accelerated in the external part of the belt since closure of the AFT system, whereas they decelerated in more internal regions of the arc.

II)

- There is a strong spatial link between long-term exhumation (documented by AFT ages at the surface, or the distance between the 4 and 2 Ma AFT isoage surfaces), present-day rock uplift and elevation in the Western Alps.
- Present-day rock uplift is not correlated with seismic energy released, and therefore probably not with convergence-related thrusting. This suggests an isostatic control of the uplift pattern, either due to glacial or erosional unloading, or to deep-seated process affecting the isostatic balance of the orogen. However, the link between uplift and long-term exhumation rules out the possibility that the uplift pattern is only controlled by recent post-glacial rebound.
- I do not demonstrate a link between long-term exhumation rates and either precipitation or seismic energy released. This may underline that present-day values of these parameters are not representative of the long-term trends, or that a deep-seated unaccounted factor (such as delamination of thickened lithosphere) plays a role in controlling the rates of uplift and long-term exhumation.

III)

- I describe significant regional differences in low-temperature thermochronology ages between the Aar and Lepontine massifs.

- A possible qualitative interpretation of the age-elevation relationships consists in a three phase scenario affecting both areas, with less denudation after 6 Ma in the Guttannen area. This scenario comprises fast exhumation between 9 and 7 Ma, slower between 7 and 5 Ma and fast again between 5 and 3 Ma.
- Age predictions using the model *Pecube* and over one hundred different exhumation and relief change scenarios in each study area yield multiple likely solutions matching measured ages.
- Among scenarios found to be likely in the Lepontine study area, figures a steady rate of ca. 0.75 km / Myr for at least the denudation of the last 6 km, in accord with previous inferences from detrital thermochronology.
- Among scenarios found to be likely in the Aar massif area, figures two pulses of exhumation at ~8 and ~4 Ma; in agreement with the qualitative interpretation of age-elevation profiles. However, the amount of exhumation associated with the 4-Ma pulse is not sufficient to explain the amount of rock uplift recorded in the Molasse Basin by flexural isostatic response to denudation of the orogen core.
- The above misfit requires an additional cause for uplift and erosion of the Molasse Basin, possibly including: differential uplift in the Molasse basin due to Pliocene deformation, under-estimation of the elastic thickness of the European lithosphere, uplift of the Molasse basin over a crustal ramp, or lithospheric mantle delamination inducing the uplift of the Molasse Basin.

References

Abrecht, J., 1994, Geologic units of the Aar massif and their pre-Alpine rock associations: a critical review: Schweitzerische Mineralogische und Petrographische Mitteilungen, v. 74, p. 5-27.

Allen, P.A., Homewood, P., Williams, G.D., 1986, Foreland basins: an introduction: Special Publication of the International Association of Sedimentologists, v. 8, p. 3-12.

Aramowicz, A., Cosca, M.A., Farley, K.A., Seward, D., Stöckli, D.F., 2007, Very high exhumation rates in the central Swiss Alps, revealed by the (U-Th)/He and fission track analyses: Goldschmidt Conference Abstracts, 55/A32.

Becker, A., 2000, The Jura Mountains - An active foreland fold-and-thrust belt? Tectonophysics, v. 321, p. 381-406.

Bernet, M., Zattin, M., Garver, J.I., Brandon, M.T., Vance, J.A., 2001, Steady-state exhumation of the European Alps: Geology, v. 29, p. 35-38.

Bigot-Cormier F., 2002, La surrection du massif cristallin externe de l'Argentera (France-Italie) et ses relations avec la déformation pliocène de la marge nord-Ligure : arguments thermochronologiques (traces de fission), géomorphologiques et interprétations de sismique marine: PhD Thesis, University of Nice, France, 352 p.

Bistacchi, A., Massironi, M., 2000, Post-nappe brittle tectonics and kinematic evolution of the north-Western Alps: an integrated approach, Tectonophysics: v. 327, p. 267-292.

Bogdanoff, S., Michard, A., Mansour, M., Poupeau, G., 2000, Apatite fission track analysis in the Argentera massif: evidence of contrasting denudation rates in the External Crystalline Massifs of the Western Alps: Terra Nova, v. 12, p. 117-125.

Bousquet, R., Goffé, B., Henry, P., Le Pichon, X., Chopin, C., 1997, Kinematic, thermal and petrological model of the Central Alps: Lepontine metamorphism in the upper crust and eclogitisation of the lower crust: Tectonophysics, v. 273, p. 105-127.

Boyce, J.W., Hodges, K.V., 2005, U and Th zoning in Cerro de Mercado (Durango, Mexico) fluorapatite: Insights regarding the impact of recoil redistribution of radiogenic ^{4}He on (U-Th)/He thermochronology: Chemical Geology, v. 219, p. 261-274.

Brandon, M.T., 1992, Decomposition of fission-track grain-age distributions: American Journal of Science, v. 292, p. 535-564.

Brandon, M.T., 1996, Probability density plot for fission-track grain-age samples: Radiation Measurements, v. 26, p. 663-676.

Brandon, M.T., Roden-Tice, M.K., Garver, J.I., 1998, Late Cenozoic exhumation of the Cascadia accretionary wedge in the Olympic Mountains, Northwest Washington State: Geological Society of America Bulletin, v. 110, p. 985-1009.

Braun, J., 2002, Quantifying the effect of recent relief changes on age-elevation relationships: Earth and Planetary Science Letters, v. 200, p. 331-343.

Braun, J., 2003, Pecube: a new finite-element code to solve the 3D heat transport equation including the effects of a time-varying, finite amplitude surface topography: Computers and Geosciences, v. 29, p. 787-794.

Braun, J., Robert, X., 2005, Constraints on the rate of post-orogenic erosional decay from low-temperature thermochronological data: application to the Dabie Shan, China: Earth Surface Processes and Landforms, v. 30, p. 1203-1225.

Braun, J., van der Beek, P., Batt, G., 2006, Quantitative Thermochronology: Numerical methods for the interpretation of thermochronological data. Cambridge University Press, Cambridge. 270 p.

Brocard, G.Y., van der Beek, P.A., Bourlès, D.L., Siame, L.L., Mugnier, J.-L., 2003, Long-term fluvial incision rates and postglacial river relaxation time in the French Western Alps from 10Be dating of alluvial terraces with assessment of inheritance, soil development and wind ablation effects: Earth and Planetary Science Letters, v. 209, p. 197-214.

Burbank, D.W., Blythe, A.E., Putkonen, J.K., Pratt-Sitaula, B.A., Gabet, E.J., Oskin, M.E., Barros, A.P., Ojha, T.P., 2003, Decoupling of erosion and precipitation in the Himalaya: Nature, v. 426, p. 652-655.

Bürgi, A., Klötzli, U., 1990, New data in the Evolutionary History of the Ivrea Zone (Northern Italy): Bulletin der Vereinigung Schweizerische Petroleum-Geologen und Ingenieur, v. 56, p. 49-69.

Burov, E., Diament, M., 1996, Isostasy, equivalent elastic thickness, and inelastic rheology ofcontinents and oceans: Geology, v. 24, p. 419-422.

Calais, E., Nocquet, J.-M., Jouanne, F., Tardy, M., 2002, Current strain regime in the Western Alps from continuous Global Positioning System measurements, 1996-2001: Geology, v. 30, p. 651-654.

Carpéna, J., 1992, Fission track dating of zircon: zircons from Mont Blanc Granite (French-Italian Alps): The Journal of Geology, v. 100, p. 411–421.

Carpéna, J., Caby, R., 1984, Fission track evidence for late Triassic oceanic crust in the French Occidental Alps: Geology, v. 12, p. 108–111.

Carpéna, J., Pognante, U., Lombardo, B., 1986, New constraints for the timing of the Alpine metamorphism in the internal ophiolithic nappes from the Western Alps as inferred from fission track data: Tectonophysics, v. 127, p. 117-127.

Cederbom, C.E., Sinclair, H.D., Schlunegger, F., Rahn, M.K., 2004, Climate-induced rebound and exhumation of the European Alps: Geology, v. 32, p. 709-712.

Challandes, N., 2001, Comportement des systèmes isotopiques 39Ar-40Ar et Rb-Sr dans les zones de cisaillement: Exemples du massif de l'Aar (massif cristallins externes) et de la nappe de Suretta (Alpes centrales suisses), Université de Neuchâtel, PhD, 268 p.

Champagnac, J.-D., Molnar, P., Anderson, R.S., Sue, C., Delacou, B., 2007, Quaternary erosion-induced isostatic rebound in the western Alps: Geology, v. 35, p 195-198.

Champagnac, J.D., van der Beek, P., Diraison, G., and Dauphin, S., 2008, Flexural isostatic response of the Alps to increased Quaternary erosion recorded by foreland basin remnants, SE France: Terra Nova, in press.

Choukroune, P., Gapais, D., 1983, Strain pattern in the Aar Granite (Central Alps): orthogneiss developed by bulk inhomogeneous flattening: Journal of Structural Geology, v. 5, p. 411-418.

Ciancaleoni, L., 2005, Deformation processes during the last stages of the continental collision: the brittle-ductile fault systems in the Bergell and Insubric areas (Eastern Central Alps, Switzerland – Italy): PhD Thesis, University of Neuchâtel, Switzerland, 202 p.

Clauzon, G., Suc, J.-P., Gautier, F., Berger, A., Loutre, M.-F., 1996, Alternate interpretation of the Messinian salinity crisis: Controversy resolved? Geology, v. 24, p. 363-366.

Dadson, S.J., Hovius, N., Chen, H., Dade, W.B., Hsieh, M.-L., Willett, S.D., Hu, J.-C., Horng, M.-J., Chen, M.-C., Stark, C.P., Lague, D., Lin, J.-C., 2003, Links between erosion, runoff variability and seismicity in the Taiwan orogen: Nature, v. 426, p. 648-651.

Daly, C., Neilson, R.P. and Phillips, D.L., 1994, A statistical-topographic model for mapping climatological precipitation over mountainous terrain: Journal of Applied Meteorology, v. 33, p. 140-158.

Davies, T.A., Hay, W.W., Southam, J.R., Worseley, T.R., 1977, Estimates of Cenozoic oceanic sedimentation rates: Science, v. 197, p. 53–55.

Davies, J.H., von Blanckenburg, F., 1995, Slab breakoff: A model of lithosphere detachment and its test in the magmatism and deformation of collisional orogens: Earth And Planetary Science Letters, v. 129, p. 85-102.

Debelmas, J., Lemoine, M., 1970, The Western Alps: Paleogeography and Structure: Earth-Science Reviews, v. 6, p. 221-256.

Delacou, B., Sue, C., Champagnac, J.-D., Burkhard, M., 2004, Present-day geodynamics in the bend of the western and central Alps as constrained by earthquake analysis: Geophysical Journal International, v. 158, p. 753-774, doi:10.1111/j.1365-246X.2004.02320.x.

Dodson, M.H., 1973, Closure temperature in cooling geochronological and petrological systems: Contributions to Mineralogy and Petrology, v. 40, p. 259-274.

Donelick, R.A., O'Sullivan, P.B., Ketcham, R.A., 2005, Apatite Fission-Track Analysis: Reviews in Mineralogy and Geochemistry, v. 58, p. 49-94.

Dunai, T.J., 2005, Forward Modeling and Interpretation of (U-Th)/He Ages: Reviews in Mineralogy and Geochemistry, v. 58, p. 259-274.

Dunkl, I., 2002, TRACKKEY: a Windows program for calculation and graphical presentation of fission track data: Computers and Geosciences, v. 28 p. 3-12.

Ehlers, T.A., Farley, K.A., Rusmore, M.E., Woodsworth, G.J., 2006, Apatite (U-Th)/He signal of large-magnitude accelerated glacial erosion, southwest British Columbia: Geology, v. 34, p. 765-768.

England, P., Molnar, P., 1990, Surface uplift, uplift of rocks, and exhumation of rocks: Geology, v. 18, p. 1173-1177.

Evans, N.J., Byrne, J.P., Keegan, J.T., Dotter, L.E., 2005, Determination of Uranium and Thorium in Zircon, Apatite, and Fluorite: Application to Laser (U-Th)/He Thermochronology: Journal of Analytical Chemistry, v. 60, p. 1159-1165.

Fantoni, R., Bersezio, R., Forcella, F., 2004, Alpine structure and deformation chronology at the Southern Alps-Po Plain border in Lombardy: Bollettino della Societa Geologica Italiana, v. 123, p. 463-476.

Farley, K.A., 2000, Helium diffusion from apatite: General behavior as illustrated by Durango fluorapatite: Journal of Geophysical Research, v. 105, p. 2903-2914.

Farley, K.A., 2002, (U-Th)/He Dating: Techniques, Calibrations, and Applications, Noble Gases in Geochemistry and Cosmochemistry, Volume 47: Reviews in Mineralogy and Geochemistry, p. 844-819.

Farley, K.A., Stockli, D.F., 2002, (U-Th)/He Dating of Phosphates: Apatite, Monazite, and Xenotime: Reviews in Mineralogy and Geochemistry, v. 48, p. 559-577.

Farley, K.A., Wolf, R.A., Silver, L.T., 1996, The effects of long alpha-stopping distances on (U-Th)/He ages: Geochimica et Cosmochimica Acta, v. 60, p. 4223-4229.

Finlayson, D.P., Montgomery, D.R., Hallet, B., 2002, Spatial coincidence of rapid inferred erosion with young metamorphic massifs in the Himalayas: Geology, v. 30, p. 219-222.

Flisch, M., 1986, Die Hebungsgeschichte der oberostalpinen Silvretta-Decke seit der mittleren Kreide: Bulletin der Vereinigung Schweizerische Petroleum-Geologen und Ingenieur, v. 53, p. 23-49.

Florineth, D., Schlüchter, C., 2000, Alpine evidence for atmospheric circulation patterns in Europe during the Last Glacial Maximum: Quaternary Research, v. 54, p. 295-308.

Foeken, J.P.T., Dunai, T.J., Bertotti, G., Andriessen, P.A.M., 2003, Late Miocene to present exhumation in the Ligurian Alps (southwest Alps) with evidence for accelerated denudation during the Messinian salinity crisis: Geology, v. 31, p. 797-800.

Foeken, J.P.T., Stuart, F.M., Dobson, K.J., Persano, C., Vilbert, D., 2006, A diode laser system for heating minerals for (U-Th)/He chronometry: Geochemistry, Geophysics, Geosystems, v. 7, p. Q04015, doi:10.1029/2005GC001190.

Frei, C., Schär, J., 1998, A precipitation climatology of the Alps from high resolution rain gauge observations: Journal of Climatology, v. 18, p. 873-900.

Frey, M., Bucher, K., Frank, E., Mullis, J., 1980, Alpine metamorphism along the Geotraverse basel-Chiasso - a review: Eclogae geologicae Helvetiae, v. 73/2, p. 527-546.

Frey, M., Ferreiro Maehlmann, R., 1999, Alpine metamorphism of the Central Alps: Schweitzerische Mineralogische und Petrographische Mitteilungen, v. 79, p. 135-154.

Fügenschuh, B., Loprieno, A., Ceriani, S., Schmid, S.M., 1999, Structural analysis of the Subbriançonnais and Valais units in the area of Moûtiers, Savoy, Western Alps: paleogeographic and tectonic consequences: International Journal of Earth Sciences, v. 88, p. 201-218.

Fügenschuh, B., Schmid, S.M., 2003, Late stages of deformation and exhumation of an orogen constrained by fission track data: A case study in the Western Alps: Geological Society of America Bulletin, v. 115, p. 1425-1440.

Gabet, E.J., Burbank, D.W., Pratt-Sitaula, B., Putkonen, J., Bookhagen, B., 2008, Modern erosion rates in the High Himalayas of Nepal: Earth and Planetary Science Letters, v. 267, p. 482-494.

Galbraith, R.F., 2005, Statistics for Fission Track Analysis: Boca Raton, Chapman and Hall/CRC, 219 p.

Galbraith R.F., Laslett, G.M., 1993, Statistical models for mixed fission track ages: Nuclear Tracks, v. 21, p. 459–70.

Gallagher, K., Brown, R., 1999, Denudation and uplift at passive margins: the record on the Atlantic margin of southern Africa: Philosophical Transactions of the Royal Society of London, v. 357, p. 835-859.

Gallagher, K., Brown, R., Johnson, C., 1998, Fission track analysis and its applications to geological problems: Annual Review of Earth and Planetary Sciences, v. 26, p. 519-572.

Gapais, D., 1985, Les massifs cristallins externes sur une transversale Guttanen-Val Bedretto (Alpes Centrales) : structures et histoire cinématique: Comptes Rendus de l'Académie des Sciences de Paris, v. 301-II, p.543-546.

Garzanti, E., Malusa, M.G., 2008, The Oligocene Alps: Domal unroofing and drainage development during early orogenic growth: Earth and Planetary Science Letters, v. 268, p. 487-500.

Genser, J., Cloetingh, S.A.P.L., Neubauer, F., 2007, Late orogenic rebound and oblique Alpine convergence: New constraints from subsidence analysis of the Austrial Molasse basin: Global and Planetary Change, v. 58, p. 214-223.

Gibson, M., Sinclair, H.D., Lynn, G.J., Stuart, F.M., 2007, Late- to post-orogenic exhumation of the Central Pyrenees revealed through combined thermochronological data and modelling: Basin Research, v. 19, p. 323-334.

Giger, M., 1991, Geochronologische und petrographische Studien an Geröllen und Sedimenten der Gonfolite Lombarda Gruppe (Südschweiz und Norditalien) und ihr Vergleich mit dem alpinen Hinterland: PhD Thesis, University of Bern, Switzerland, 227 p.

Glotzbach, C., Reinecker, J., Danišík, M., Rahn, M., Frisch, W., Spiegel, C., 2008, Exhumation of the Mont Blanc and Gotthard massifs, forced by tectonics or climate?: Geophysical Research Abstracts, v. 10, SRef-ID: 1607-7962/gra/EGU2008-A-08040.

Green, P.F., Crowhurst, P.V., Duddy, I.R., Japsen, P., Holford, S.P., 2006, Conflicting (U-Th)/He and fission track ages in apatite: Enhanced He retention, not anomalous annealing behaviour: Earth And Planetary Science Letters, v. 250, p. 407-427.

Green, P.F., Duddy, I.R., Laslett, G.M., Hegarty, K.A., Gleadow, A.J.W., Lovering J. F., 1989, Thermal annealing of fission tracks in apatite 4. Quantitative modelling techniques and extension to geological timescales: Chemical Geology, v. 79, p. 155–182.

Grosjean, G., Sue, C., Burkhard, M., 2004, Late Neogene extension in the vicinity of the Simplon fault zone (central Alps, Switzerland): Eclogae geologicae Helvetiae, v. 97, p. 33-46.

Gutenberg, B, Richter, C.F., 1954, Seismicity of the Earth and Associated Phenomena: Princeton University Press, Princeton, New Jersey, 245 pp.

Haug, G.H., Tiedemann, R., 1998, Effect of the formation of the Isthmus of Panama on Atlantic Ocean thermohaline circulation: Nature, v. 393, p. 673-676.

Hendricks, B.W.H., Redfield, T.F., 2005, Apatite fission track and (U-Th)/He data from Fennoscandia: An example of underestimation of fission track annealing in apatite: Earth and Planetary Science Letters, v. 236, p. 443-458.

Herman, F., Braun, J., 2006, Fluvial response to horizontal shortening and glaciations: A study in the Southern Alps of New Zealand: Journal Of Geophysical Research-Earth Surface, v. 111, p. F01008, doi:10.1029/2004JF000248.

Hinderer, M., 2001, Late Quaternary denudation of the Alps, valley and lake fillings and modern river loads: Geodinamica Acta, v. 14, p. 231-263.

Homewood, P., Allen, P.A., Williams, G.D., 1986, Dynamics of the Molasse Basin of western Switzerland: Special Publication of the International Association of Sedimentologists, v. 8, p. 199-217.

Hourigan, J.K., Reiners, P.W., Brandon, M.T., 2005, U-Th zonation-dependent alpha-ejection in (U-Th)/He chronometry: Geochimica et Cosmochimica Acta, v. 69, p. 3349-3365.

Hunziker, J.C., Desmons, J., Hurford, A.J., 1992, Thirty-two years of geochronological work in the Central and Western Alps: a review on seven maps: Memoires de Geologie (Lausanne), v. 13, 59 p.

Hurford, A.J., 1986, Cooling and uplift patterns in the Lepontine Alps, South Central Switzerland and an age of vertical movement of the Insubric fault line: Contributions to Mineralogy and Petrology, v. 92, p. 413-427.

Hurford, A.J., 1991, Uplift and cooling pathways derived from fission track analysis and mica dating: a review: Geologische Rundschau, v. 80, p. 349-368.

Hurford, A.J., Green, P.F., 1982, A user's guide to fission track dating calibration: Earth and Planetary Science Letters, v. 59, p. 343-354.

Hurford, A.J., Green, P.F., 1983, The Zeta age calibration of fission-track dating: Chemical Geology, v. 1, p. 285-317.

Hurford, A.J., Hunziker, J.C., 1985, Alpine cooling history of the Monte Mucrone eclogites: Schweizerische Mineralogische und Petrographische Mitteilungen, v. 65, p. 325-334.

Hurford, A.J., Hunziker, J.C., 1989, A revised thermal history for the Gran Paradiso massif: Schweizerische Mineralogische und Petrographische Mitteilungen, v. 69, p. 319-329.

Hurford, A.J., Hunziker J.C., Stöckhert, B., 1991, Constraints on the late thermotectonic evolution of the Western Alps: Evidence for episodic rapid uplift: Tectonics, v. 10, p. 758-769.

Keller, L.M., Fügenschuh, B., Hess, M., Schneider, B., Schmid, S. M., 2006, Simplon fault zone in the western and central Alps: Mechanism of Neogene faulting and folding revisited: Geology, v. 34, p. 317-320.

Keller, L.M., Hess, M., Fügenschuh, B., Schmid, S., 2005, Structural and metamorphic evolution of the Camughera-Moncucco, Antrona and Monte Rosa units southwest of the Simplon line, Western Alps: Eclogae geologicae Helvetiae, v. 98, p. 19-49.

Knaus, A., 1990, Apatit-Spaltspurendatierungen in Rätikon (Arosazone, Östalpen), part 1: Diploma Thesis, University of Tübingen, Germany, 60 p.

Kuhlemann, J., 2000, Post-collisional sediment budget of circum-Alpine basins (Central Europe): Memorie di Scienze Geologiche, Padova, v. 52, p. 1-91.

Kuhlemann, J., 2007, Paleogeographic and paleotopographic evolution of the Swiss and Eastern Alps since the Oligocene: Global and Planetary Change, v. 58, p. 224-236.

Kuhlemann, J., Frisch, W., Székely, B., Dunkl, I., and Kázmér, M., 2002, Post-collisional sediment budget history of the Alps: tectonic versus climatic control: International Journal of Earth Sciences, v. 91, p. 818-837.

Laslett, G.M., Green, P.F., Duddy, I.R., Gleadow, A.J.W., 1987, Thermal annealing of fission tracks in apatite 2. A Quantitative Analysis: Chemical Geology (Isotope Geoscience Section), v. 65, p. 1-13.

Lelarge, L., 1993, Thermochronologie par la méthode des traces de fission d'une marge passive (Dome de Ponta Grossa, SE Brésil) et au sein d'une chaîne de collision (zone externe de l'arc alpin, France): PhD Thesis, University of Grenoble, France, 252 p.

Leloup, P.H., Arnaud, N., Sobel, E.R., Lacassin, R., 2005, Alpine thermal and structural evolution of the highest external crystalline massif: The Mont Blanc: Tectonics, v. 24, p. TC4002, doi:10.1029/2004TC001676.

Lihou, J., Hurford, A., Carter, A., 1995, Preliminary fission-track ages on zircons and apatites from the Sardona unit, Glarus Alps, eastern Switzerland: late Miocene-Pliocene exhumation rates: Schweizerische Mineralogische und Petrographische Mitteilungen, v. 75, p. 177-186.

Lippitsch, R., Kissling, E., Ansorge, J., 2003, Upper mantle structure beneath the Alpine orogen from high-resolution teleseismic tomography: Journal of Geophysical Research B: Solid Earth, v. 108, p. doi:10.1029/2002JB002016.

Loget, N., Davy, P., Van Den Driessche, J., 2006, Mesoscale fluvial erosion parameters deduced from modeling the Mediterranean sea level drop during the Messinian (late Miocene): Journal of Geophysical Research, v. 111, p. F03005, doi:10.1029/2005JF000387.

Lyon-Caen, H., Molnar, P., 1989, Constraints on the deep structure and dynamic processes beneath the Alps and adjacent regions from an analysis of gravity anomalies: Geophysical Journal International, v. 99, p. 19-32.

Malusa, M.G., Polino, R., Zattin, M., Bigazzi, G., Martin, S., Piana, F., 2005, Miocene to Present differential exhumation in the Western Alps: Insights from fission track thermochronology: Tectonics, v. 24, p. TC3004, doi:10.1029/2004TC001782.

Marquer, D., Burkhard, M., 1992, Fluid circulation, progressive deformation and mass-transfer processes in the upper crust: the example of basement-cover relationships in the External Crystalline Massifs, Switzerland: Journal of Structural Geology, v. 14, p. 1047-1057.

Marquer, D., Gapais, D., 1985, Les massifs cristallins externes sur une transversale Guttannen-Val Bedretto (Alpes Centrales): structures et histoires cinématiques: Comptes Rendus de l'Académie des Sciences de Paris, v. 301,II, p. 543-546.

Meesters, A.G.C.A., Dunai, T.J., 2002, Solving the production-diffusion equation for finite diffusion domains of various shapes. Part II. Application to cases with a-ejection and nonhomogeneous distribution of the source: Chemical Geology, v. 186, p. 347-363.

Meesters, A.G.C.A., Dunai, T.J., 2005, A noniterative solution of the (U-Th)/He age equation: Geochemistry, Geophysics, Geosystems, v. 6, p. Q04002, doi:10.1029/2004GC000834.

Michalski, I., Soom, M., 1990, The Alpine thermo-tectonic evolution of the Aar and Gotthard massifs, Central Switzerland: Fission-Track ages on zircons and apatites and K-Ar mica ages: Schweizerische Mineralogische und Petrographische Mitteilungen, v. 70, p. 373-387.

Milnes, A.G., 1974, Structure of the Pennine Zone (Central Alps): A New Working Hypothesis: Geological Society of America Bulletin, v. 85, p. 1727-1732.

Molnar, P., 2004, Late Cenozoic Increase in Accumulation Rates of Terrestrial Sediment: How Might Climate Change Have Affected Erosion Rates?: Annual Review Earth and Planetary Sciences, v. 32, p. 67-89.

Molnar, P., England, P., 1990, Late Cenozoic uplift of mountain ranges and global climate change: chicken or egg?: Nature, v. 346, p. 29-34.

Montgomery, D.R., Balco, G., Willett, S.D., 2001, Climate, tectonics, and the morphology of the Andes: Geology, v. 29, p. 579-582.

Morris, R.G., Sinclair, H.D., Yelland, A.J., 1998, Exhumation of the Pyrenean orogen: implications for sediment discharge: Basin Research, v. 10, p. 69-85.

Mosar, J., 1999, Present-day and future tectonic underplating in the western Swiss Alps: reconciliation of basement/wrench-faulting and decollement folding of the Jura and Molasse basin in the Alpine foreland: Earth and Planetary Science Letters, v. 173, p. 143-155.

Noether, G.E., 1981, Why Kendall Tau?: Teaching Statistics, v. 3, p. 41-43.

Pawlig, S., 2001, Geological Evolution of the Monte Rosa: Constraints from Geochronology and Geochemistry of a Talc-Kyanite-Chloritoid Shear Zone within the Monte Rosa Granite (Monte Rosa Nappe, Italian Western Alps): PhD Thesis, University of Mainz, Germany, 149 p.

Persaud, M., Pfiffner, O.A., 2004, Active deformation in the eastern Swiss Alps: post-glacial faults, seismicity and surface uplift: Tectonophysics, v. 385, p. 59-84.

Pfiffner, O.A., 1986, Evolution of the north Alpine foreland basin in the Central Alps: Special Publications of the International Association of Sedimentologists, v. 8, p. 219-228.

Pfiffner, O.A., Schlunegger, F., Buiter, S.J.H., (2002), The Swiss Alps and their peripheral foreland basin: Stratigraphic response to deep crustal processes: Tectonics, v. 21, p. 1009, 10.1029/2000TC900039.

Pieri, M., Groppi, G., 1981, Subsurface geological structure of the Po Plain. Consiglio Nazionale delle Richerche, Pubblicazione 414 del Progetto Finalizzato Geodinamica, 23 p.

Platt, L.B., 1966, Discussions Orogeny and Geochronology: American Journal of Science, v. 264, p. 745-750.

Platt, J.P., England, P.C., 1993, Convective removal of lithosphere beneath mountain belts: thermal and mechanical consequences: American Journal of Science, v. 293, p. 307-336.

Rahn, M.K., 1994, Incipient metamorphism of the Glarus Alps: Petrology of the Taveyanne Greywacke and fission track dating: PhD Thesis, University of Basel, Switzerland, 209 p.

Rahn, M.K., 2005, Apatite fission track ages from the Adula nappe: late-stage exhumation and relief evolution: Schweitzerische Mineralogische und Petrographische Mitteilungen, v. 85, p. 233-245.

Rahn, M.K., Grasemann, B., 1999, Fission track and numerical thermal modeling of differential exhumation of the Glarus thrust plane (Switzerland): Earth and Planetary Science Letters, v. 169, p. 245-259.

Rahn, M.K., Hurford, A.J., Frey, M., 1997, Rotation and exhumation of a thrust plane: apatite fission-track data from he Glarus thrust, Switzerland: Geology, v. 25, p. 599-602.

Raymo, M.E., Ruddiman, W.F., 1992, Tectonic forcing of late Cenozoic climate: Nature, v. 359, p. 117-122.

Reiners, P.W., Ehlers, T.A., Mitchell, S.G., Montgomery, D.R., 2003, Coupled spatial variations in precipitation and long-term erosion rates across the Washington Cascades: Nature, v. 426, p. 645-647.

Reiners, P.W., Ehlers, T.A., Zeitler, P.K., 2005, Past, Present, and Future of Thermochronology: Reviews in Mineralogy and Geochemistry, v. 58, p. 1-18.

Reiners, P.W., Spell, T.L., Nicolescu, S., Zanetti, K.A., 2004, Zircon (U-Th)/He thermochronometry: He diffusion and comparison with 40Ar/39Ar dating: Geochimica et Cosmochimica Acta, v. 68, p. 1857-1887.

Ring, U., Brandon, M.T., Willett, S.D., Lister, G.S., 1999, Exhumation processes: Geological Society, London, Special Publications, v. 154, p. 1-27.

Roe, G.H., Stolar, D.B., and Willett, S.D., 2006, Response of a steady-state critical wedge orogen to changes in climate and tectonic forcing: Geological Society of America Special Paper, v. 398, p. 227-239.

Rosenbaum, G., Lister, G.S., 2005, The Western Alps from the Jurassic to Oligocene: spatio-temporal constraints and evolutionary reconstructions: Earth-Science Reviews, v. 69, p. 281-306.

Sabil, N., 1995, La datation par traces de fission : aspects méthodologiques et applications thermochronologiques en contextes alpins et de marge continentale: PhD Thesis, University of Grenoble, France, 238 p.

Scardia, G., Muttoni, G., Sciunnach, D., 2006, Subsurface magnetostratigraphy of Pleistocene sediments from the Po Plain (Italy): Constraints on rates of sedimentation and rock uplift: Geological Society of America Bulletin, v. 118, p. 1299-1312.

Schär, J.P., Reimer, G.M., Wagner, G.A., 1975, Actual and ancient uplift rate in the Gotthard region, Swiss Alps: A comparison between precise levelling and fission track apatite age: Tectonophysics, v. 29, p. 293-300.

Schlatter, A., 2007, Das neue Landeshöhennetz der Schweiz LHN95; Geodätisch-geophysikalische Arbeiten in der Schweiz, Schweizerische Geodätische Kommission

Schlatter, A., Schneider, D., Geiger, A., Kahle, H.-G., 2005, Recent vertical movements from precise levelling in the vicinity of the city of Basel, Switzerland: International Journal of Earth Sciences, v. 94, p. 507-514.

Schlunegger, F., Hinderer, M., 2001, Crustal uplift in the Alps: why the drainage pattern matters: Terra Nova, v. 13, p. 425-432.

Schlunegger, F., Hinderer, M., 2003, Pleistocene/Holocene climate change, re-establishment of fluvial drainage network and increase in relief in the Swiss Alps: Terra Nova, v. 15, p. 88-95.

Schlunegger, F., Matter, A., Burbank, D.W., Leu, W., Mange, M., Matyas, J., 1997, Sedimentary sequences, seismofacies and evolution of depositional systems of the Oligo/Miocene Lower Freshwater Molasse Group, Switzerland: Basin Research, v. 9, p. 1-26.

Schlunegger, F., Willett, S.D., 1999, Spatial and temporal variations in exhumation of the central Swiss Alps and implications for exhumation mechanisms: Geological Society, London, Special Publications, v. 154, p. 157-179.

Schmid, S.M., Fügenschuh, B., Kissling, E., Schuster, R., 2004, Tectonic map and overall architecture of the Alpine orogen: Eclogae geologicae Helvetiae, v. 97, p. 93-117.

Schmid, S.M., Kissling, E., 2000, The arc of the western Alps in the light of geophysical data on deep crustal structure: Tectonics, v. 19, p. 62-85.

Schmid, S.M., Pfiffner, O.A., Froitzheim, N., Schönborn, G., Kissling, E., 1996, Geophysical-geological transect and tectonic evolution of the Swiss-Italian Alps: Tectonics, v. 15, p. 1036-1064.

Schwarb, M., Daly, C., Frei, C., Schär, C., 2001, Mean annual and seasonal precipitation in the European Alps 1971-1990, Hydrological Atlas of Switzerland: Berne, Switzerland, Institute of Geography of the University of Berne, p. Plates 2.6 and 2.7.

Schwartz, S., 2000, La zone piémontaise des Alpes occidentales : un paléo-complexe de subduction. Arguments métamorphiques, géochronologiques et structuraux: PhD Thesis, University of Lyon 1, France, 341 p.

Selverstone, J., 2005, Are the Alps collapsing?: Annual Review of Earth and Planetary Sciences, v. 33, p. 113-132.

Serpelloni, E., Anzidei, M., Baldi, P., Casula, G., and Galvani, A., 2005, Crustal velocity and strain-rate fields in Italy and surrounding regions: new results from the analysis of permanent and non-permanent GPS networks: Geophysical Journal International, v. 161, p. 861-880.

Seward, D., Ford, M., Bürgisser, J., Lickorish, H., Williams, E.A., Meckel, L.D.III, 1999, Preliminary results of fission track analyses in the Southern Pelvoux area, SE France: Memorie di Scienze Geologiche Padova, v. 51, p. 25-31.

Seward, D., Mancktelow, N.S., 1994, Neogene kinematics of the central and Western Alps: Evidence from fission-track dating: Geology, v. 22, p. 803-806.

Shuster, D.L., Farley, K.A., 2005, 4He/3He thermochronometry: Theory, Practice, and Potential Complications: Reviews in Mineralogy and Geochemistry, v. 58, p. 181-203.

Shuster, D.L., Flowers, R.M., Farley, K.A., 2006, The influence of natural radiation damage on helium diffusion kinetics in apatite: Earth and Planetary Science Letter, v. 249, p. 148-161.

Sinclair, H.D., 1996, Plan-view curvature of foreland basins and its implications for the palaeostrength of the lithosphere underlying the western Alps: Basin Research, v. 8, p. 173-182.

Sinclair, H.D., 1997, Flysch to molasse transition in peripheral foreland basins; the role of the passive margin versus slab breakoff: Geology, v. 25, p. 1123-1126.

Soom, M.A., 1990, Abkühlungs- und Hebungsgeschichte der Externmassive und der penninischen Decken beidseits der Simplon-Rhone-Linie seit dem Oligozän: Spaltspurdatierung and Apatit/Zirkon und K-Ar-Datierungen an Biotit/Muskovit (westliche Zentralalpen): PhD Thesis, University of Bern, Switzerland, 64 p.

Spencer, A.S., Kohn, B., Gleadow, A., Norman, M., Belton, D., Carter, T., 2004, The importance of residing in a good neighbourhood: rechecking the rules of the game for apatite (U-Th)/He thermochronometry: Proceedings of the 10th International Conference on Fission Track Dating and Thermochronololgy, Amsterdam, The Netherlands, p. 20.

Stampfli, G.M., Mosar, J., Marquer, D., Marchant, R., Baudin, T., Borel, G., 1998, Subduction and obduction processes in the Swiss Alps: Tectonophysics, v. 296, p. 159-204.

Steiner, H., 1984, Mineralogisch-petrographische, geochemische und isotopengeologische Untersuchungen an einem Meta-Lamprophyr und seinem granodioritischen Nebengestein (Matorello-Gneis) aus der Maggia-Decke: Schweizerische Mineralogische und Petrographische Mitteilungen, v. 64, p. 227-259.

Stephenson, J., Gallagher, K., Holmes, C.C., 2006, Low temperature thermochronology and strategies for multiple samples 2: Partition modelling for 2D/3D distributions with discontinuities: Earth and Planetary Science Letters, v. 241, p. 557-570.

Stüwe, K., White, L., Brown, R., 1994, The influence of eroding topography on steady-state isotherms. Application to fission track analysis: Earth and Planetary Science Letters, v. 124, p. 63-74.

Sue, C., Delacou, B., Champagnac, J.-D., Allanic, C., Burkhard, M., 2007a, Aseismic deformation in the Alps: GPS vs. seismic strain quantification: Terra Nova, v. 19, p. 182-188.

Sue, C., Delacou, B., Champagnac, J.-D., Allanic, C., Tricart, P., Burkhard, M., 2007b, Extensional neotectonics around the bend of the Western/Central Alps: an overview: International Journal of Earth Sciences, v. 96, p. 1001-1029.

Timar-Geng, Z., Grujic, D., Rahn, M., 2004, Deformation at the Leventina-Simano nappe boundary, Central Alps, Switzerland: Eclogae geologicae Helvetiae, v. 97, p. 265-278.

Trautwein, B., 2000, Detritus provenance and thermal history of the Rhenodanubian flysch zone: mosaicstones for the reconstruction of the geodynamic evolution of the Eastern Alps. Tübinger Geowissenschaftliche Arbeiten v. 59, 75 p.

Tricart, P., 2004, From extension to transpression during the final exhumation of the Pelvoux and Argentera massifs, Western Alps: Eclogae geologicae Helvetiae, v. 97, p. 429-439.

Tricart, P., van der Beek, P., Schwartz, S., Labrin, E., 2007, Diachronous late-stage exhumation across the Western Alpine arc: constraints from apatite fission track thermochronology between the Pelvoux and Dora-Maira Massifs: Journal of the Geological Society, London, v. 163, p. 1-12.

Trümpy, R., 1960, Paleotectonic evolution of the central and Western Alps: Bulletin of the Geological Society of America, v. 71, p. 843-908.

van der Beek, P., Bourbon, P., 2008, A quantification of the glacial imprint on relief development in the French Western Alps: Geomorphology, v. 97, p. 52-72.

van der Beek, P., Robert, X., Mugnier, J.-L., Bernet, M., Huyghe, P., Labrin, E., 2006, Late Miocene-Recent exhumation of the central Himalaya and recycling in the foreland

basin assessed by apatite fission track thermochronology of Siwalik sediments, Nepal: Basin Research, v. 18, p. 413-434.

Vance, J.A., 1999, Zircon fission track evidence for a Jurassic (Tethyan) thermal event in the Western Alps: Memorie di Scienze Geologiche, Padova, v. 51, p. 473-476.

Vernon, A.J., van der Beek, P.A., Sinclair, H.D., Rahn, M.K., 2008, Increase in late Neogene denudation of the European Alps confirmed by analysis of a fission-track thermochronology database: Earth And Planetary Science Letters, v. 270, p. 316-329.

Vidal, L., Bickert, T., Wefer, G., Röhl, U., 2002, Late Miocene isotope stratigraphy of SE Atlantic ODP Site 1085: Relation to Messinian events: Marine Geology, v. 180, p. 71-85.

Viola, G., 2000, Kinematics and timing of the Periadriatic fault system in the Giudicarie region (central-Eastern Alps): PhD Thesis, n° 13590, ETH Zürich, Switzerland, 206 p.

von Raumer, J., Abrecht, J., Bussy, F., Lombardo, B., Menot, R.P., Schaltegger, U., 1999, The Palaeozoic metamorphic evolution of the Alpine External Massifs: Schweitzerische Mineralogische und Petrographische Mitteilungen, v. 79, p. 5-22.

Wagner, G.A., Miller, D.S., Jäger, E., 1979, Fission track ages on apatite of Bergell rocks from central Alps and Bergell boulders in Oligocene sediments:Earth and Planetary Science Letters, v. 45, p. 355-360.

Wagner, G.A., Reimer, G.M., 1972, Fission track tectonics: The tectonic interpretation of fission track apatite ages: Earth and Planetary Science Letters, v. 14, p. 263-268.

Wagner, G.A., Reimer, G.M., Jäger, E., 1977, Cooling ages derived by apatite fission track, mica Rb-Sr and K-Ar dating: the uplift and cooling history of the Central Alps: Memorie di Scienze Geologiche, Padova, v. 30, p. 1-27.

Watson, D., 1999, The natural neighbor series manuals and source codes: Computers and Geosciences, v. 25, p. 463-466.

Weh, M., 1998, Tektonische Entwicklung der penninischen Sediment-Decken in Graubünden (Prättigau bis Oberhalbstein): PhD Thesis, University of Basel, Switzerland, 230 p.

Whipple, K.X., 2001, Fluvial landscape response timescale: How plausible is steady-state denudation?: American Journal of Science, v. 301, p. 313-325.

Willett, S.D., Schlunegger, F., Picotti, V., 2006, Messinian climate change and erosional destruction of the central European Alps: Geology, v. 34, p. 613-616.

Williamson, J.H., 1968, Least squares fitting of a straight line: Canadian Journal of Physics, v. 46, p. 1845-1847.

Wittmann, H., von Blanckenburg, F., Kruesmann, T., Norton, K.P., and Kubik, P.W., 2007, The relation between rock uplift and denudation from cosmogenic nuclides in river sediment in the Central Alps of Switzerland: Journal of Geophysical Research, v. 112, p. F04010, doi:10.1029/2006JF000729.

Wobus, C.W., Hodges, K.V., and Whipple, K.X., 2003, Has focused denudation sustained active thrusting at the Himalayan topographic front?: Geology, v. 31, p. 861-864.

Zhang, P., Molnar, P., Downes, W.R., 2001, Increased sedimentation rates and grain sizes 2-4 Myr ago due to the influence of climate change on erosion rates.: Nature, v. 410, p. 891-897.

Zwingmann, H., Mancktelow, N., 2004, Timing of Alpine fault gouges: Earth and Planetary Science Letters, v. 223, p. 415-425.